PB87-194783

Status and Evaluation of Calcitic SO2 Capture: Analysis of Facilities Performance

Energy and Environmental Research Corp.
Irvine, CA

Prepared for

Environmental Protection Agency
Research Triangle Park, NC

May 87

U.S. Department of Commerce
National Technical Information Service
NTIS

EPA/600/7-87/014
May 1987

PB87-194783

STATUS AND EVALUATION OF CALCITIC SO_2 CAPTURE: ANALYSIS OF FACILITIES PERFORMANCE

by:

G. D. Silcox, S. L. Chen, W. D. Clark, J. C. Kramlich,
J. F. La Fond, J. M. McCarthy, D. W. Pershing and W. R. Seeker

Energy and Environmental Research Corporation
18 Mason
Irvine, California 92718-2798

EPA Contract 68-02-4208

EPA Project Officer: Charles Masser
Air and Energy Engineering Research Laboratory
Office of Environmental Engineering and Technology Development
Research Triangle Park, NC 27711

AIR AND ENERGY ENGINEERING RESEARCH LABORATORY
OFFICE OF RESEARCH AND DEVELOPMENT
U.S. ENVIRONMENTAL PROTECTION AGENCY
RESEARCH TRIANGLE PARK, NC 27711

REPRODUCED BY
U.S. DEPARTMENT OF COMMERCE
NATIONAL TECHNICAL
INFORMATION SERVICE
SPRINGFIELD, VA 22161

TECHNICAL REPORT DATA

(Please read Instructions on the reverse before completing)

1. REPORT NO. EPA/600/7-87/014	2.	3. RECIPIENT'S ACCESSION NO. PB87-194783/AS
4. TITLE AND SUBTITLE Status and Evaluation of Calcitic SO_2 Capture: Analysis of Facilities Performance		5. REPORT DATE May 1987
		6. PERFORMING ORGANIZATION CODE
7. AUTHOR(S) G. D. Silcox, S. L. Chen, W. D. Clark, J. C. Kramlich, J. F. LaFond, J. M. McCarthy, D. W. Pershing, and W. R. Seeker		8. PERFORMING ORGANIZATION REPORT NO.
9. PERFORMING ORGANIZATION NAME AND ADDRESS Energy and Environmental Research Corporation 18 Mason Irvine, California 92718-2798		10. PROGRAM ELEMENT NO.
		11. CONTRACT/GRANT NO. 68-02-4208
12. SPONSORING AGENCY NAME AND ADDRESS EPA, Office of Research and Development Air and Energy Engineering Research Laboratory Research Triangle Park, NC 27711		13. TYPE OF REPORT AND PERIOD COVERED Final; 9/84 - 12/86
		14. SPONSORING AGENCY CODE EPA/600/13

15. SUPPLEMENTARY NOTES AEERL project officer is Charles C. Masser, Mail Drop 61, 919/541-7586.

16. ABSTRACT

The report gives results of a characterization of the current state of knowledge regarding SO2 capture by dry calcitic sorbent injection. A key difficulty in reviewing the literature on the subject is the apparent diversity in the experimental results, caused by the extreme complexity of simulating the practical sorbent utilization process. Variables include sorbent properties, furnace experimental parameters, and furnace equipment (e.g., injectors, sampling system). Failure to control or report all possible variables in each experiment produces a diversity of results. In this project, the experimental data on dry sorbent injection are compiled and critically compared. Sulfation and activation models are developed and used to identify sorbent properties and furnace environment parameters likely to be of importance. The results of the examination of data and the model evaluation indicated areas where original experimental work could be applied to resolve key issues. The experimental portion of the program developed information on injection temperature, quench rate, and sorbent properties. These results are used to define the overall optimum injection condition for a variety of furnace configurations.

17. KEY WORDS AND DOCUMENT ANALYSIS

a. DESCRIPTORS		b. IDENTIFIERS/OPEN ENDED TERMS	c. COSATI Field/Group	
Pollution	Coal	Pollution Control	13B	21D
Sulfur Dioxide	Combustion	Stationary Sources	07B	21B
Sorbents		Dry Sorbent Injection	11G	
Calcines			11B	
Mathematical Models			12A	
Sulfation			07C	

18. DISTRIBUTION STATEMENT Release to Public	19. SECURITY CLASS *(This Report)* Unclassified	21. NO. OF PAGES 376
	20. SECURITY CLASS *(This page)* Unclassified	22. PRICE

EPA Form 2220-1 (9-73)

NOTICE

This document has been reviewed in accordance with U.S. Environmental Protection Agency policy and approved for publication. Mention of trade names or commercial products does not constitute endorsement or recommendation for use.

TABLE OF CONTENTS

Section Page

1.0 EXECUTIVE SUMMARY. 1-1
1.1 Program Objectives and Approach 1-1
1.2 Modeling Approach 1-3
1.3 Process Fundamentals 1-10
1.3.1 Activation 1-10
1.3.2 Sulfation. 1-14
1.4 Influence of Process Parameters 1-21
1.5 Full-Scale Process Performance 1-27

2.0 INTRODUCTION 2-1
2.1 Background 2-1
2.2 Program Objectives 2-2
2.3 Program Approach 2-3
2.4 Report Organization 2-4

3.0 ACTIVATION FUNDAMENTALS. 3-1
3.1 Compilation of Experimental Results 3-2
3.1.1 Calcination Data for Carbonates. 3-2
3.1.2 Calcination Data for Hydrates. 3-6
3.1.3 Physical Consequences of Activation. 3-10
3.2 Modeling Approach 3-19
3.3 Comparison with Data and Applications 3-27
3.3.1 CO_2 Partial Pressure and Surface Area Profiles . 3-27
3.3.2 Comparison of Model to Data. 3-32
3.3.3 Hydrates and Carbonates 3-40
3.4 Conclusions 3-43

4.0 SULFATION FUNDAMENTALS (ISOTHERMAL PRECALCINES). 4-1

TABLE OF CONTENTS (Continued)

Section Page

4.1 Compilation of Experimental Results 4-1
  4.1.1 Fundamental Sulfation Kinetics 4-1
  4.1.2 Time Resolved Sulfation. 4-4
  4.1.3 Particle Size Effects. 4-14
  4.1.4 SO_2 Concentration Effects. 4-20
  4.1.5 Influence of Injection Temperature 4-20
  4.1.6 Closure. 4-24
4.2 Modeling Approaches 4-24
  4.2.1 The Grain Model. 4-25
  4.2.2 The Distributed Grain Size Model 4-31
  4.2.3 Random Pore Model. 4-33
  4.2.4 The Distributed Pore Model 4-37
  4.2.5 Comparison of Model Formulations 4-40
4.3 Analysis of Experimental Results. 4-42
  4.3.1 Differential Reactor Data. 4-43
  4.3.2 Time-Resolved Isothermal Results 4-43
  4.3.3 Influence of Injection Temperature 4-54
  4.3.4 Closure. 4-60

5.0 COUPLED ACTIVATION AND SULFATION 5-1
5.1 Compilation of Experimental Results 5-1
  5.1.1 Time-Resolved Sulfation. 5-1
  5.1.2 Particle Size. 5-9
  5.1.3 Injection Temperature. 5-13
  5.1.4 Closure. 5-20
5.2 Modeling Approaches 5-22
  5.2.1 Initialization Model 5-22
  5.2.2 Progressive Shell Model. 5-23
5.3 Analysis of Experimental Results. 5-28
  5.3.1 Time-Resolved Predictions. 5-28
  5.3.2 Influence of Particle Heating Rate 5-30

TABLE OF CONTENTS (Continued)

Section Page

6.0 PROCESS PARAMETER STUDIES: A COMPILATION OF BENCH SCALE RESULTS. 6-1
6.1 Thermal History 6-1
6.2 Sorbent Particle Size and Type 6-11
6.3 SO_2 Concentration 6-14
6.4 Conclusions and Key Experimental Issues 6-14

7.0 EXPERIMENTAL RESULTS - THIS PROGRAM. 7-1
7.1 Experimental Facilities 7-1
7.1.1 Isothermal Reactor, Control Temperature Tower and Boiler Simulator Furnace 7-1
7.1.2 Measurement Systems and Analytical Methods . . . 7-7
7.1.3 Sorbents and Fuels 7-10
7.1.4 Sorbent Injection Technique. 7-10
7.2 Influence of Thermal History. 7-12
7.2.1 Injection Temperature. 7-17
7.2.2 Quench Rate. 7-21
7.3 Influence of Sorbent Properties 7-32
7.3.1 Sorbent Type 7-32
7.3.2 Particle Size. 7-32

8.0 ANALYSIS OF PROCESS PARAMETERS 8-1
8.1 Analysis of Process Parameters 8-1
8.2 Particle Size 8-7
8.3 SO_2 Concentration 8-7
8.4 Conclusions 8-10

9.0 LARGE-SCALE TEST RESULTS 9-1
9.1 Compilation of Experimental Results 9-1
9.2 The Overall Sulfation Modeling Approach 9-24
9.3 Comparison 9-30

TABLE OF CONTENTS (Continued)

Section Page

10.0 CONCLUSION 10-1

11.0 REFERENCES 11-1

APPENDICES

Appendix A - Descriptions of Various Experimental Systems . . . A-1
Appendix B - Detailed Descriptions of Various Computer Models . B-1
Appendix C - Tabulation of Experimental Data. C-1
Appendix D - Quality Assurance. D-1
Appendix E - Southern Research Institute Subcontractor Report . E-1

LIST OF FIGURES

Figure | Page

1-1 Program structure 1-2

1-2 Schematic of the calcination model 1-4

1-3 A schematic of the grain model. The enlarged view of the porous particle shows a dark band of product of radius r_g', the initial grain radius, r_g, and the radius of the unreacted core of reactant, r. 1-6

1-4 Schematics of the distributed pore model showing (a) the porous spherical CaO particle and (b) a closeup of a sulfated pore 1-7

1-5 The differential reactor data of Borgwardt and Bruce (1986) for 1 μm precalcined Fredonia limestone 1-9

1-6 The relative rates of hydrate and carbonate calcination as measured by Bortz and Flament (1985) at 900°C using 6 μm particles and an isothermal reactor. 1-11

1-7 Surface area development and decay at 1000°C 1-12

1-8 Activation model predictions 1-13

1-9 Comparison of measured pore size distribution as a function of time 1-15

1-10 Comparison of distributed pore model and experimental data. Sulfation conditions for sorbent in a) and b): 1256K, 2000 ppm SO_2, and Ca/S = 2 (Newton, 1986). Sulfation conditions for sorbents in c) and d): 1273K, 3100 ppm SO_2, and Ca/S = 2 (results generated under EPA Contract 68-02-3633). 1-16

1-11 Grain model predictions of EER's ITR data. The predictions include the loss of sorbent surface area due to sintering. . . 1-18

1-12 Time-resolved capture for Linwood atmospheric hydrate when injected into the CTT at 1260°C (2300°F) under two different quench rates 1-19

1-13 Pore size distribution of Longview Lime with and without SO_2 . 1-20

1-14 The effect of injection temperature on SO_2 capture at Ca/S = 2 for hydrated limes. See Table 6-2 for an explantion of the plotting symbols 1-22

1-15 Capture at elevated injection temperatures 1-23

LIST OF FIGURES (CONTINUED)

Figure		Page
1-16	Comparison of the impact of quench rate on sorbent injection temperature for Linwood hydrate and Vicron carbonate	1-24
1-17	Comparison of sulfur capture for four different sorbents as particle size is varied.	1-26
1-18	Controlled Temperature Tower (CTT) data obtained with Linwood atmospheric hydrate for three different fuels. The data were used to calibrate the sulfation model as indicated by the solid line.	1-29
1-19	A comparison of SO_2 capture results from Tiefstack (see Figure 9-14 with grain model predictions. The grain model was calibrated against the bench-scale data of Figure 1-18 and then used to extrapolate to the Tiefstack conditions . . .	1-30
3-1	Arrhenius plot for calcium carbonate decomposition, from Borgwardt (1985)	3-4
3-2	Comparison of kinetic model with time resolved data for 10 micron Fredonia limestone. Source: Borgwardt (1985) . . .	3-5
3-3	Arrhenius plot for calcium carbonate decomposition, from Snow (1985).	3-7
3-4	Decomposition of $CaCO_3$ particles in the IFRF isothermal reactor (Bortz and Flament, 1985)	3-8
3-5	Correlation of time for 50 percent calcination with peak particle temperature (data generated under EPA Contract 68-02-3995).	3-9
3-6	Decomposition of $Ca(OH)_2$ particles in the IFRF isothermal reactor (Bortz and Flament, 1985)	3-11
3-7	Sintering extents of CaO under nitrogen in the EPA differential reactor (Borgwardt et al., 1985).	3-13
3-8	Acceleration of sintering in the presence of CO_2 in the EPA reactor (Borgwardt et al., 1985)	3-14
3-9	Short time desurfacing profiles under isothermal flue-gas conditions for a 32 m^2/g precalcine.	3-15
3-10	Surface area development and decay at 1000°C	3-17
3-11	Particle size distributions for Vicron 45-3 pulverized limestone before and after flame treatment	3-18

LIST OF FIGURES (CONTINUED)

Figure		Page
3-12	Schematic of the calcination model	3-20
3-13	The isothermal flow reactor data of Borgwardt (1984) for a calcine prepared at 1000°C. The precalcine particles were conveyed in pure N_2. The solid lines are model predictions based on Equations 3.16 and 3.18	3-26
3-14	Model predictions of peak CO_2 partial pressure at the CaO-$CaCO_3$ interface for calcination at isothermal conditions with a bulk gas CO_2 pressure of 0.065 atm	3-28
3-15	Model predictions showing the influence of time on the extent of calcination and the CO_2 partial pressure at the $CaCO_3$-CaO interface.	3-29
3-16	Model predictions showing CO_2 pressure gradients and the surface area profile for a 50 μm particle being calcined at 2200°F.	3-30
3-17	Model predictions showing CO_2 pressure gradients and the surface area profile for a 5 m particle being calcined at 2200°F. The extent of calcination is 48 percent and the bulk gas CO_2 pressure is 0.065 atm	3-31
3-18	The calcination data of Borgwardt (1985) for Georgia marble compared to model predictions showing the effect of particle size. The marble was calcined in N_2 at 710°C in a differential reactor	3-33
3-19	The data of Borgwardt (1985) for 10 M Fredonia limestone calcined in N_2 in a flow reactor. The solid lines are model predictions.	3-34
3-20	The B.E.T. surface area data of Slaughter (1986) obtained in a natural gas-burning, flow reactor at isothermal conditions and a residence time of 0.5 sec. The solid lines are model predictions at particle diameters of 1, 11, and 50 μm.	3-35
3-21	The data of Slaughter (1986) showing the effect of time on surface area for Vicron 45-3 at 1800°F, isothermal conditions. The solid lines are model predictions for several particle diameters.	3-37
3-22	Model predictions showing the effect of time on surface area development at 2200°F for 1 and 11μm particles for 1 and 5 μm hydrates and carbonates	3-38

LIST OF FIGURES (Continued)

Figure Page

3-23 Isothermal, flow-reactor data of EER showing the effect of time on surface area for a 10μm, precalcined limestone. The solid lines are model predictions. 3-39

3-24 The relative rates of hydrate and carbonate calcination as measured by Bortz and Flament (1985) at 900°C using 6 μm particles and an isothermal reactor 3-41

3-25 Activation model predictions of the effect of sorbent type for 1 and 5 μm hydrates and carbonates 3-42

4-1 Reactivity of 3.0-m^2/g CaO as a function of temperature at P_{SO_2} = 304 Pa (3000 ppm). Results from Borgwardt and Bruce (1986) 4-3

4-2 Reactivity of CaO at 800°C as a function of its specific surface area. P_{SO_2} = 304 Pa. Results are from Borgwardt and Bruce (1986) 4-5

4-3 The maximum conversion attained at long SO_2-exposure times also increases with specific surface area (S_g, in m^2/g). Temperature = 800°C, P_{SO_2} = 304 Pa. Results are from Borgwardt and Bruce (1986) 4-6

4-4 Effect of specific surface area and temperature on CaO reactivity at constant SO_2 partial pressure (304 Pa). Results are from Borgwardt and Bruce (1986). 4-7

4-5 Effect of SO_2 partial pressure on CaO reactivity. Results are from Borgwardt and Bruce (1986). 4-8

4-6 Isothermal reactivity of calcined sorbents at 1000°C in the the EER isothermal reactor at Ca/S = 1.0 (data generated under EPA Contract 68-02-3633) 4-10

4-7 Isothermal reactivity of calcined sorbents at 1200°C in the EER isothermal reactor at Ca/S = 1.0 (data generated under EPA Contract 68-02-3633. 4-12

4-8 SO_2 capture profiles for sintered and unsintered 10- and 20 μm diameter precalcines in the EER isothermal reactor (data generated under EPA Contract 68-02-3633) 4-13

4-9 SO_2 capture profiles at Ca/S = 1, 2, and 3 for a 1.7 μm precalcine sulfated at 980°C and 2000 ppm SO_2. Results from Newton (1986) 4-15

LIST OF FIGURES (Continued)

Section Page

4-10 SO_2 capture profiles at Ca/S = 1, 2, and 3 for a 6.8 μm precalcine sulfated at 1260 K and 2000 ppm SO_2. Results from Newton (1986) 4-16

4-11 Effect of surface area on SO_2 capture profile. Results from Bortz et al. (1986) 4-17

4-12 Sulfation conversion of pre-decomposed limestone effect of residence time (Snow, 1985). 4-18

4-13 Influence of precalcine particle size on sorbent reactivity. (EER data generated under EPA Contract 68-02-3633) 4-19

4-14 Mean pore diameter of precalcines as a function of particle diameter (EER data generated under EPA Contract 68-02-3995 . . 4-21

4-15 Effect of SO_2 concentration on percent SO_2 capture and percent calcium utilization for precalcined sorbents 4-22

4-16 Effect of temperature on calcium utilization of precalcine sorbents (EER data generated under EPA Contract 68-02-3995). . 4-23

4-17 A schematic of the grain model. The enlarged view of the porous particle shows a dark band of product of radius r_g', the initial grain radius, r_g, and the radius of the unreacted core of reactant, r. 4-29

4-18 Distributed grain model predictions where no sintering is allowed, the average surface area is 54.5 m^2/g, the temperature is 1100°C and constant, the porosity is 0.5, and the particle diameter is 5 μm. 4-32

4-19 Conceptual illustration of pore model for CaO/SO_2 reaction . . 4-35

4-20 Application of random pore model to data of Borgwardt (1970). Solid lines represent the current model calculations, dotted lines represent Bhatia & Perlmutter's calculations (1981). . . 4-38

4-21 Schematics of the distributed pore model showing (a) the porous spherical CaO particle and (b) a closeup of a sulfated pore. 4-39

4-22 The differential reactor data of Borgwardt and Bruce (1986) for 1 μm precalcined Fredonia limestone. The solid lines are the model fit to the data. 4-44

LIST OF FIGURES (Continued)

Section		Page
4-23	The differential reactor data of Borgwardt and Bruce (1986) at 800^{0}C for 1 μm precalcined Fredonia limestone. The solid lines are model predictions.	4-45
4-24	The differential reactor data of Borgwardt and Bruce (1986) for precalcined 1 μm Fredonia limestone. The solid lines are model predictions.	4-45
4-25	The differential reactor data of Borgwardt and Bruce (1986) for precalcined 1 μm Georgia marble. The solid lines are model fits	4-47
4-26	The differential reactor data of Borgwardt and Bruce (1986) for 1 μm precalcined Fredonia limestone. The solid lines are model fits	4-48
4-27	Data of Borgwardt et al. (1986) and model predictions for 1 micron, 3 m^2/g particles at 3000 ppm SO_2	4-49
4-28	SO_2 capture profiles for a 2 μm precalcine at 1000^{o}C and 1200^{o}PC in the presence of 3100 ppm SO_2. The solid curves represent model predictions for the conditions shown based upon the measured physical properties of the sorbents.	4-51
4-29	Comparison of distributed pore model and experimental data. Sulfation conditions for sorbents in a) and b): 1256K, 2000 ppm SO_2, and Ca/S = 2. Sulfation conditions for sorbents in c) and d): 1273K, 3100 ppm SO_2, and Ca/S = 2 (EER data generated under EPA Contract 68-02-3633)	4-52
4-30	SO_2 concentration and radial profiles within a pore.	4-53
4-31	Loss of initial surface area due to pore mouth closure as predicted by the distributed pore model	4-55
4-32	Grain model predictions showing the effect of reaction or injection temperature for both isothermal and quenched systems. Sorbent surface area loss was allowed to occur during sulfation due to sintering.	4-56
4-33	Comparison of distributed pore model(with and without sintering) and experimental data (EER data generated under EPA Contract 68-02-3995)	4-57
5-1	Time-resolved SO_2 capture for Vicron 45-3 and Linwood hydrate hydrate at 1100^{o}C (Comparison of Straight vs Venturi precombustors. U of U data added for comparison (Newton, 1986). (EER data generated under EPA Contract 68-02-4239) . .	5-2

LIST OF FIGURES (Continued)

Figure Page

5-2 Sulfation performance of the various sorbents in the isothermal reactor at 1000°C and 3000 ppm SO_2 (data generated under EPA Contract 68-02-4239) 5-4

5-3 Conversion of carbonates to sulfates in various isothermal facilities 5-6

5-4 High temperature sulfation of limestone (Snow, 1985) 5-7

5-5 High temperature sulfation of limestone: fraction of CaO sulfated (Snow, 1985). 5-8

5-6 Comparison of facilities performance for calcium hydrates. (EER/ITR data generated under EPA Contract 68-02-4239) 5-10

5-7 Time resolved sulfation data in the University of Utah isothermal reactor at 1100°C and 1950-2118 ppm SO_2 for Longview hydrate (Newton, 1986). 5-11

5-8 Dependence of sorbent utilization on carbonate particle size (data generated under EPA Contract 68-02-3995) 5-12

5-9 Dependence of sorbent utilization on hydrate particle size (Bortz et al., 1986) 5-14

5-10 Effect of particle diameter on high temperature sulfation (Snow, 1985) 5-15

5-11 Isothermal hydrate conversions near the high temperature limit for sulfation in the EER isothermal reactor (data from Section 7.0). 5-16

5-12 Influence of isothermal reactor temperature on the utilization of limestone sorbents. 5-18

5-13 Influence of isothermal reactor temperature on the utilization of hydrated sorbents (EER data generated under EPA Contract 68-02-3633) 5-19

5-14 High temperature sulfation of limestone: effect of temperature (Argon highlighted) (Snow, 1985) 5-21

5-15 The predicted surface area development for 1 μm $Ca(OH)_2$ and 5 μm $CaCO_3$ at an isothermal temperature of 2000°F. 5-24

5-16 The data of Bortz and Flament (1985) showing the relative rates of calcination for 6 μm $Ca(OH)_2$ and $CaCO_3$ at 900°C. The materials were calcined in combustion gases. 5-25

LIST OF FIGURES (Continued)

Figure Page

5-17 Predicted sulfur capture level based on initial surface areas estimated with the activation model. A constant temperature of 2000°F and a SO_2 concentration of 2000 ppm were assumed 5-26

5-18 Grain model predictions of EER's ITR data. The predictions do not account for surface area loss due to sintering. 5-29

5-19 Grain model predictions of EER's ITR data. The predictions include the loss of sorbent surface area due to sintering. . . 5-31

5-20 Pore model predictions compared to Longview hydrate data; Utah isothermal data 5-32

5-21 Grain model predictions showing the unreasonably high surface areas required to fit EER's ITR data. A uniform grain size was assumed. 5-33

5-22 Comparison of ITR sulfation data with pore model predictions with and without rapid heating 5-35

6-1 The effect of injection temperature on SO_2 capture at Ca/S = 2 for hydrated limes. See Table 6-2 for an explanation of the plotting symbols 6-3

6-2 The effect of injection temperature on SO_2 capture at Ca/S = 2 for calcium carbonates. See Table 6-3 for an explanation of the plotting symbols. 6-6

6-3 The effect of quench rate on SO_2 capture at Ca/S = 2 for hydrates and carbonates. See Table 6-4 for an explanation of the plotting symbols. 6-7

6-4 The effect of residence time on SO_2 capture at Ca/S = 2 for hydrates and carbonates. See Table 6-5 for an explantion of the plotting symbols 6-9

6-5 The effect of particle size on SO_2 capture at Ca/S = 2 for hydrates and carbonates. See Table 6-6 for an explanation of the plotting symbols. 6-12

6-6 The effect of SO_2 concentration on SO_2 capture at Ca/S = 2 for hydrates and carbonates. See Table 6-7 for an explanation of the plotting symbols. 6-15

7-1 Schematic of the isothermal reactor (ITR). 7-2

7-2 Schematic detail of the precombustor/sliding burner assembly . 7-3

LIST OF FIGURES (Continued)

Figure Page

7-3 Cross-sectional views of the control temperature tower 7-5

7-4 Boiler simulator furnace (BSF) 7-6

7-5 Continuous monitoring sampling system. 7-8

7-6 SO_2 continuous monitoring system 7-9

7-7 BSF sorbent injector 7-13

7-8 Mixing for BSF sorbent injector. 7-14

7-9 Comparison of mixing for radial and axial injectors. 7-15

7-10 Influence of sorbent mixing on SO_2 capture 7-16

7-11 Influence of injection temperature on SO_2 capture. 7-18

7-12 Influence of injection temperature on time resolved capture. . 7-19

7-13 Furnace temperature downstream of sorbent injection. 7-20

7-14 Capture at elevated injection temperatures 7-22

7-15 Temperature profiles experienced by the sorbent in the CTT when injecting near a temperature of 1260°C (2300°F) 7-23

7-16 Sulfur capture for three sorbents under two different furnace quench rate conditions (Tinj = 1260°C (2300°F)) for each case) 7-25

7-17 Time-resolved capture for Linwood atmospheric hydrate when injected into the CTT at 1260°C (2300°F) under two different quench rates 7-27

7-18 Time-resolved capture for Vicron carbonate when injected into the CTT at 1260°C (2300°F) under two different quench rates. 7-28

7-19 Comparison of the impact of quench rate on sorbent injection temperature for Linwood hydrate and Vicron carbonate 7-30

7-20 Examples of temperature profiles from the BSF and CTT at similar injection temperatures 7-31

7-21 Comparison of sulfur capture capability for four different sorbent materials (Overmoe et al., 1986) 7-33

LIST OF FIGURES (Continued)

Figure		Page
7-22	Comparison of sorbent size distributions as measured by sedigraph technique.	7-35
7-23	Comparison of sulfur capture for four different sorbents as particle size is varied	7-36
7-24	Comparison of sulfur capture for four different sorbents at varied specific surface areas	7-38
7-25	Linwood hydrate (2.0 μm size cut).	7-39
7-26	Colton hydrate (5.1 μm size cut)	7-40
7-27	Linwood hydrate (2.0 μm) vs. Linwood carbonate (2.2 μm). . . .	7-42
7-28	Carbonate comparison: Vicron (8.8 μm) vs. Linwood (8.6 μm). .	7-44
8-1	Grain model predictions showing the effect of injection temperature and quench rate assuming initial and asympototic surface areas of 80 and $5 m^2/g$, a SO_2 concentration of 1500 ppm (wet, as meas.), and particle size of 2 μm	8-3
8-2	A schematic of the progress of the sulfation reaction for sorbent injected at temperatures in excess of the stability limit of $CaSO_4$	8-4
8-3	Grain model predictions showing the effect of residence time at different quench rates assuming an injection temperature of 2200°F and a sampling point temperature of 1600°F	8-6
8-4	Grain model predictions showing the effect of a particle diameter for different initial surface areas	8-8
8-5	Grain model predictions (assuming initial and asymtotic surface areas of 80 and $5 m^2/g$) and distributed pore model predictions showing the effect of SO_2 concentration.	8-9
9-1	Schematic of Shawnee Unit 10 showing injection locations . . .	9-2
9-2	Measured temperature profiles for the planes including the Shawnee unit's arch and lower rear injectors	9-3
9-3	Average SO_2 capture levels for three sorbents at the Shawnee steam plant: aragonite, marl, and Fredonia limestone.	9-4
9-4	A schematic of the Hoot Lake boiler showing the location of the sorbent injectors.	9-6

LIST OF FIGURES (Continued)

Figure		Page
9-5	Temperature distribution at furnace center plane for the Hoot Lake boiler as predicted by EER's boiler heat transfer code	9-7
9-6	SO_2 capture measurements for high-calcium hydrate at Hoot Lake for two injection levels and two boiler loads: floor 4 at full load, floor 4 at reduced load, and floor 3 at full load	9-8
9-7	The 50 x 10^6 Btu/hr IHI test facility as depicted by Vatsky and Schindler (1985), from "Limestone Injection Reduces SO_2 and NO_x Emissions." Mechanical Engineering, November 1985	9-9
9-8	The 110,000 pounds/hr DuPont boiler as depicted by Vatsky and Schindler (1985), from "Limestone Injection Reduces SO_2 and NO_x Emissions." Mechanical Engineering, November 1985	9-10
9-9	Pilot- and full-scale, limestone injection results as reported by Vatsky and Schindler (1985), from "Limestone Injection Reduces SO_2 and NO_x Emissions." Mechanical Engineering, November 1985	9-12
9-10	A schematic of Ontario Hydro's Lakeview G.S. Unit 4 showing the location of the sorbent injectors at an elevation of 339 ft	9-13
9-11	The SO_2 capture results of Cameron and Arnott (1986) for $Ca(OH)_2$ and $CaCO_3$ at two different loads	9-14
9-12	A schematic of the Tiefstack boiler 6	9-16
9-13	The time-temperature profile for the Tiefstack boiler based upon 3-D heat transfer calculations and on measurements	9-17
9-14	Sulfur capture results for the Tiefstack boiler	9-18
9-15	Sulfur capture data reported by Staudinger and Schrofelbauer for pulverized limestone and dolomite	9-19
9-16	SO_2 capture results obtained on EER's Large Water Tube Simulator (LWS)	9-21
9-17	A schematic of the LWS with the burner plate detached	9-22
9-18	Controlled Temperature Tower (CTT) data obtained with Linwood atmospheric hydrate for three different fuels	9-25

LIST OF FIGURES (Continued)

Figure Page

9-19 Schematic of procedure for sulfur capture modeling for jets in crossflow 9-26

9-20 Jet and sulfation model calculations showing sorbent jet properties and the corresponding overall sulfur capture levels 9-28

9-21 Sulfur capture predictions for Edgewater boiler using JICFIA and grain models showing the effect of incomplete mixing of the sorbent jet with the bulk furnace gases. 9-29

9-22 A comparison of SO_2 capture results from Tiefstack (see Figure 9-14) with grain model predictions. 9-31

A-1 Cross-sectional views of the control temperature tower A-2

A-2 A schematic of the BSF A-3

A-3 A schematic of the reactor used by Teixeira, et al. (1986) . . A-5

A-4 A schematic of the pilot combustor system of Beittel, et al., (1986) A-6

A-5 A schematic of the small boiler simulator. A-9

A-6 A schematic of the tower reactor A-10

A-7 A schematic of the flow reactor of Coutant, et al. (1971). . . A-11

B-1 A schematic of the grain model B-2

D-1 Continuous monitoring sampling system. D-4

D-2 Phase discrimination probe D-5

D-3 SO_2 continuous monitoring system D-6

D-4 Gas temperature measurement system D-12

D-5 Suction pyrometer aspirator pressure calibration for CTT . . . D-13

D-6 Suction pyrometer aspirator pressure calibration for BSF . . . D-14

D-7 Example of sorbent particle size distribution. D-21

LIST OF TABLES

Table		Page
1-1	Large-Scale Facility Comparison	1-28
4-1	Summary of Phenomena Considered	4-41
5-1	Pressure Hydrator Conditions	5-5
6-1	The Effect of Conveying Air on Reactant Gas Temperature	6-2
6-2	Symbol Key for Figure 6-1	6-4
6-3	Symbol Key for Figure 6-2	6-8
6-4	Symbol Key for Figure 6-3	6-8
6-5	Symbol Key for Figure 6-4	6-10
6-6	Symbol Key for Figure 6-5	6-13
6-7	Symbol Key for Figure 6-6	6-16
7-1	Properties of Sorbents	7-11
7-2	Calculated Distribution Between Hydrate and Carbonate for Four Different Sorbents and Their Size Cut Counterparts	7-43
9-1	Large-Scale Facility Comparison	9-23
A-1	System Configurations and Quench Rates	A-7
C-1	ITR Data Table	C-1
C-2	CTT Data Table	C-2
C-3	Mixing: SO_2 Tracer Data	C-5
C-4	SO_2 Capture Data	C-7
D-1	BSF and CTT Instrumentation	D-3
D-2	Precision, Accuracy and Completeness Data for Gas Species Instruments	D-8
D-3	Solid Analyses Precision and Accuracy Data	D-10
D-4	Typical Data for Temperature Variations Within the Isothermal Reactor - Nominal 1000°C Condition	D-15

LIST OF TABLES (Concluded)

Table Page

D-5 Calibration Procedures. D-17

D-6 Calibration Gases D-18

GEN 4208 F/R (1)

1.0 EXECUTIVE SUMMARY

1.1 Program Objectives and Approach

This report summarizes the theoretical and experimental studies conducted by EER as part of the Combustion System Similarity Criteria modeling study (EPA contract 68-02-4208). The objectives of this study were:

- To compile and compare the existing data on dry sorbent injection for SO_2 control as a function of experimental scale, sorbent type, injection conditions, etc.
- To identify differences in the experimental results and, where possible, to reconcile these discrepancies in terms of experimental system characteristics.
- To develop overall sulfation models which include consideration of the physical and chemical processes likely to be a major importance in upper furnace injection of dry, calcium based sorbents and validate these models using existing fundamental data.
- To use the overall sulfation models in conjunction with the experimental data to define the process fundamentals, establish combustion parameters critical to the overall optimization of sorbent injection, and define the optimum sorbent injection conditions.

Thus, the overall purpose of the program was to characterize the current state of knowledge regarding SO_2 capture by dry sorbent injection through a careful analysis of the existing experimental data base in conjunction with appropriate mathematical models and newly acquired experimental results.

The overall project approach is illustrated in Figure 1-1; the program consisted of four major tasks:

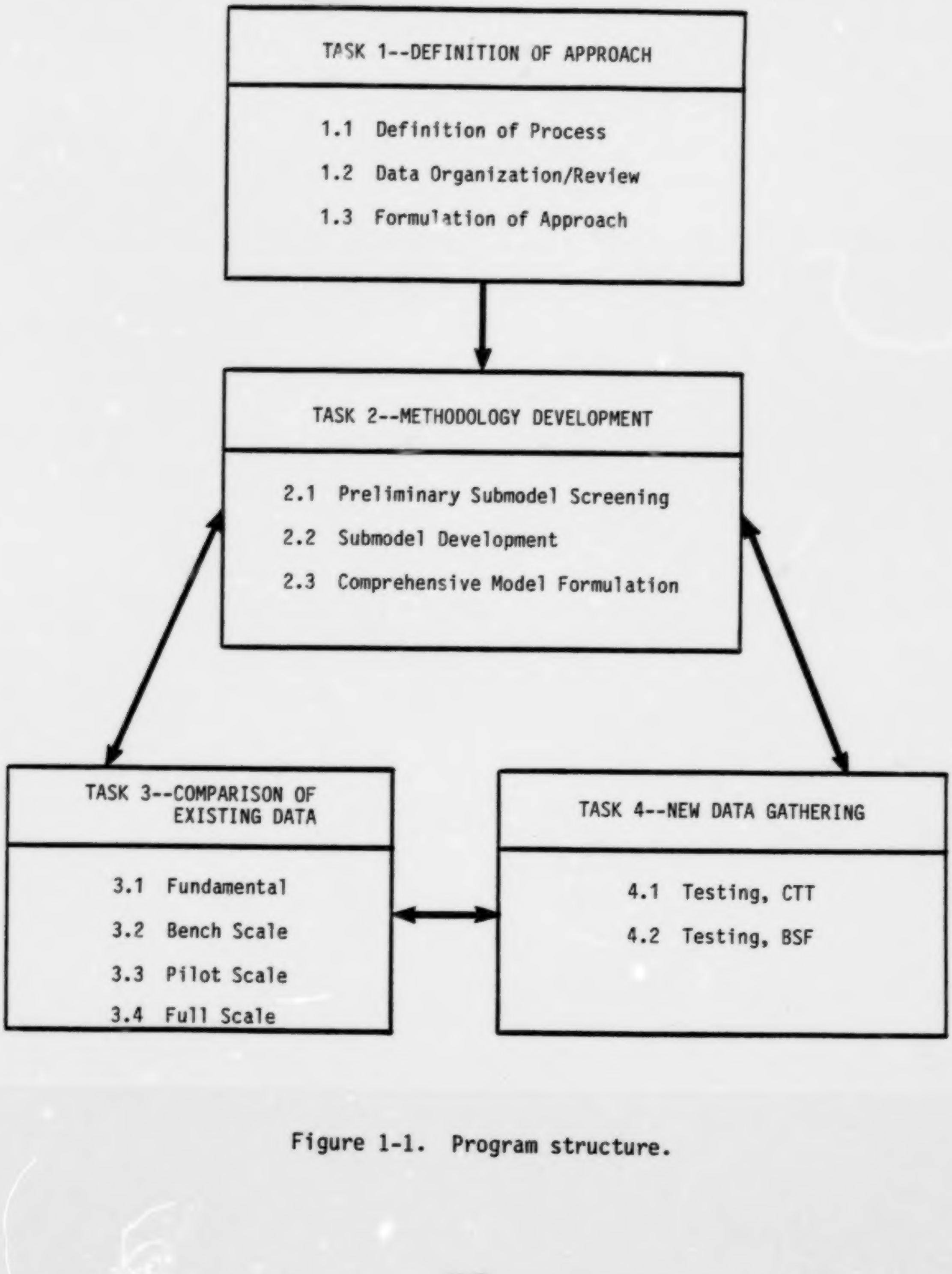
TASK 1--DEFINITION OF APPROACH
1.1 Definition of Process
1.2 Data Organization/Review
1.3 Formulation of Approach
TASK 2--METHODOLOGY DEVELOPMENT
2.1 Preliminary Submodel Screening
2.2 Submodel Development
2.3 Comprehensive Model Formulation
TASK 3--COMPARISON OF EXISTING DATA
3.1 Fundamental
3.2 Bench Scale
3.3 Pilot Scale
3.4 Full Scale
TASK 4--NEW DATA GATHERING
4.1 Testing, CTT
4.2 Testing, BSF

Figure 1-1. Program structure.

- Task 1 - Definition and formulation of approach.

- Task 2 - Development of the required sub-models and overall sorbent utilization modeling procedure

- Task 3 - Compilation and evaluation of the existing data base for fundamental, bench, pilot and full-scale experiments.

- Task 4 - Gathering of critical new data identified as missing from the current data base.

The data base for all four scales of experimentation was continuously expanded throughout the program because of the considerable activity at all levels of sorbent research.

One overall conclusion from the study is that the available experimental data at a particular scale are, on the whole, reasonably consistent and most of the apparent disagreements are the result of differences in experimental systems, sorbent characteristics, terminology and test conditions. Unfortunately the overall process is extremely complex; no single process step is universally rate controlling throughout the time and temperature regime typical of sorbent injection of a pulverized coal boiler. The availability and accessability of the calcium are controlled by the rates of calcination, sintering, and pore closure. The overall sulfation rate is also influenced by the intrinsic chemical rate and rates of pore and product layer diffusion. The mixing between the sorbent particles and the bulk is are important because mixing controls both the particle temperature and the local SO_2 concentration.

1.2 Modeling Approach

The first step in the sorbent injection process is the calcination of the injected hydrate or carbonate to form porous CaO. An activation model, illustrated schematically in Figure 1-2, was developed to simulate simultaneous calcination and surface area loss. It includes consideration of

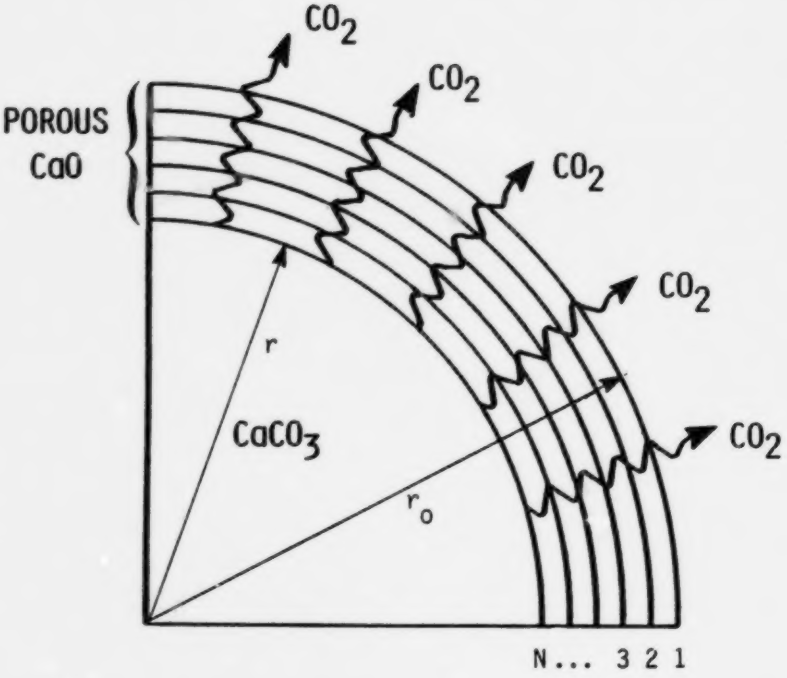
CO$_2$
CO$_2$
CO$_2$
CO$_2$
CO$_2$
POROUS
CaO
r
CaCO$_3$
r$_o$
N... 3 2 1

Figure 1-2. Schematic of the calcination model.

calcium carbonate decomposition at the CaO-$CaCO_3$ interface, diffusion of CO_2 through the CaO to the particle surface, diffusion of CO_2 from the particle surface to the bulk gas, and continuous, finite-rate surface area loss for all calcined material. The calcination process is represented by a spherical, shrinking core model with the intrinsic calcination rate dependent only on the chemical rate. The diffusion of gaseous CO_2 in the porous lime is assumed to occur by Knudsen and molecular diffusion. The rate of sintering is assumed to depend on the CO_2 concentration and the surface area.

Two types of sulfation models were used extensively on this program: a grain model and a distributed pore model. Both approaches assume that the reactive particles are spherical and fully calcined to CaO prior to the onset of sulfation.

The grain model (Figure 1-3) treats the CaO particle as a conglomerate of spherical CaO grains. The size distribution of the grains is set to match the measured BET surface area. Sulfation proceeds on the surface of each grain, with the result that the reaction may be limited by product layer buildup, which may both shield the grains and block access to the particle interior. A distribution of grain sizes is allowed. The current version of the model also includes grain growth (sintering) as a competitive process which occurs in parallel with sulfation and reduces the available, active surface area.

In the distributated pore model (Figure 1-4), the particle is assumed to be perforated by a long, non-intersecting, cylindrical pores of variable length. The size distribution of these pores is explicitly matched to that measured experimentally by mercury and nitrogen porosimetry. Calcium sulfate formation is allowed to occur on the external surface of the particle as well as on the internal surface of each pore. Since CaO formation is calculated as a function of the location in the pore, this model can predict the occlusion of small pores by plugging at the pore mouth while simultaneously predicting uniform filling of large pores. The distributed pore model allows for both normal and sulfate promoted sintering.

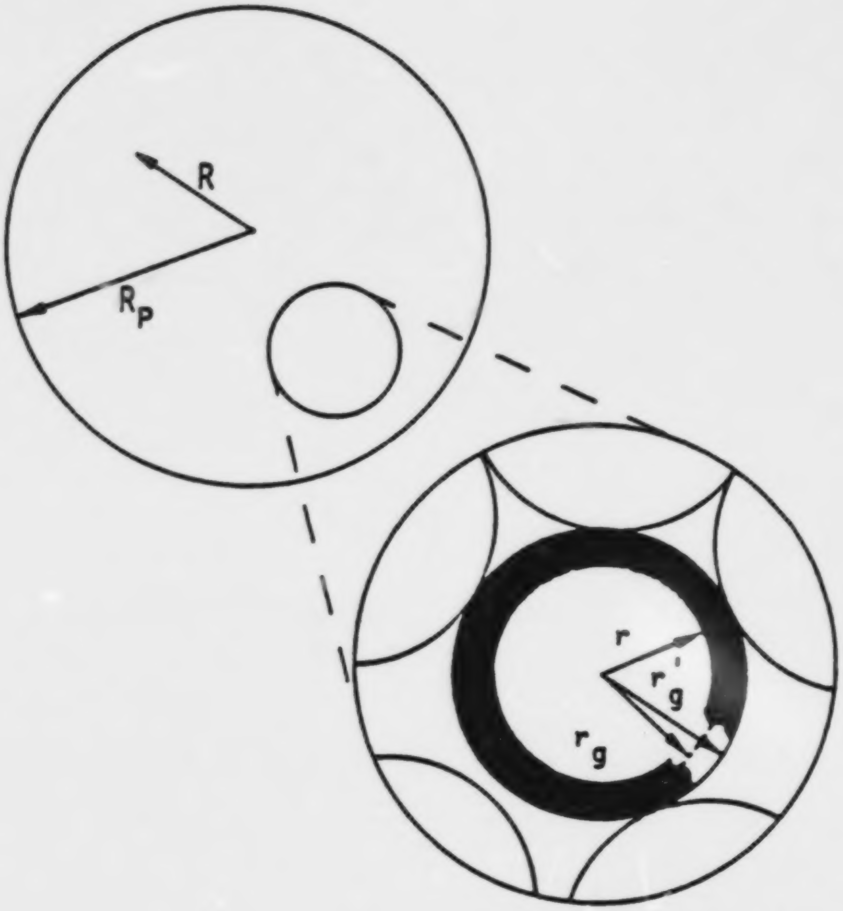

Figure 1-3. A schematic of the grain model. The enlarged view of the porous particle shows a dark band of product of radius r_g', the initial grain radius, r_g, and the radius of the unreacted core of reactant, r.

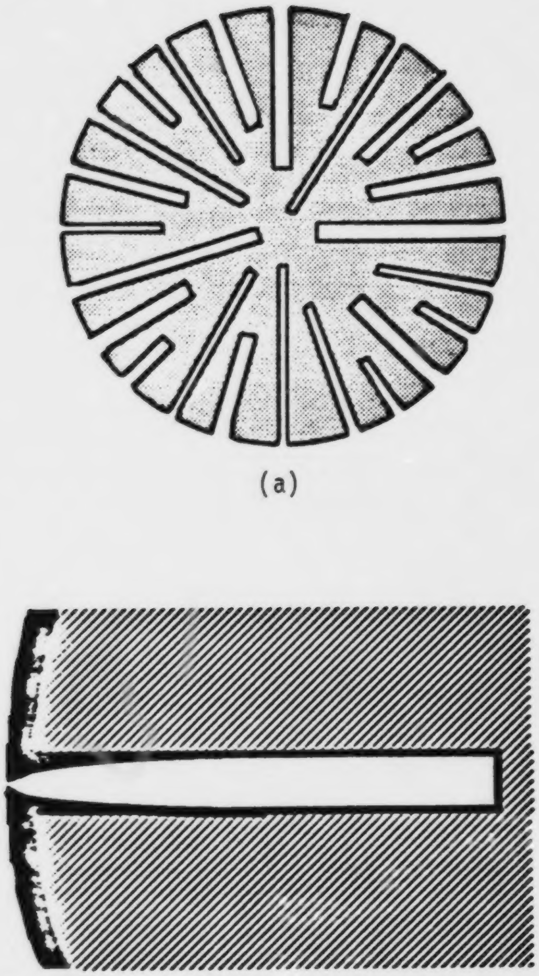

(a)

(b)

Figure 1-4. Schematics of the distributed pore model showing (a) the porous spherical CaO particle and (b) a closeup of a sulfated pore.

Both models include all of the sequential resistance thought to be of potential importance in the sulfation process:

- external mass transfer from the free stream to the particle surface,
- pore diffusion from the particle surface to the particle interior,
- diffusion of the reacting sulfur species through any previously formed calcium sulfate, and
- hetrogenous chemical reaction to form calcium sulfate.

In addition, both of the models currently allow for a distribution of characteristic internal sizes consistent with the available surface area are porosimetry data. The external mass transfer coefficient is based a literature correlation; the pore diffusivity includes consideration of both Knudsen and molecular diffusion. The product layer diffusivity is based on the differential reactor data of Borgwardt and Bruce (1986). Figure 1-5 illustrates the fit of the grain model to the data for one micron precalcined limestone. The major difference between the physical parameters used in the two models is associated with the estimation of the heterogenous chemical reaction rate. The reaction rate in the grain model is determined by using the initial times points in the Borgwardt and Bruce data to estimate the chemical rate. In the distributated pore model the intrinsic chemical reaction rate is assumed to large and not rate controlling. Both approaches are consistant with the available literature because at present there are no high temperature, short times sulfation data available from which the intrinsic chemical rate can be explicitly derived.

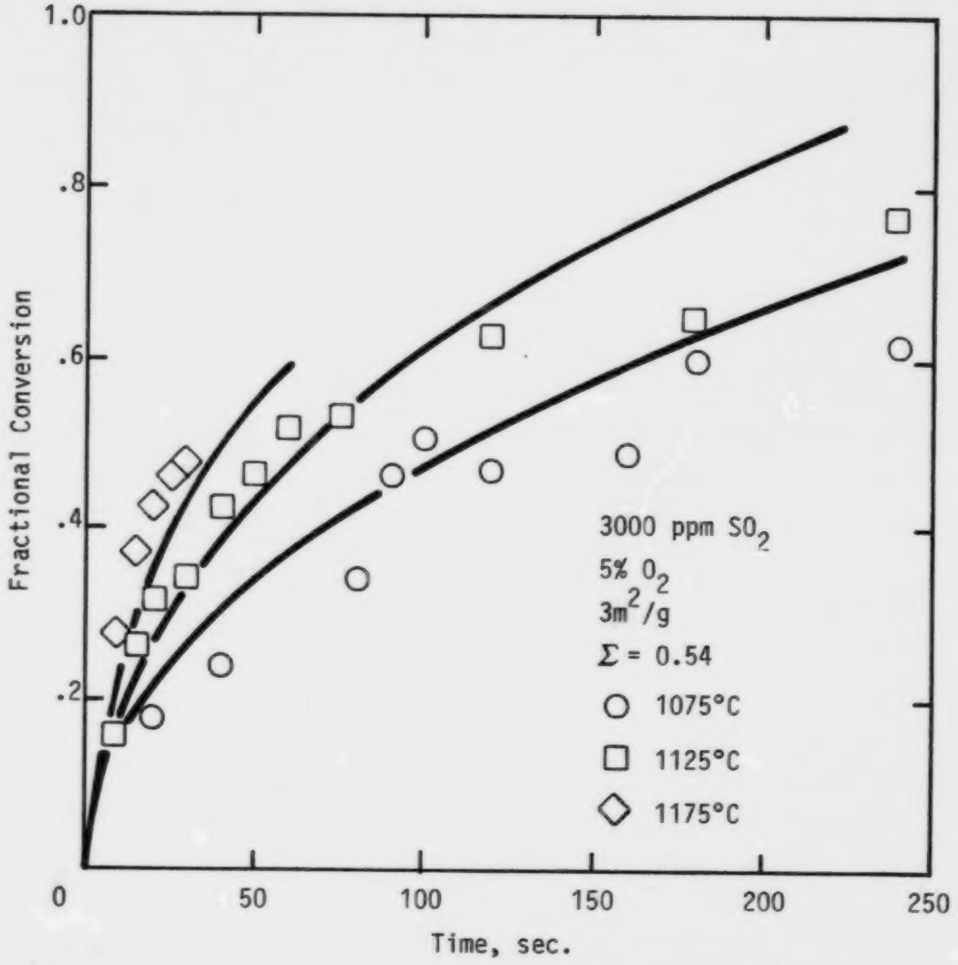

Figure 1-5. The differential reactor data of Borgwardt and Bruce (1986) for 1μm precalcined Fredonia limestone.

1.3 Process Fundamentals

1.3.1 Activation

The activation step is of major importance to the overall sulfation process because it controls the physical characteristics of the sorbent at the onset of sulfation, in particular, the available surface area and porosity. Three phenomenon appear to be of major significance in the overall activation process:

- the rate of calcination,
- the local development of high surface area associated with metastable CaO, and
- the sintering of previously formed CaO catalyzed by H_2O, CO_2, and probably sulfate ions with its associated grain (pore) growth and porosity loss.

Figure 1-6 shows relative calcination rates for hydrate and carbonate sorbents at 900°C in an isothermal reactor. These data illustrate one of the major differences between the two sorbent classes: carbonates lose less than 10% of their CO_2 in the time required for almost 80% dehydration to occur. Hence, hydrated sorbents are available for reaction with SO_2 far quicker than are carbonates. Figure 1-7 shows typical surface area development and decay for hydrates, carbonates, and a 10 m precalcine. The fact that the hydrated material shows higher reactivity suggests that a high surface area may be available early in its calcination, and that by the measurement point this surface area is lost to sintering. These data also show the importance of surface area loss due to sintering even at 1000°C. The 32 m^2/g precalcine had lost almost one-third of its surface area by the first sampling point.

Figure 1-8 shows activation model predictions on surface area development and loss for typical hydrate and carbonate particles at 1100°C. These data clearly indicate why the activation process can have a strong

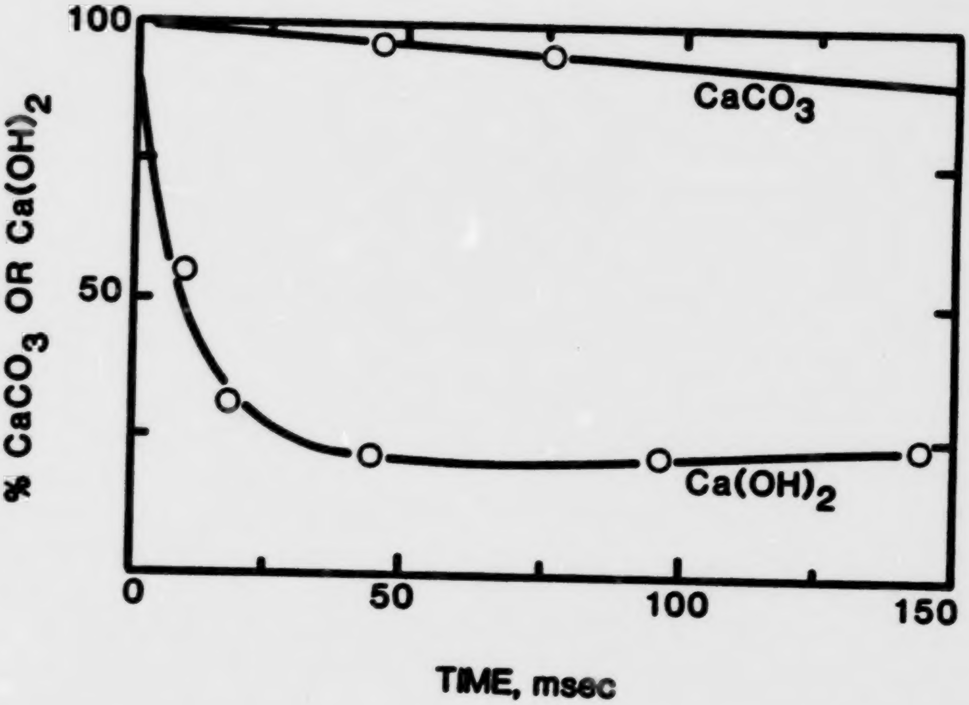

Figure 1-6. The relative rates of hydrate and carbonate calcination as measured by Bortz and Flament (1985) at 900°C using 6 μm particles and an isothermal reactor.

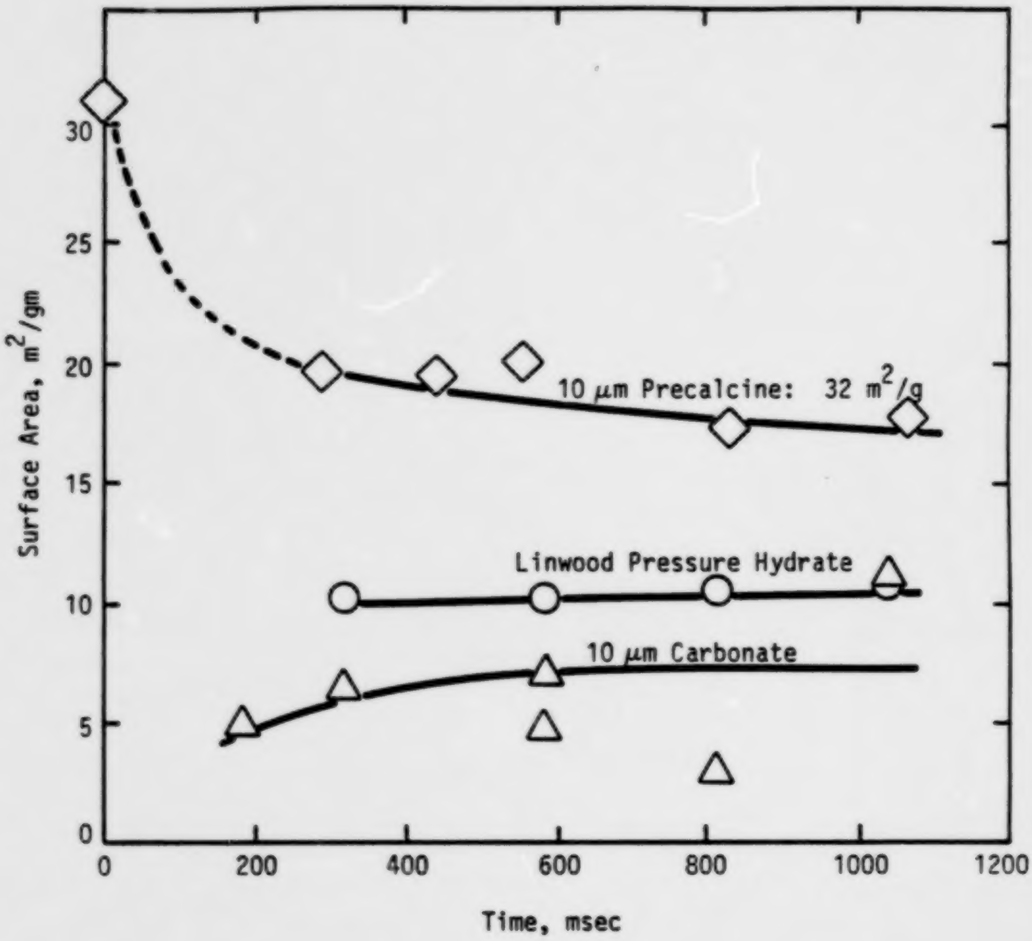

Figure 1-7. Surface area development and decay at 1000°C.

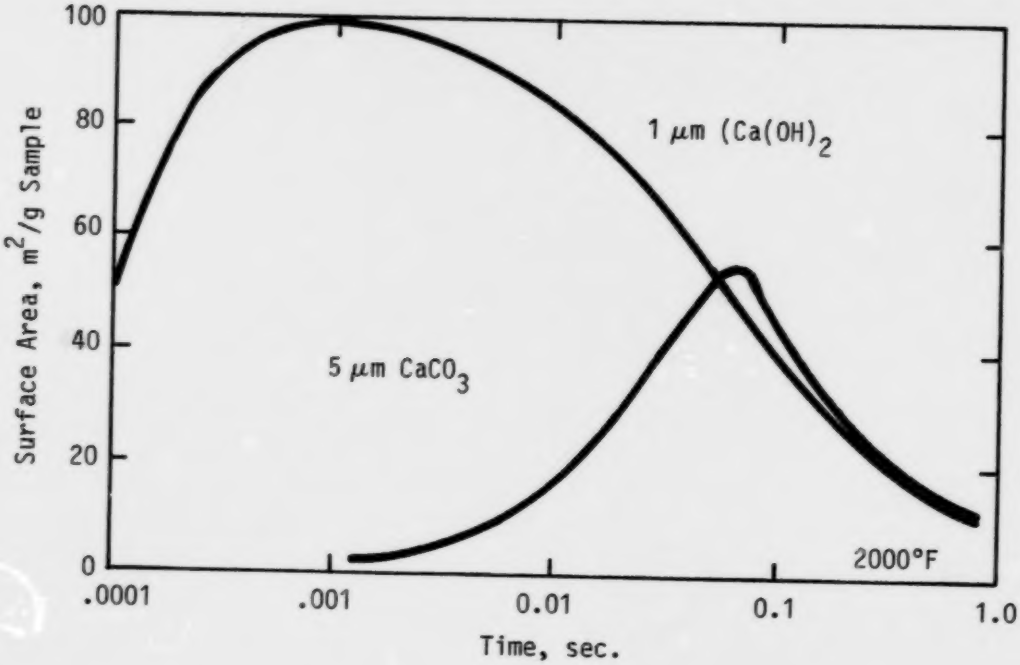

Figure 1-8. Activation model predictions.

influence on the overall extent of calcium utilization. The hydrate particles calcine so rapidly that the rate of calcination and surface area development far exceed the rate of sintering; hence, there exist regions of very high surface area. In contrast, the five micron carbonate particle calcines much slower and the sintering front can more closely follow the calcination front through the particle. At higher temperatures with even larger carbonate particles, the model predicts a simple steady rise in surface area because sintering follows calcination completely.

The previous discussion addressed the importance of calcium availability as indicated by surface area. Of equal importance, is calcium accessibility which is more accurately reflected by the detailed pore structure within the particle. Figure 1-9 shows time resolved porosity measurements made with a sized, precalcined hydrate. The time zero line corresponds to the pore size distribution of the precalcined sorbent prior to injection. These data show that internal porosity is progressively lost as the sorbent moves through the reactor; even by 600 ms most of the microporosity has been lost in this instance.

In summary, the available theoretical and experimental results suggest that the activation process can be optimized by using hydrated sorbents and minimizing their exposure to high temperature prior to the point at which the SO_2 is fully available for sulfation reactions.

1.3.2 Sulfation

Figure 1-10 summarizes time resolved sulfation data for sized, precalcined sorbents prepared from both hydrates and carbonates. These data characterize the sulfation process specifically because sulfation has been decoupled from calcination through the use of precalcined materials. Initial sulfation is very rapid with the majority of the calcium utilization occurring in the first 200 ms. Subsequently the process slows dramatically and further sulfation is relatively limited. Thus, some chemical or physical mechanism rapidly reduces the calcium availability or accessibility and limits the overall SO_2 capture. The solid line shows the distributed pore

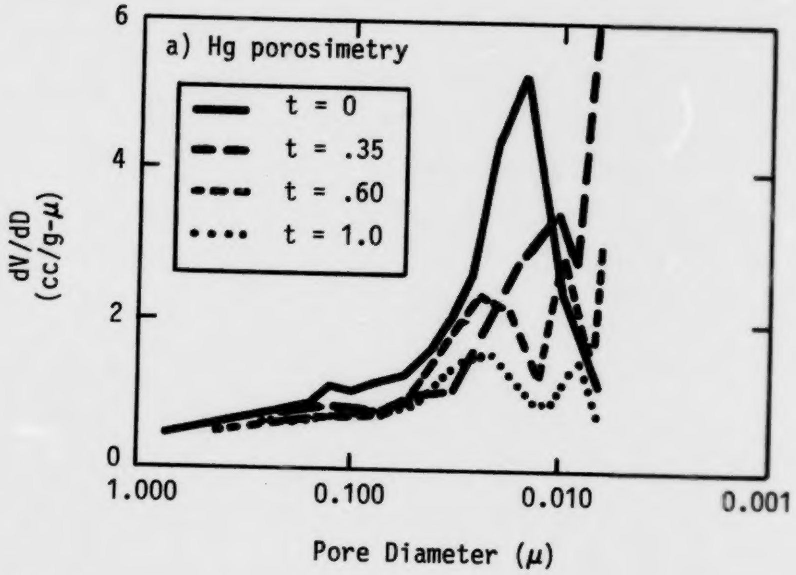

Figure 1-9. Comparison of measured pore size distribution as a function of time.

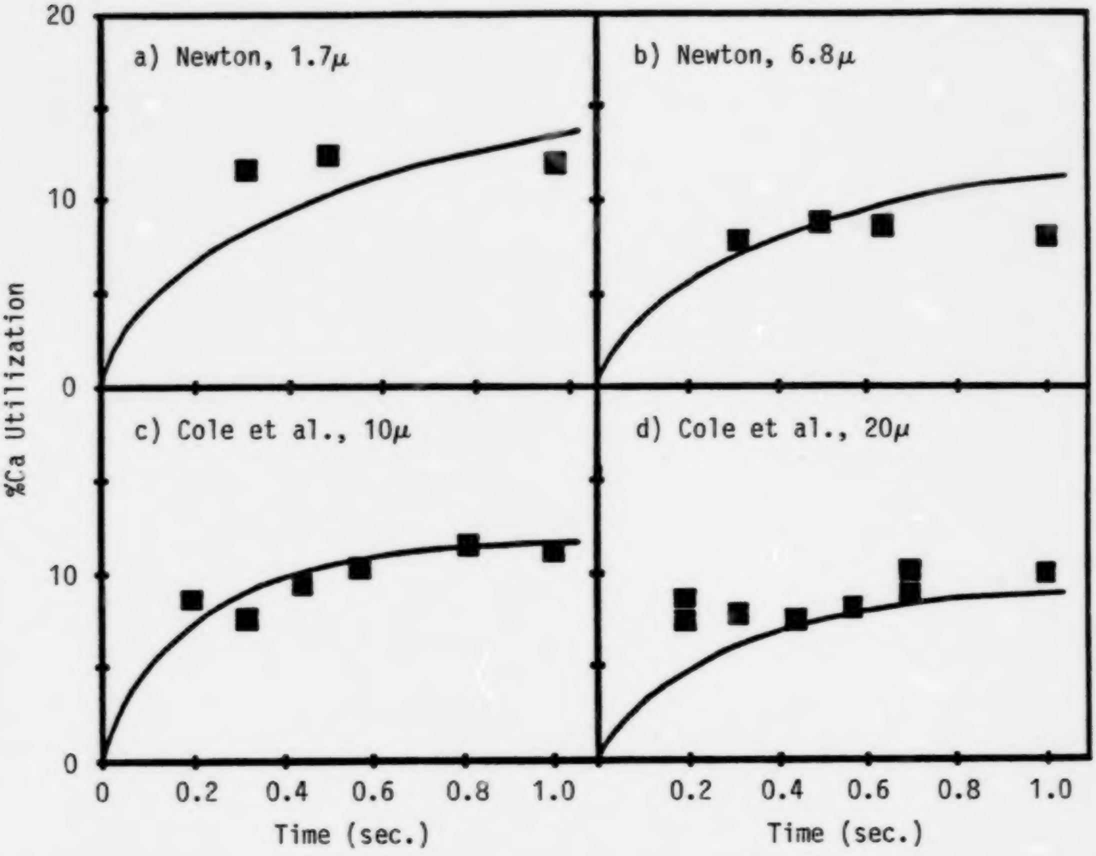

Figure 1-10. Comparison of distributed pore model and experimental data. Sulfation conditions for sorbents in a) and b): 1256K, 2000 ppm SO_2, and Ca/S = 2 (Newton, 1986). Sulfation conditions for sorbents in c) and d): 1273K, 3100 ppm SO_2, and Ca/S = 2 (results generated under EPA Contract 68-02-3633).

model predictions for the four different size particles. In each case the measured pore size distribution of the injected material was used to define the pore size distribution in the model. No parameters were adjusted to improve the agreement between the model and the experimental data. These results suggest that the distributed pore model can predict the form and the level of the time resolved SO_2 capture data. Detailed analysis of the model predictions indicates that the slowing in the overall sulfation rate at times beyond approximately 200 ms occurs due to a decrease in calcium availability resulting from catalized thermal sintering and a decrease in calcium accessibility resulting from pore mouth closure of the smallest pores. Figure 1-11 shows similar results at 1000 and 1200°C for commercial atmospheric hydrates. (These sorbents were not precalcined prior to injection.) These data also show the same rapid initial rise and slower subsequent increase in SO_2 capture. In this figure the solid lines represent the grain model predictions including sintering. Again there is good agreement between the experimental measurements and the model predictions.

Figure 1-12 shows time resolved capture data for the Linwood atmospheric hydrate when injected into the bench-scale furnace at 1260°C with two different quench rates (downstream temperature profiles). Even these larger scale data show the rapid initial rise particularly in the high quench rate case. These profiles are somewhat less sharp than the isothermal reactor measurements, perhaps because of mixing limitations in the larger scale experiment.

In summary, the fundamental sulfation data suggest that initial sulfation rate is very rapid but the overall rate soon slows due a pore blockage of and catalyzed thermal sintering. Figure 1-13 shows typical pore size distribution data obtained from analysis of solid Longview lime samples with and without SO_2 present. These isothermal reactor results confirm the dramatic effect that a small amount of calcium sulfate formation can have on calcium accessability; these samples (obtained at 1370K, 2000 ppm SO_2, and 500 ms) exhibited a 50 percent loss in measurable pore volume below 500 A with only 16 percent of the calcium utilized.

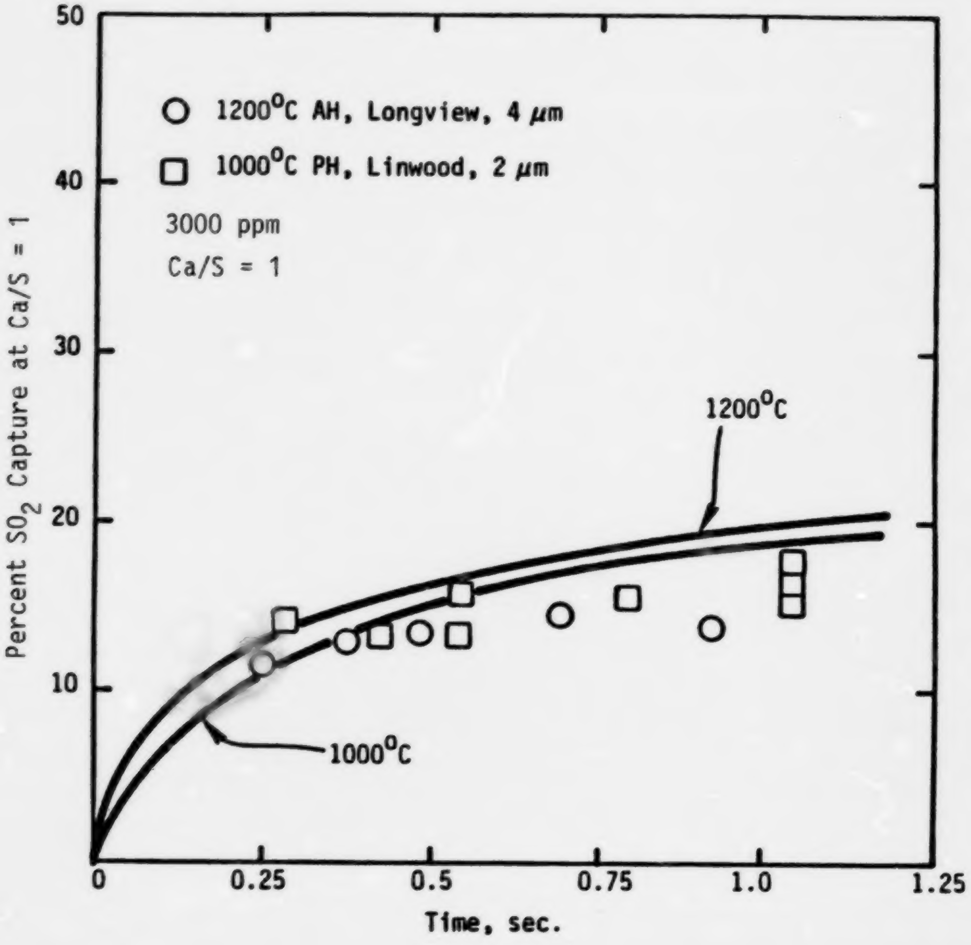

Figure 1-11. Grain model predictions of EER's ITR data. The predictions include the loss of sorbent surface area due to sintering.

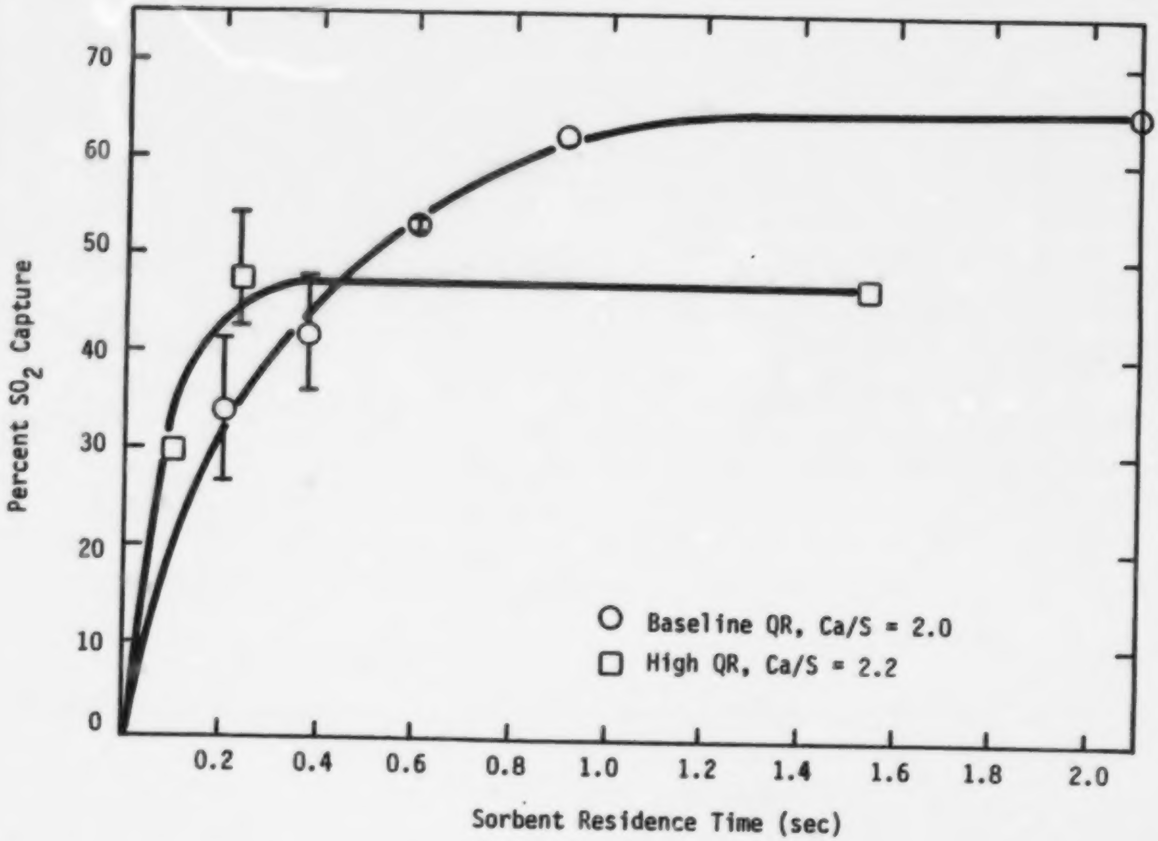

Figure 1-12. Time-resolved capture for Linwood atmospheric hydrate when injected into the CTT at 1260°C (2300°F) under two different quench rates.

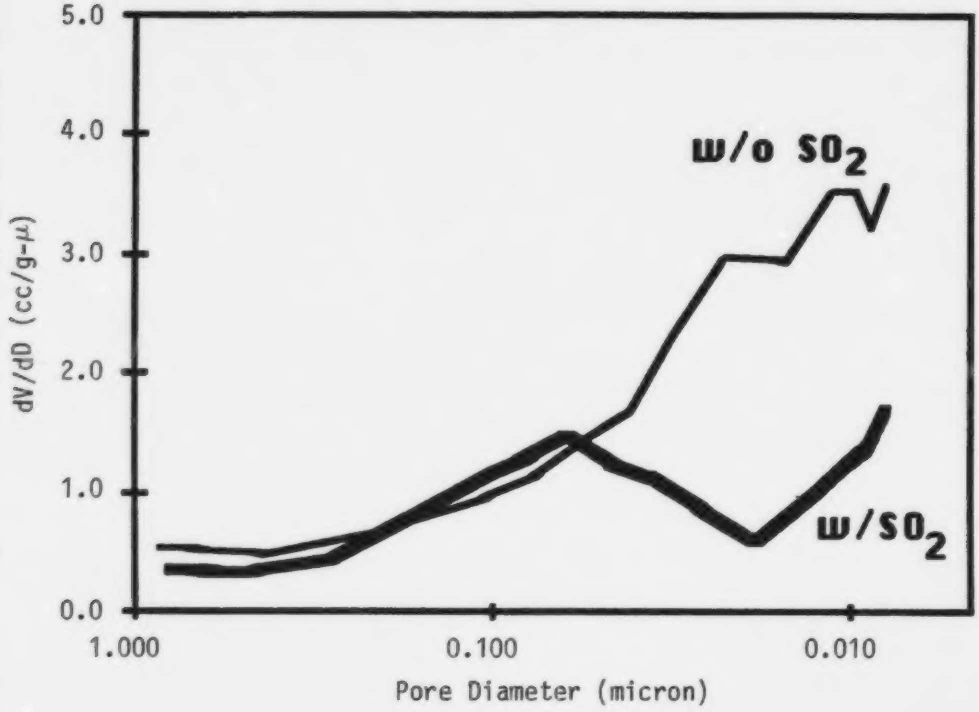

Figure 1-13. Pore size distribution of Longview Lime with and without SO_2.

1.4 Influence of Process Parameters

Temperature has a strong influence on calcination, thermal sintering, pore and product layer diffusion, and probably the intrinsic chemical reaction. Therefore, influence of both sorbent injection temperature and downstream thermal profile have been studied extensively in previous programs. Figure 1-14 summarizes the available bench- and pilot-scale information on the influence of injection temperature at Ca/S = 2 for hydrated lime. The observed capture levels range from 25 to 65 percent and optimum injection temperature appears to be about 2050°F. An absolutely critical point in resolving the optimum injection temperature from the various experiments is evaluating the peak temperature experienced by the sorbent. For example, in some experiments the maximum utilization was obtained at 2300°F, where the temperature was measured in the absence of the sorbent flow. The peak temperatures experienced by the sorbent would actually be closer to that obtained by mixing the furnace gas with the sorbent and its carrier gas. In other words, the furnace gas heats the sorbent carrier, and the carrier cools the furnace gas to some mass mean average. This mean temperature most closely represents the peak temperature experienced by the sorbent. All of the temperature data of Figure 1-14 were adjusted on a "mixed temperature after injection" basis. This allows direct comparison between experiments for which dissimilar sorbent carrier flows were used. Plotted on this basis, the maximum utilization occurs at 2050°F. The only sorbent for which shows a markedly different optimum is an alcohol hydrate; these sorbents are thought to have an additional advantage at lower temperatures due to their high surface area, but they loose this advantage at higher temperatures due to accelerated sintering. Thus, all of the data indicate an optimum peak sorbent temperature of approximately 2000 ± 100°F which in direct agreement with the fundamental isothermal reactor data. Both models suggest that the decreasing capture at the higher temperatures is the result of increased sintering rates and ultimately decreased stability of the $CaSO_4$. Figure 1-15 summarizes isothermal reactor testing conducted as part of this program to clearly define the upper limit of calcium sulfate stability. Capture decreased dramatically at temperatures above 2200°F which is in good agreement with the calculated thermodynamic limit of 2250°F.

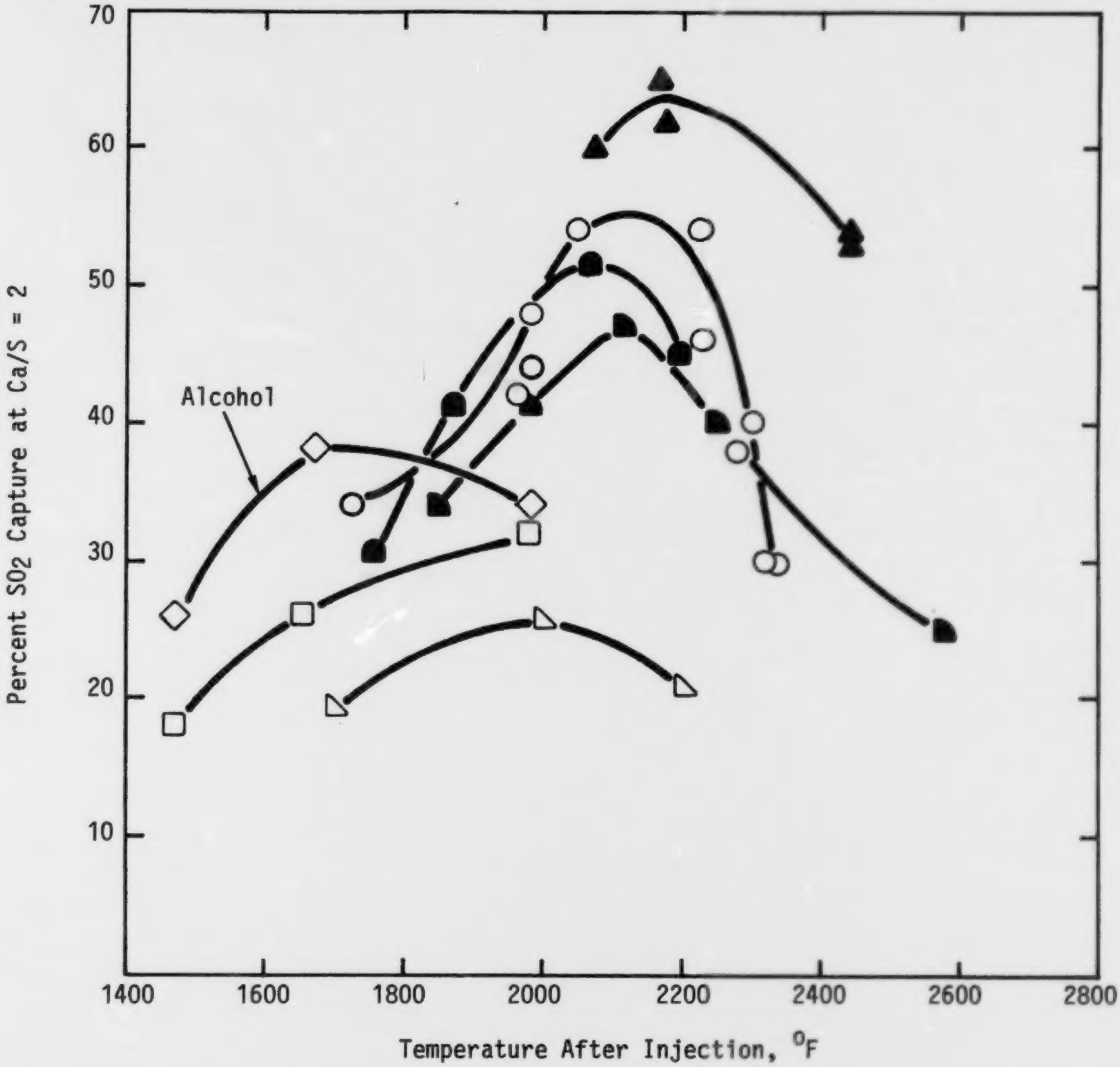

Figure 1-14. The effect of injection temperature on SO_2 capture at Ca/S = 2 for hydrated limes. See Table 6-2 for an explanation of the plotting symbols.

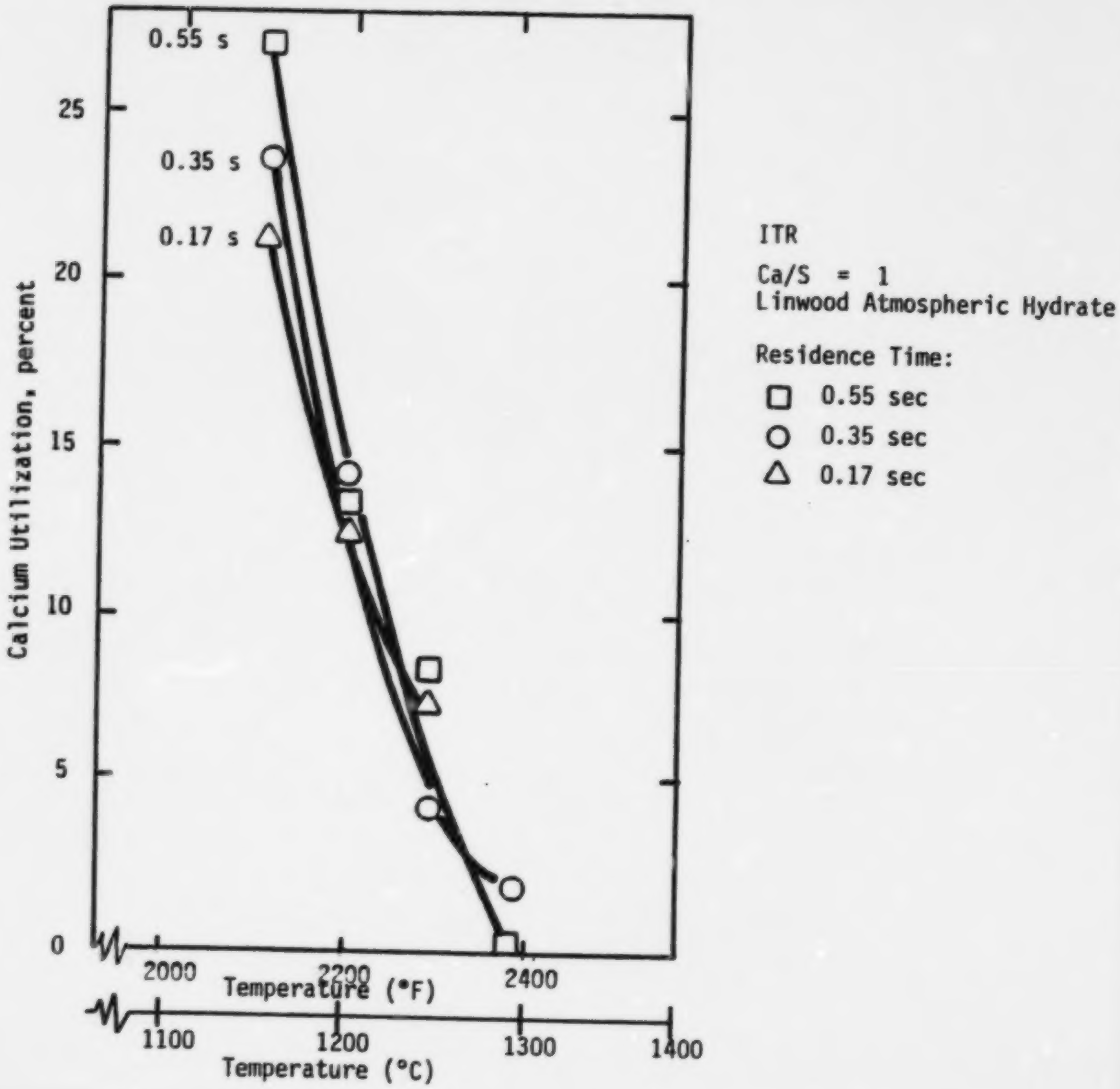

Figure 1-15. Capture at elevated injection temperatures.

The second major thermal consideration is the temperature profile downstream of the point of sorbent injection. Figure 1-16 summarizes the new experimental results for both atmospheric hydrate and limestone sorbents with high (1000°F/s) and low (160°F/s) quench rates. Increasing the quench rate (1) reduces the peak capture level, (2) shifts the optimum sorbent injection temperature to a slightly higher value, and (3) reduces the disadvantage of high temperature injection (by dramatically changing the curve shape above the optimum injection temperature). All of these effects are the direct result of sintering influences. Under the low quench rate (and isothermal) test conditions the optimum injection temperature is determined by competition between increased chemical and diffusion rates and increased catalyzed thermal sintering. Under high quench rate conditions residence time at a particular temperature becomes more critical and high temperature injection is less detrimental. In essence, a high quench rate serves to mitigate the detrimental aspects of sintering; less time is spent at the high temperature so the sintering is reduced. In addition, the overall relative insensitivity to an extreme change in quench rate at the optimum injection temperature supports the previous fundamental and pilot-scale data showing very rapid initial sulfation; the bulk of the sulfation occurs on a time scale that is short relative to typical boiler quench rates.

The other parameters which are of a major interest in the overall process optimization are sorbent composition and particle size. Figure 1-17 summarizes data obtained in this study to characterize the influence of particle size for two limestones and two atmospheric hydrates. Decreasing the mean particle size increased the resulting SO_2 capture as predicted theoretically; however, even on a common size basis the hydrate sorbents performed significantly better than the carbonate sorbents. The difference is believed to be associated with more rapid availability of the CaO in the hydrate case, higher local peak surface areas, and a more favorable (slightly larger) pore size distribution.

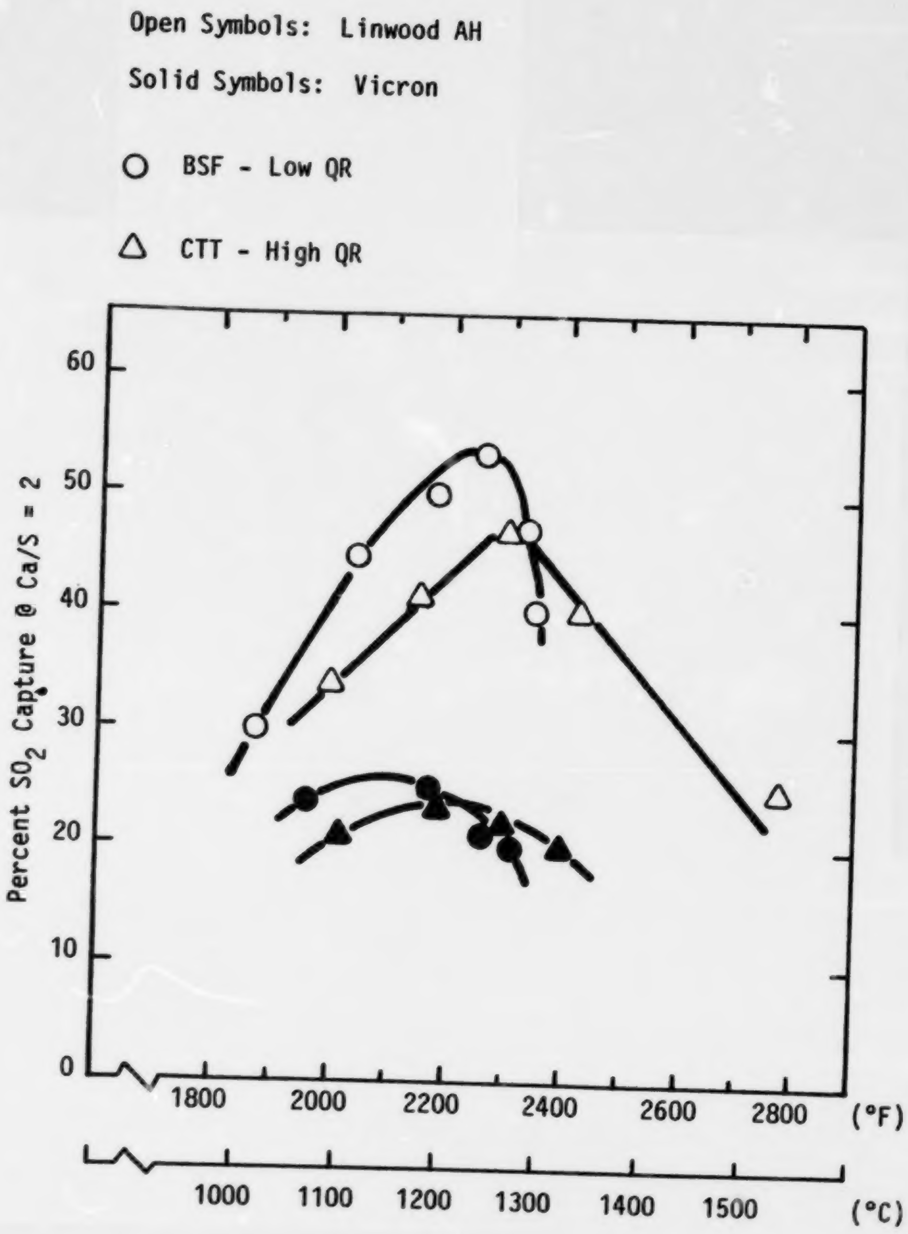

Figure 1-16. Comparison of the impact of quench rate on sorbent injection temperature for Linwood hydrate and Vicron carbonate.

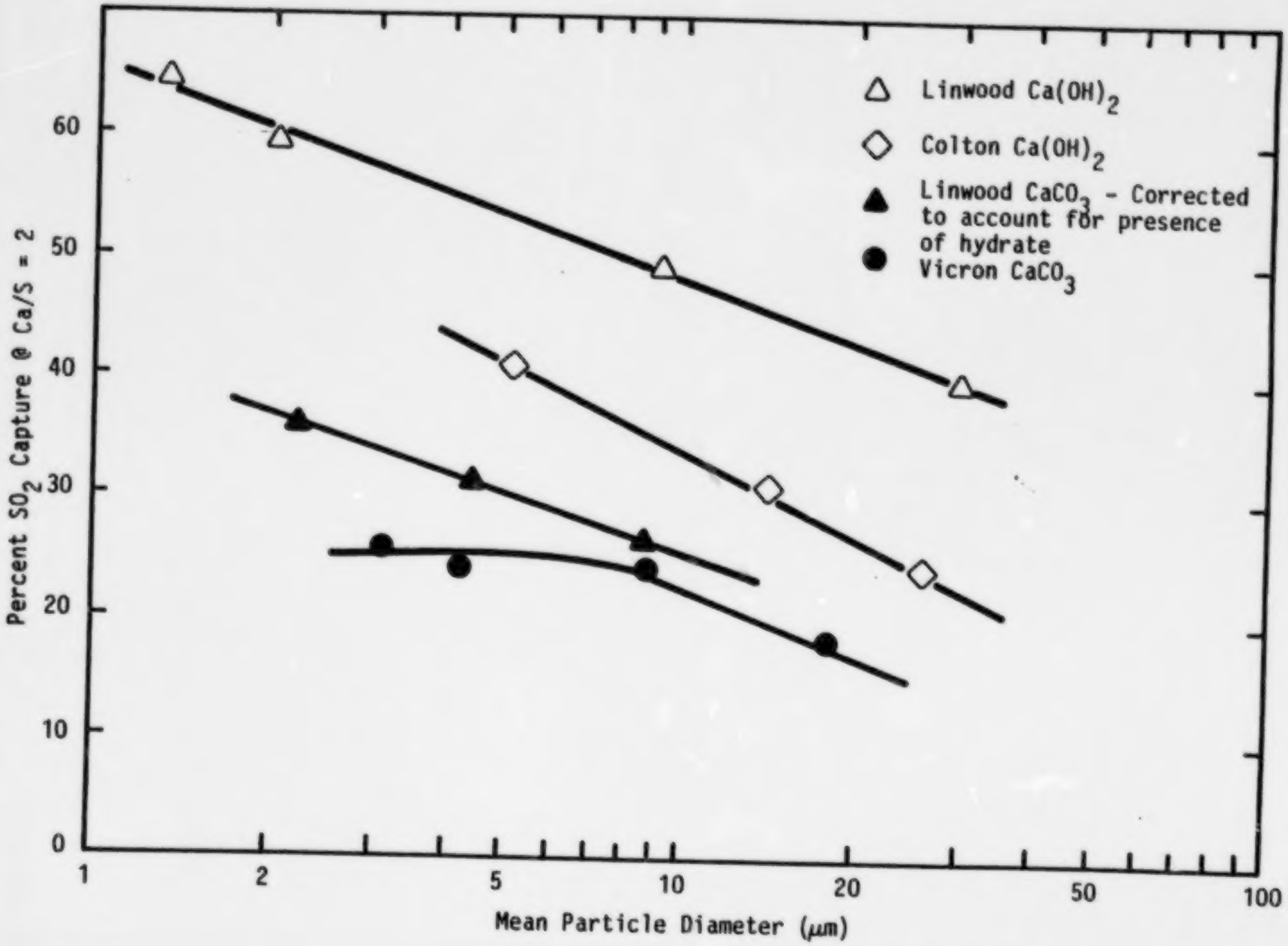

Figure 1-17. Comparison of sulfur capture for four different sorbents as particle size is varied.

1.5 Full-Scale Process Performance

The literature on all the previous, large scale sorbent injection evaluations was reviewed and Table 1-1 summarizes these results. Generally sulfur capture with limestone injection was approximately 25 ± 5 percent at Ca/S = 2 under optimum conditions. The one notable exception to this is the testing which was conducted at IHI and Dupont. The sulfur capture for large scale injection of hydrated sorbents ranges from 35 to 55 percent with 45 percent SO_2 capture at Ca/S = 2 as a reasonable estimate of the current technology.

To evaluate the consistency between the full-scale and previously discussed small-scale experimental results, grain model predictions were made for the Tiefstack tests. The grain model was first calibrated against the experimental hydrate data shown in Figure 1-18 for the CTT furnace fired with natural gas or coal. Figure 1-19 compares the model predictions with the actual full-scale measurements at Tiefstack. The sorbent injection temperature was 2280°F and the actual SO_2 concentration was 600 ppm. The good agreement between the model and the full-scale data demonstrates the usefulness of the overall modeling approach and suggests that the full-scale data are indeed consistent with the bench- and pilot-scale results for similar sorbents.

TABLE 1-1. LARGE-SCALE FACILITY COMPARISON

Facility	Load	Type	Percent(1) Capture w/$CaCO_3$	Percent(1) Capture w/$Ca(OH)_2$	Optimum Injection T, °F
Shawnee	140 MW	Wall-fired	14-18	--	2100
Shawnee	75 MW	Wall-fired	16-26	--	--
Hoot Lake	44 MW	T-fired	--	35-50	--
Hoot Lake	34 MW	T-fired	--	35(2)	--
IHI	$50x10^6$Btu/hr	Wall-fired	40	--	--
Dupont	110,000 lb/hr	Wall-fired	40	--	--
Lakeview	290 MW	T-fired	20	--	--
Lakeview	220 MW	T-fired	27	--	--
Lakeview	220 MW	T-fired	--	54	--
Tiefstack	352,000 lb/hr	T-fired	22	42	--
Tiefstack	250,000 lb/hr	T-fired	27	--	--
Voitsberg	330 MW	T-fired	29	--	--
LWS	$100x10^6$Btu/hr	Wall-fired	32	44	--
Bench/CTT	$1x10^5$Btu/hr	Down-fired	21-26	40-58	2000
Bench/BSF	$1x10^6$Btu/hr	Down-fired	26	54	2000

(1) AT CA/S = 2

(2) ESTIMATED FROM CAPTURE AT CA/S = 1

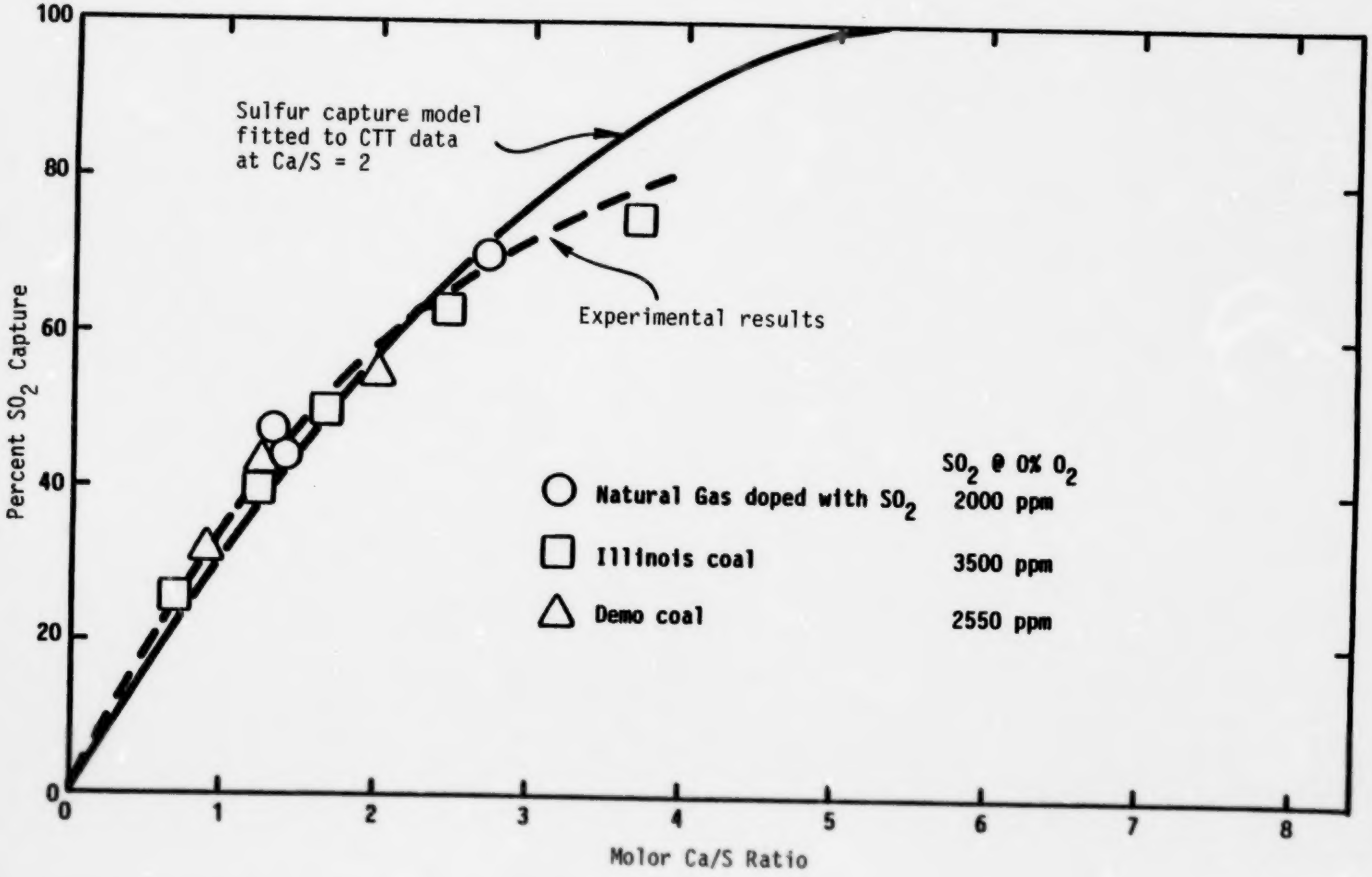

Figure 1-18. Controlled Temperature Tower (CTT) data obtained with Linwood atmospheric hydrate for three different fuels. The data were used to calibrate the sulfation model as indicated by the solid line.

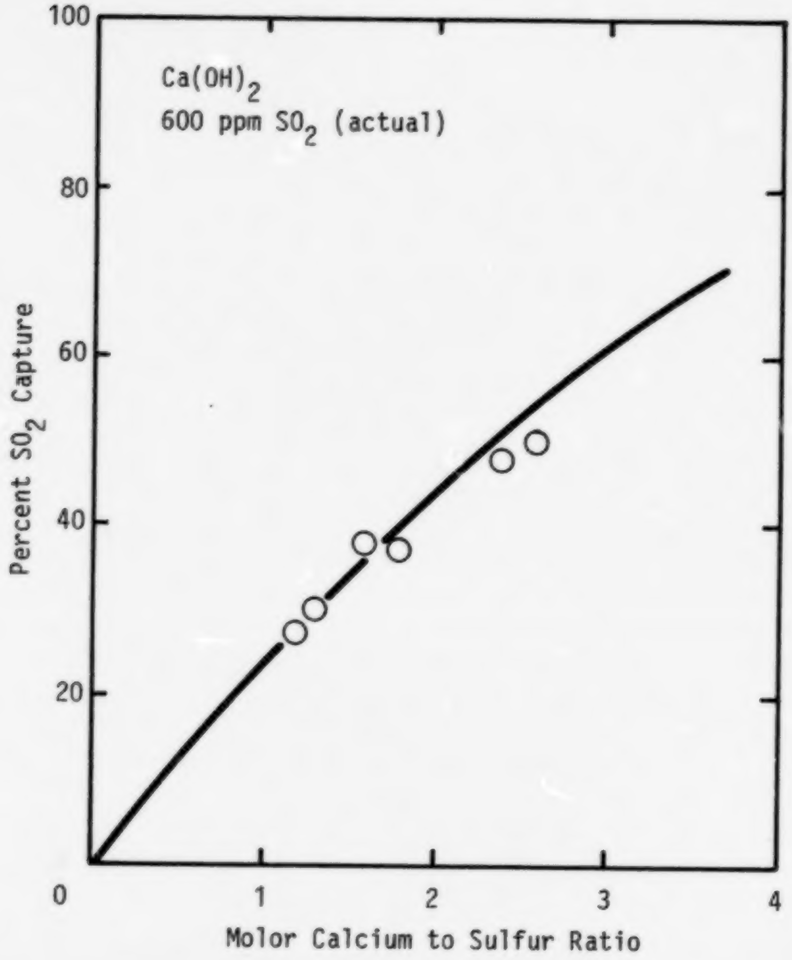

Figure 1-19. A comparison of SO$_2$ capture results from Tiefstack (see Figure 9-14) with grain model predictions. The grain model was calibrated against the bench-scale data of Figure 1-18 and then used to extrapolate to the Tiefstack conditions.

GEN. 4208 F/R (2)

2.0 INTRODUCTION

2.1 Background

Sulfur capture by calcium based sorbents has been the subject of extensive research over the last three decades. Furnace injection of limestone was tested in the early 1970s and abandoned because of the lack of performance which was attributed to a combination of:

- decreased sorbent activity due to dead burning at furnace temperatures,
- inadequate dispersion of the sorbent throughout the combustion products, and
- operational problems associated with air heater plugging.

Interest in the technique was revived approximately one decade later because of a need to develop a low cost, retrofitable, SO_x control technology. Since that time a wide spectrum of research and development programs have been conducted in laboratory, bench-, and pilot-scale facilities. In addition, there have been several field evaluation tests completed in both the United States and Europe.

Unfortunately, the information currently available on the applicability of dry sorbent injection often appears to be inconsistent:

- The SO_2 capture at the 1970 demonstration test (TVA, Shawnee) ranged from 14 to 18 percent at full load with Ca/S = 2. In recent testing at Dupont, full load capture levels of 40 percent were reported for limestone injection under relatively similar conditions.
- Several extensive bench-scale investigations of the optimum sorbent injection temperature with hydrated limes have concluded that

capture can be maximized by injecting the sorbent near the beginning of the sulfation window at approximately 2300^{o}F. However, an equal number of investigations have "definitively" shown that the optimum injection temperature is between 1800 and 2000^{o}F for hydrated limes (see discussion in Section 6.0).

- Bench-scale results from various investigators have suggested that calcium utilization can be influenced by the temperature profile downstream of the injection point and that the residence time within a sulfation window in important, yet recent fundamental studies have conclusively demonstrated that the majority of the sulfation occurs within approximately 200 milliseconds of injection. Thus, the overall bench-scale behavior may be a combination of the rapid reaction, and a finite mixing rate that carries a portion of the reaction downstream.

- Calculations with a first generation sulfation model accurately predicted the influence of injection location and sorbent composition using a simple correlation based on experimental surface area measurements to initialize the calculation. Comparison of the model predictions with detailed, time-resolved data, however, indicated that the temporal behavior of the model predictions was incorrect at short times.

Thus, although the sorbent injection process has been studied extensively, the process effectiveness and rate controlling steps have not been fully defined.

2.2 Program Objectives

This report summarizes the work that was completed under the EPA program 68-02-4208 entitled "Combustion Systems Similarity Criteria Modeling Study." The overall goals were three-fold:

- To compile and compare the available sulfation data on high temperature sorbent injection as a function of scale, sorbent type, injection conditions, etc. This included identification of clear differences in results and, where possible, reconciliation in terms of experimental system characteristics.

- To develop sulfation models which include consideration of physical and chemical processes likely to be a major importance for dry sorbent injection in the upper furnace regions of the boiler.

- To use the sulfation models in conjunction with the available experimental data to define the process fundamentals and rate controlling steps, to determine which apparent differences in the experimental data from various facilities were due to system characteristics and which represented true conflicts, to identify gaps in the current sorbent injection data bank, and finally to define the optimum sorbent injection conditions.

The program was also designed, as a result of the theoretical and experimental evaluation activities, to develop a calculational procedure which could be used to predict dry sorbent injection performance in various full-scale applications and to assess which sorbent injection alternatives should be emphasized in future research and development activities.

2.3 Program Approach

The program effort was divided into the four major tasks:

- Task 1 - Definition of Approach

- Task 2 - Methodology Development

- Task 3 - Compilation and Evaluation of Existing Experimental Data and

- Task 4 - Experimental Studies to Provide Missing Data.

In the methodology development phase of the program, various sulfur models were reviewed and the grain and distributed pore models were selected for use in this program. They were then upgraded to account for variable length scales of the internal particle structure and grain (pore) growth due to catalyzed thermal sintering.

In the data compilation and comparison phase of the work, the available literature was reviewed and organized by size of experimental facility and experimental conditions. These data were then evaluated and areas of missing information or major conflict were identified and subsequently investigated in the Task 4 data gathering portion of the program.

2.4 Report Organization

This Final Report is organized primarily on the basis of process scale because it is necessary to clearly understand the fundamentals of the sulfur capture process before it is possible to consider systems where sulfation is in turn influenced by heat transfer and fluid mechanical considerations. The first three chapters focus on our current understanding of the process fundamentals, based on data obtained in well-defined, dispersed phase experiments where the temperature and concentration field surrounding individual sorbent particles was known:

- 3.0 Activation Fundamentals - examination of the sorbent calcination and sintering process as they occur in the absence of sulfation.

- 4.0 Sulfation Fundamentals - examination of the sulfation step alone based on experimental and theoretical studies of precalcined sorbents.

- 5.0 Coupled Activation and Sulfation - fundamentals of the overall sulfur capture process as it occurs when raw sorbents are injected into a high temperature, combustion environment.

Each of these chapters begins by considering the available experimental results. Next, the associated theoretical (computer) modeling approach is reviewed. (Thus, Chapter 4 contains the details of all of the sulfation models which were considered in this study.) Finally, each of these chapters concludes with comparisons of the respective model predictions and the available experimental data.

The next three chapters (6 through 8) focus on bench- and small pilot-scale results. Chapter 6 examines the information available on the key process parameters (e.g., thermal history, particle size, SO_2 concentration, and sorbent type) for a wide spectrum of experimental studies. This chapter concludes with discussion of the key experimental uncertainties which were identified by the program. Chapter 7 is a comprehensive review of the experimental work conducted in conjunction with this study to provide the data needed for reconciliation of the key experimental issues. Finally, Chapter 8 presents an analysis of the new experimental results using the activation and sulfation models.

Chapter 9 contains a compilation of all of the large-scale test results and a detailed discussion of the overall sulfation modeling approach for predicting sorbent performance in a full-scale application. This section concludes with the comparison of model predictions and full-scale field data from a recent demonstration project.

Finally, Chapter 10 contains conclusions from the overall study. The report appendices contain details of the various experimental systems which were considered, and a comprehensive tabulation of all experimental results.

EPA.4908--3

3.0 ACTIVATION FUNDAMENTALS

The present program has focused primarily on sulfation. However, other contemporary projects have been directed at the related process of sorbent activation. Because of the importance of activation for the understanding of sulfation, a fairly detailed discussion of the former is given below. Included in the discussion is a mathematical model of the activation process.

High temperature sulfation proceeds according to the following overall reaction:

$$CaO + (1/2)\ O_2 + SO_2 = CaSO_4$$

Commercially manufactured CaO has not proven to be a very reactive sorbent towards SO_2, and it is difficult to prevent its reaction with atmospheric CO_2 and water during storage. The accepted alternative is to prepare CaO from hydrate or carbonate either within the furnace, or in an on-line side chamber. In either case, the reactions are

$$CaCO_3 = CaO + CO_2$$

$$Ca(OH)_2 = CaO + H_2O$$

The physical consequences of these reactions are to open up a porous structure within the particle upon which the sulfation reaction can proceed. Key issues include:

- The rate at which the calcination proceeds.
- The rate at which internal surface area is opened up.
- The rate at which desurfacing, or sintering, competes with surface area development.
- The influence of miscellaneous effects, such as particle fragmentation, stress fracture, and metastable CaO crystal forms.

Section 3.1 presents a compilation of experimental results. Section 3.2 describes a model used to compare results and develop a fundamental understanding of the consequences of calcination behavior. Section 3.3 consists of the results of exercising the model against the data.

3.1 Compilation of Experimental Results

The calcination of hydrates and carbonates occurs at such dissimilar rates that they can be logically considered as separate phenomena. Thus, the results are placed in separate sections.

3.1.1 Calcination Data for Carbonates

The calcination of calcium carbonate can conceivably be limited by rate of the inherent reaction, the rate at which heat is supplied to the carbonate to drive the reaction, and the rate at which the product CO_2 is convected away. As discussed by Borgwardt (1985) the rate for pieces of carbonate typical of kiln feedstocks appears to be controlled by heat transfer. For smaller particles more typical of furnace sorbents, the heat transfer and CO_2 diffusion resistances can be expected to lessen, which will increase the importance of the underlying chemical rate. Indeed, Borgwardt (1985) found that a chemical rate controlled the calcination of limestone particles under LIMB conditions. The condition of chemical rate control appears to be met only when the particles are in dispersed phase. In packed beds (e.g., TGA decomposition) the interparticle resistances to heat and mass transport become important, as evidenced by the dependence of rate on sample size.

Borgwardt (1985) found that the calcination rate of carbonate particles was kinetically controlled under dispersed phase conditions. The rate was consistent with a model which was first order in the surface area of the unreacted carbonate:

$$d(CaCO_3)/dt) = - KA_{CaCO_3}$$

where ($CaCO_3$) is the moles of undecomposed carbonate in the sample, K is the surface specific rate constant (moles/cm^2-sec), and A_{CaCO_3} is the surface area of the carbonate. If the assumption is made that the specific surface area of the unreacted carbonate does not change while the other portions of the particle are reacting, then the carbonate surface area within the sample is proportional to the original specific surface area of the carbonate, S_g, and the unreacted carbonate. This is:

$$A_{CaCO_3} = S_g(CaCO_3)$$

Following substitution and integration, (Borgwardt, 1985) the model for the isothermal calcination of small particles becomes:

$$\ln (1 - X) = -KS_g t$$

where X is fraction of carbonate remaining and t is time. Using this model, Borgwardt was able to correlate his calcination data with an activation energy of 49 kcal/mole, as is shown in Figure 3-1. Figure 3-2 illustrates the ability of the model to resolve temporal data. The key point is that the reaction appears to be kinetically controlled to about 80 percent conversion. Beyond this point an additional hinderance appears to slow the reaction rate. This has been attributed to the resistance of the fine CaO pores to CO_2 diffusion at high particle conversions. Snow (1985) lends indirect support to this conclusion by his finding that all sorbents, save one, showed reduced reactivity at long times. The single sorbent that showed a rapid approach to full calcination, Ireland Spar, also showed large structural cracks on microscopic examination. One hypothesis holds that these cracks opened access to the particle interior, and this reduced the resistance to the transport of CO_2 under high conversion conditions.

F 3-1
3-2

Snow's (1985) work used an entrained flow reactor to examine the activation of calcium carbonates under furnace-type conditions. Since the reactor was not strictly isothermal, but rather showed a maximum of a 150°C variation over its active length, the kinetic data had to be interpreted in a stepwise manner. His data effectively extended the high temperature end of

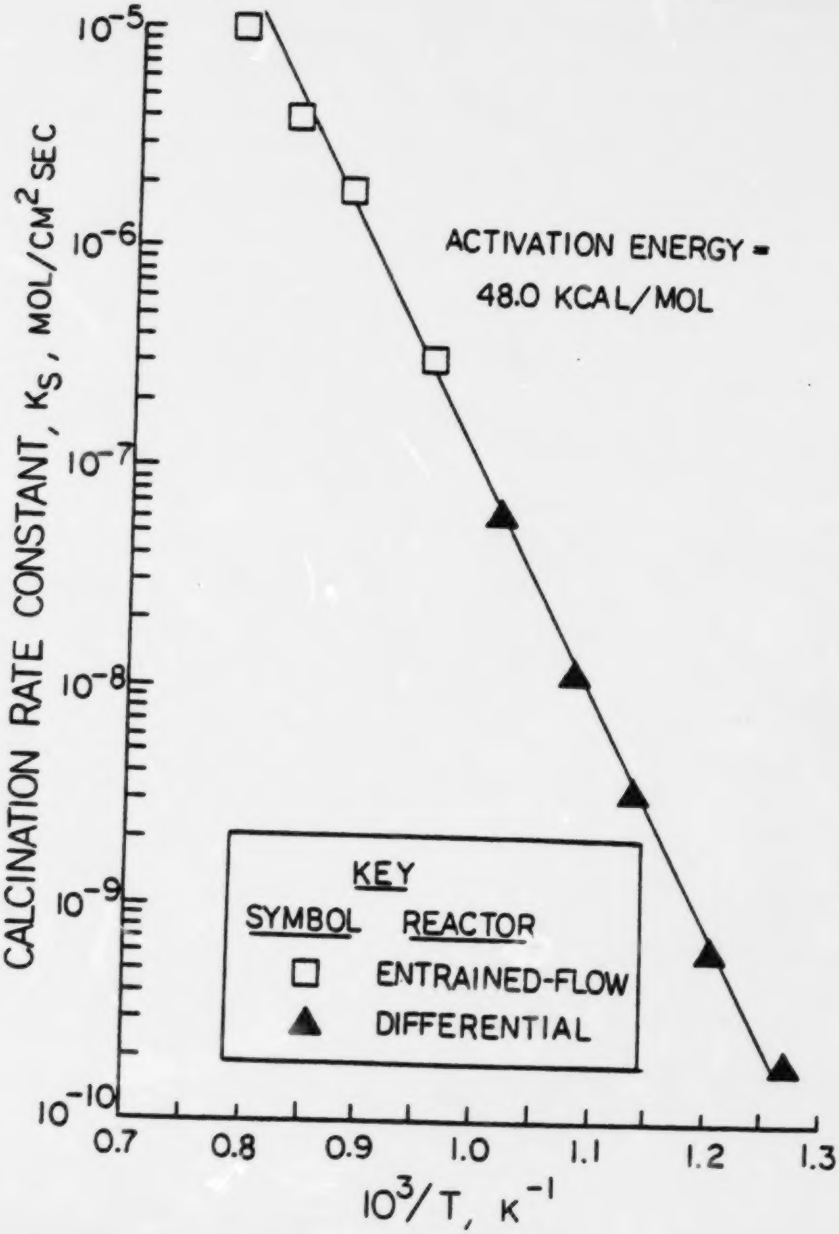

Figure 3-1. Arrhenius plot for calcium carbonate decomposition, from Borgwardt (1985).

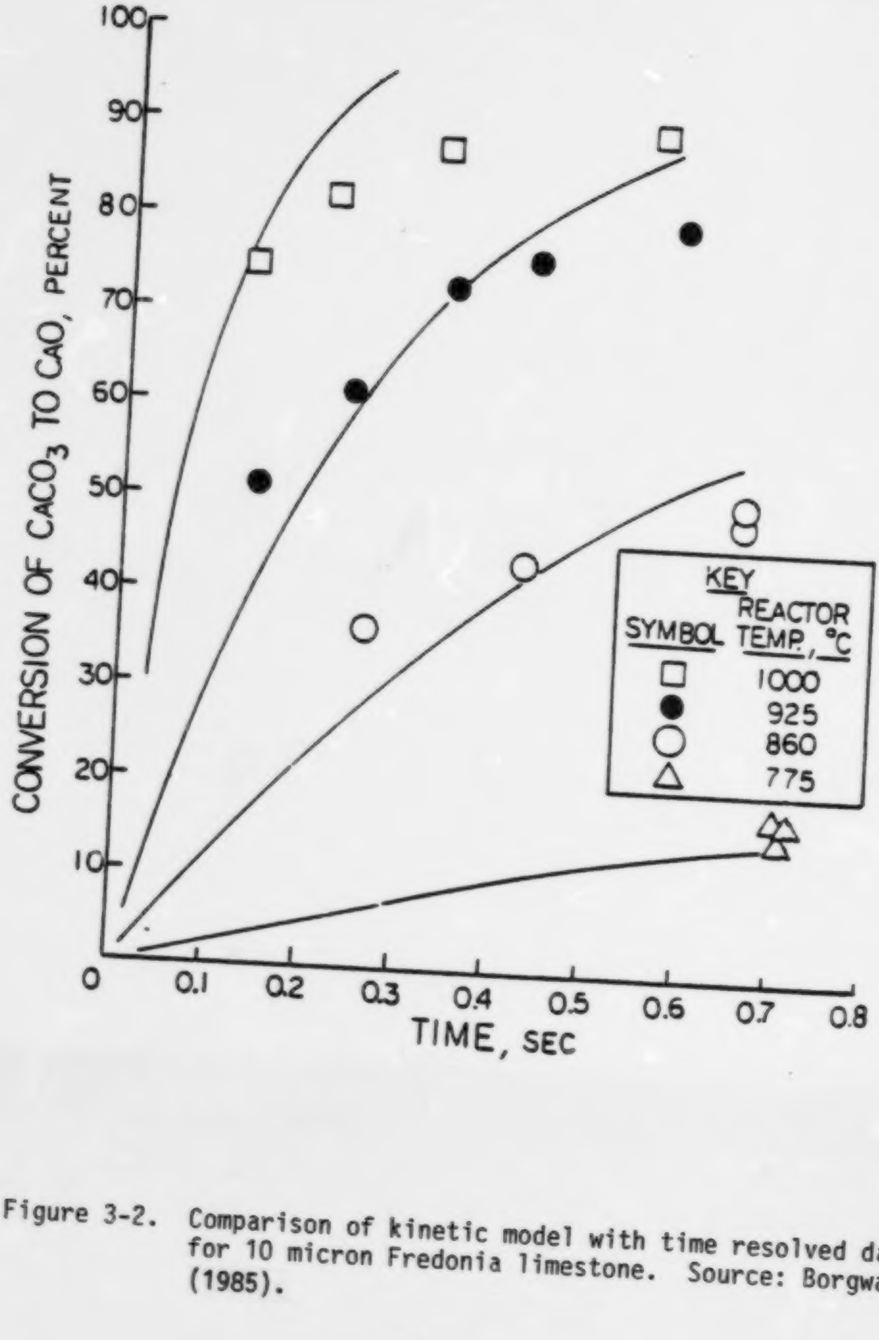

Figure 3-2. Comparison of kinetic model with time resolved data for 10 micron Fredonia limestone. Source: Borgwardt (1985).

Borgwardt's data. The data support the Arrhenius plot shown in Figure 3-3. At high temperatures the rates drop considerably below those that would be obtained by extrapolating Borgwardt's results beyond their high temperature limit. In fact, the high temperature rates show almost no temperature sensitivity. The only exceptions are the data that show a rapid 100 percent conversion; these rates cannot be assigned a definite value, but the dashed line on the figure indicates the minimum value associated with 100 percent conversion. The general lack of temperature dependence above 950°C would suggest that a new rate controlling process has become dominant, and that this rate is not strongly dependent on temperature. One suggestion is the CO_2 mass transfer limitation discussed earlier.

Another recent set of carbonate activation data was generated at the IFRF Bortz and Flament (1985). The results of Figure 3-4 show calcination extents for powdered carbonates at various temperatures in an isothermal flow reactor. These data stand at somewhat of a variance with that of Snow (1985) in that the reaction is accelerated by temperatures beyond 1000°C.

Figure 3-5 correlates the peak temperature experienced by the particle with the time required for 50 percent calcination (a value closely related to a first order rate constant). This plot again illustrates a change in the rate controlling mechanism above 1000°C, relative to the temperature dependence established at lower temperatures (Ishihara, 1970; Borgwardt and Harvey, 1982).

3.1.2 Calcination Data for Hydrates

Calcium hydroxide decomposes at a much lower temperature than the carbonate. In nitrogen it dissociates in the 3-400°C range. Under low temperatures, the rate has been examined in a TGA by Snow (1982). The results, if extrapolated to high temperatures, suggest a rate that is much faster than the carbonate rate.

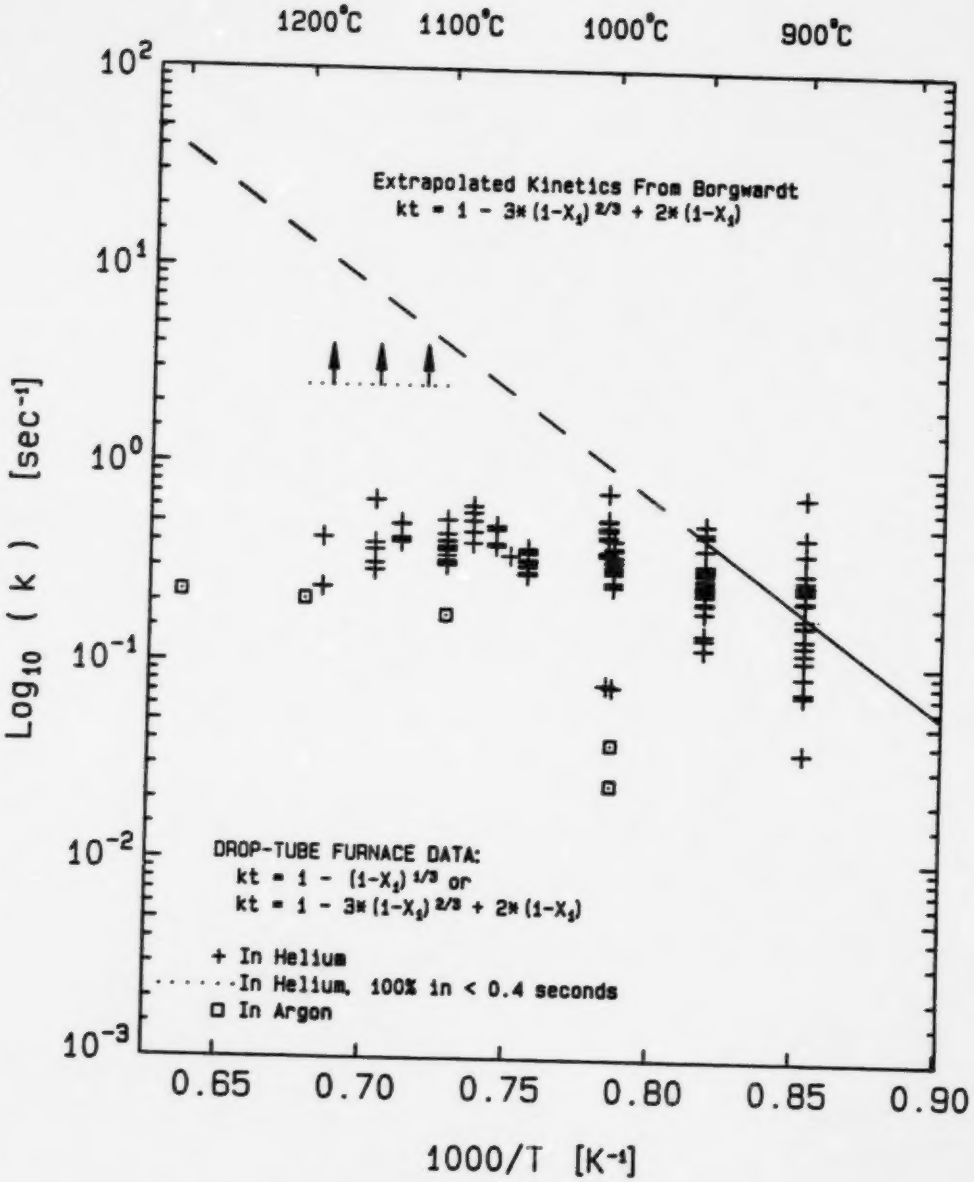

Figure 3-3. Arrhenius plot for calcium carbonate decomposition, from Snow (1985).

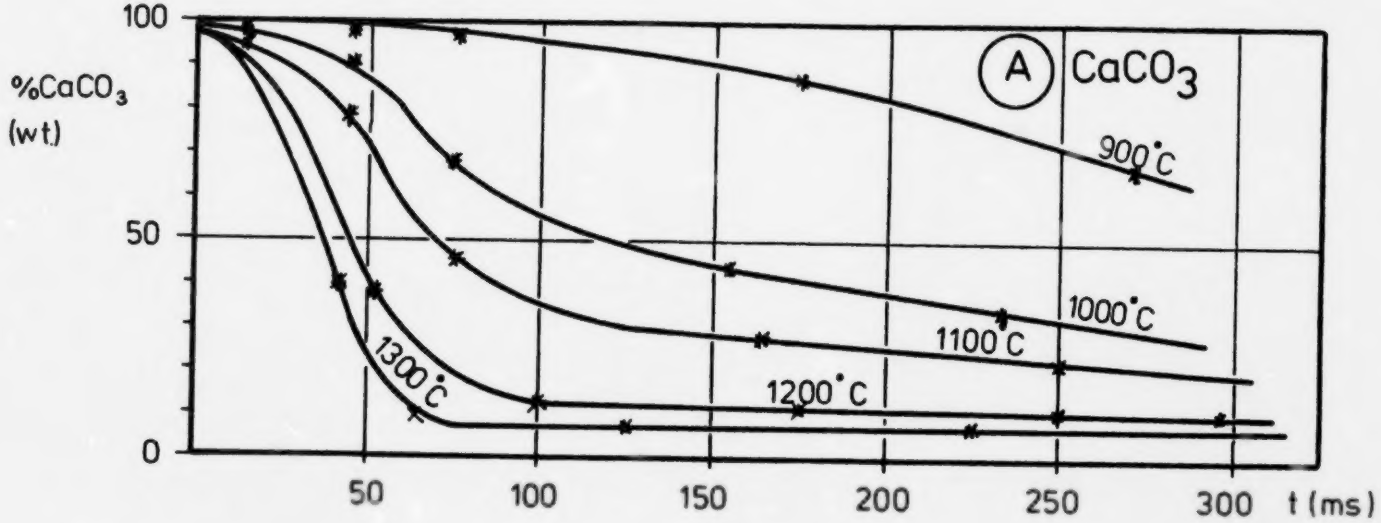

Figure 3-4. Decomposition of $CaCO_3$ particles in the IFRF isothermal reactor (Bortz and Flament, 1985).

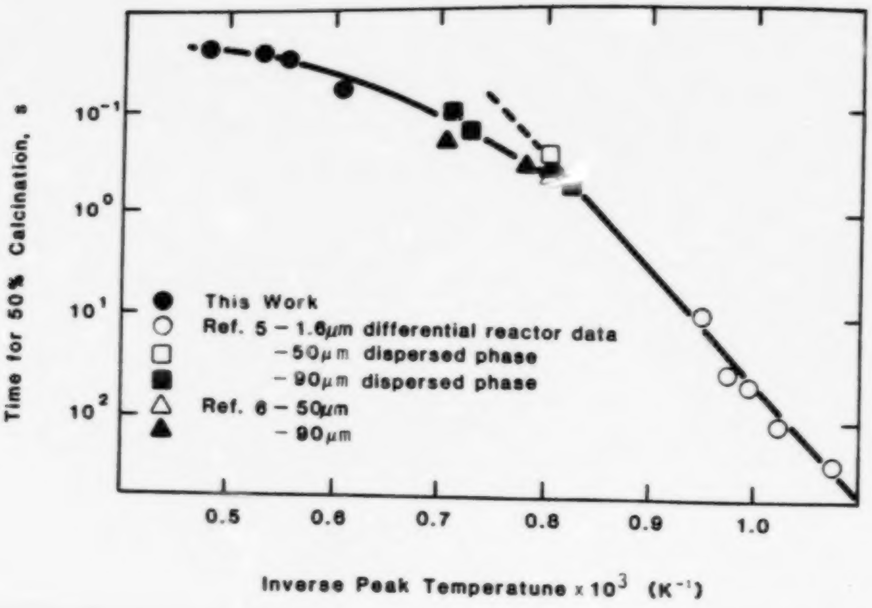

Figure 3-5. Correlation of time for 50 percent calcination with peak particle temperature (data generated under EPA Contract 68-02-3995.

Because of the experimental difficulties involved, there have been relatively few attempts to characterize the hydrate decomposition rate under furnace injection conditions. The IFRF Bortz and Flament (1985) measured calcination extents of a hydrate in the isothermal reactor mentioned previously. These results are shown in Figure 3-6. The results suggest an extremely rapid rate which is beyond the time resolution of the experiment to define. The fact that the reaction has been essentially completed within the first 10 msec suggests that in practical systems (and potentially laboratories also) the calcination rate is governed by the rate at which the sorbent carrier gas is heated by mixing. Thus, a truly high temperature calcination rate may not be of practical importance. The key activation variable may be the influence of heating rate on reactivity.

3.1.3 Physical Consequences of Activation

The calcination reaction not only provides the CaO reactant that participates in the sulfation reaction, but it also results in physical changes to the stone that influence reactivity. These changes include the development of an internal porous structure, and the fragmentation of particles.

Pure crystalline calcium carbonate will yield a structure that is 54 percent porous if it is calcined without shrinking or swelling. Most of the surface area seems to reside in micropores that are generally monosized in the 100-300A range. If the ideal 45 percent porous structure is assumed to be made up of 150A pores, then the specific surface area of the calcine is about 93 m^2/gm. This value agrees qualitatively with the highest surface areas obtained by careful vacuum calcination, and also the surface areas generated by flash calcination in the EPA differential reactor (Borgwardt, 1985). This number may represent the fundamental limit on microporosity achievable, and may also represent the surface area that is available in the freshly generated CaO, near the $CaCO_3$ interface during calcination.

This point is difficult to prove during high temperature calcination because of a concurrent desurfacing reaction. As will be discussed presently, the presence of CO_2 or water vapor act to accelerate the

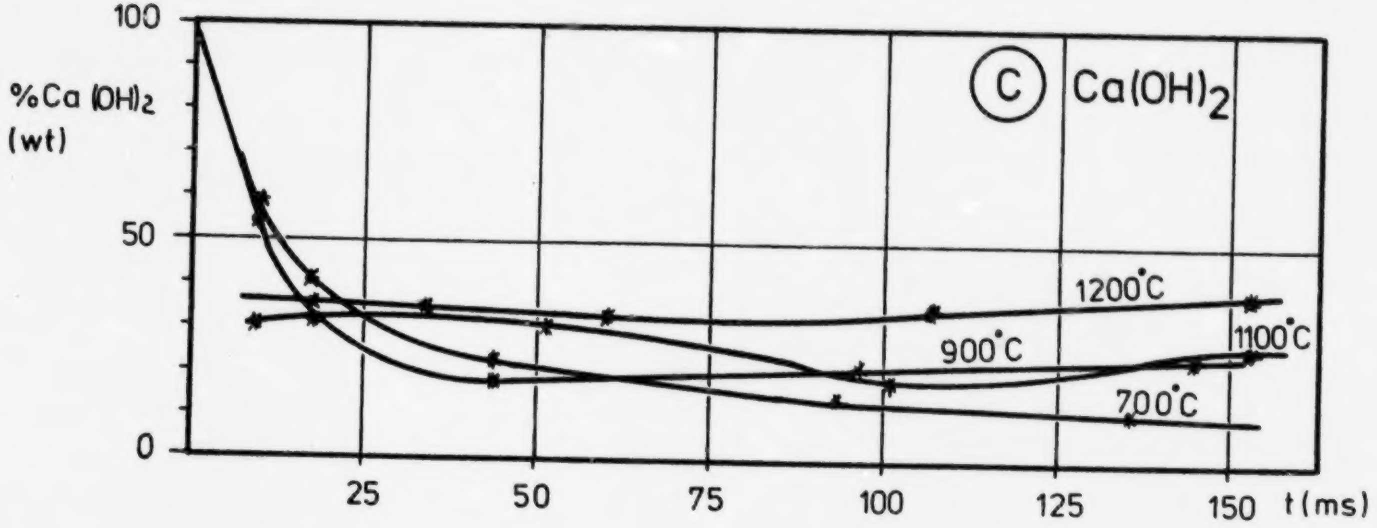

Figure 3-6. Decomposition of $Ca(OH)_2$ particles in the IFRF isothermal reactor (Bortz and Flament, 1985).

desurfacing process. Since these species are present in flue gas at concentrations that are known to be a factor in desurfacing, the very high surface areas of the fresh sorbent may indeed be reduced by contact after it has been generated. Also, under some circumstances the CO_2 or water produced within the particle during hydrate or carbonate calcination may act to reduce surface area.

The simplest way to approach the surface area development/desurfacing problem is to decouple the desurfacing step from the activation/surface area development step. The desurfacing characteristic can be developed independently, and can be subsequently applied to the activation step.

Borgwardt et al. (1985) have developed surface area loss data in the EPA differential reactor. These are illustrated in Figure 3-7 for inert sweep gas. The first general observation is the slowness of the reaction. At 1000°C, approximately 3 minutes are necessary to lose half the surface area of 70-90 m^2/g stones. This would extrapolate to an insignificant loss under furnace conditions. The second point is that at the lower temperatures the surface area seems to decay to a specific value and stop. This apparent asymptotic surface area probably represents some shift in mechanism between a fast and a slow decay rate. This illustrates that desurfacing may require a more complex treatment than as a simple one-step reaction rate.

Figure 3-8 illustrates that the sintering rate is substantially accelerated in the presence of CO_2 (Borgwardt et al., 1985). These data are difficult to extrapolate to furnace time scales, and the influence of temperature on this CO_2 acceleration has not been defined.

At EER, the short time desurfacing characteristic of 10 micron materials precalcined to 32 m^2/g have been measured in an entrained flow isothermal reactor. Figure 3-9 shows the specific surface areas resulting from isothermal exposure to methane/air combustion gas at the indicated temperatures. The following points are noted:

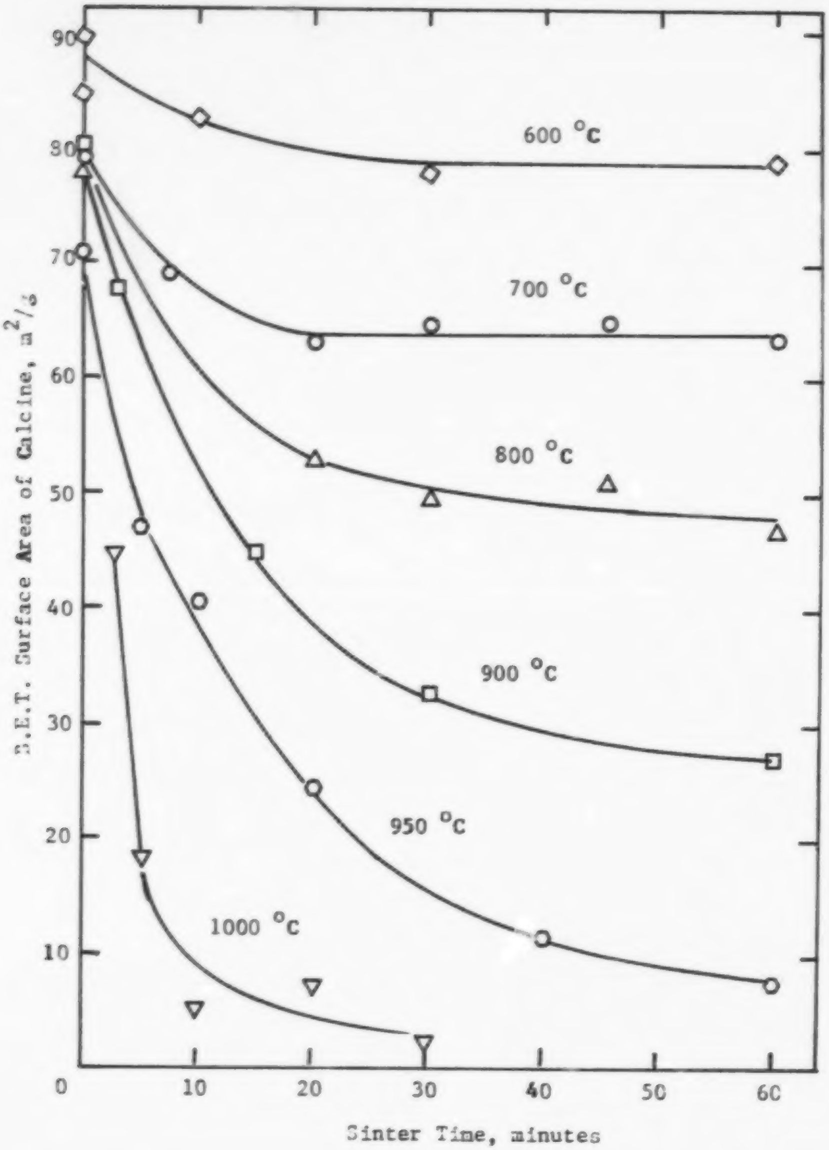

Figure 3-7. Sintering extents of CaO under nitrogen in the EPA differential reactor (Borgwardt et al., 1985).

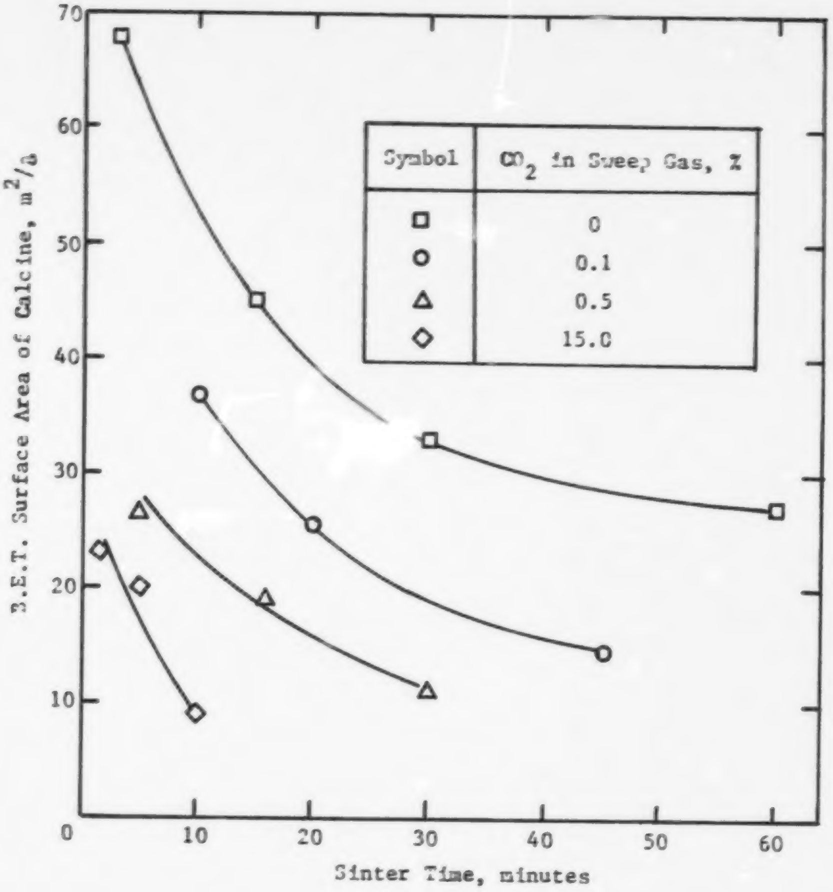

Figure 3-8. Acceleration of sintering in the presence of CO_2 in the EPA reactor (Borgwardt et al., 1985).

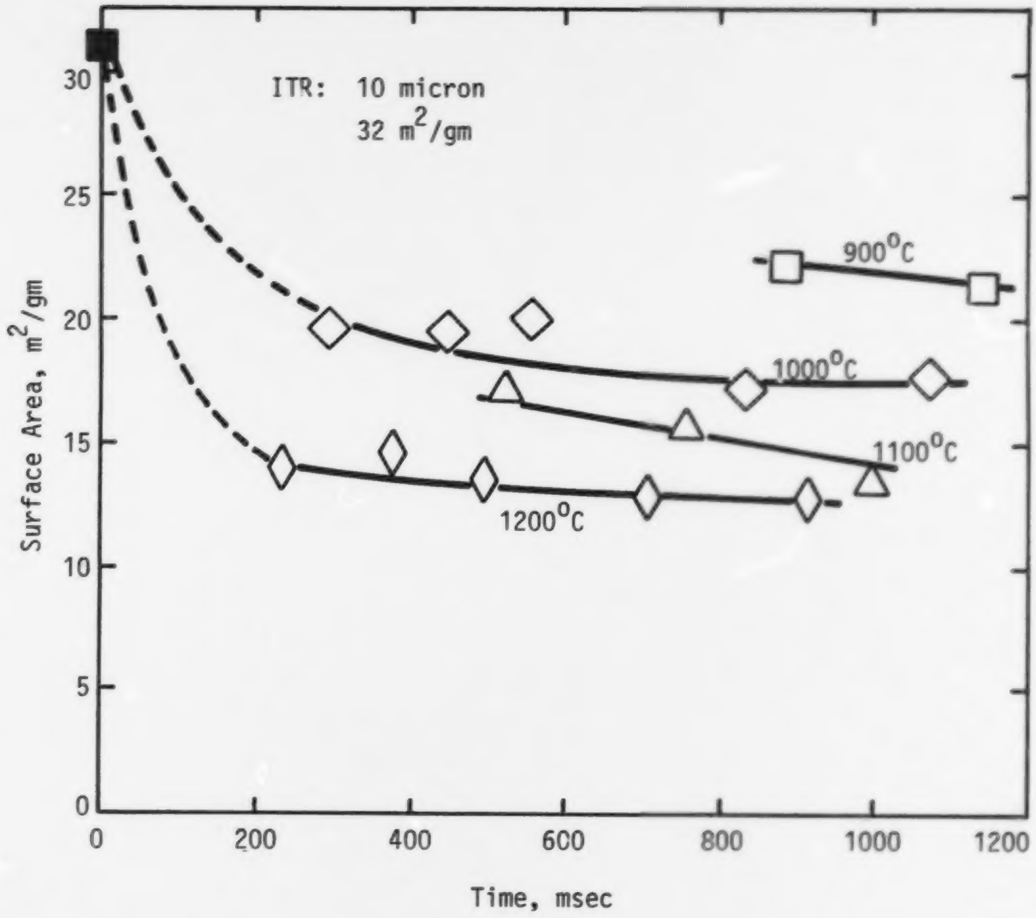

Figure 3-9. Short time desurfacing profiles under isothermal flue-gas conditions for a 32 m^2/g precalcine.

- The exposure of high surface area materials to CO_2 and water vapor within the sampling system has been shown to result in some desurfacing. Thus, there is no guarantee that the surface areas reported in Figure 3-9 were not influenced by sampling system desurfacing.

- However, the results do indicate that temperature does influence desurfacing.

- The desurfacing appears to be rapid within the first 200 ms, and it goes to a much slower rate at larger times.

- The question of how desurfacing depends on initial surface area has not been addressed.

These surface areas compare in an unusual way with those generated when raw sorbent is treated to the same environment. Figure 3-10 shows the specific surface areas obtained when a 10 micron carbonate, its 32 m^2/g precalcine, and a raw Linwood pressure hydrate are all exposed to identical 1000^oC environments. Interestingly, although both the carbonate and hydrate show lower surface areas than the precalcines, both generally show superior sulfation performance. This may be an indication that the short-time behavior of these materials plays a key role in establishing sulfation performance. This short time region is not accessible in the present reactor.

Besides surface area growth and decay, another physical phenomena accompanying calcination is particle fragmentation. Figure 3-11 shows the change in particle size distribution that accompanies the calcination of Vicron 45-3 limestone particles. For a 1830^oC peak flame exposure, the reduction in mean size is from 11 to 5 microns, which corresponds to a 10:1 fracture ratio. At 1360^oC the reduction is from 11 to 9 microns, which corresponds to just below a 2:1 fracture ratio. Thus, it would appear that little fracture of limestones occurs at the optimum injection temperatures for furnace injection.

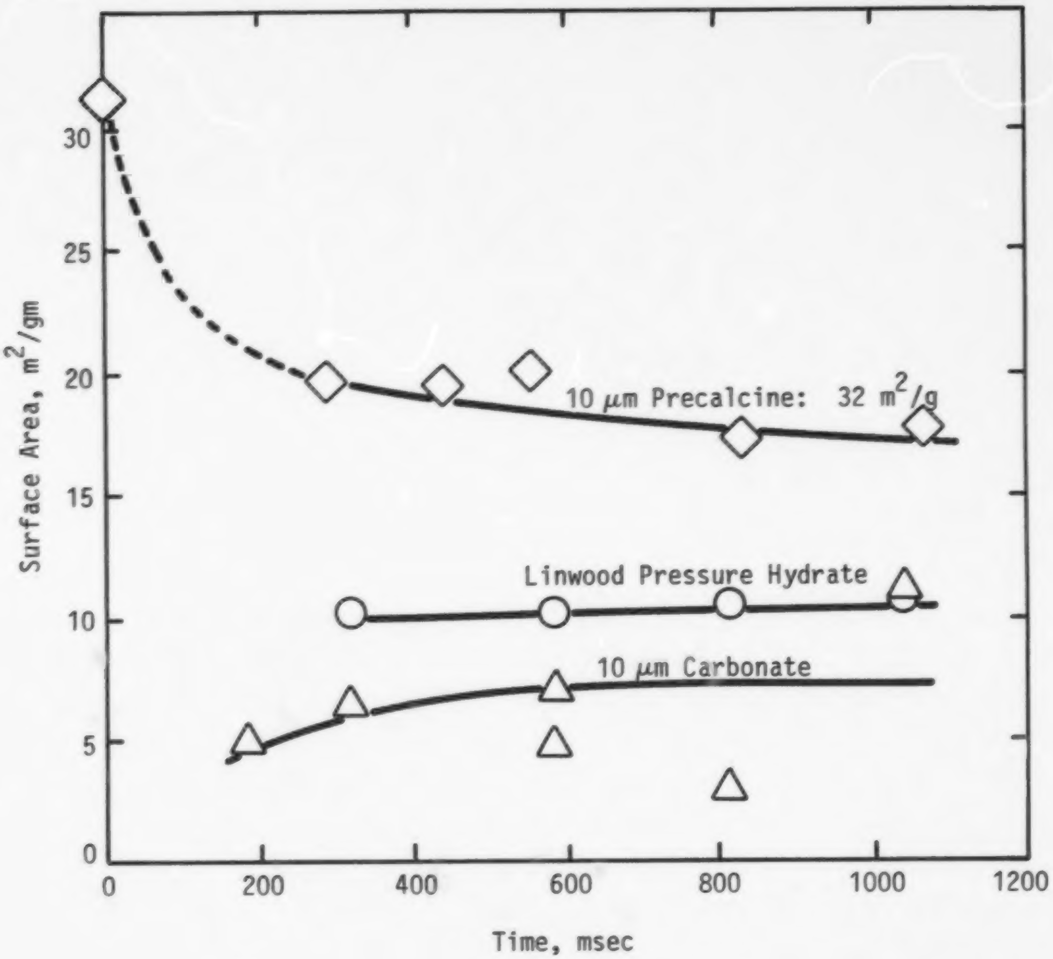

Figure 3-10. Surface area development and decay at 1000°C.

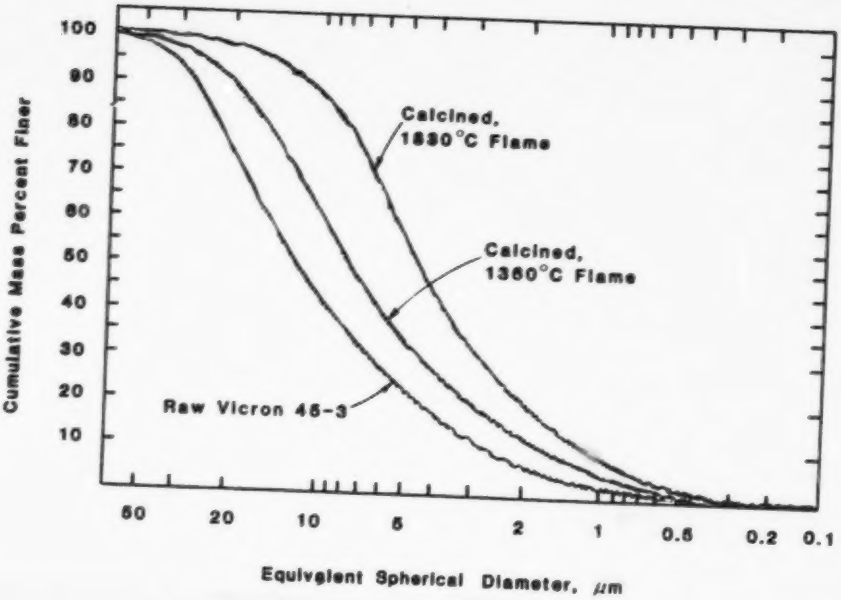

Figure 3-11. Particle size distributions for Vicron 45-3 pulverized limestone before and after flame treatment.

3.2 Modeling Approach

The calcination and subsequent surface area loss of calcining $CaCO_3$ and $Ca(OH)_2$ particles are described using a correlative mathematical model with model parameters based on the data of Borgwardt (1985) and Borgwardt, et al. (1986). The model describes the decomposition of $CaCO_3$ at the reaction interface followed by the deactivation of the CaO. The following description of the model will focus on carbonates but it should be understood that all equations are directly applicable to hydrates, with minor changes.

The following steps were considered in describing the calcination and surface area loss process:

- Decomposition of $CaCO_3$ at the CaO-$CaCO_3$ interface.
- Diffusion of CO_2 through the CaO to the particle surface.
- Diffusion of CO_2 from the particle surface to the bulk gas.
- Continuous surface area loss for all calcined material.

The overall concept for the model is shown in Figure 3-12. The calcination process was represented by the shrinking core model for a sphere with the intrinsic calcination rate dependent only on chemical factors as reported by Borgwardt (1985).

The equations governing the movement of the calcination front are

- $\frac{dr}{dt} = - \frac{M}{\rho} R_D$, m s^{-1} (3.1)
- at $t = 0$, $r = r_o$ (3.2)
- $R_D = K_D(P_e - P)$, kgmol m^{-2} sec^{-1} (3.3)
- $k_D = 0.00122 * \exp(-4026/T)$ kgmol m^{-2} s^{-1} atm^{-1}
- $Pe = \exp(17.74 - 0.00108T + 0.332\ln T - 22020/T)$, atm

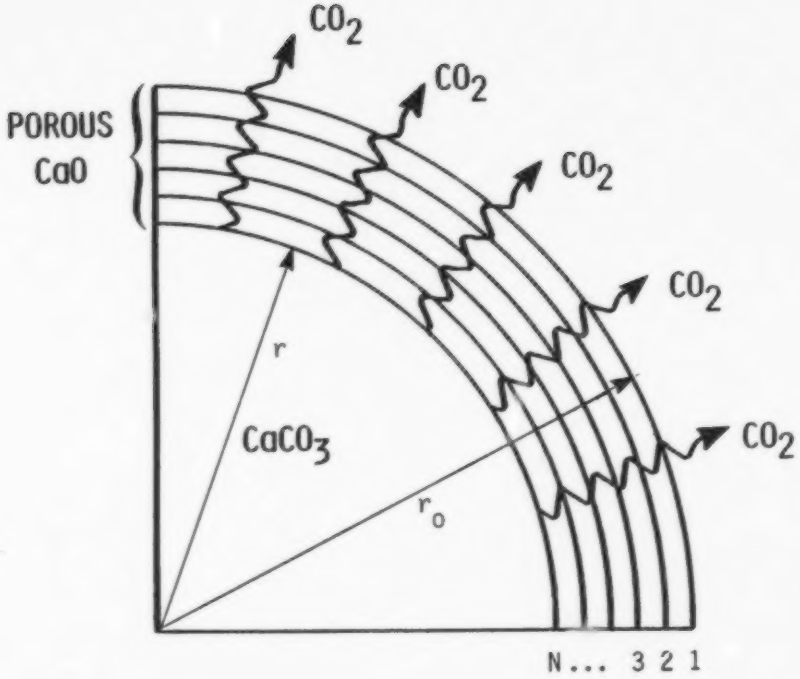
CO2
CO2
CO2
CO2
CO2
POROUS CaO
r
CaCO3
r0
N... 3 2 1

Figure 3-12. Schematic of the calcination model.

where r is radius of the shrinking core of $CaCO_3$, t is time, M is the molecular weight of $CaCO_3$, ρ is the density (kg m^{-3}) of $CaCO_3$, R_D is the rate of decomposition, r_0 is the initial particle radius, which is assumed constant, k_D is a rate constant, P_e is the equilibrium dissociation pressure of CO_2 in atmospheres, P is the CO_2 partial pressure at the CaO-$CaCO_3$ interface, and T is the absolute temperature in degrees Kelvin. Note that the rate of decomposition, R_D, approaches zero as P approaches P_e. This provides a means of allowing the decomposition reaction to slow itself down should diffusion impede the escape of generated CO_2.

Several investigators, including Darroudly and Searcy (1981) and Hyatt, et al. (1958), have examined the effects of CO_2 pressure on decomposition kinetics; however, no one has yet developed an expression which is capable of explaining all of the data. The mechanism of decomposition is still uncertain. The CO_2 pressure dependence of Equation 3.3 is consistent with the theory of Searcy and Beruto (1978) in which the rate limiting step is solid-state diffusion of CO_2 or possibly a surface step for CO_2.

The diffusion of gaseous CO_2 in porous line was studied by Campbell, et al. (1981) who determined that the process was controlled by Knudsen diffusion. As part of the present study the relative importance of ordinary diffusion, Knudsen diffusion, and hydrodynamic flow were examined. It was concluded that, at the calcination conditions which are appropriate to sorbent injection, Knudsen diffusion was the controlling transport mechanism for CO_2 in porous lime; however, for a moderately sintered sorbent in which pore diameters are larger, ordinary diffusion may become important. For this reason the diffusion coefficient is calcualted as

$$D = (D_K^{-1} + D_{AB}^{-1})^{-1},\ m^2\ s^{-1} \qquad (3.4)$$

where

$$D_K = 0.00881 T^{1/2} S^{-1},\ m^2\ s^{-1} \qquad (3.5)$$

and

$$D_{AB} = 0.000139 \left(\frac{T}{273}\right)^{1.75} P_t^{-1},\ m^2\ s^{-1}. \qquad (3.6)$$

Finally, the effective diffusivity for the porous material is given by

$$D_{eff} = D\ {}^{2} \qquad (3.7)$$

where ε is the porosity of the calcine. Equation 3.7 approximates the calcine's tortuosity as ε^{-1}. In the above equations D is the diffusion coefficient for the pore, D_K is the Knudsen diffusion coefficient, D_{AB} is the molecular diffusion coefficient for CO_2 in air, T is temperature in degrees Kelvin, S is the BET surface area in $m^2\ kg^{-1}$, and P_t is the total pressure in atmospheres.

The differential equation governing the diffusion of CO_2 through the porous lime is

$$\frac{\partial^2 P}{\partial R^2} + \left(\frac{2}{R} + \frac{1}{D_e}\frac{D_e}{R}\right)\frac{\partial P}{\partial R} = \frac{1}{D_e}\frac{\partial P}{\partial t} \qquad (3.8)$$

with two boundary conditions:

$$\text{at } R = r_o,\ -D_e \frac{\partial P}{\partial R} = k_f(P - P_b) \qquad (3.9)$$

$$\text{at } R = r,\ -\frac{D_e}{R_g T}\frac{\partial P}{\partial R} = k_D(P_e - P) \qquad (3.10)$$

where R is the radial position within the calcined layer, k_f is the mass transfer coefficient for a spherical particle, P_b is the CO_2 partial pressure in the bulk gas, and R_g is the gas constant. Equation 3.8 can be simplified by applying the pseudo steady approximation for gas-solid reactions as described by Luss (1968):

$$\frac{d^2P}{dR^2} + \frac{2}{R}\frac{dP}{dR} = 0 \qquad (3.11)$$

Equations 3.11, 3.9, and 3.10 are readily solved by dividing the shell of calcine into nodes as shown in Figure 3-12. If the calcine shell between each node is assumed homogeneous, then the problem is completely analogous to the spherical, composite wall situation in heat transfer. The positions of the nodes can be defined by solving Equation 3.1 over short time intervals, i.e., for a time step of Δt

$$r(t + \Delta t) = r(t) + \left.\frac{dr}{dt}\right|_{t} \Delta t \;. \qquad (3.12)$$

The solution to Equations 3.11, 3.9, and 3.10 is

- For node 1

$$P_1 = P_b + \frac{R_N k_D R_g T}{R_1^2 k_f} (P_e - P_n) \qquad (3.13)$$

- For nodes 2 through N-1

$$P_i = P_{i-1} + \frac{F R_g T}{4\,(D_e)_{i-1}} \left(\frac{1}{R_i} - \frac{1}{R_{i-1}}\right) \qquad (3.14)$$

where

$$F = 4\pi R_N^2 k_D (P_e - P_N)$$

- For node N

$$P_N = \frac{P_e + BP_b}{1 + B} \qquad (3.15)$$

where

$$B = \frac{A_1 U_1}{4\,R_N^2\,k_D}$$

$$A_1 = \frac{4\pi R_1^2}{R_g T}$$

$$\frac{1}{U_1} = R_1^2 \sum_{j=1}^{N-1} \frac{1}{(D_e)_j} \left(\frac{1}{R_{j+1}} - \frac{1}{R_j} \right) + \frac{1}{k_f} \ .$$

Having determined the CO_2 profile in the lime shell, one returns to Equation 3.12 to calculate the thickness of the next shells of CaO to be added to the nodal grid. Recall that the rate of calcination is a function of CO_2 partial pressure; hence, the equations 3.12, 3.13, 3.14, and 3.15 are all coupled. Finally, as each layer of CaO is formed it immediately begins to lose its high initial surface area to grain agglomeration or sintering.

The previous discussion dealt primarily with mathematical ways of describing the decomposition of $CaCO_3$. This section focuses on the sintering of CaO which has been formed from the decomposition of either $CaCO_3$ or $Ca(OH)_2$. Borgwardt, et al. (1985) has convincingly shown that the rate of surface area loss is a strong function of time, temperature, nitrogen sweep rate, and H_2O and CO_2 partial pressures. The complicated nature of the process necessitates an empirical approach to modeling. Typical surface area loss results of Borgwardt, et al. (1985) were shown in Figure 3-7. Note that the data are characterized by a rapid initial rate of BET surface area decrease followed by a slow rate of decrease. At longer times the surface area approaches an asymptotic value which is a strong function of temperature; however, at temperatures of practical importance for sulfation (1000°C or greater) the asymptote is roughly $5 m^2/g$. For subsequent analysis, an asymptotic value of $5 m^2/g$ is assumed for all conditions at or above 1000°C.

The form of the rate expression which best describes the data in Figure 3-7 is

$$\frac{dS}{dt} = -k(S-S_{as})^2, \ m^2 kg^{-1} s^{-1} \qquad (3.16)$$

where S is the BET surface area, t is time, k is a rate constant, and S_{as} is the asymptotic surface area. The data in Figure 3-7 were obtained in a differential reactor with pure N_2 sweep gas. The importance of the CO_2 concentration in the sweep gas is shown in Figure 3-8. CO_2 concentrations as low as 1000 ppm have a pronounced effect on the rate of sintering.

To account for the acceleration of surface area loss by CO_2, the rate constant in Equation 3.16 was written in the following form

$$k = A \exp\left(- \frac{E}{R_g T}\right) \exp\left(\frac{BP^m}{R_g T}\right), \text{ kg m}^{-2}\text{s}^{-1} \qquad (3.17)$$

where A is a preexponential factor, E is an activation energy, P is the CO_2 partial pressure (atm.), and m is a dimensionless exponent. The second exponential on the right in Equation 3.17 has the effect of lowering the activation energy for the sintering process. Based on the data in Figure 3-8 and on other CO_2 concentration data from Borgwardt, et al.[9] values of -0.111 and -314 atm m^3 $kgmol^{-1}$ were calculated for m and B, respectively. The activation energy E and the preexponential factor A were determined from the data of Borgwardt[8] which are shown in Figure 3-13. A CO_2 concentration of 5000 ppm was assumed in order to account for the incomplete calcination of the precalcine. The data in Figure 3-13 were selected for analysis because of the fact that they are the only known data for a very high surface area precalcine obtained at temperatures and times which approach those found in a boiler. The sintering rates derived from Figure 3-13 greatly exceed the rates obtained from Figure 3-7. The former are used as basis for modeling because of their more realistic data base. The complete expression for the sintering rate constant becomes

$$k = 286 \exp \frac{-14500 - 3820P^{-0.111}}{T}, \text{ kgm}^{-2}\text{s}^{-1} . \qquad (3.18)$$

The solid lines in Figure 3-13 are calculated based on Equations 3.16 and 3.18. If water also contributes to the rate of surface area loss, Equation 3.17 can be extended by the addition of another exponential term.

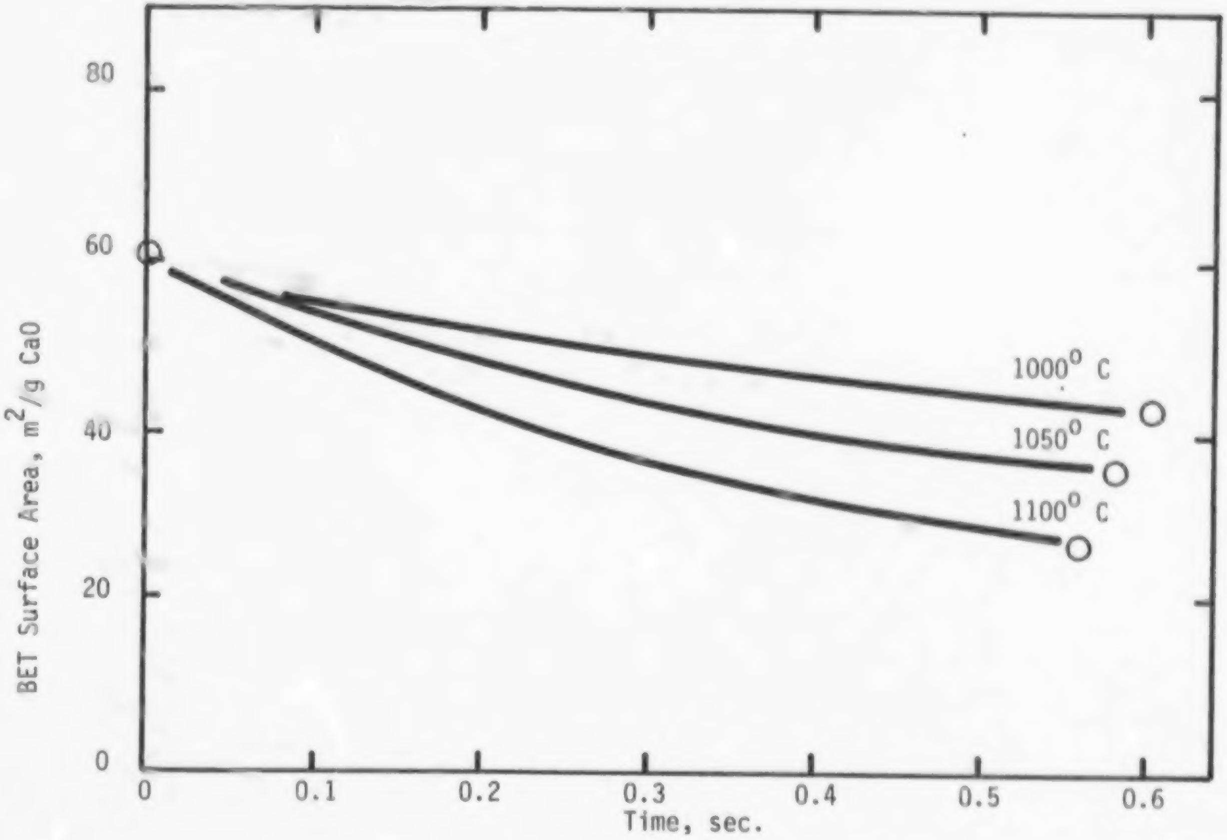

Figure 3-13. The isothermal flow reactor data of Borgwardt (1984) for a calcine prepared at 1000° C. The precalcine particles were conveyed in pure N_2. The solid lines are model predictions based on Equations 3.16 and 3.18.

Equations 3.18 and 3.16 are coupled to Equation 3.1, 3.9, 3.10, and 3.11 by the CO_2 partial pressure. All six equations must be solved simultaneously to describe the calcination of $CaCO_3$ and the subsequent surface area loss of the CaO.

3.3 Comparison with Data and Applications

3.3.1 CO_2 Partial Pressure and Surface Area Profiles

The semi-theoretical model described above was used to predict CO_2 pressure build-up and surface area development during the calcination of carbonates. The variables examined with the model include temperature, particle size, and time. The calculations assume an initial BET surface area of 100 m^2/g and an asymptotic value of 5 m^2/g.

Figure 3-14 shows peak CO_2 partial pressures as a function of calcination temperature for particle diameters ranging from 1 to 50 μm. Peak pressures increase with increasing particle size and temperature. The dashed line in the figure indicates the equilibrium dissociation pressure of $CaCO_3$. At the highest temperature and for a 50 μm particle, the peak pressure was roughly 3 atm which is well below the equilibrium value. Hence, it does not appear that the calcination process is impeded by equilibrium constraints at conditions of practical interest.

The effect of time on the extent of calcination and the development of CO_2 pressure is shown in Figure 3-15 for a 50 μm particle. The calculations indicate that the peak CO_2 pressure at the interface occurs when the particle is 90 percent calcined.

Surface area and CO_2 profiles are shown in Figure 3-16 for a 50 μm particle at 2200°F and in Figure 3-17 for a 5 μm particle at the same temperature. Both figures show instantaneous profiles for particles which are calcined. The 50 μm case shows steep surface area and CO_2 gradients relative to the 5 μm particle. The steep gradients are due to the 50 μm particle's large size which not only offers a larger resistance to the

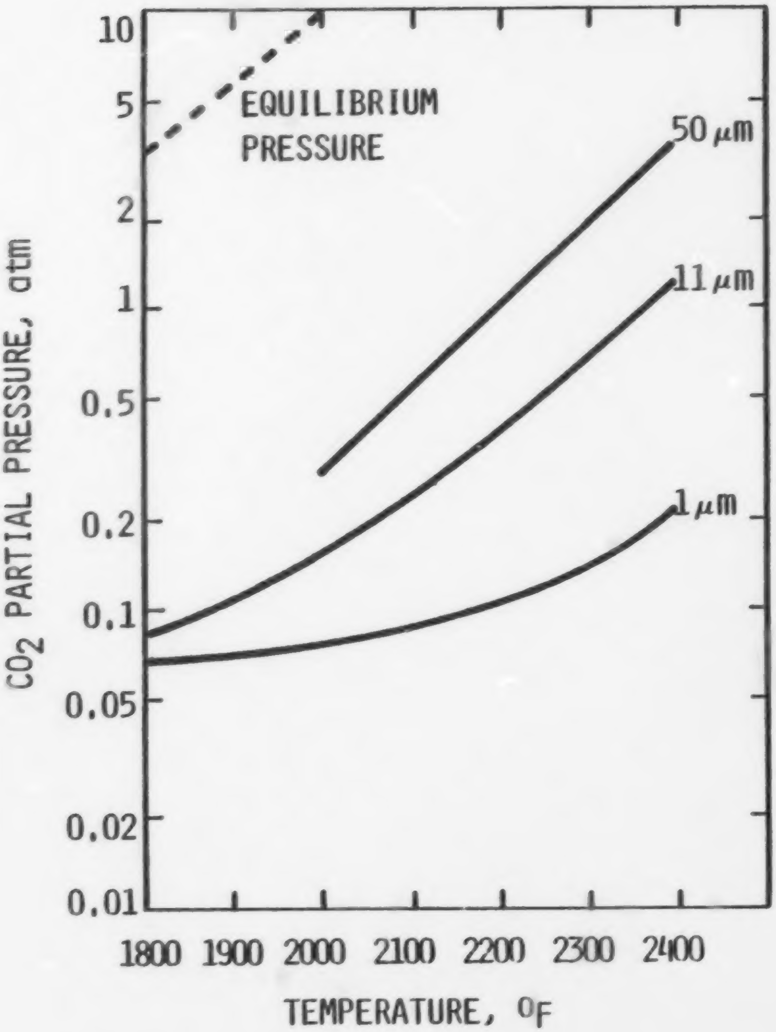

Figure 3-14. Model predictions of peak CO_2 partial pressure at the $CaO-CaCO_3$ interface for calcination at isothermal conditions with a bulk gas CO_2 pressure of 0.065 atm.

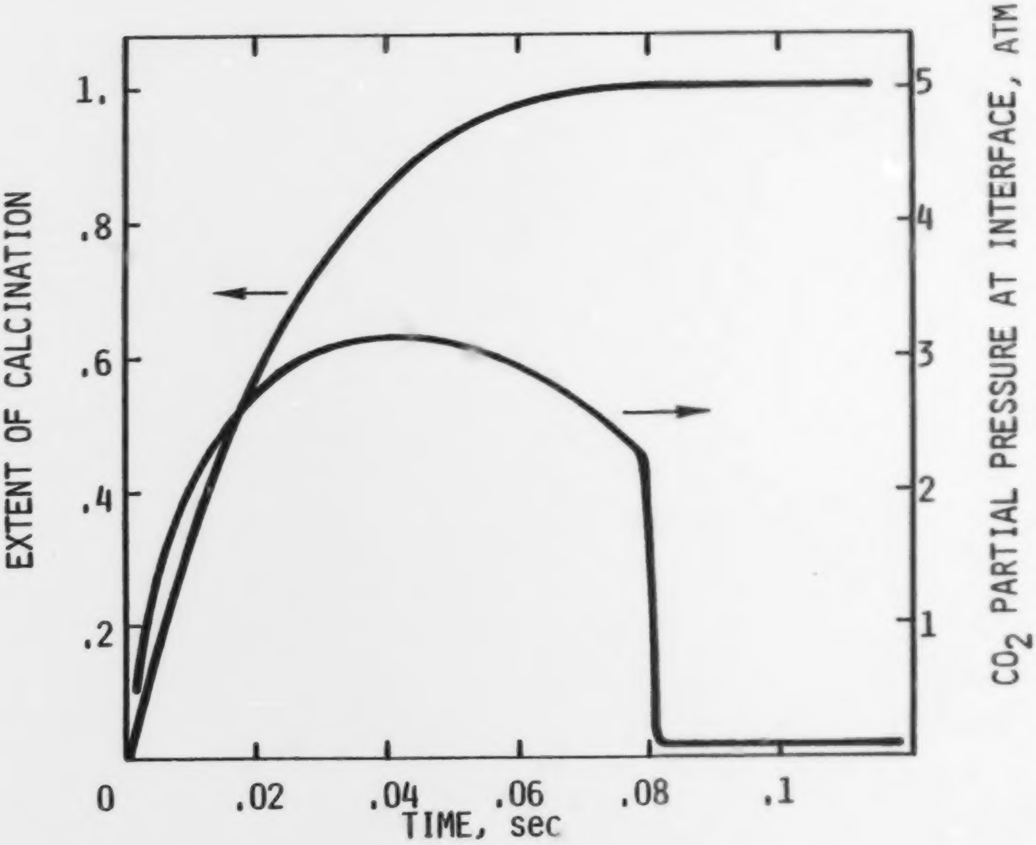

Figure 3-15. Model predictions showing the influence of time on the extent of calcination and the CO_2 partial pressure at the $CaCO_3$-CaO interface. The calculations assumed a constant temperature of 2400° F, a 50μm particle, and a bulk gas CO_2 pressure of 0.065 atm.

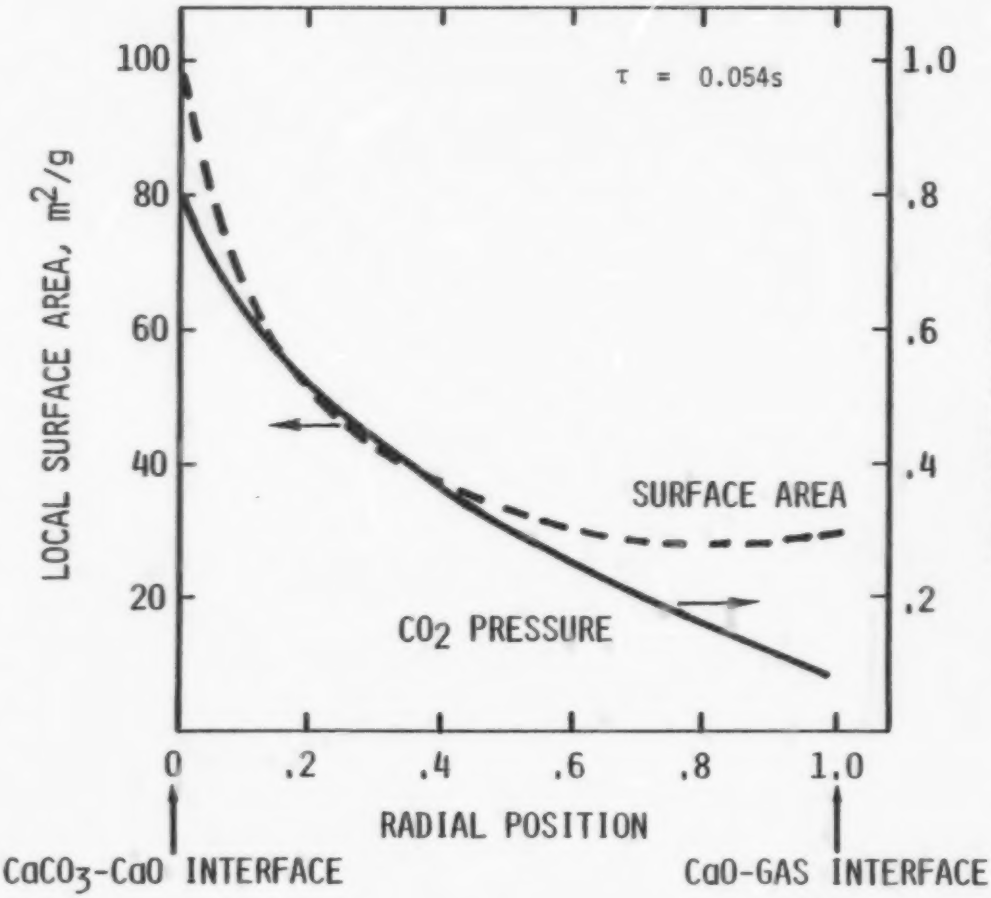

Figure 3-16. Model predictions showing CO_2 pressure gradients and the surface area profile for a 50μm particle being calcined at 2200° F. The extent of calcination is 50 percent and the bulk gas CO_2 pressure is 0.065 atm.

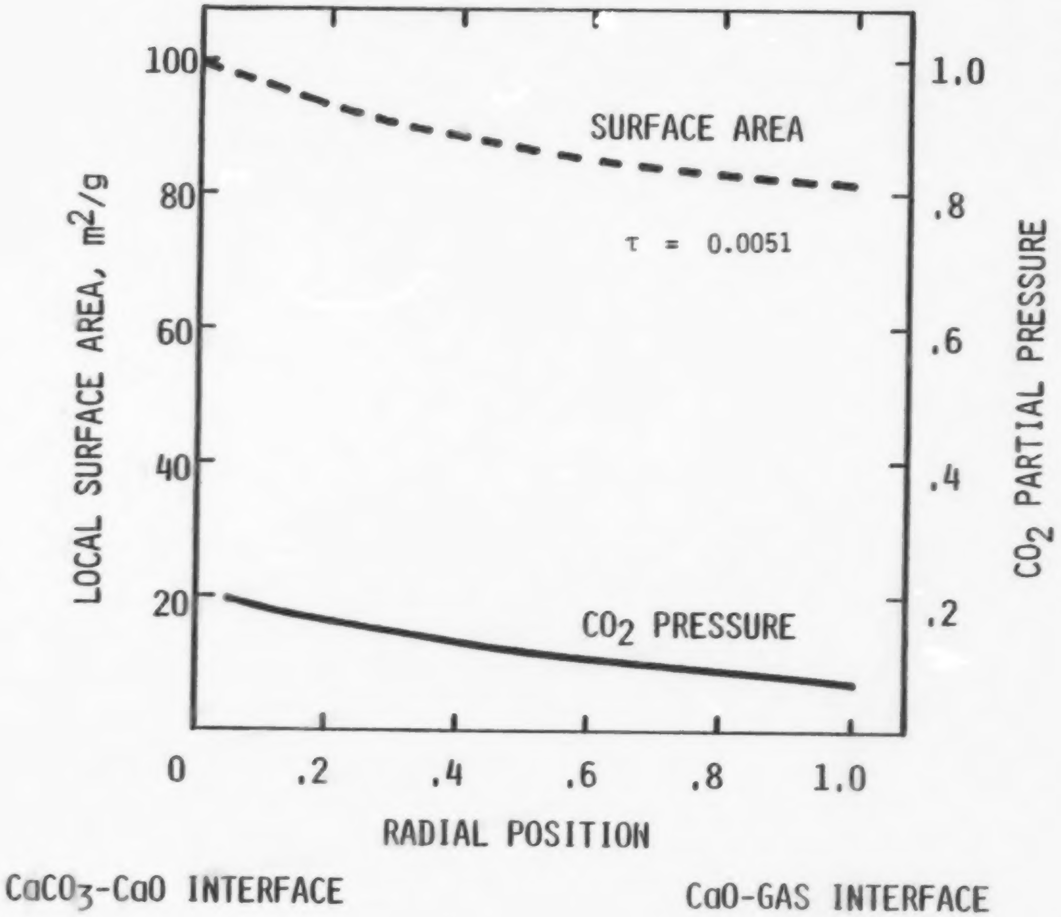

Figure 3-17. Model predictions showing CO_2 pressure gradients and the surface area profile for a 5μm particle being calcined at 2200° F. The extent of calcination is 48 percent and the bulk gas CO_2 pressure is 0.065 atm.

diffusion of CO_2 but also requires a longer time to reach 50 percent calcination. It is the latter time factor which explains the steep surface area profile in the 50 μm particle: the larger particle's CaO has existed longer and has sintered more extensively. These calculations show the advantage of using smaller particles if calcination and sulfation are occurring simultaneously or after a short delay. These conclusions cannot be applied to hydrates whose calcination times are extremely short.

3.3.2 Comparison of Model to Data

The model described above considers the simultaneous calcination and sintering of $CaCO_3$ or $Ca(OH)_2$. Comparisons of the model to the differential reactor, calcination data of Borgwardt (1985) are shown in Figure 3-18. Figure 3-18 is a plot of percent conversion of $CaCO_3$ to CaO versus time for three different particle diameters. As particle size decreases, the rate of calcination increases. The solid lines are model predictions and the agreement between the model and the data is good. Note that in making the calculations the particle diameter was estimated from the BET surface area of the raw stone. The diameters reported in Figure 3-18 are larger than those based upon the BET surface area.

F 3-18
19
20

Borgwardt (1985) also obtained flow reactor data. Figure 3-19 is a plot of percent conversion of $CaCO_3$ to CaO versus time at three different temperatures. The rate of calcination increases with increasing temperature. The solid lines are model predictions which agree well with the data; however, at all temperatures there is a tendency for the model to overpredict the rate of reaction. The data imply that it becomes more difficult to calcine the stone as calcination proceeds. It is conceivable that CO_2 is chemisorbed on CaO surfaces, which slows the apparent rate of reaction.

The effect of calcination temperature on surface area is demonstrated by the data of Slaughter (1986) in Figure 3-20. A high purity, calcitic limestone, Vicron 45-3, was used in the studies. Vicron 45-3 ranges in size from 0.3 to 45 μm with a mean size of 11 μm. The $CaCO_3$ was calcined for 0.5 second at isothermal conditions and shows a distinct optimum temperature for

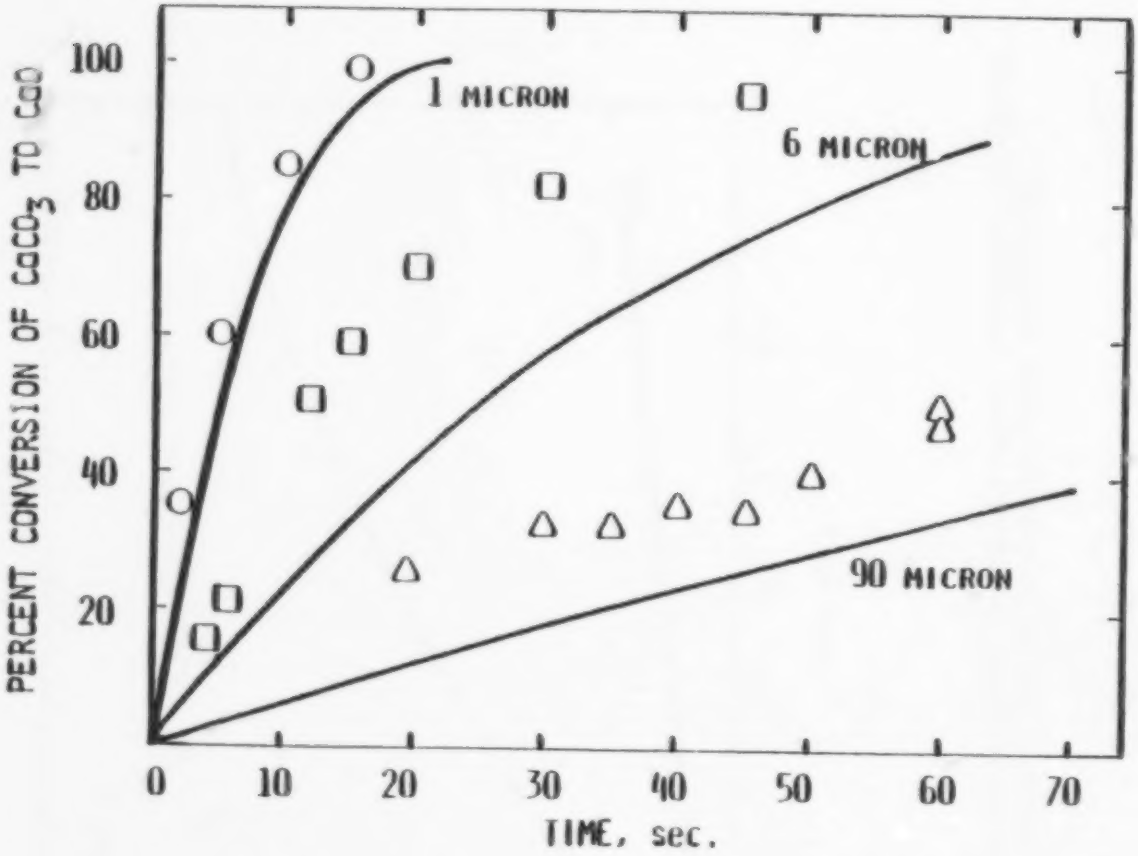

Figure 3-18. The calcination data of Borgwardt (1985) for Georgia marble compared to model predictions showing the effect of particle size. The marble was calcined in N_2 at 710° C in a differential reactor.

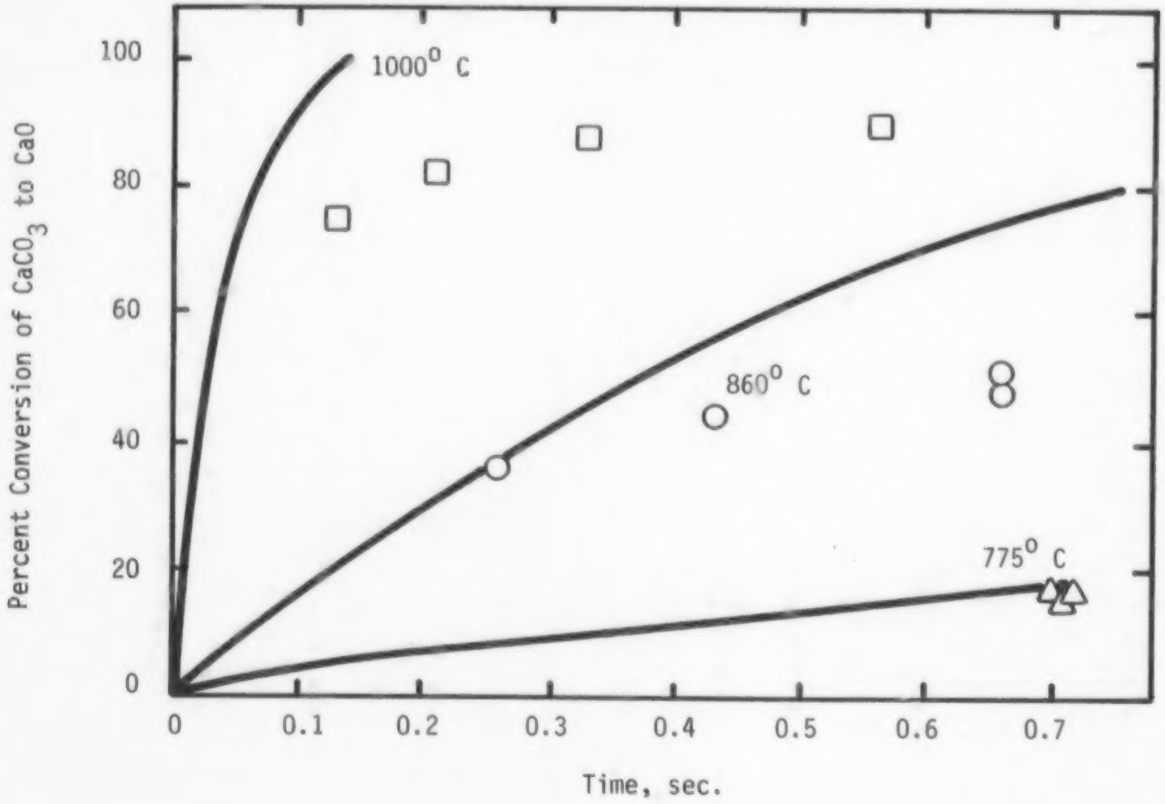

Figure 3-19. The data of Borgwardt (1985) for 10 μm Fredonia limestone calcined in N_2 in a flow reactor. The solid lines are model predictions.

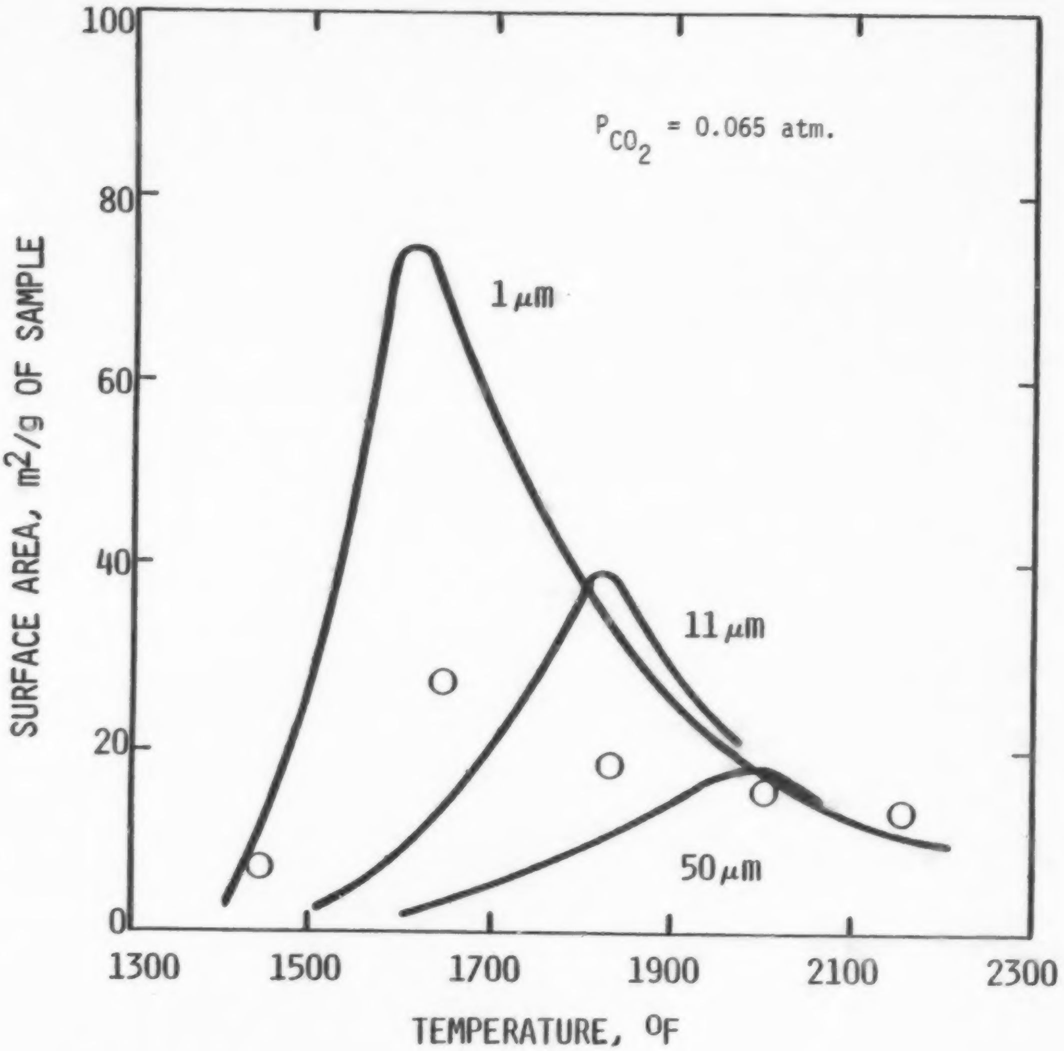

Figure 3-20. The B.E.T. surface area data of Slaughter (1986) obtained in a natural gas-burning, flow reactor at isothermal conditions and a residence time of 0.5 sec. The solid lines are model predictions at particle diameters of 1, 11, and 50μm.

maximum surface area. The solid lines in Figure 3-20 are model predictions based on $CaCO_3$ particle sizes of 1, 11, and 50 μm. The 11 μm predictions agree closely with the trends seen in the data. These and all subsequent model predictions are based on an initial surface area for CaO of 100 m^2/g and on an asymptotic value of 5 m^2/g, unless otherwise noted.

The effect of time on surface area development is shown in Figure 3-21 where the isothermal, flow-reactor data of Slaughter (1986) are plotted. The solid lines are model predictions for a range of particle sizes. The agreement between the model and the data is poor. One possible cause for the disagreement lies in the fact that the $CaCO_3$ may not immediately experience the 1800°F temperature of the isothermal reactor. The limestone was Vicron 45-3.

Figure 3-22 shows model predictions of the BET surface area as a function of time at 2200°F. At both 1800 and 2200°F there is a distinct difference between the surface area development of large and small particles. The 1 μm particles develop a high initial surface area which then sinters rapidly. The 11 μm particles calcine more slowly but sinter at the same rate as the 1 μm particles and for this reason never develop as high an initial surface area. Hence, in looking at the ability of a carbonate to capture SO_2, the activation model predicts that there is a distinct advantage for smaller sorbent particles due to their ability to calcine rapidly. This advantage is strengthened by the ability of SO_2 to react uniformly with sorbents whose diameter is approximately 5 μm or less.

Isothermal, flow-reactor data obtained at EER showing the effect of sintering time on precalcined CaO is presented in Figure 3-23. The 10 μm precalcine had an initial BET surface area of 32 m^2/g. The reactor's CO_2 partial pressure was 0.087 atm and data were obtained at temperatures of 1000 and 1200°C. The solid lines are model predictions which correctly indicate a decrease in surface area with increasing temperature. An asymptotic surface area of 5 m^2/g was assumed.

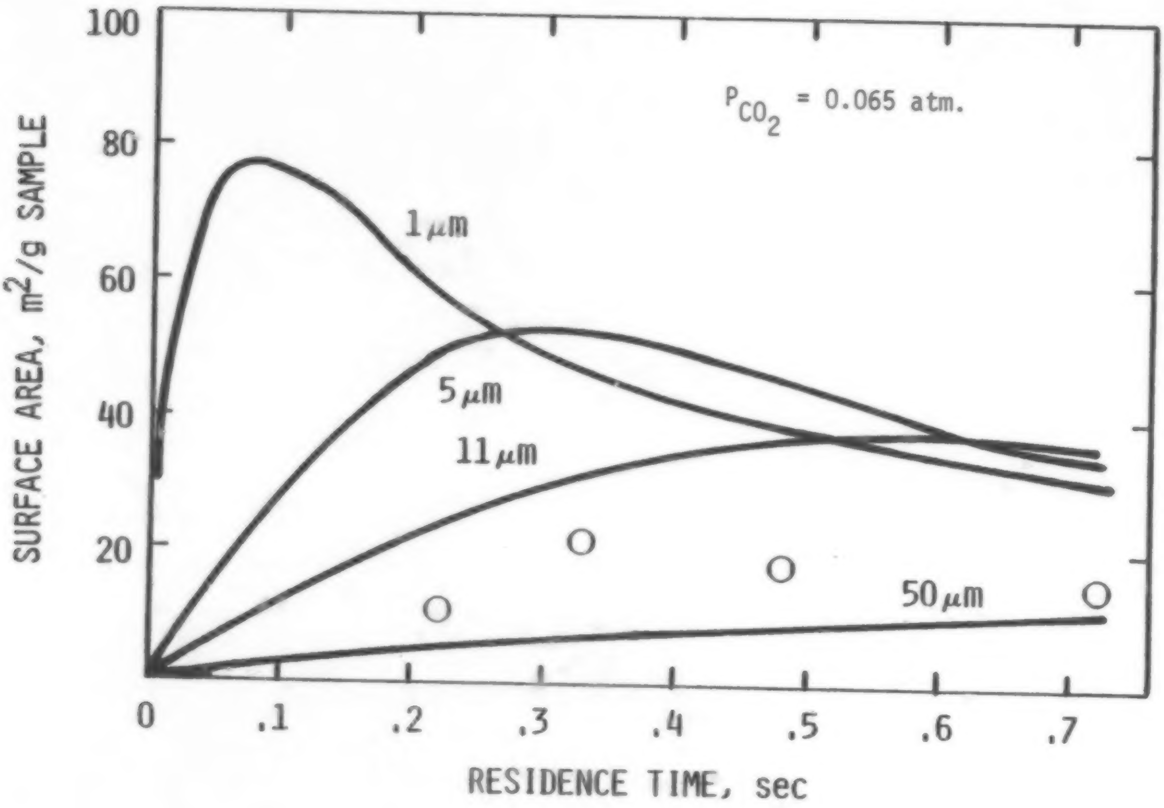

Figure 3-21. The data of Slaughter (1986) showing the effect of time on surface area for Vicron 45-3 at 1800° F, isothermal conditions. The solid lines are model predictions for several particle diameters.

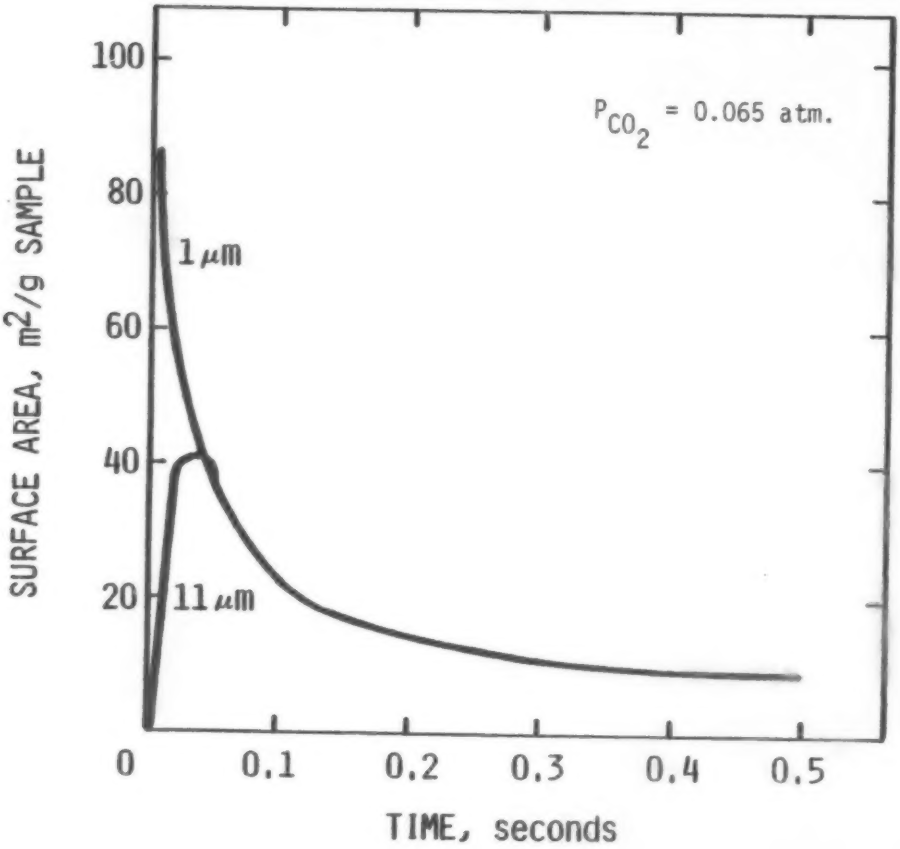

Figure 3-22. Model predictions showing the effect of time on surface area development at 2200° F for 1 and 11μm particles.

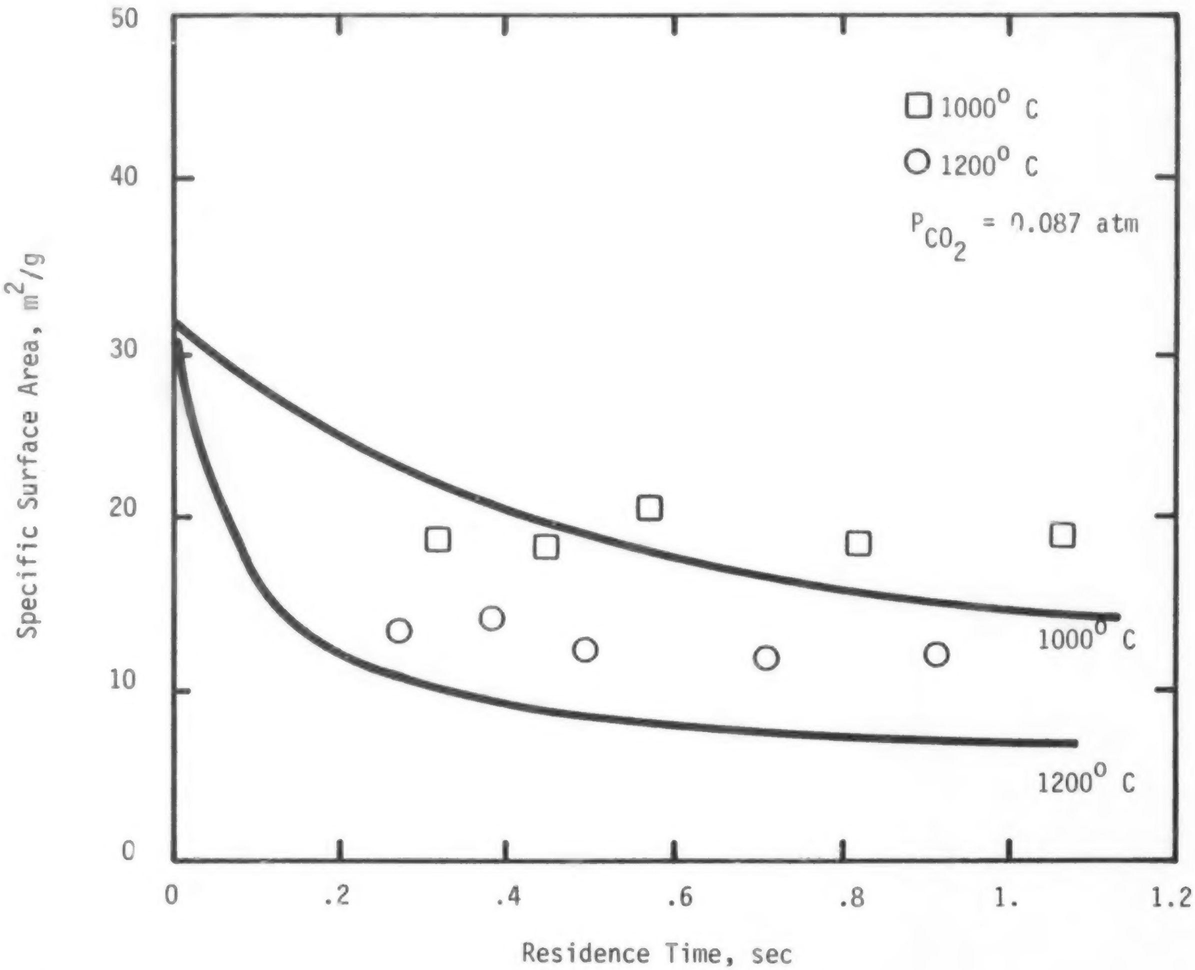

Figure 3-23. Isothermal, flow-reactor data of EER showing the effect of time on surface area for a 10 μm, precalcined limestone. The solid lines are model predictions.

3.3.3 Hydrates and Carbonates

The effect of sorbent type, i.e., hydrates versus carbonates, on activation has received relatively little attention. Relative rates of calcination were obtained by Bortz and Flament (1985) in an isothermal flow reactor. Their data are shown in Figure 3-24 for particle diameters of roughly 6 μm. The rate of hydrate decomposition is much faster than that of carbonates. Hydrate decomposition is complete in less than 25 msec. The $Ca(OH)_2$ which remains after 25 msec is probably formed in the sampling system.

Because hydrate particles calcine rapidly they become almost immediately available for reaction, i.e., they are converted to CaO which then reacts with SO_2. Carbonate particles calcine relatively slowly and it is possible that this delay adversely affects the ability of carbonates to react with SO_2, especially for diameters of 10 μm or larger.

Using the activation model described above, a qualitative estimate of the effect of sorbent type on calcine reactivity can be obtained. Figure 3-24 compares the predicted surface area development and decay for carbonates and hydrates. Calculations were performed for 1 and 5 μm particles calcining at 2000°F. The rate of hydrate decomposition was assumed to be 50 times that for carbonates. The results of this assumption are apparent in Figure 3-25 and can be summarized as follows. Hydrates reach their full surface area potential, which is here assumed to be 100 m^2/g, before significant surface area loss can occur. This is not true of carbonates where for the 5 μm case a maximum surface area of 50 m^2/g is predicted. Hydrate surface area development is insensitive to particle size; there is little or no practical difference in hydrate activation between 1 and 5 μm particles. This is not true of carbonates where calcination times may be long enough to have some effect on sorbent reactivity and where increases in sorbent size are important. For example, increasing carbonate size from 1 to 5 μm increases the time required to reach peak surface area from roughly 0.02 to 0.1 sec. This factor of five increase also occurs with hydrates but there the 5 μm particle requires less than 0.01 seconds to develop peak surface area.

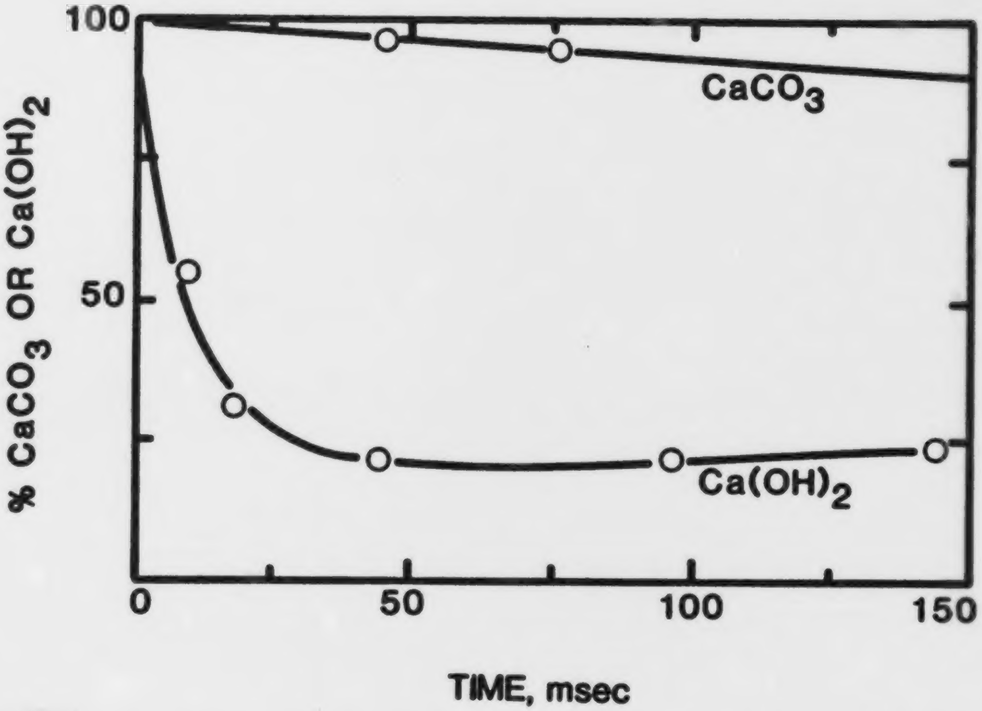

3-24. The relative rates of hydrate and carbonate calcination as measured by Bortz and Flament (1985) at 900 °C using 6 μm particles and an isothermal reactor.

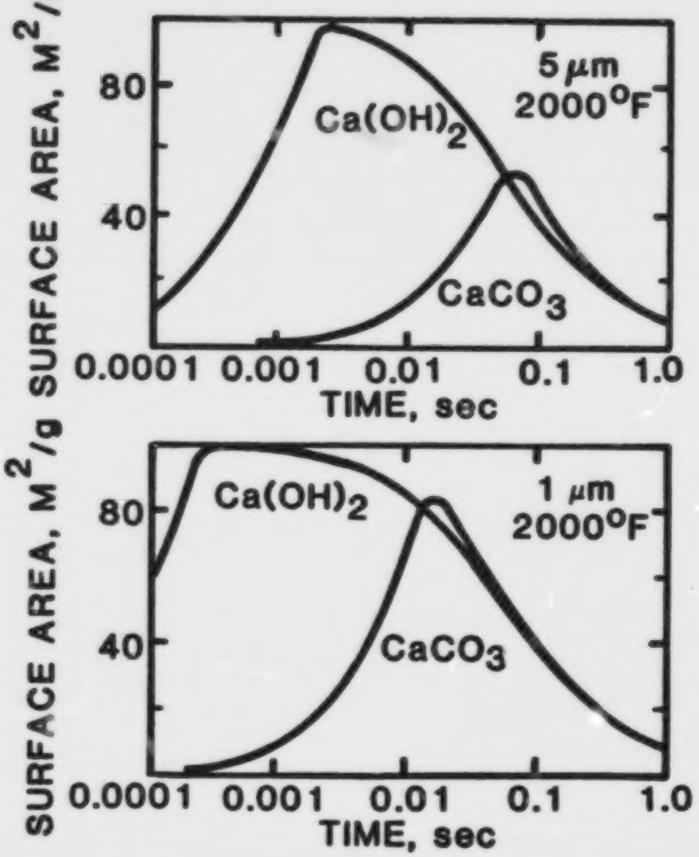

Figure 3-25. Activation model predictions of the effect of sorbent type for 1 and 5 μm hydrates and carbonates.

3.4 Conclusions

The current understanding of the sorbent activation process is approximately described by the mathematical model outlined above. Important conclusions relate principally to the differences between hydrates and carbonates, i.e., hydrates calcine much more rapidly than carbonates and as a result they develop higher surface areas and can react more uniformly, when compared on an equal diameter basis.

The extremely short times required for hydrate calcination suggests that the calcination is accomplished during sorbent heatup. Thus, hydrate calcination will likely be influenced by the rate at which the sorbent is heated, i.e., the dynamics of the mixing of the sorbent carrier gas into the furnace gas. In light of the apparent importance of short-time sulfation, one cannot assume the hydrate calcination parameters do not influence its reactivity, even if calcination and sulfation are not likely to occur simultaneously. Certainly, when considering the calcination and sulfation of carbonates, especially those with diameters in excess of 5 microns, a complete decoupling of the two processes cannot be justified.

4.0 SULFATION FUNDAMENTALS (ISOTHERMAL PRECALCINES)

In this section of the report the fundamentals of the sulfation process are examined by first reviewing and comparing the available experimental data. Various theoretical modeling approaches are then discussed and finally the model predictions are compared to the experimental data. Like Section 3.0, this portion of the report considers only one portion of the process, sulfation, in a decoupled fashion by focusing exclusively on precalcined sorbents. (Activation and sulfation are considered together in Chapter 5.)

Precalcined sorbents are defined as raw sorbents or processed sorbents which are precalcined to form quicklime prior to utilization in the furnace. The raw materials can be limestones or any of the various types of slaked lime. When raw sorbents are directly injected into the furnace, the activation process must occur under a limited range of time-temperature histories and in a flue-gas compositional environment. Precalcines are attractive from a practical standpoint because the activation step is decoupled from the furnace environment. Activity can be optimized within a wide range of conditions that may not be available within the furnace. Because in-furnace activation is not needed for these sorbents, these materials were originally hoped to behave differently than raw materials, particularly with respect to optimal furnace injection location for maximum sulfur uptake.

Precalcined sorbents have turned out to be of interest primarily as a research tool. The overall sulfation of a raw calcitic material involves the substeps of calcination, surface area development, sintering, and sulfation. The individual contributions of the subprocesses are extremely difficult to define from sulfation results on raw materials due to the complex intercoupling of the subprocesses. Precalcines offer an opportunity to examine sulfation phenomenon without the complexity of concurrent activation.

4.1 Compilation of Experimental Results

4.1.1 Fundamental Sulfation Kinetics

Precalcine sulfation data can be divided into two classes. The simpler class involves experiments in which the reacting surface of the calcine is external. The other class of experiments addresses the reactivity of calcines with significant internal surface area and is necessarily complicated by sintering, pore diffusion resistance, and pore mouth plugging or filling. The simpler experiments will ideally allow direct focusing on inherent reactivity and fundamental transport resistances, without the encumbrance of complex sorbent structure.

In-house work at EPA by Borgwardt and co-workers developed a means of obtaining very narrow size cuts of limestone. A 1 micron cut has been calcined and sintered under controlled conditions to yield a 1 micron - 3 m^2/g specific surface area CaO (Borgwardt, et al., 1986). This approaches the theoretical external surface area for a 1 micron CaO particle sufficiently that internal porosity resistances cannot be expected to limit the reaction. These CaO particles were generated from Fredonia limestone, and were sulfated in the EPA differential reactor (Borgwardt and Bruce, 1986).

The results of Borgwardt and Bruce (1986) are not from a combustion system, and thus should not be included in the combustion system similarity data base. However, these data represent a very clean source of rate data against which models can be calibrated. Thus, although test data are obtained at lower temperatures and longer times than are representative of furnace conditions, the results provide key benchmark data against which any model of high temperature sulfation can be tested.

Figure 4-1 illustrates the reactivity of the 3 m^2/g CaO as a function of time and temperature in the differential reactor. The authors interpreted their data in terms of a product (i.e., sulfate) layer diffusion rate controlling step. The lines on the figure chart the reaction progress as

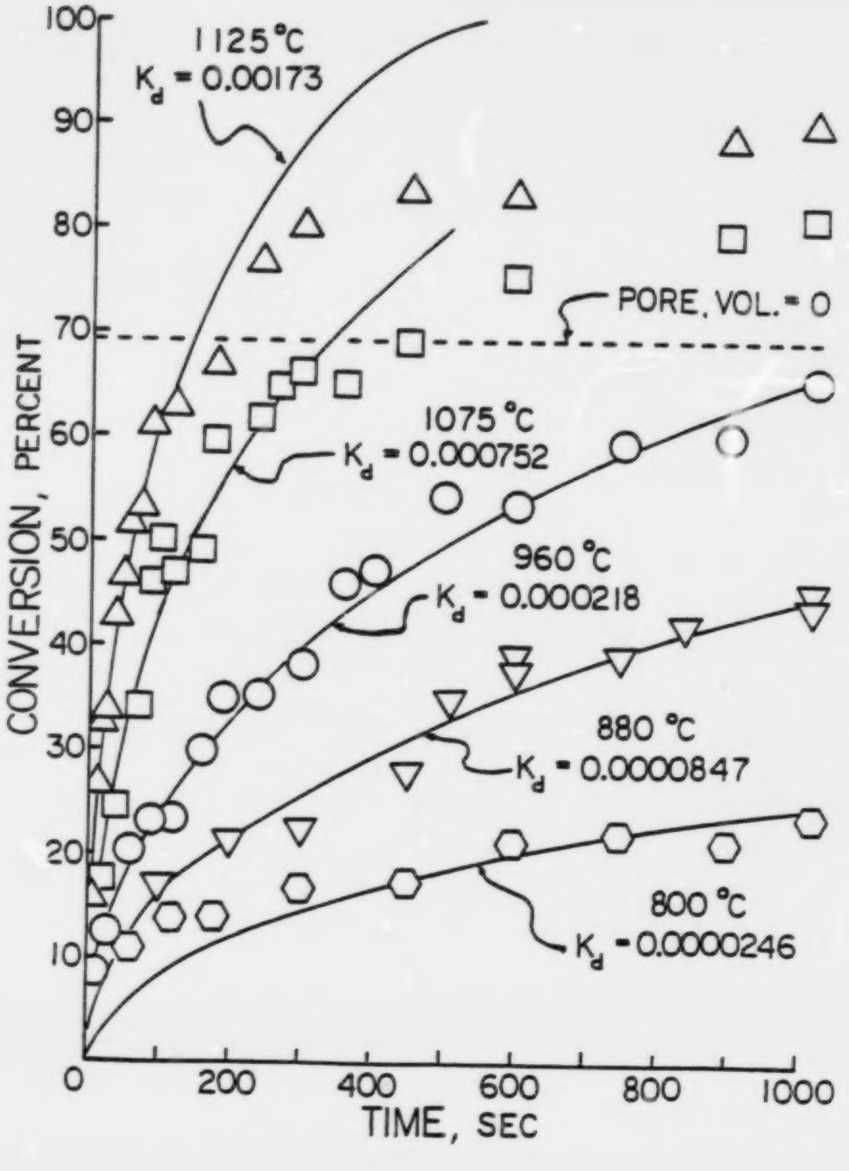

Figure 4-1. Reactivity of 3.0-m^2/g CaO as a function of temperature at P_{SO_2} = 304 Pa (3000 ppm). Results from Borgwardt and Bruce (1986).

calculated from a model presented in the paper. Note that the dashed line represents conversion at the point where the internal structure is completely plugged with product. At very high conversions the data fall below the simple product layer diffusion correlation, indicating the introduction of an additional rate controlling resistance. The fact that conversions exceed the theoretical level is likely an indication of the importance of external surface reaction for these highly sintered particles, i.e., the reaction on the external surface is not limited by available pore volume. Changes in particle diameter (i.e., swelling during calcination or sintering) may be another explanation for the data exceeding the theoretical limit.

The influence of surface area on reactivity at 800°C is illustrated in Figure 4-2. Although intent of sulfation is shown to depends markedly on the sorbent surface area the data also indicate that incremental increases in surface area, do not result in proportional increases in utilization. Figure 4-3 shows that these trends continue when the reaction is extended to very long times and the extent of sulfation appears to approach an asymptote in all cases but one (11.5 m^2/g). Note that the percent conversion for the high surface area case exceeds the theoretical limit for CaO which is initially 54 percent porous.

The data shown in Figure 4-4 provide a comparison of the combined effects of time and temperature on the 1 micron particle reactivity. Figure 4-5 illustrates the influence of SO_2 partial pressure on the conversion. Later figures will present crossplots to directly show the effect of these variables.

4.1.2 Time Resolved Sulfation

Advances in modeling and understanding the fundamental database clearly show that the high temperature/short time sulfation phenomenon represents a coupling between the reaction rate parameters and the structure of the sorbent. Efforts to understand the sulfation phenomenon require that data be obtained on sorbent under realistic time/temperature environments in order that the sorbent structure participate in a realistic manner. Thus, the

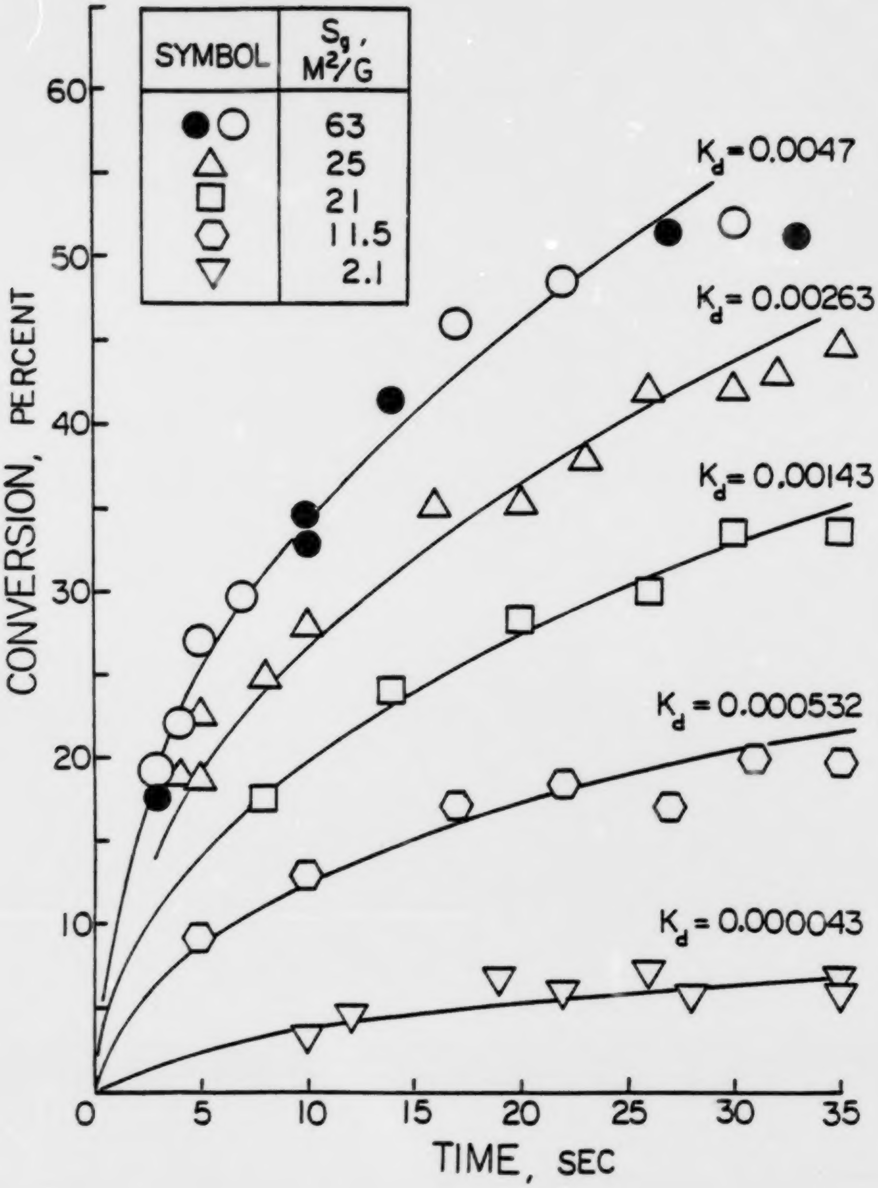

Figure 4-2. Reactivity of CaO at 800°C as a function of its specific surface area. P_{SO_2} = 304 Pa. Results are from Borgwardt and Bruce (1986).

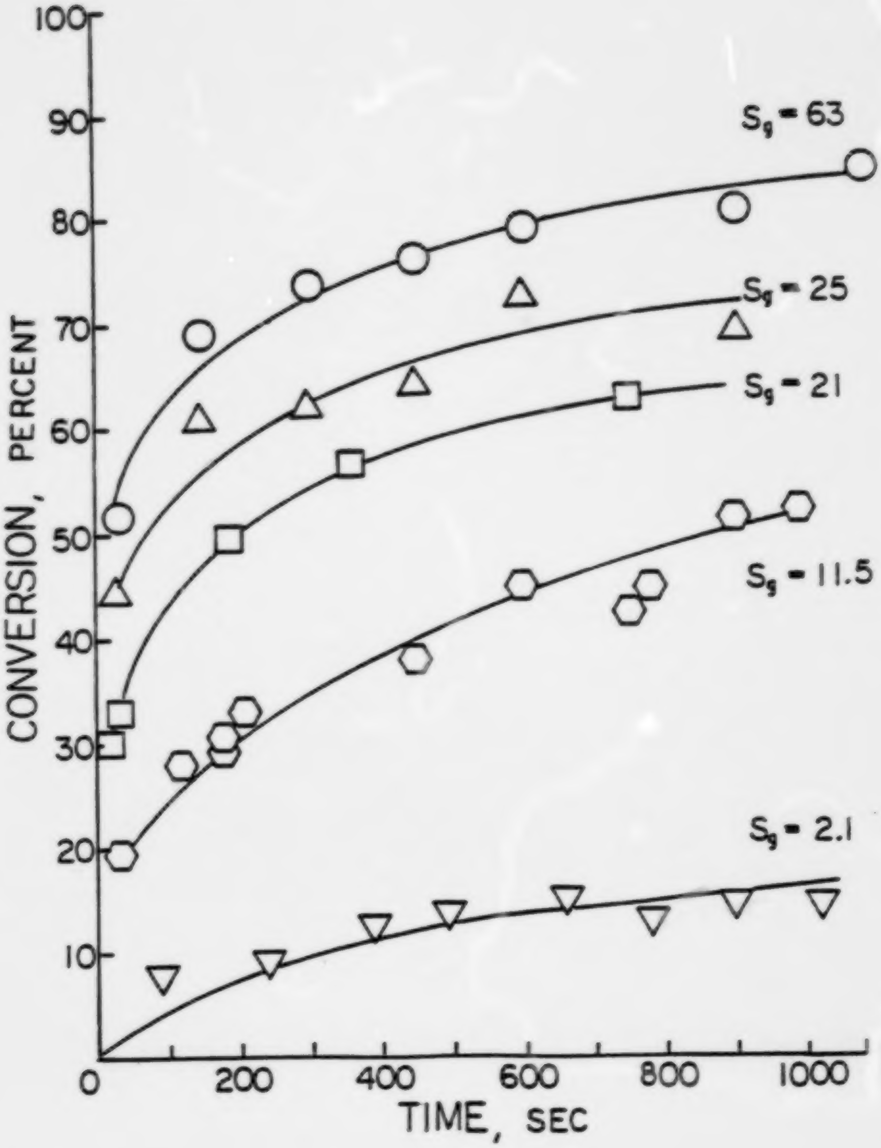

Figure 4-3. The maximum conversion attained at long SO_2-exposure times also increases with specific surface area (S_g, in m^2/g). Temperature = 800°C, P_{SO_2} = 304 Pa. Results are from Borgwardt and Bruce (1986).

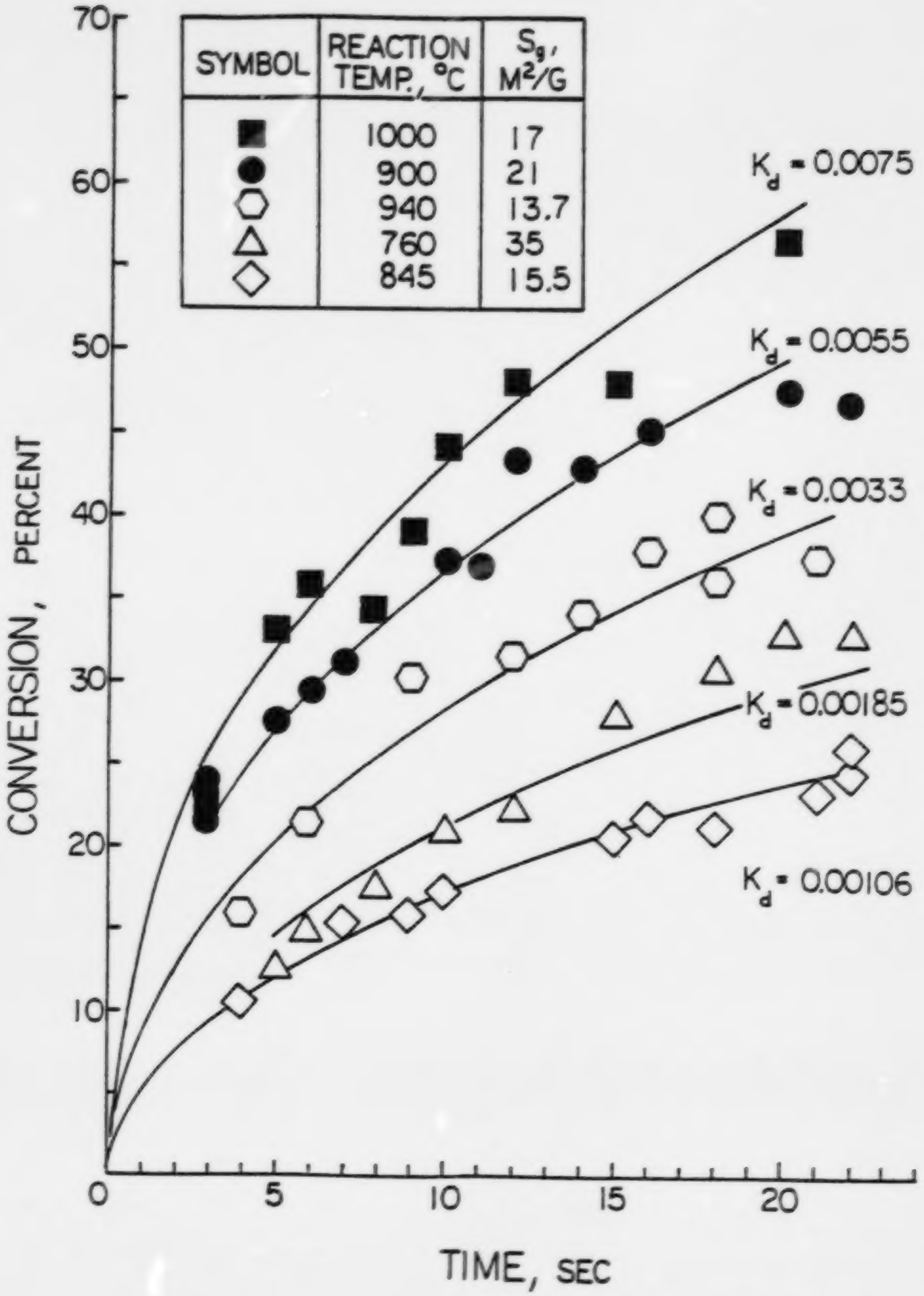

Figure 4-4. Effect of specific surface area and temperature on CaO reactivity at constant SO_2 partial pressure (304 Pa). Results are from Borgwardt and Bruce (1986).

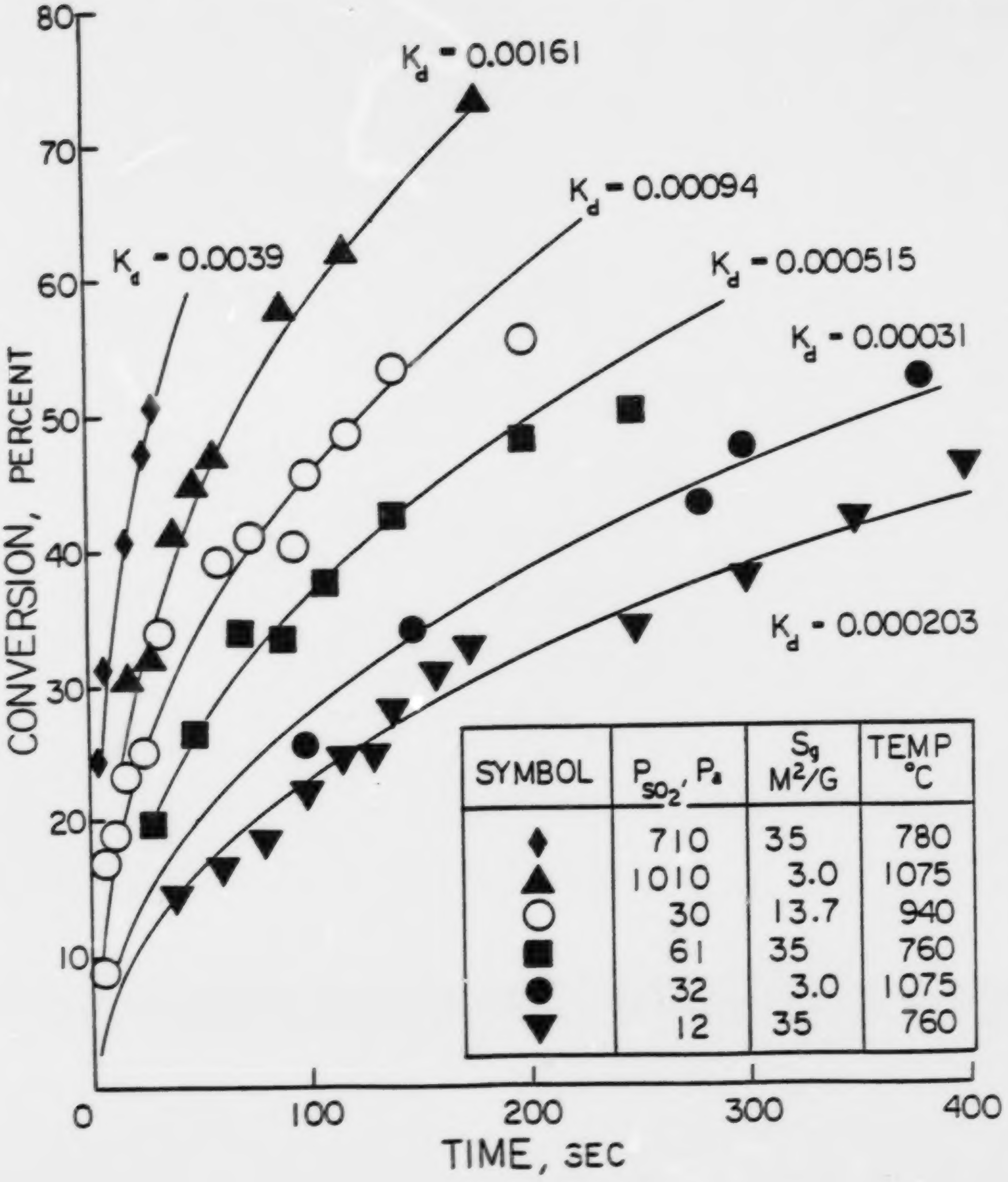

SYMBOL	P_{SO_2}, Pa	S_g M^2/G	TEMP °C
♦	710	35	780
▲	1010	3.0	1075
○	30	13.7	940
■	61	35	760
●	32	3.0	1075
▼	12	35	760

Figure 4-5. Effect of SO_2 partial pressure on CaO reactivity. Results are from Borgwardt and Bruce (1986).

remainder of the data presented in this section will deal with results obtained at isothermal conditions under the times and temperatures representative of furnace injection.

A study at EER used CaO prepared from sized carbonates to study the effect of particle size on the isothermal sulfation behavior of quicklimes. A series of sized carbonate materials were obtained. The three larger size cuts were obtained by aerodynamic classification of a pulverized high purity limestone. The smaller sized materials were commercial products prepared by controlled precipitation. These materials are too costly to be used as a commercial sorbent, but they represent a valuable research tool. Each material was calcined in a 700°C transpired bed calciner to approximately 27-32 m^2/g surface area. The materials were then sulfated under identical 1000°C and 1200°C isothermal conditions to define the influence of particle size on sulfation when sorbent activation is not occurring (Cole et al., 1985).

The calcines were prepared from:

- 20 micron aerodynamically classified Marblewhite limestone
- 10 micron cut of Marblewhite
- 10 and 20 micron Marblewhite sintered to approximately 12 m^2/g
- 2 micron cut of Marblewhite (actually fines, nominally below 4 microns)
- Albacar
- Albagloss
- Multifex.

The last three materials are prepared from precipitated calcium carbonates and have very uniform sizes of 2, 0.8, and 0.07 microns, respectively. Both the Albagloss and the Multifex are regularily shaped crystals, while the Albacar has a needle-like structure with a high aspect ratio.

Figure 4-6 shows the time resolved plots for data taken at 1000°C for each of the calcines in the EER isothermal reactor. The results also show

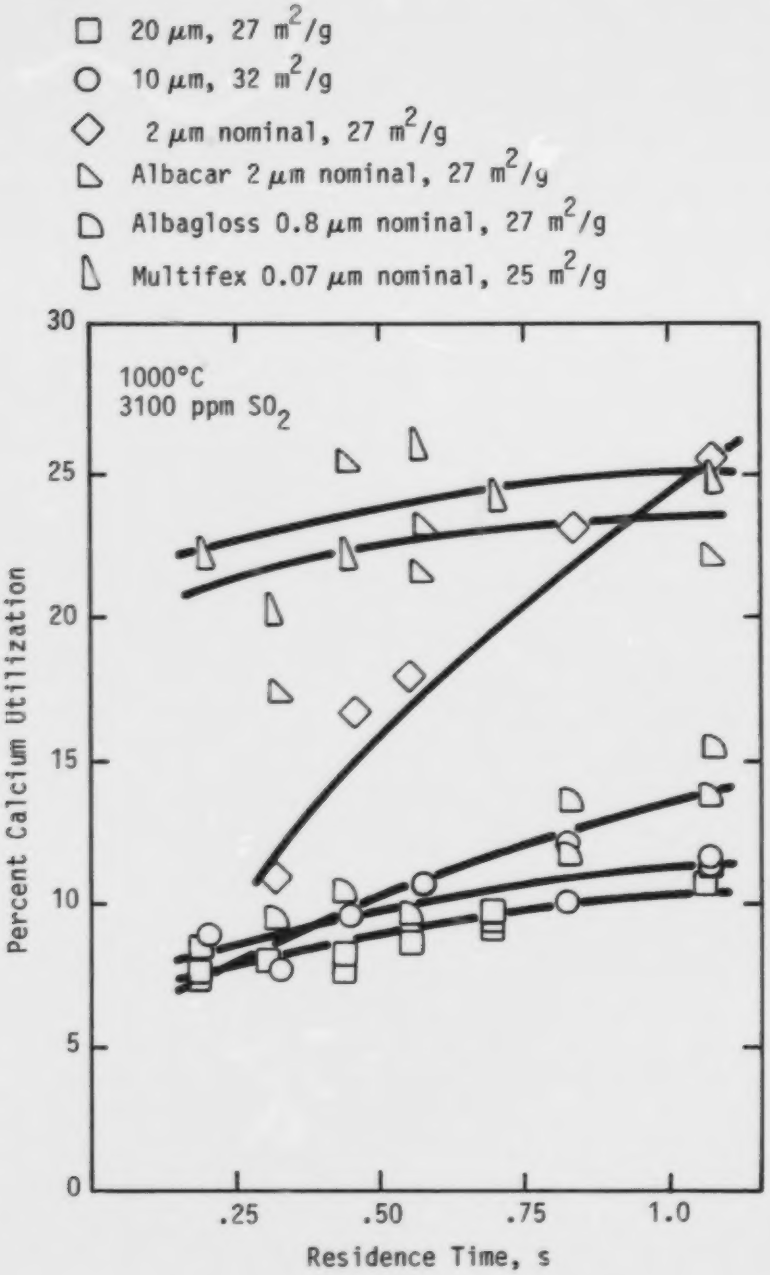

Figure 4-6. Isothermal reactivity of calcined sorbents at 1000°C in the EER isothermal reactor at Ca/S = 1.0 (data generated under EPA Contract 68-02-3633.

that for most of the sorbents a significant portion of the utilization has occurred within the first 200 msec. The results of Section 3.0 suggest that for small sized materials a high surface area transient may exist at short times, which would yield a high reactivity in the first 200 msec. However, the fully calcined materials used here would not be expected to increase in surface area when injected. Thus, at least for small precalcines, another mechanism exists which allows high reactivity early in the injection sequence.

The results also confirm the conclusion that smaller sized particles show higher reactivity. It is easy to overlook the significance of this finding here because:

- There is no activation step involved, so the particle size effect is not entirely dependent on the favorable particle size influence on activation noted in Chapter 3. Another mechanism controls here.

- There is no variation in surface area between the different sizes.

Figure 4-7 shows similar data on the ITR precalcines obtained at 1200°C. The capture levels are generally comparable to the 1000°C data. The nominal 2 micron cut shows higher performance than any of the other materials. This may be due to the fact that it is a broadly size material containing a substantial fines fraction. Also, the Albacar (nominally 2 microns) outperforms the Albagloss (nominally 0.8 microns). This may be an artifact of the unusual aspect ratio of these two sorbents (Cole et al., 1985).

The influence of precalcine surface area for the 10 and 20 micron precalcines are shown in Figure 4-8. The original 27-32 m^2/g sorbents were sintered in the bed calciner to about 12 m^2/g. The sulfation testing indicated that at 20 microns the reduction in surface area had little influence on reactivity; however, at 10 microns the reactivity was reduced by a factor of 2.

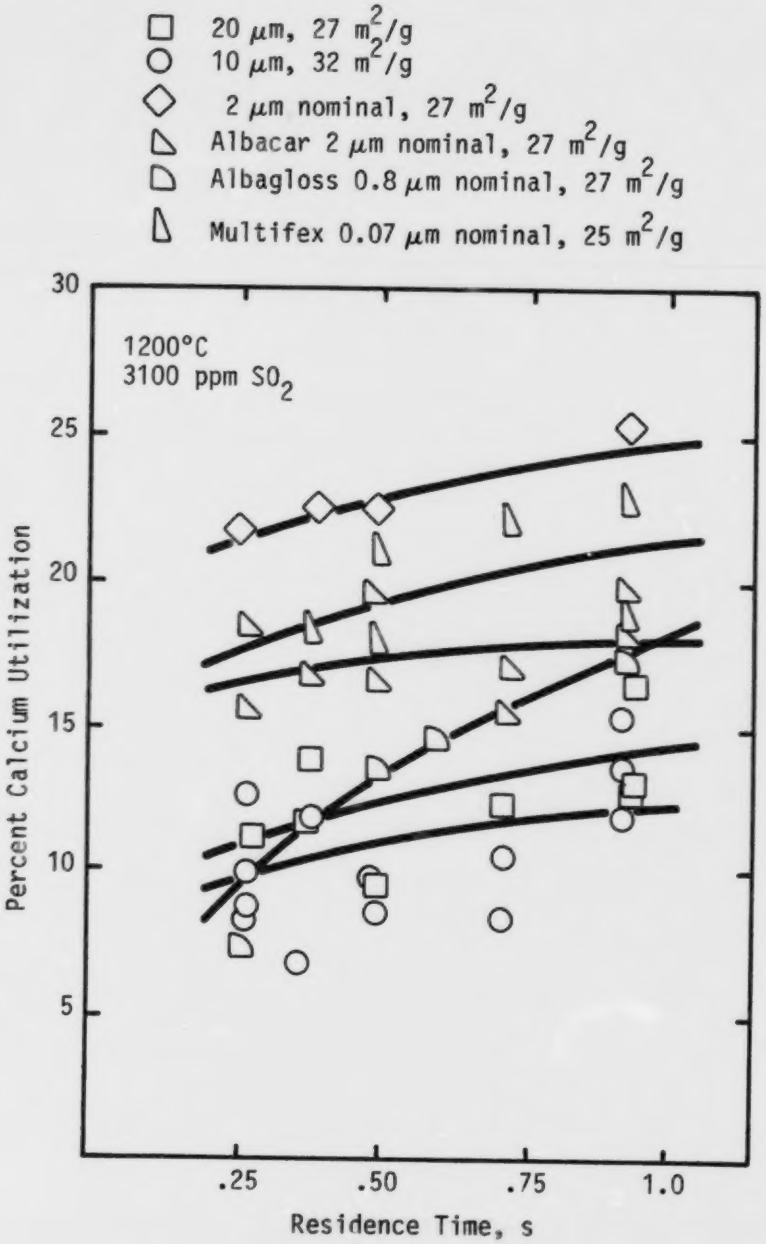

Figure 4-7. Isothermal reactivity of calcined sorbents at 1200°C in the EER isothermal reactor at Ca/S = 1.0 (data generated under EPA Contract 68-02-3633.

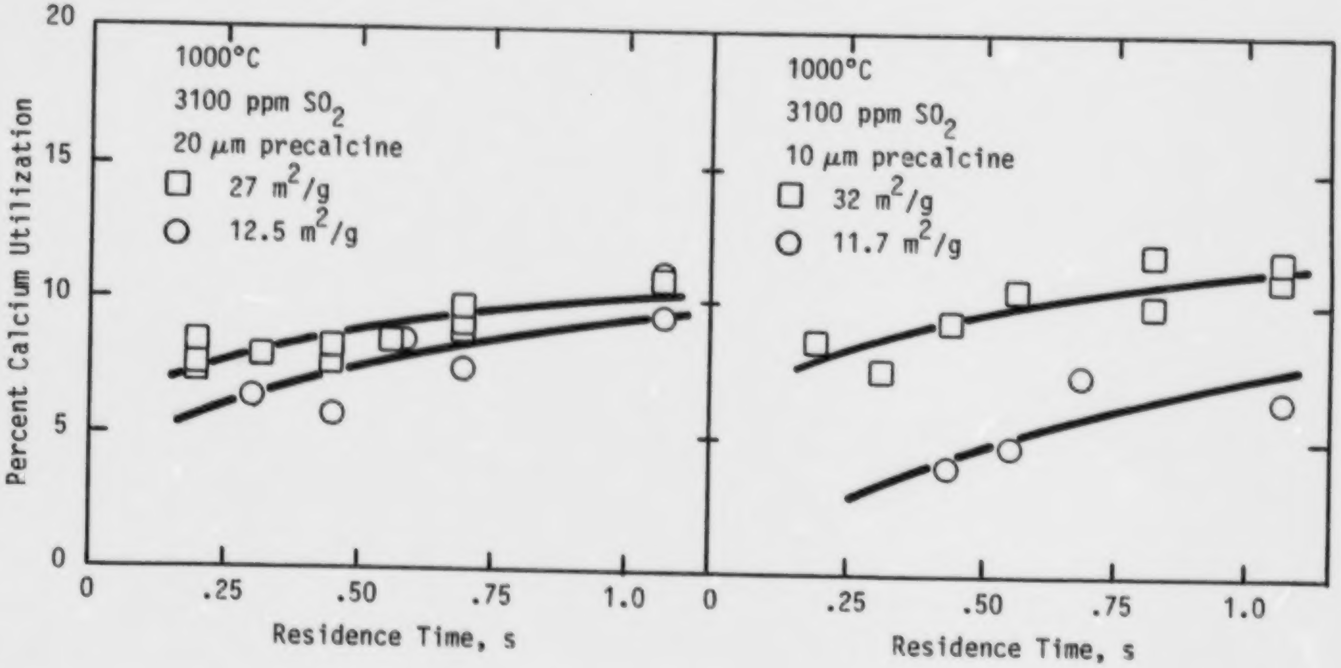

Figure 4-8. SO$_2$ capture profiles for sintered and unsintered 10- and 20-μm diameter precalcines in the EER isothermal reactor (data generated under EPA Contract 68-02-3633.

Newton (1986) at the University of Utah examined the isothermal capture of sulfur by precalcined hydrates. Figure 4-9 shows the SO_2 capture occurring when a precalcined Linwood hydrate was sulfated in the Utah isothermal reactor. The data are for a 1.7 micron size cut which was exposed to 2000 ppm SO_2 at 980°C. The results are qualitatively similar to those of Cole et al. (1985) in that:

- The overall sorbent utilization is of the same order.
- The sulfation appears to consist of a very rapid rate at short times followed by a second, slower rate regime.

Figure 4-10 shows similar results for a 6.8 micron sorbent of the same material, which illustrates a small but significant reduction in reactivity. Figure 4-11 shows time resolved sulfation profiles for limestones calcined to 20 and 30 m^2/g (Bortz et al., 1986).

Snow (1986) measured the sulfation performance of precalcined Iceland Spar and Rigsby limestone (45-53 microns) in the MIT isothermal reactor. The materials had a BET surface area of 33 and 19 m^2/g, respectively. As shown in Figure 4-12, these materials did not experience as high a level of conversion as noted in the preceeding plots. This is likely due to the suboptimal temperature (900°C) and the relatively large size of the sorbent.

4.1.3 Particle Size Effects

The discussion in Section 3.0 suggested that smaller sized particles are favored in terms of surface area development at short times. The material presented in Section 4.1.1 suggest that even for fully calcined particles, the smaller size cuts will experience a higher utilization.

Figure 4-13 presents a correlation of the data with particle size. The results suggest that very fine particles are required to obtain a significant enhancement of reactivity. However, the apparent scatter is likely a real indication that effects other than particle size may also influence

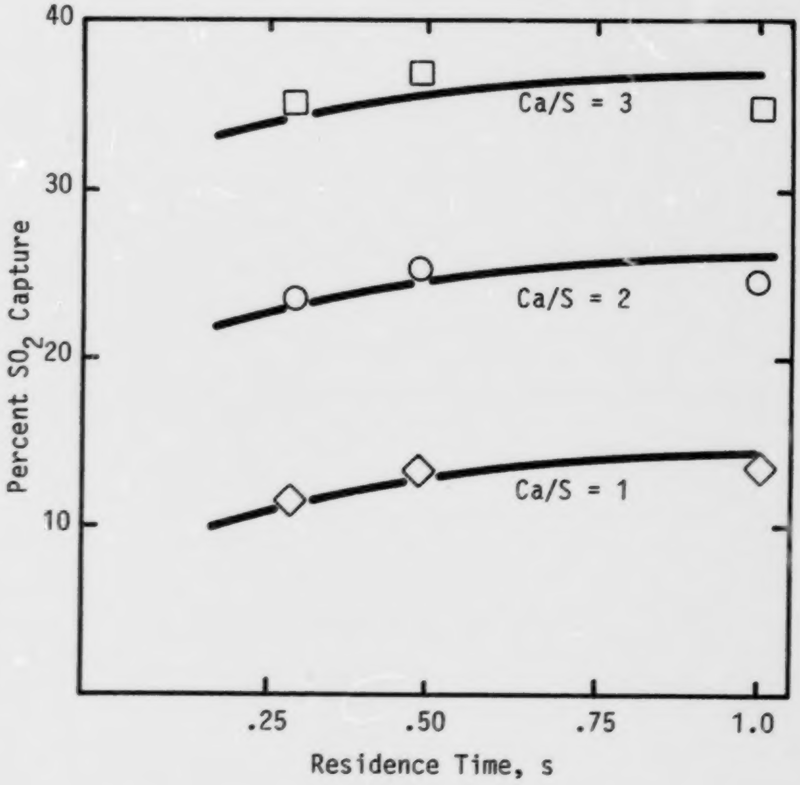

Figure 4-9. SO_2 capture profiles at Ca/S = 1, 2, and 3 for a 1.7 μm precalcine sulfated at 980°C and 2000 ppm SO_2. Results from Newton (1986).

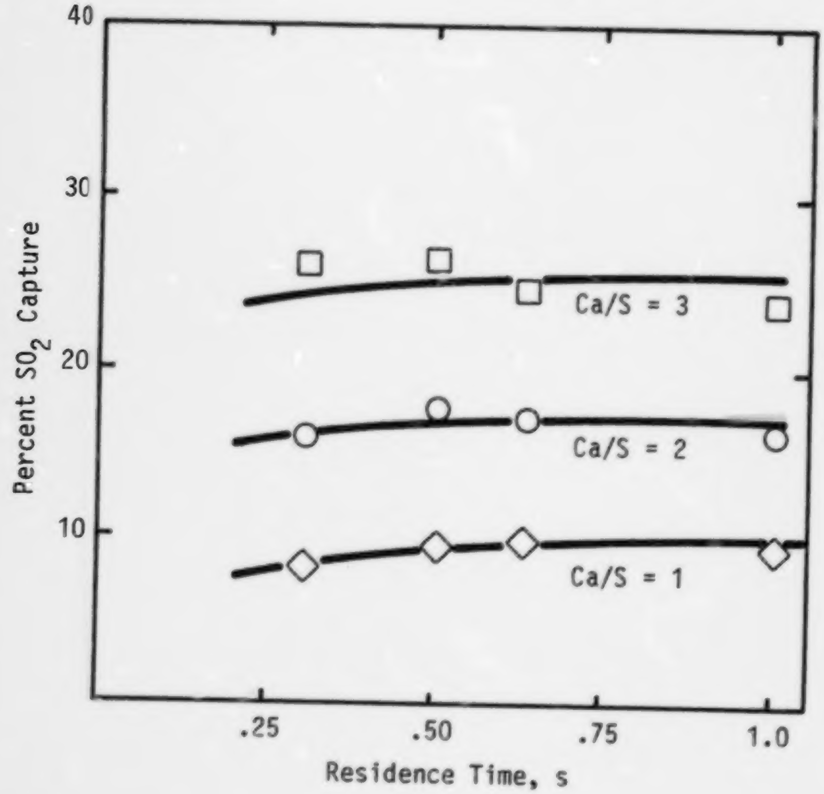

Figure 4-10. SO_2 capture profiles at Ca/S = 1, 2, and 3 for a 6.8 μm precalcine sulfated at 1260 K and 2000 ppm SO_2. Results from Newton (1986).

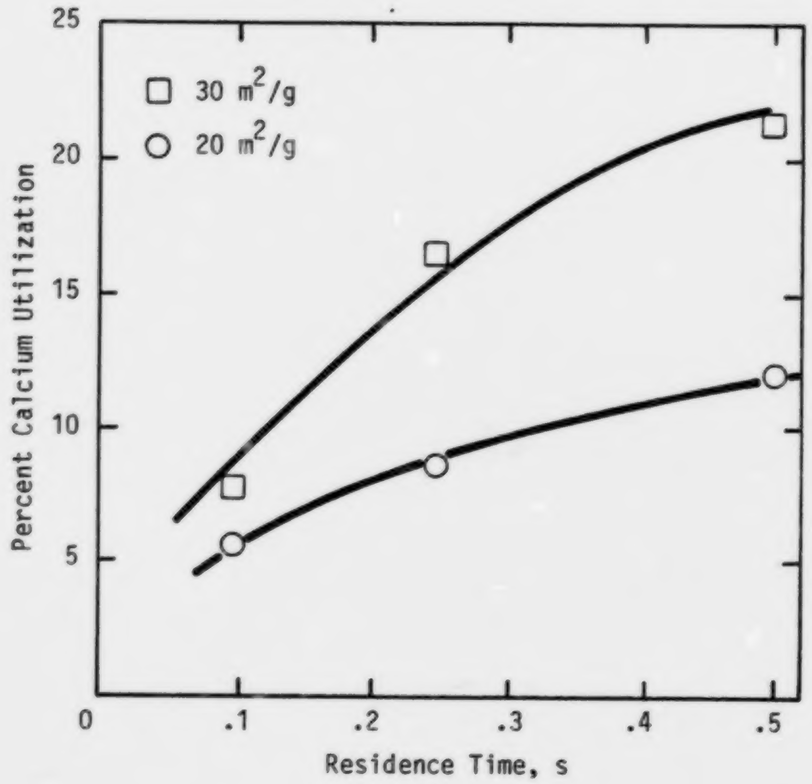

Figure 4-11. Effect of surface area on SO_2 capture profile. Results from Bortz et al. (1986).

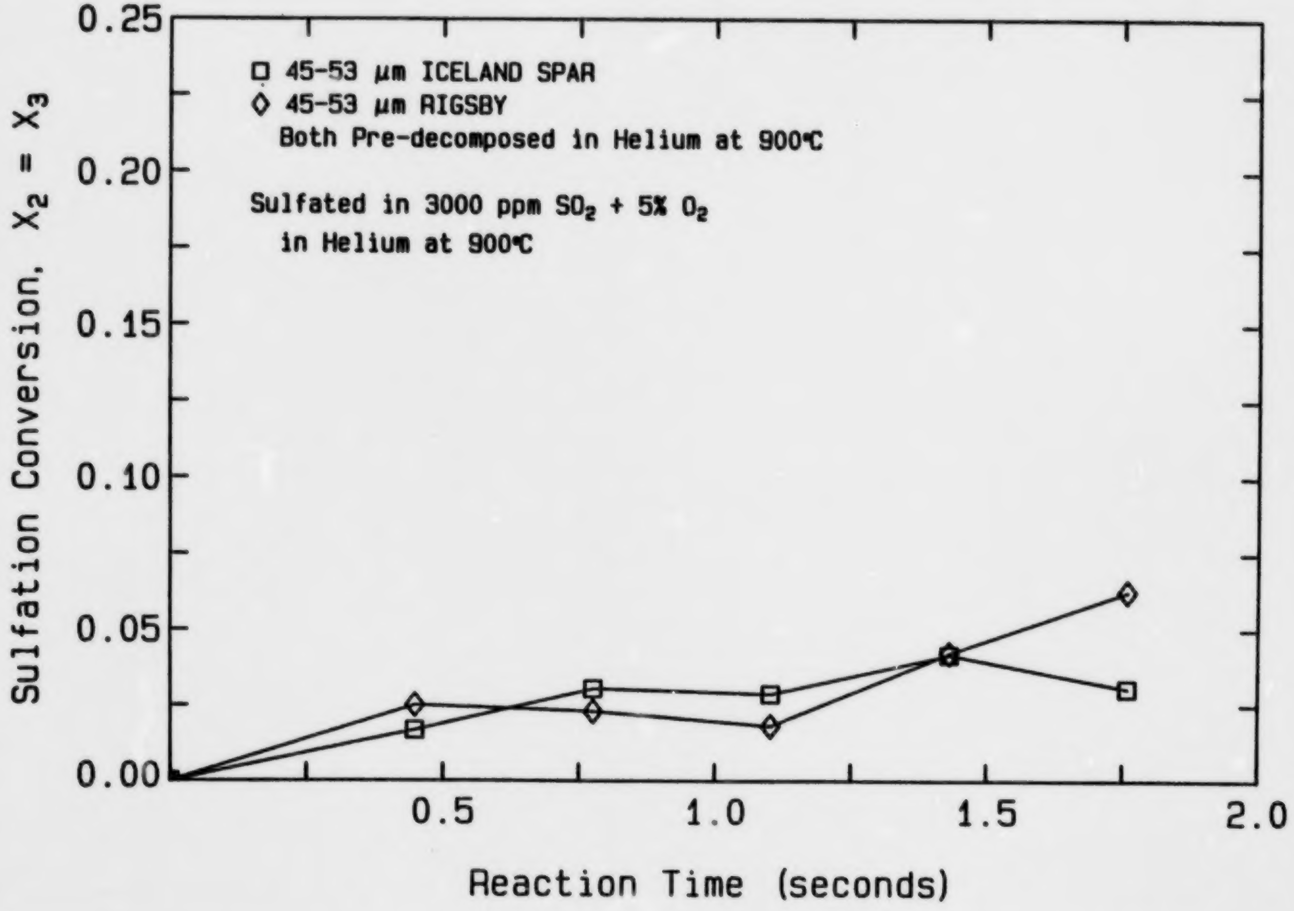

Figure 4-12. Sulfation conversion of pre-decomposed limestone effect of residence time (Snow, 1985).

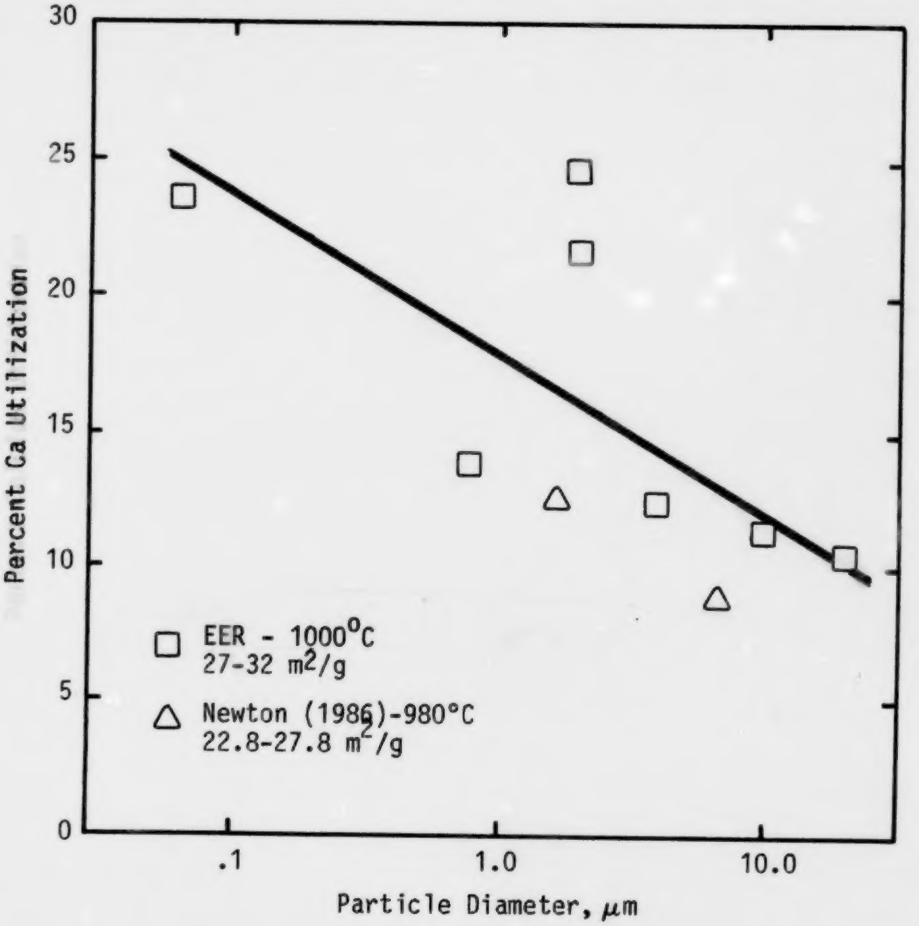

Figure 4-13. Influence of precalcine particle size on sorbent reactivity. (EER data generated under EPA Contract 68-02-3633).

reactivity. For example, Figure 4-14 shows that the mean pore size is also changing with particle size, with the the larger pores occurring in the finer particles. One possible reason for this is that the higher calcination rates associated with smaller particles leave additional time for sintering. The key point is that changing sorbent particle size can also be expected to change other structural features.

4.1.4 SO_2 Concentration Effects

The influence of SO_2 concentration on sorbent conversion has a markedly different effect depending on the reaction conditions. Figure 4-15 shows data from Borgwardt and Bruce (1986) and Newton (1986). These results suggest a strong dependence on SO_2 concentration for lower reaction temperature and longer reaction times, and a relatively weak dependence when the sorbent is treated at short times under furnace conditions.

4.1.5 Influence of Injection Temperature

The influence of injection temperature on the capture of sulfur by isothermal precalcines is shown as Figure 4-16. The figure suggests the importance of pore structure in setting the optimum injection temperature. The Borgwardt material has little fine pore structure to hinder reaction, so the sulfation rate may be expected to increase with temperature until the thermal stability limit of the sulfate is reached. The reaction for the more finely pore structured CaO at EER and Utah may be expected to hinder the reaction of temperatures well below the thermal stability limit. At least two mechanisms are possible:

- Thermal sintering of the fine structure, which dominates reactive surface area.
- Closing of the mouths of fine pores at the surface by a high local sulfation rate. This seals unreacted CaO from SO_2.

Detailed structure measurements will be necessary to define the true mechanism.

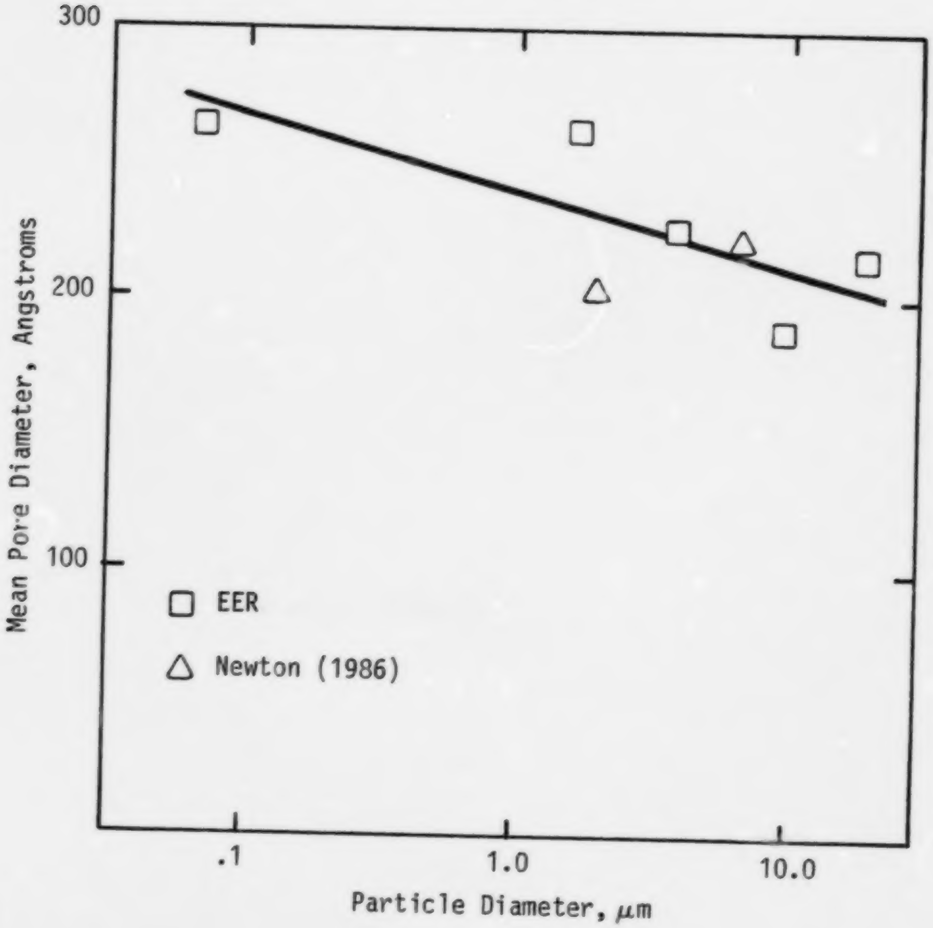

Figure 4-14. Mean pore diameter of precalcines as a function of particle diameter (EER data generated under EPA Contract 68-02-3995.

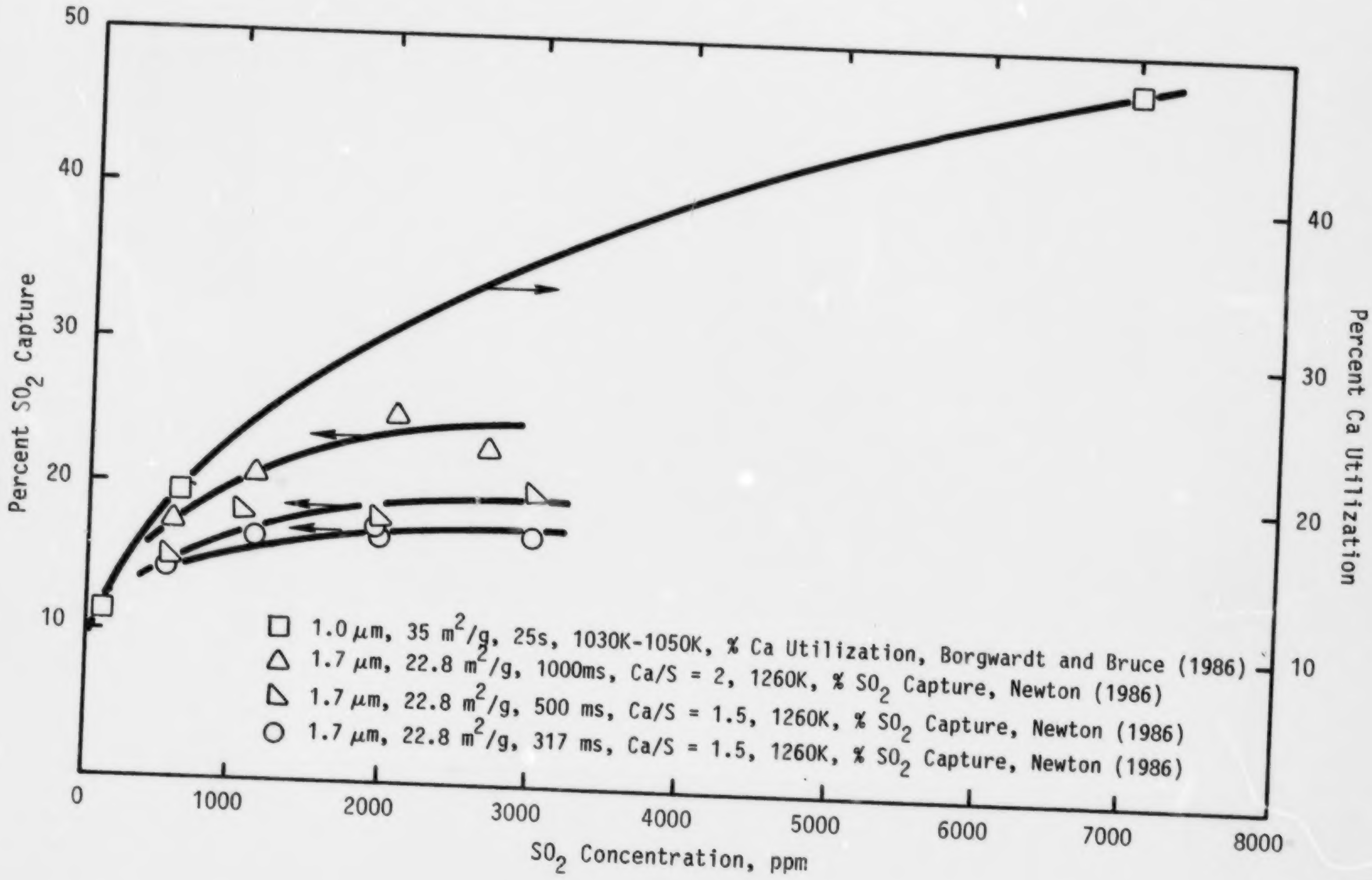

Figure 4-15. Effect of SO_2 concentration on Percent SO_2 capture and percent calcium utilization for precalcined sorbents.

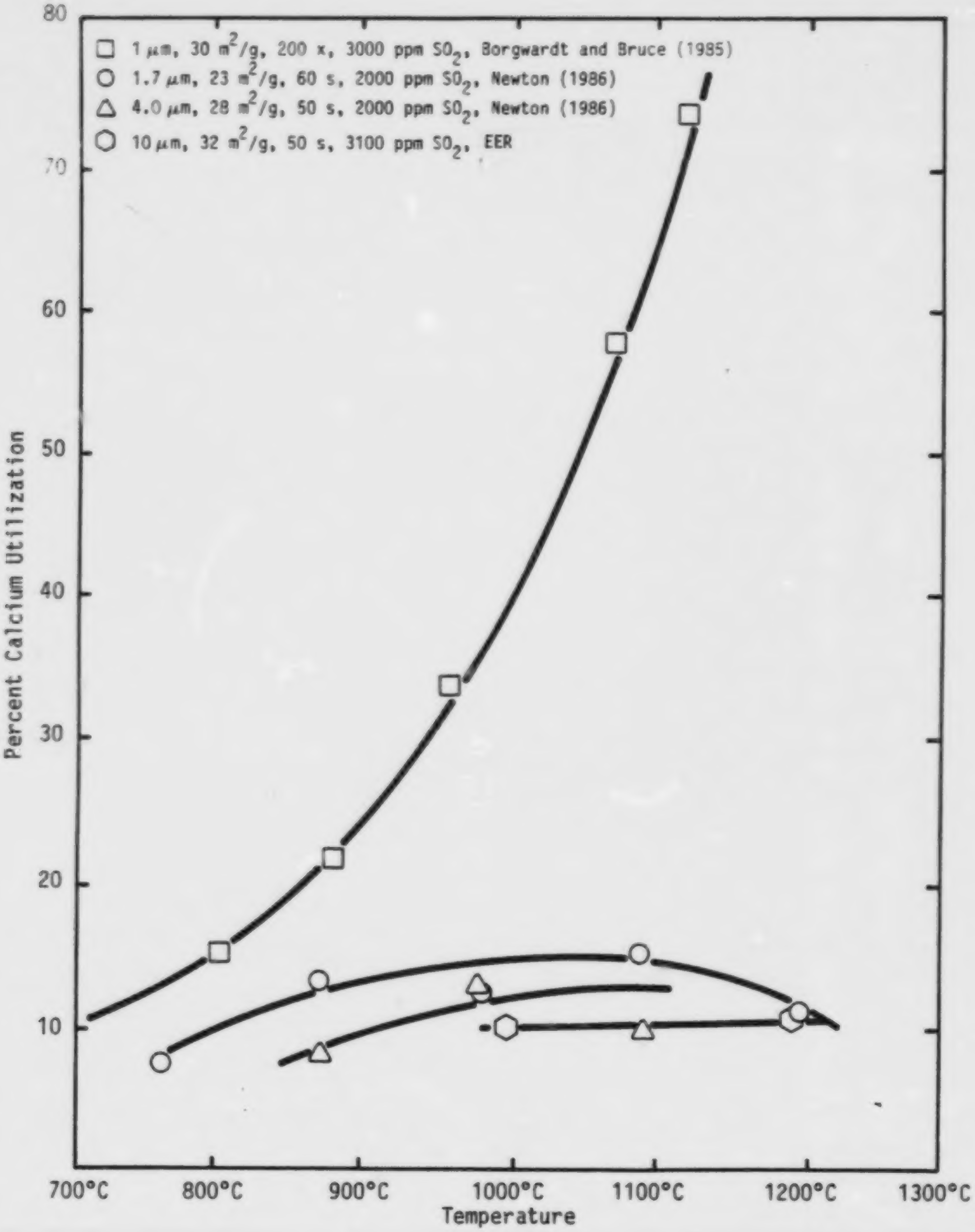

Figure 4-16. Effect of temperature on calcium utilization of precalcined sorbents. (EER data generated under EPA Contract 68-02-3995.

4.1.6 Closure

The available experimental data on the sulfation of precalcined sorbents suggest that at temperatures of interest for upper furnace sorbent injection:

1. Sulfation is initially rapid, occurring on a time scale less than 200 msec, with subsequent sulfation proceeding at a much slower rate.

2. Calcium utilization does not correlate with particle size, primarily because of differences in internal porosity.

3. Sorbents dominated by internal surface area are far less sensitive to SO_2 concentration than those dominated by external surface area (highly sintered) suggesting a surface accessability loss with the more reactive materials.

The available data are insufficient to clearly define the optimum sulfation temperature although it appears to be 1000-1100°C.

4.2 Modeling Approaches

Three different sulfation modeling approaches were considered in this program: a grain formulation, a random pore formulation and a distributed pore formulation. All three approaches assume that the sorbent particles are spherical and fully calcined prior to the onset of sulfation.

The grain model treats the CaO particle as an agglomerate of CaO grains. The size distribution of the grains is set to match the measured BET surface area. Sulfation proceeds on the surface of each grain, with the result that the reaction may be limited by product layer buildup, which may both shield the grains and block access to the particle interior. A distribution of grain sizes is allowed. The current version of the model also includes grain growth (sintering) as a competitive process which occurs in parallel with sulfation and reduces the available, active surface area.

In the distributed pore model, the particle is assumed to be perforated by long, nonintersecting pores of variable length. The size distribution of these pores is explicitly matched to that measured experimentally by mercury and nitrogen porosymetry. Calcium sulfate formation is allowed to occur on the external surface of the particle as well as on the internal surface of each pore. Since $CaSO_4$ formation is calculated as a function of location in the pore, this model can predict the plugging of small pores at the pore mouth while simultaneously predicting uniform filling of larger pores.

The random pore model is similar to the distributed pore model with respect to the assumption of long, cylindrical pores; however, in the random pore formulation, overlapping (intersection) of pores is assumed to occur.

Each of the modeling approaches is described in detail in the following sections. The grain model was utilized for most of the modeling activities in this program because of its early success in predicting overall bench- and pilot-scale results. The other formulations were used to evaluate potential differences in the controlling fundamentals.

4.2.1 The Grain Model

4.2.1.1 Introduction

The sulfation reaction is represented by the overall equation

$$CaO + 1/2\ O_2 + SO_2 = CaSO_4 \qquad (4.1)$$

This reaction occurs only under oxidizing conditions and is heterogeneous. It is complicated by the fact that the product, $CaSO_4$, is a solid. The steps leading to reaction include:

- diffusion of gaseous reactants to the particle's surface;
- diffusion through pores to the particle's interior;
- diffusion through the product layer;
- reaction at the $CaO - CaSO_4$ interface.

There is some uncertainty as to which steps in the process are rate controlling. The only step which can be safely ignored is the first, diffusion of gaseous reactants to the particle surface. Ishiliara (1970) and Silcox (1985) all reached this conclusion for particle diameters less than about 50 μm. Data showing the relative importance of pore and product-layer diffusion are difficult to find and are complicated by particle size effects. Borgwardt and Bruce (1986) eliminated the complication of pore diffusion by performing their experiments with 1 μm lime particles. They concluded that under these conditions the reaction rate was controlled by product layer diffusion but they also observed a nonlinear dependence on SO_2 concentration. The later can be explained by a pore-plugging model or a surface reaction model. The pore-plugging approach is unconvincing when applied to Borgwardt and Bruce's data because their lime particles possessed very little internal surface area as indicated by a B.E.T. surface area of 3 m^2/g. The importance of pore diffusion increases with increasing particle size and data are presented later in this report which show a decrease in sorbent utilization with increasing particle size.

If a surface reaction model is the most appropriate way to describe the sulfation reaction, then the question arises as to whether reaction is occurring at the CaO - $CaSO_4$ interface or whether reaction occurs at the gas - CaO interface. It is also possible that both are occurring. Under these circumstances the relationship between product layer diffusion and surface reaction is complicated. Finally, both a surface-reaction model and a pore-closure model may be appropriate for describing the SO_2-lime reaction. In the discussion of the grain models which follow, the assumption is made that the surface reaction model is most appropriate.

4.2.1.2 Reaction Order and Mechanism

The SO_2-lime reaction has been the subject in intensive experimental study and a number of different values have been reported for the intrinsic reaction order with respect to SO_2 concentration. Borgwardt and Bruce (1986) performed differential reactor studies on 1 μm lime particles and reported an order of 0.6. Coutant, et al. (1971) used a flow reactor with 90 μm particles to determine an order of 0.5. The generally accepted order is one, as reported by Borgwardt (1970) who based his value on data obtained in a differential reaction, using 1mm particles. However, Borgwardt believes that his more recent value of 0.6 is correct and that the older value of 1.0 resulted from the higher pore diffusional resistances associated with 1mm particles. One possible explanation for the observed nonlinear SO_2 dependence is a surface reaction model. To show that a surface reaction model predicts a nonlinear dependence, a simple reaction mechanism is postulated and analyzed below.

The mechanism includes five steps:

1. $I + X = (IX)$
2. $SO_2 + X = (SO_2X)$
3. $O_2 + 2X = 2\ (OX)$
4. $(SO_2X) + (OX) = (SO_3X) + X$
5. SO_3 dissolves in and diffuses through product layer

where I is an inert species such as CO_2 or N_2, X is a vacant site, and parentheses enclose absorbed species. Steps 4 and 5 are assumed rate controlling with the rate of 4 equal to that of 5. All other steps are considered at equilibrium. Adopting an ideal surface model results in a complex rate expression,

$$\text{Rate} = \frac{(SO_2)(O_2)^{1/2}}{\dfrac{(1+K_1(SO_2^{\frac{1}{2}})+K_2(O_2)^{\frac{1}{2}}+K_3(I))^2}{K^*} + \dfrac{(1+K_1(SO_2)+K_2^{\frac{1}{2}}(O_2)+K_3(I))r^2(\frac{1}{r}-\frac{1}{r'_g})}{D^*}} \tag{4.2}$$

where it has been assumed that the $CaSO_4$ surface is spherical and of radius r'_g and that the $CaO - CaSO_4$ interface is spherical and of radius r. Equation 4.2 implies a less than first-order dependence on SO_2 and a less than 1/2-order dependence on O_2. The analysis also shows that the reaction order will be a function of temperature since K_1, K_2, and K_3 are all functions of temperature. A simplified form of Equation 4.2 may be obtained by noting that O_2 and I concentrations are roughly constant. A simple power law expression can then serve as an approximation,

$$\text{Rate} = \frac{(SO_2)^n}{\frac{1}{K} + \frac{r^2}{D}\left(\frac{1}{r} - \frac{1}{r_g'}\right)} \qquad (4.3)$$

where K and D are analogous to a rate constant and a diffusion coefficient, respectively. According to the data of Borgwardt and Bruce (1986), n has a value of about 0.6 and K and D can be expressed as Arrhenius-type functions of temperature. The discussion of the grain and distributed grain models which follow assumes a rate expression of the form given by Equation 4.3 with values for K, D, and n based on an analysis of the data of Borgwardt and Bruce (1986).

4.2.1.3 Grain Model Description

The grain model, as it was originally developed by Pigford and Sliger (1973) and Hartman and Coughlin (1976) for the SO_2-lime reaction, represents a porous lime particle as a conglomerate of spherical grains of solid CaO. The basic features of the model are shown in Figure 4-17. The grains and the pores between them are assumed to be uniform in size. As the reaction proceeds each grain is surrounded by a layer of $CaSO_4$, indicated in the figure by the heavy black band surrounding an unreacted core of CaO. In formulating the grain model it is assumed that $CaSO_4$ is the final reaction product, that its formation is irreversible, and that the overall rate of reaction can be modeled with standard, two-parameter Arrenius expressions. Equilibrium constraints on the reaction are included to prevent any $CaSO_4$ formation unless the partial pressure of SO_2 is greater than the equilibrium value.

The following additional assumptions are made:

- The lime particles are fully calcined.
- Excess oxygen is present and its concentration is constant.

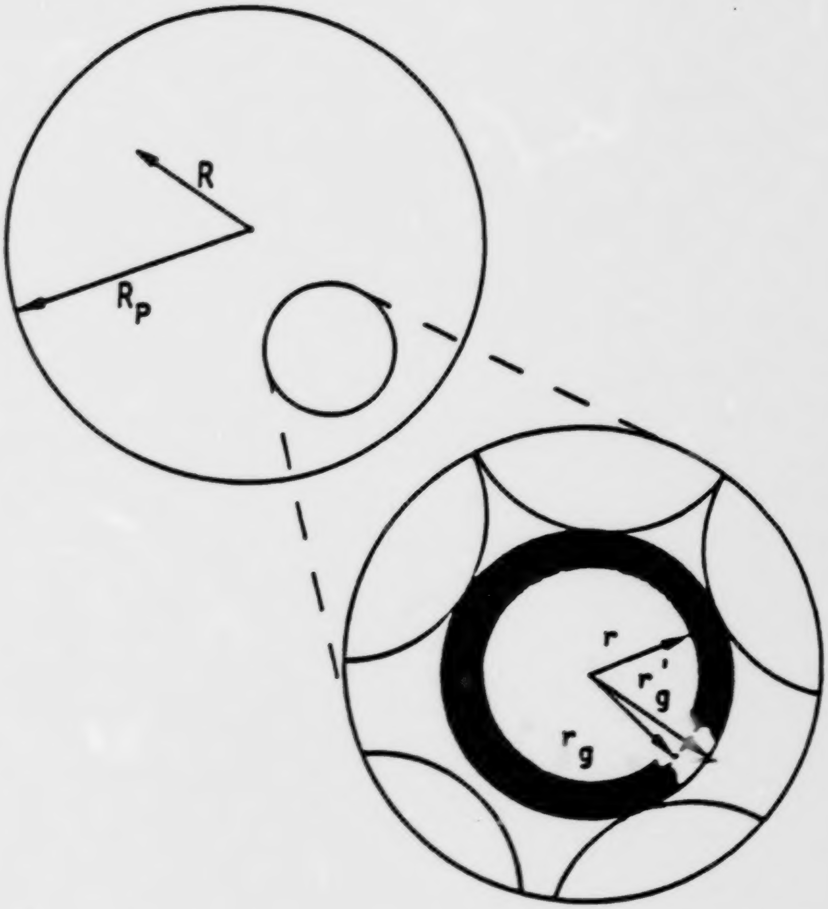

Figure 4-17. A schematic of the grain model. The enlarged view of the porous particle shows a dark band of product of radius r_g', the initial grain radius, r_g, and the radius of the unreacted core of reactant, r.

- The lime particles are spherical and isothermal.

Using these assumptions, the governing equations are obtained by making material balances for sulfur over the particles and over the constituent grains. For details the reader is referenced to the Appendix. The intrinsic rate of reaction is given by Equation 4.3 with a 0.55-order dependence on SO_2 concentration. The order is based on an analysis of data obtained by Borgwardt and Bruce (1986).

Important physical parameters used to describe the calcined lime include the particle diameter, the porosity, and the B.E.T. surface area. The latter is used to estimate the average grain size used in the model. The porosity determines the particle's capacity for reaction based on the molar volumes of CaO and $CaSO_4$. The surface area and porosity together determine the average pore diameter and the particle diameter influences the extent to which the particle can react uniformly. Note that as the reaction proceeds, the porosity and average pore diameter decrease due to the accumulation of product.

Additional parameters which determine the rate of SO_2 capture include the SO_2 concentration, the thermal environment, the rate of mixing between reactants, and the molar ratio of calcium to sulfur (Ca/S). The grain model as developed in the program includes the ability to examine the effects of all of the parameters listed above.

Section 3.0 of this report includes a discussion of the surface area loss of CaO at temperatures characteristic of combustion environments. It is possible that this loss continues during sulfation at rates which exceed that which can be attributed to pore closure by $CaSO_4$. This possibility has been included in the grain model by allowing the CaO grain radius to increase and to asymptotically approach a specified value according to the equation:

$$\frac{ds}{dt} = -k\ (S - S_{as})^2 \qquad (4.4)$$

where S is the surface area corresponding to the grain radius, S_{as} is the asymptotic value, and t is time.

4.2.2 The Distributed Grain Size Model

The motivation behind the development of a distributed grain size model was to provide a mechanism in the grain model to account for the variable internal length scales which are clearly indicated by pore size distribution data. In essence, introducing a distribution of grain sizes increases the model's flexibility in describing the dependence of reaction rate on time. This is possible because of the different rates at which small and large grains react. The situation is analogous to the parallel reactions

$$A \longrightarrow C \quad \text{(fast)}$$

and

$$B \longrightarrow C \quad \text{(slow)}$$

where the first reaction is faster than the second. The fast reaction will immediately produce a large amount of C until all of the A is exhausted. The slow reaction will continue producing C when all of the A is exhausted. Hence, a rapid initial reaction rate is followed by a much slower one.

The distributed grain model includes a discrete distribution of grain sizes and up to 7 size fractions can be specified. Typical predictions are shown in Figure 4-18 where for case 1 weight fractions of 0.1 and 0.9 are assumed for grain sizes corresponding to 500 and 5 m^2/g, respectively, and for case 2 a single surface area of 54.5 m^2/g is assumed. The average surface areas for cases 1 and 2 are the same but their responses to sulfation are quite different. Case 1 shows a rapid initial rate followed by a slower rate while case 2 shows a fairly sustained rate. Thus, the distributed grain approach is capable of predicting the observed dependence of capture on time (Section 4.1). The alternate approach described above allows the grains of CaO to sinter or grow. It is possible that a combination of grain growth and distributed grain sizes contributes to the observed behavior. The distributed grain model is capable of simultaneously treating both approaches.

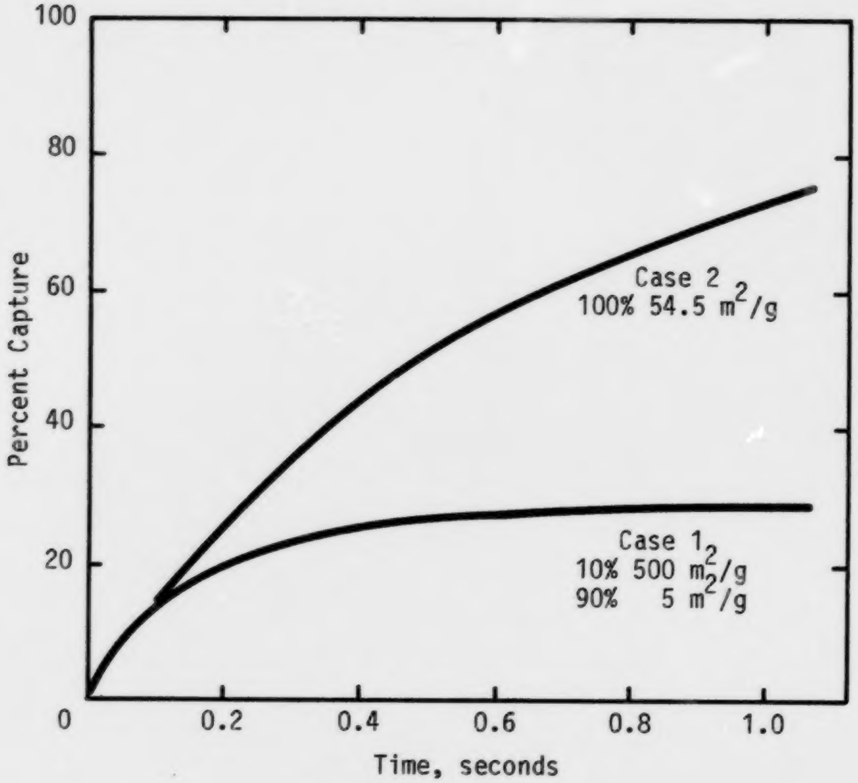

Figure 4-18. Distributed grain model predictions where no sintering is allowed, the average surface area is 54.5 m^2/g, the temperature is 1100°C and constant, the porosity is 0.5, and the particle diameter is 5 μm.

Finally, in addition to the distributed grain model, a model was developed which includes a distribution of particle sizes. This model incorporates up to seven discrete sorbent diameters. The predicted effects of the distribution of Vicron 45-3 are considered here. Vicron 45-3 has a mean size of 11 μm and a distribution of sizes ranging from 3 to 45 μm. At typical boiler conditions, the model shows almost no difference between a calculation based on the mean size and a calculation based on the full distribution.

However, this conclusion is not necessarily general and does not apply to all possible distributions. Screening calculations performed with only two particle sizes indicate that for mean sorbent diameters of about 10 μm or less the overall sorbent utilization is insensitive to size distribution. For mean diameters of 20 μm or more the overall capture is strongly affected by the distribution. The distributed grain model does not have the capability of describing particle size distribution effects. This limitation is not important for most sorbents of practical interest because their mean sizes are generally well below 10 μm.

In summary, the distributed grain model includes the following important features:

- Flexible specification of the grain size distribution,
- Ability to allow the sorbent jet to mix slowly with surrounding, SO_2-containing gases,
- Complete flexibility in specifying the thermal history of the sorbent, and
- Allowance for surface area loss due to sintering, if desired.

4.2.3 Random Pore Model

The random pore model was originally developed by Bhatia and Perlmutter (1981). It treats sorbent particles as spheres enveloping a random distribution of cylindrical pores which provide the overall particle surface area. A computer program of this random pore model applied to the SO_2-lime reaction has been coded for use at EER.

The model considers the internal structure of the particle to be given by a set of overlapping, random-sized, cylindrical pores. Their reaction is initiated at the pore surface and a layer of reaction product (calcium-sulfate) forms around the pore. This product layer separates the pore surface and the solid reactant surface. The gas (SO_2) must diffuse through the product layer to the surface of the solid reactant (CaO) where the sulfation reaction takes place. The model also considers boundary layer diffusion and pore diffusion of the gaseous reactant. The model scheme for a single particle is shown conceptually in Figure 4-19.

The order of the chemical reaction with respect to SO_2 concentration is a subject of debate. Borgwardt (1970) originally observed a first-order dependence; however, most EER data correlates better with zero-order kinetics.

The resulting governing equations for first-order kinetics are:

$$\frac{1}{r^2}\frac{\partial}{\partial_r} \quad D_e r^2 \frac{\partial C}{\partial r} = \frac{\rho(1-\epsilon_0)}{M D_{eo}} \frac{dX}{dt} \tag{4.5}$$

and

$$\frac{dX}{dt} = \frac{K_s S_0 C\ (1-X) \quad 1 - \sqrt{\psi \ln(1-X)}}{(1-\epsilon_0)\ [1 + \frac{\beta Z}{\psi}\ (\sqrt{1 - \psi \ln(1-X)} - 1)]} \tag{4.6}$$

where:

C = local concentration of SO_2 (mole/cm^3)
D_e = effective diffusivity of SO_2 in pores (cm^2/sec)
D_{eo} = initial value of D_e
D_p = effective diffusivity of SO_2 in product layer (cm^2/sec)

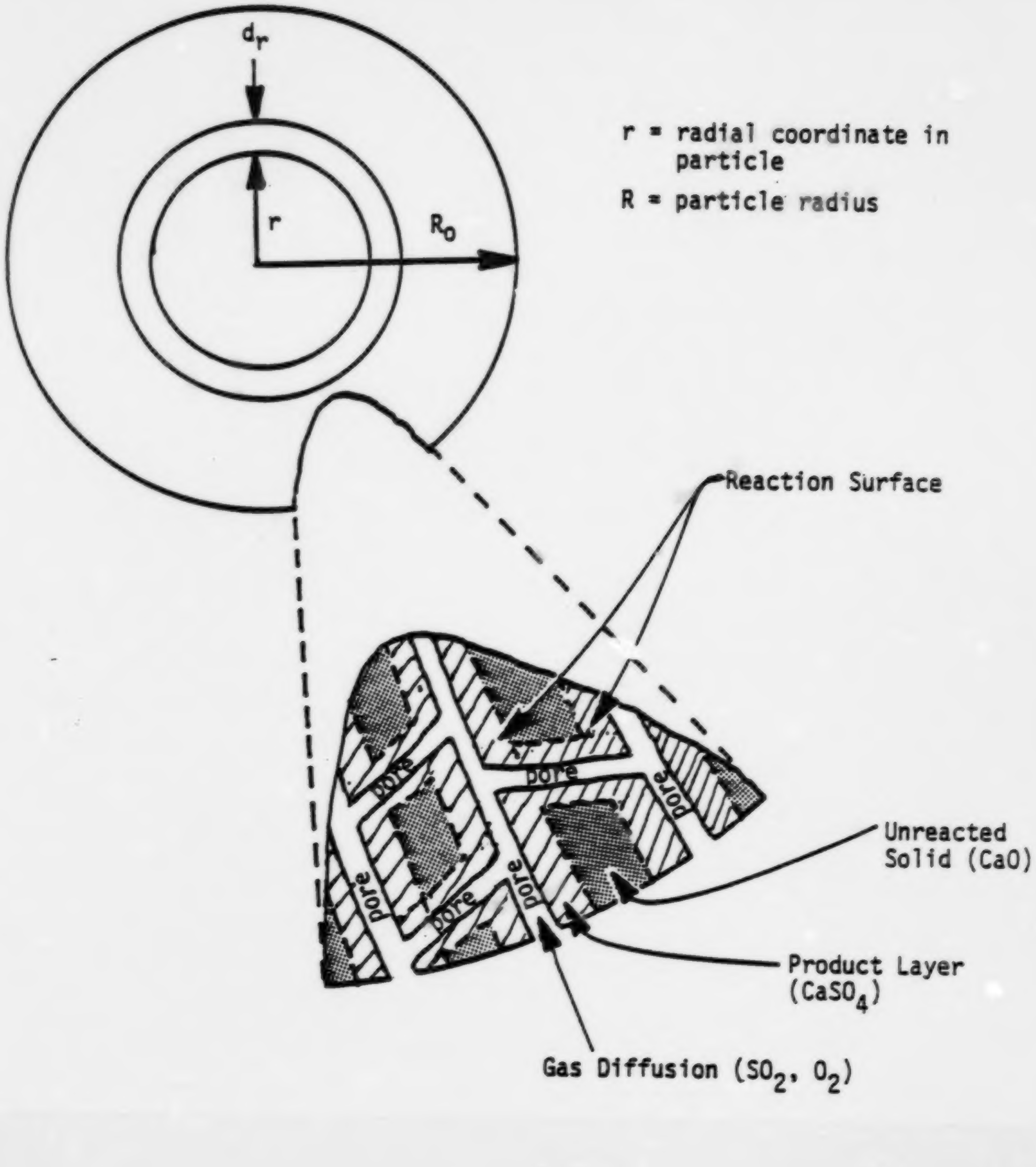
d_r
r = radial coordinate in particle
R = particle radius
r
R_0
Reaction Surface
pore
pore
pore
pore
pore
pore
Unreacted Solid (CaO)
Product Layer ($CaSO_4$)
Gas Diffusion (SO_2, O_2)

Figure 4-19. Conceptual illustration of pore model for CaO/SO_2 reaction.

L_o = total length of pore system per unit volume (cm/cm^3)
K_s = rate constant for surface reaction cm^4/mole-sec
M = Molecular weight of CaO (9/mole)
r = distance from the particle center (cm)
R = particle radius
S_o = initial pore surface area per kunit volume (cm^2/cm^2)
t = time (sec)
X = local conversion
Z = ratio of volume of solid phase after reaction to that before reaction

$$\beta = \frac{2K_s \quad (1-\epsilon_o)}{M \, D_p \, S_o}$$

ϵ_o = Initial porosity (cm^3/cm^3)

$$\psi = \frac{4\pi L_o \, (1 - \epsilon_o)}{\nu \, S_o^2}$$

ρ = Mass of CaO per unit volume of solid phase

Equation 4.5 describes the diffusion of gaseous reactant into the pore while Equation 4.6 gives the local rate of conversion (accounting for the effect of the product layer diffusional resistance).

The boundary conditions are:

$$\frac{\partial C}{\partial r} = 0 \qquad \text{at } r = 0 \tag{4.7}$$

and

$$D_e \frac{\partial C}{\partial r} = k_b \, (C_\infty - C) \qquad \text{at } r = R \tag{4.8}$$

where κ_b is the boundary layer mass transfer coefficient and C is the concentration of gaseous reactant at the free stream. The governing equations, (4.5) and (4.6) and the boundary conditions equations (4.7) and (4.8) constitute the complete system for the pore model. These equations are nondimensionalized and solved numerically in the following manner:

- Equation (4.5) and boundary conditions (4.7) and (4.8) are integrated numerically by finite-difference method to give the intraparticle concentration distribution.

- Equation (4.6) is simultaneously integrated (using a fourth-order Runge-Kutta scheme) to give local conversion.

In order to test the program, the SO_2-lime reaction calculations, identical to those performed by Bhatia & Perlmutter (1981) were repeated. The results of these calculations (presented in terms of overall lime conversion as a function of time for various temperatures) are plotted in Figure 4-20. For comparison, the predictions Bhatia & Perlmutter (1981) results and the data of Borgwardt (1970) are also shown in Figure 4-20. The calculations and the data are in reasonable agreement. Slight discrepancies between the EER calculations and Bhatia's calculations may be attributed to the differences in numerical method of solution. The calculations assumed first-order SO_2 dependence and constant free-stream SO_2 concentrations (3000 ppm) at constant temperature. It should be noted that these data can be fit equally well with zero-order kinetics.

4.2.4 The Distributed Pore Model

A schematic of the basic features of the distributed pore model is given in Figure 4-21. The model represents porous, spherical particles of CaO using nonintersecting pores of various lengths and diameters, all of which are directed radially outward. The average pore length is one-third the particle radius. Based on preliminary calculations using a single pore model, with a pore diameter characteristic of calcined lime, it can be shown that pore mouth closure at the particle surface will limit the extent of

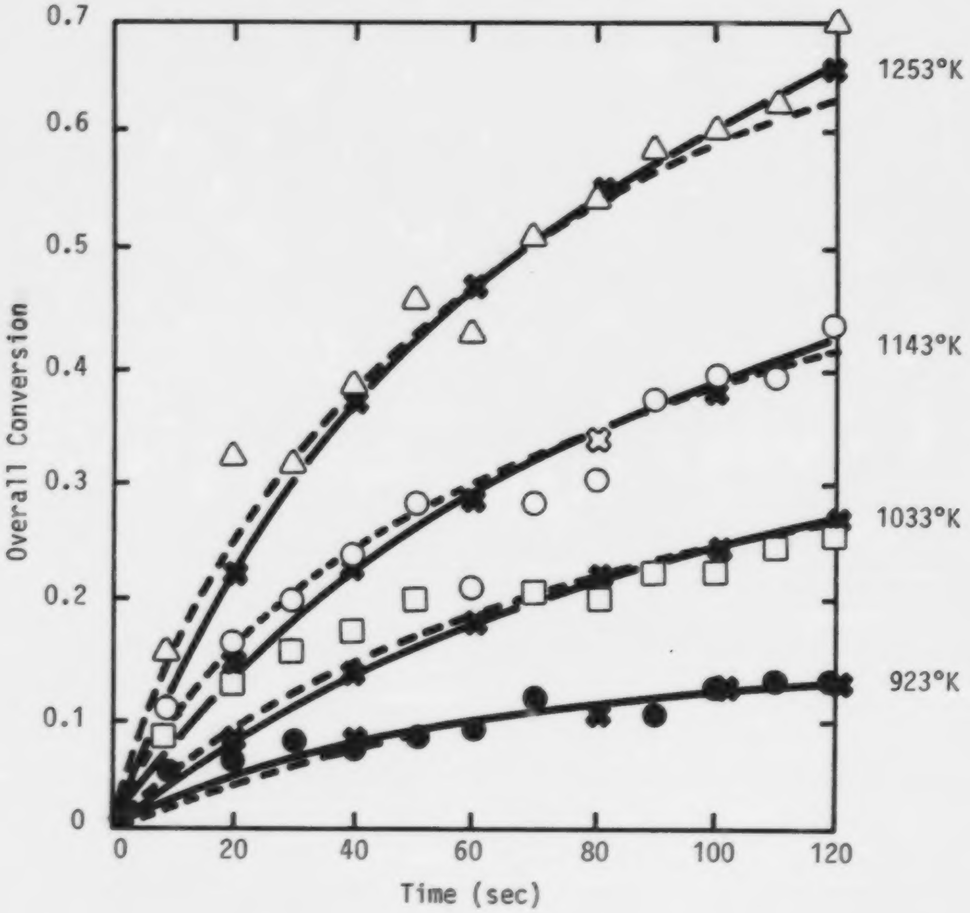

Figure 4-20. Application of random pore model to data of Borgwardt (1970). Solid lines represent the current model calculations, dotted lines represent Bhatia & Perlmutter's calculations (1981).

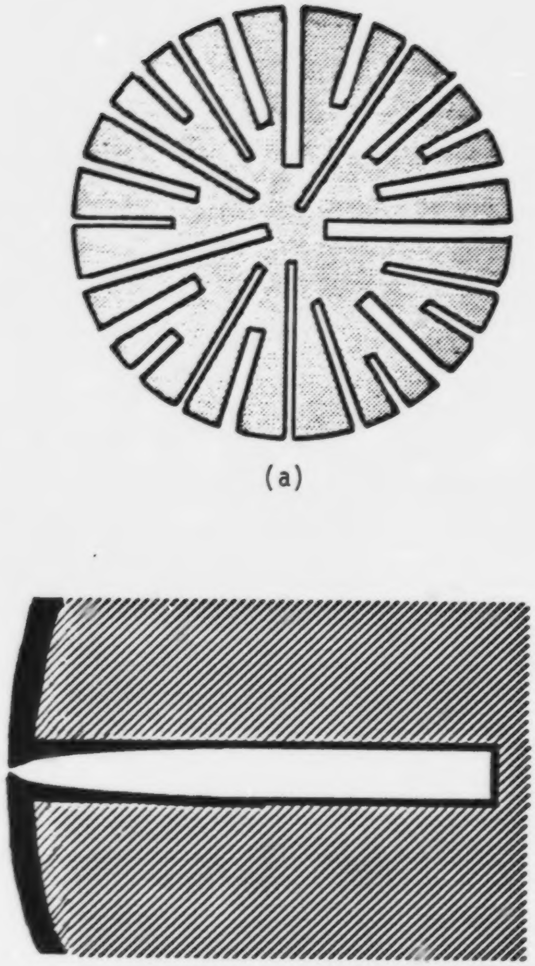

(a)

(b)

Figure 4-21. Schematics of the distributed pore model showing (a) the porous spherical CaO particle and (b) a closeup of a sulfated pore.

sulfation at short times. The model therefore assumes that the interior structure of the particle is unimportant and that an average pore length of one-third will adequately represent the pores.

The governing equations used in the model account for the diffusion of SO_2 to the particle surface, through the cylindrical pores, and through the $CaSO_4$ product layer. The SO_2 then reacts at the $CaO-CaSO_4$ interface with the reaction being first-order in SO_2. The pore geometry is allowed to change with the accumulation of $CaSO_4$. A distribution of initial pore sizes and sintering (pore growth) are also considered. Sulfation is also allowed on the particle surface.

The key reaction parameters in the model are the diffusivity of SO_2 in the pores, the solid diffusion coefficient for SO_2 in $CaSO_4$, and the chemical reaction rate constant. The effective diffusivity of SO_2 in porous CaO is estimated from molecular theory. The solid product layer diffusion coefficient is based on the data of Borgwardt and Bruce (1986). The kinetic rate constant is assumed to be large and not rate controlling based on isothermal reactor (ITR) studies performed at EER.

Because the initial pore size distribution in the model is set equal to the experimentally measured distribution, the model can more easily reflect subtle differences between precalcines. This need for detailed PoSD data does, however, limit the applicability of the model to precalcines at present. Before the distributed pore model can be used to predict raw sorbent behavior, it will be necessary to develop a theoretical or empirical correlation between raw sorbent properties and in-situ pore size distribution.

4.2.5 Comparison of Model Formulations

Table 4-1 summarizes the phenomena considered by each of the three models. Currently all of the models include the sequential resistances thought to be of potential importance in the sulfation process:

TABLE 4-1. SUMMARY OF PHENOMENA CONSIDERED

	GRAIN	RANDOM PORE	DIST. PORE
A. ACTIVATION			
- Calcination	NO	NO	NO
- Sintering	✓	NO	✓
B. SULFATION			
- External Mass Transfer	✓	✓	✓
- Pore Diffusion	✓	✓	✓
- Product Layer Diffusion	✓	✓	✓
- Heter. Chemical RXN	✓	✓	✓
- Multiple Pore (Grain) Sizes	✓	✓	✓

- external mass transfer from the free stream to the particle surface,
- pore diffusion from the particle surface to the particle interior,
- diffusion of the reacting sulfur species through any previously formed calcium sulfate, and
- heterogeneous chemical reaction to form calcium sulfate.

In addition all of the models currently allow for a distribution of characteristic internal sizes which is consistent with the available surface area and porosimetry data.

Detailed analysis of the model predictions for typical boiler injection conditions (2300-1800°F, 1-2s) has indicated that the controlling resistances are predicted to be different for each of the models:

TABLE 4-2.

	Grain	Random-Pore	Dist. Pore
Initial Rate	- 0.55 Order Kinetics	- First Order Kinetics	- Product Layer Diffusion
Deactivation of Sorbent	- Product Layer Diffusion & Sintering	- Pore Filling	- Pore Plugging

Unfortunately, the available fundamental data are insufficient to allow complete resolution of the correct formulation; short time (0-200 ms), high temperature sulfation data for sized precalcines are urgently needed.

4.3 Analysis of Experimental Results

An analysis of fundamental sulfation data form differential and flow reactors is presented in this section. The analysis includes comparisons between the sulfation models and sulfation data obtained with precalcined sorbents, i.e., CaO.

4.3.1 Differential Reactor Data

The differential reactor data of Borgwardt and Bruce (1986) were shown in Figure 4-1 to 4-5. The grain model was fit to these data in order to obtain the rate constant as a function of temperature and to determine the reaction order with respect to SO_2. Figure 4-22 shows an example of the fit obtained using the 3 m^2/g temperature data. Similar results were obtained at lower temperatures. Figures 4-23 and 4-24 are predictions of the effect of sorbent surface area. In both figures the model predicts the observed trends.

Figures 4-25 and 4-26 show the fit obtained using a reaction order of 0.55 in SO_2. The model successfully correlates Borgwardt and Bruce's results at SO_2 concentrations ranging from 120 to 10,000 ppm.

In the case of the distributed pore and random pore models, the product layer diffusivity was also determined from the experimental data of Borgwardt et al. (1985). Figure 4-27 compares the distributed pore model fit to the experimental data. These results can be correlated with the pore model because the surface area is essentially completely external (1 μm particles with 3 m^2/g). The higher surface area data can not be studied with the distributed pore model because the required pore size distribution data are not available.

4.3.2 Time-Resolved Isothermal Results

This reaction focuses on comparisons of pore and grain model predictions with the experimental results of sized precalcines. These results differ from the differential reactor data just discussed because they were obtained at higher temperatures and much shorter times in dispersed phase flow reactors. In addition, the CO_2 and H_2O present in actual combustion systems can greatly enhance the surface area/porosity loss of highly reactive precalcines.

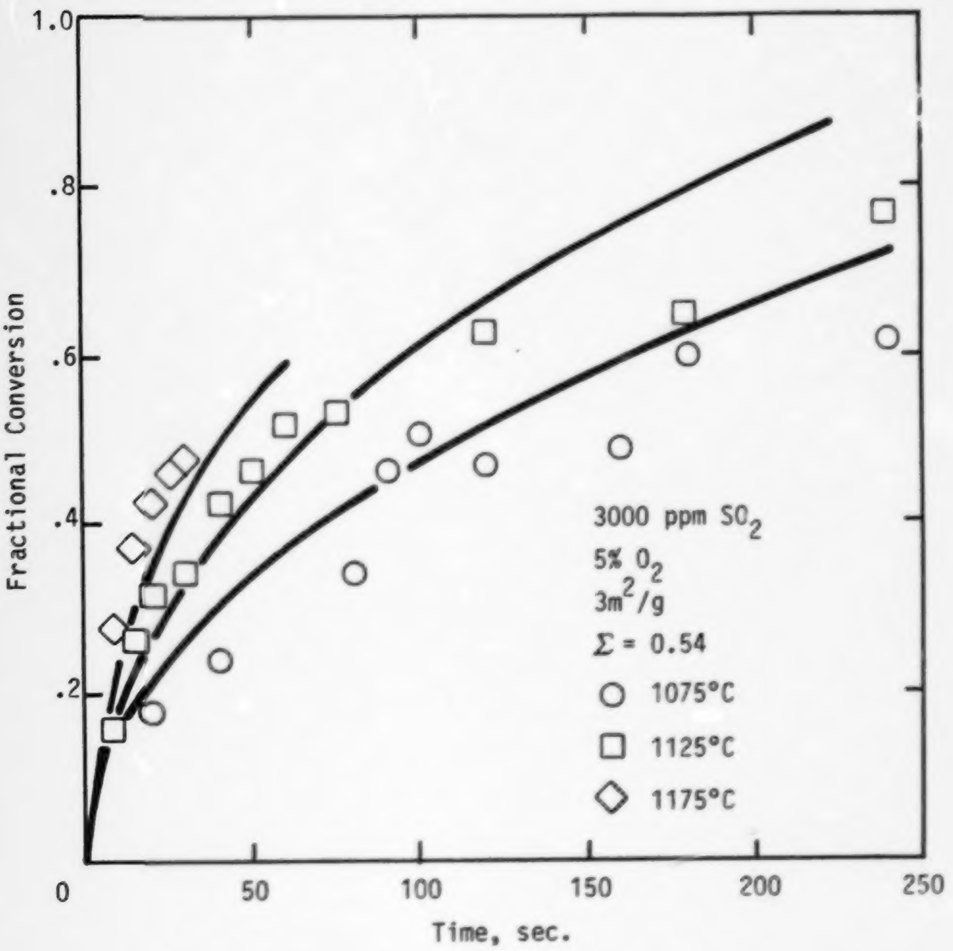

Figure 4-22. The differential reactor data of Borgwardt and Bruce (1986) for 1 μm precalcined Fredonia limestone. The solid lines are the model fit to the data.

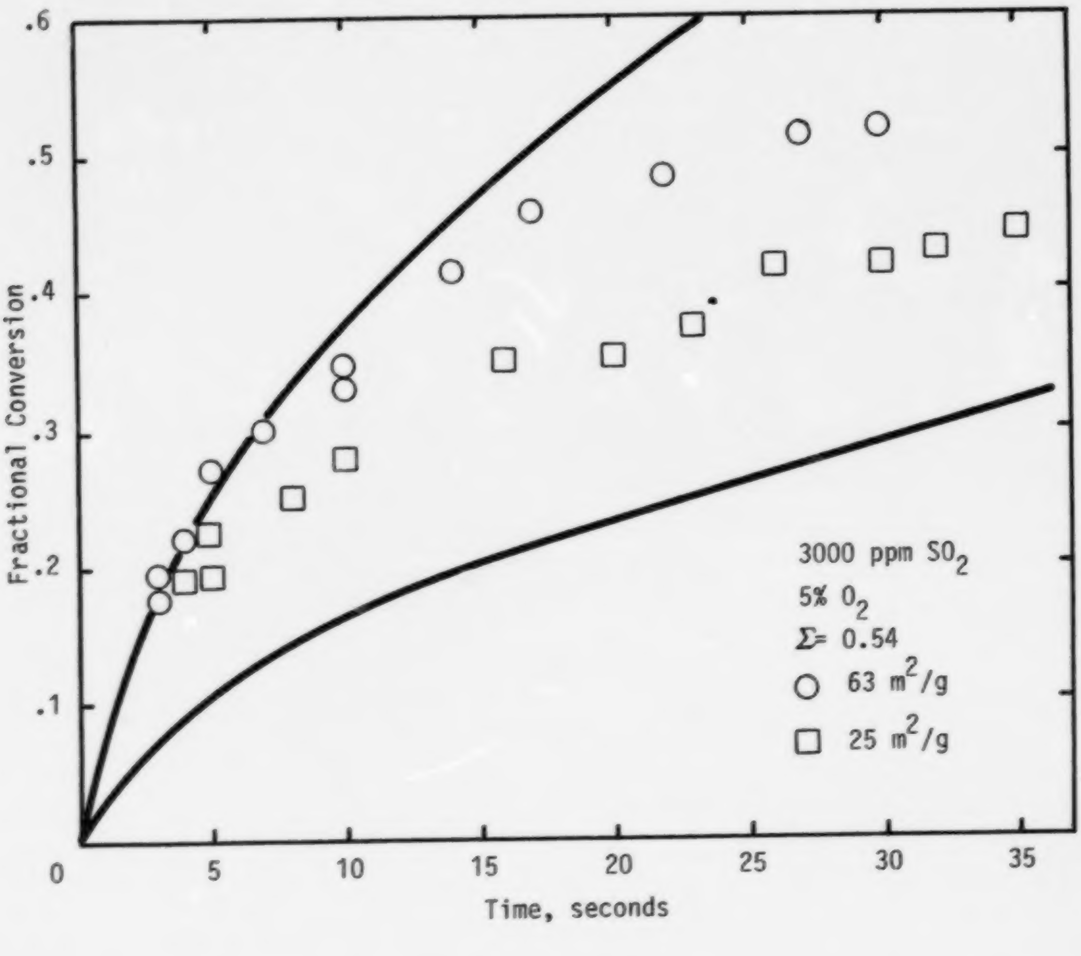

Figure 4-23. The differential reactor data of Borgwardt and Bruce (1986) at 800°C for 1 μm precalcined Fredonia limestone. The solid lines are model predictions.

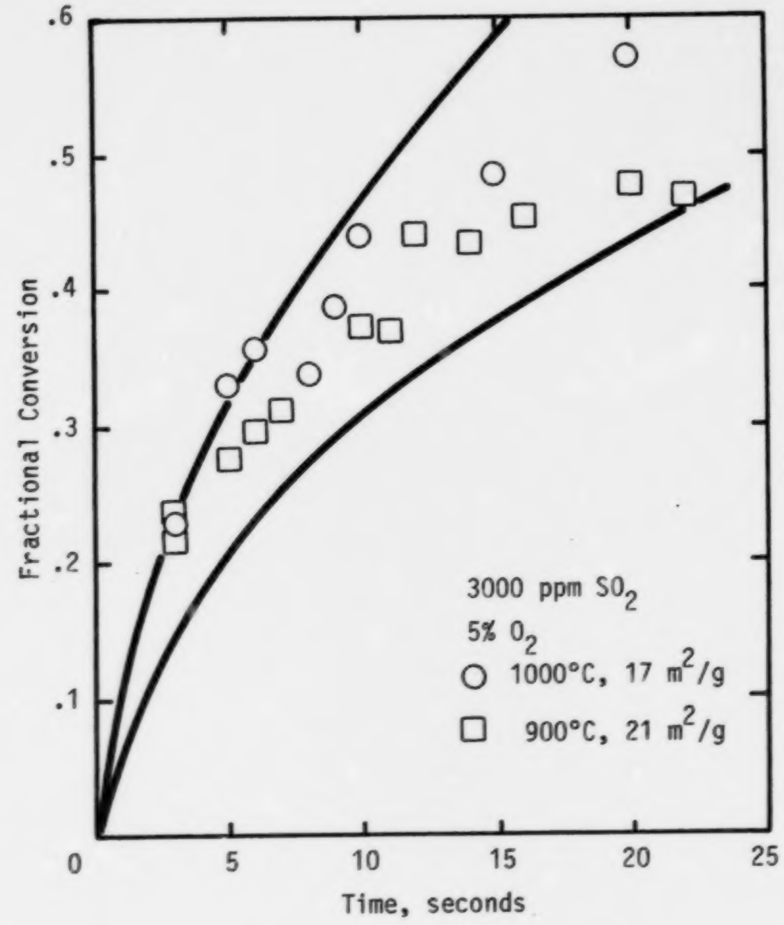

Figure 4-24. The differential reactor data of Borgwardt and Bruce (1986) for precalcined 1 μm Fredonia limestone. The solid lines are model predictions.

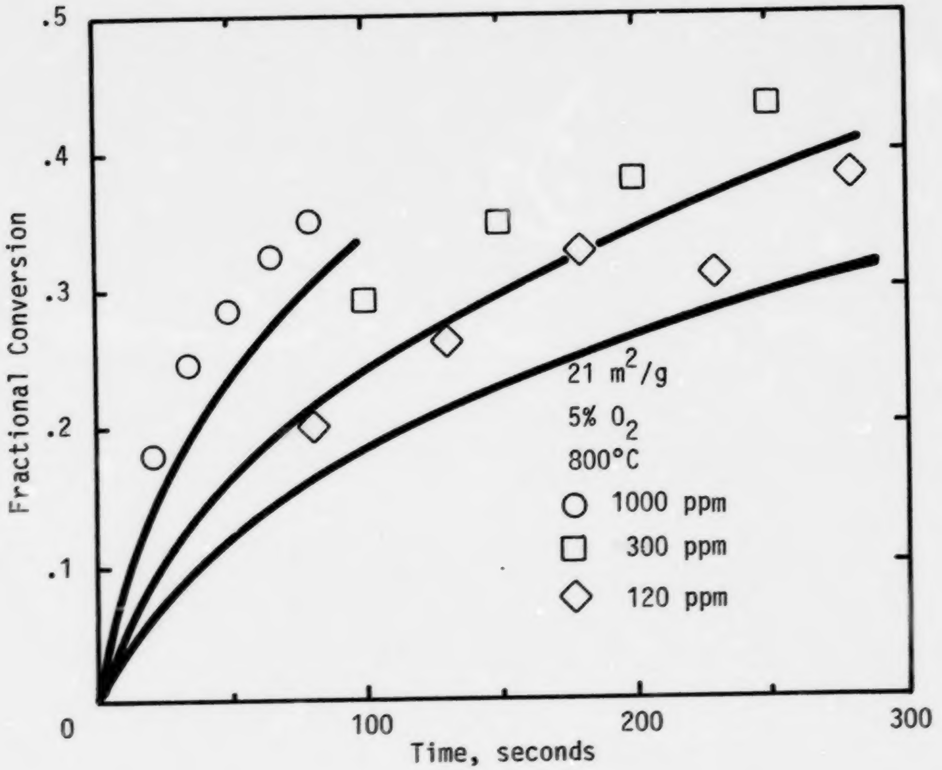

Figure 4-25. The differential reactor data of Borgwardt and Bruce (1986) for precalcined 1 μm Georgia marble. The solid lines are model fits.

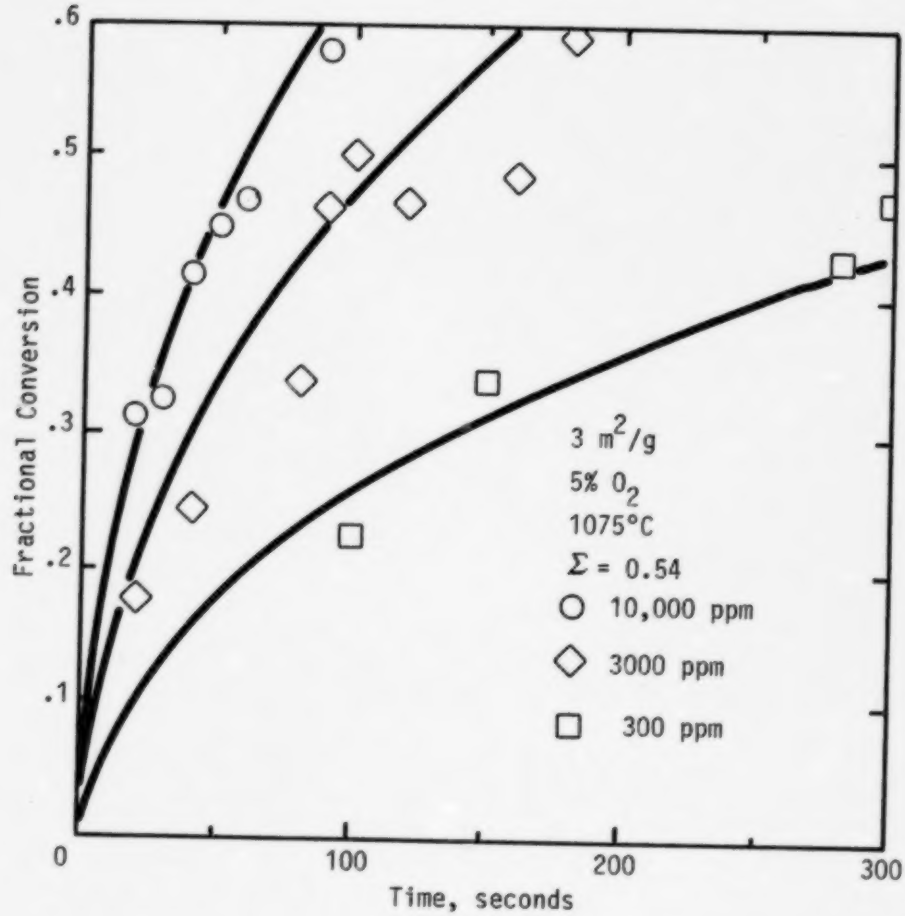

Figure 4-26. The differential reactor data of Borgwardt and Bruce (1986) for 1 μm precalcined Fredonia limestone. The solid lines are model fits.

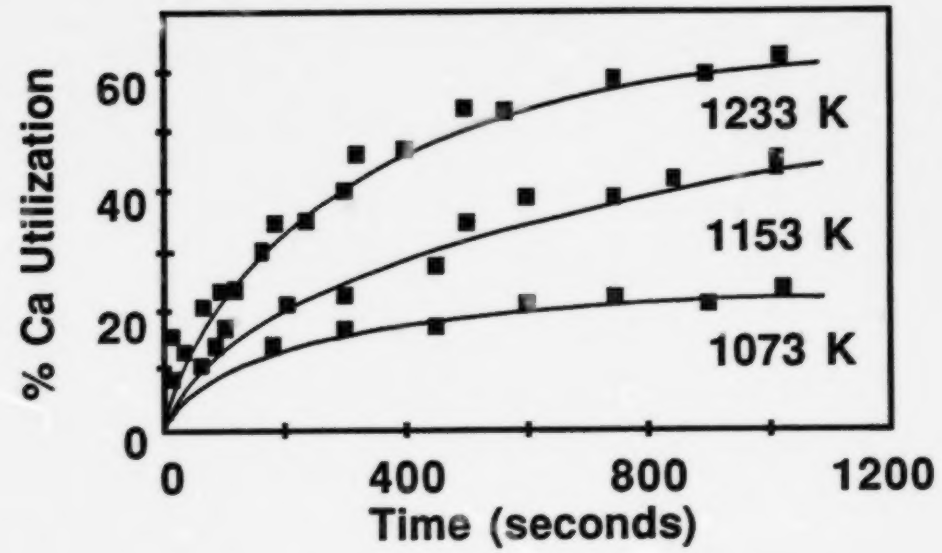

Figure 4-27. Data of Borgwardt et al. (1986) and model predictions for 1 micron, 3 m^2/g particles at 3000 ppm SO_2.

Figure 4-28 shows grain model predictions and isothermal reactor (ITR) data obtained at 1000 and 1200^{o}C with 2 μm CaO. The solid lines are grain model predictions with sintering included. The sorbent surface area was allowed to decrease from 80 m^2/g toward 5 m^2/g at a rate which increases with increasing temperature in an Arrhenius fashion. Allowing this to occur results in a prediction which agrees quite closely with the data both in terms of the effects of time and the effects of temperature.

An alternate way of obtaining the curve shape shown in Figure 4-3 is to use a distribution of grain sizes. For example, a distribution which includes only a large size and a much smaller size will exhibit the same behavior shown in Figure 4-3, i.e., a rapid initial reaction followed by a relatively slow reaction. However, the distributed grain size approach can not account for the unsensitivity to temperature shown in Figure 4-3.

Figure 4-29 compares distributed pore model predictions with the data of sized precalcines. The solid lines in Figure 4-29 show model predictions for the four sorbents based on the experimentally measured pore size distributions; no parameters have been adjusted to improve the agreement between the experimental data and the distributed pore model. The model predicts a rapid rise in capture during the first 250 ms followed by slow growth in capture. The model predictions suggest that the sulfation rate decreases dramatically beyond approximately 250 ms because the small pores (< 0.02 μm) are rapidly blocked (not filled) by calcium sulfate formation at the pore mouth.

Figure 4-30 shows the initial SO_2 concentration (t=o) as a function of axial distance in an 80 Å pore (1.7 μm length), as predicted by the distributed pore model. (The pore intersects the particle surface at x=1). Even before the product layer begins to grow, the SO_2 concentration drops off sharply and is negligible below a dimensionless axial distance of 0.6 due to the relative rates of pore diffusion and chemical reaction. Since the gas-solid reaction is first order with respect to SO_2 concentration, product layer growth occurs primarily near the pore mouth. The resulting radial profile also shown in Figure 4-30 at the time of pore closure (r = 0 @ x = 1)

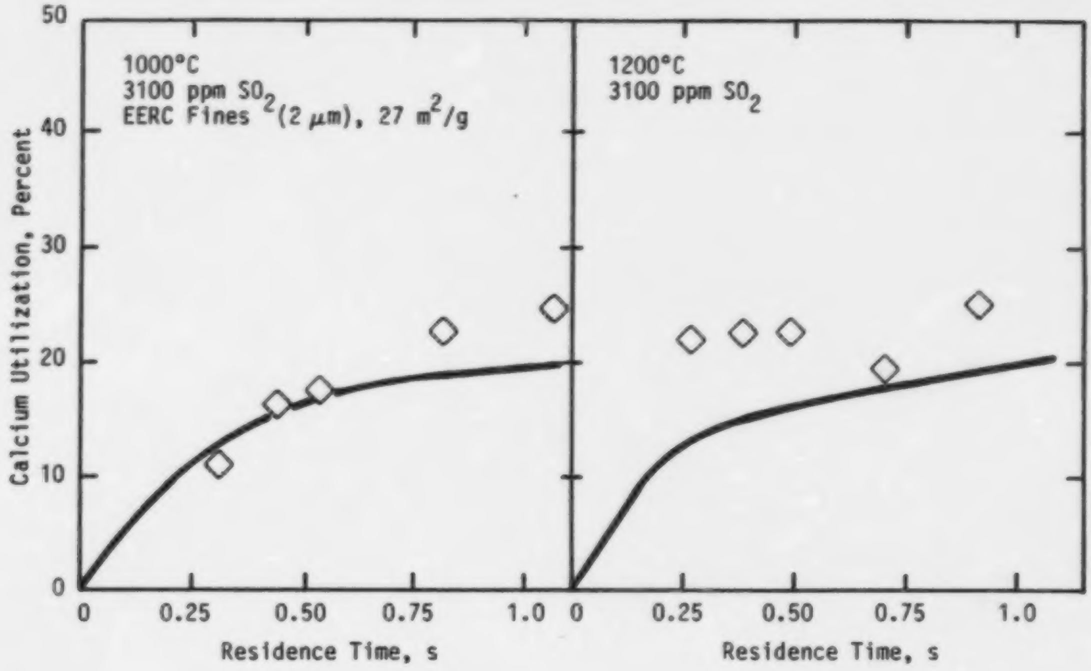

Figure 4-28. SO_2 capture profiles for a 2 μm precalcine at 1000°C and 1200° in the presence of 3100 ppm SO_2. The solid curves represent model predictions for the conditions shown based upon the measured physical properties of the sorbents.

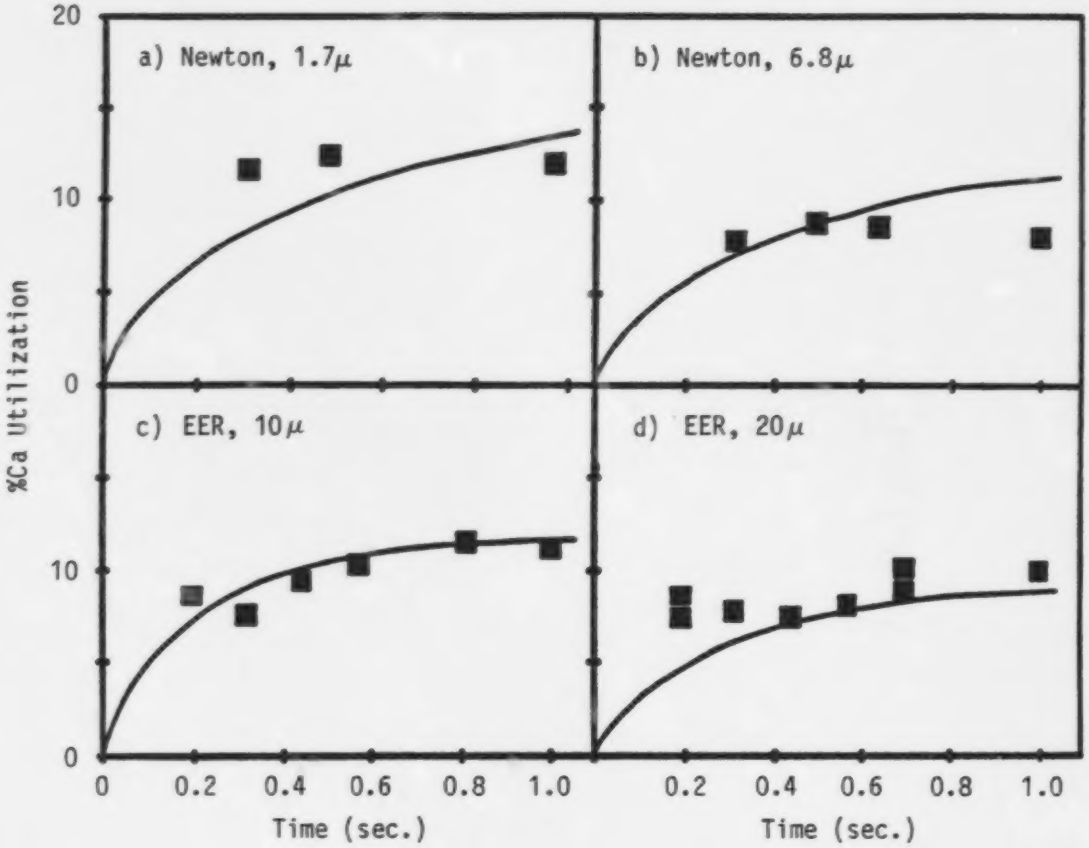

Figure 4-29. Comparison of distributed pore model and experimental data. Sulfation conditions for sorbents in a) and b): 1256K, 2000 ppm SO_2, and Ca/S = 2. Sulfation conditions for sorbents in c) and d): 1273K, 3100 ppm SO_2, and Ca/S = 2 (EER data generated under EPA Contract 68-02-3633.

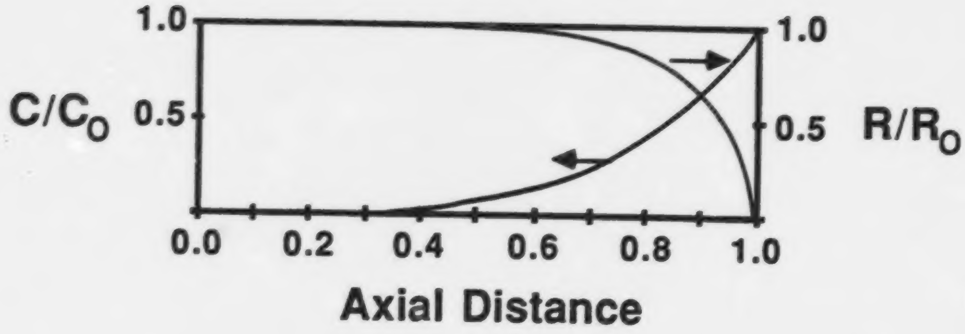

Figure 4-30. SO_2 concentration and radial profiles within a pore.

demonstrates the lack of calcium utilization which can occur in small pores due to pore mouth closure.

Model predictions of surface area loss as a function of time in the reaction zone are illustrated in Figure 4-31 for a 1.7 μm precalcined sulfate at 1260 K and 2000 ppm SO_2 (analagous to the conditions of Figure 4-27). These calculations suggest that almost 50 percent of the available surface area is lost, primarily due to pore closure, during the initial 300 ms in the reaction zone.

4.3.3 Influence of Injection Temperature

Both the grain and pore models were used to examine the effect of reaction temperature in flow reactors. The experimental data (summarized in Section 4.1.5) suggest the optimum isothermal reactor temperature is roughly 1250 - 1350 K (1800-2000°F), but even the data are not in good agreement. Grain model predictions which include surface area loss due to sintering, are shown in Figure 4-32 for both quenched and isothermal systems. The isothermal results suggest that SO_2 capture should increase with increasing temperature until the temperature at which $CaSO_4$ is stable is exceeded. For the conditions of Figure 4-32 that temperature is approximately 2150°F. This temperature is much higher than the 1800°F observed by Newton (1986). This may be due to an incomplete description of the sulfation-sintering process. For comparison Figure 4-32 also includes prediction for a nonisothermal system with a quench rate of -500°F/s.

Figure 4-33 compares distributed pore model predictions to the available data for a variety of precalcines as a function of reaction temperature. The data presented in Figure 4-33a are for a 4 μm Longview precalcine sulfated at 1750 ppm SO_2, 600 ms, and Ca/S = 2. Capture rises from 1030 K to 1140 K and then remains approximately constant up to 1370 K where it begins to decline. Model predictions without the sintering mechanism, the dashed line, indicate that at lower temperatures, the sulfation reaction is primarily controlled by product layer diffusion, not the pore closure mechanism. Above approximately 1250 K pore closure limits the extent of calcium utilization and prevents

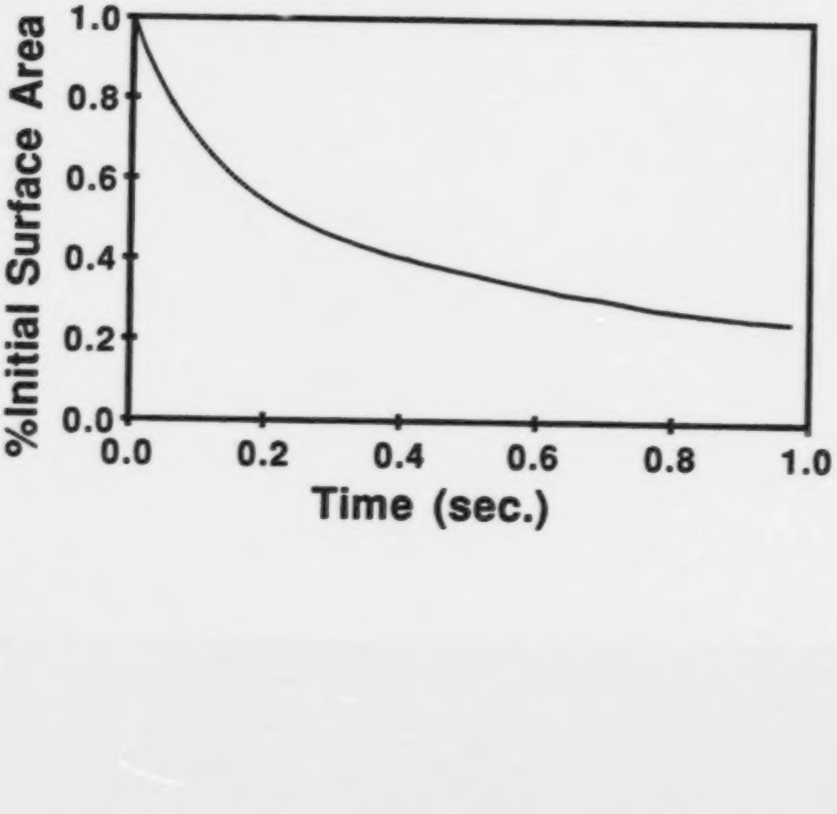

Figure 4-31. Loss of initial surface area due to pore mouth closure as predicted by the distributed pore model.

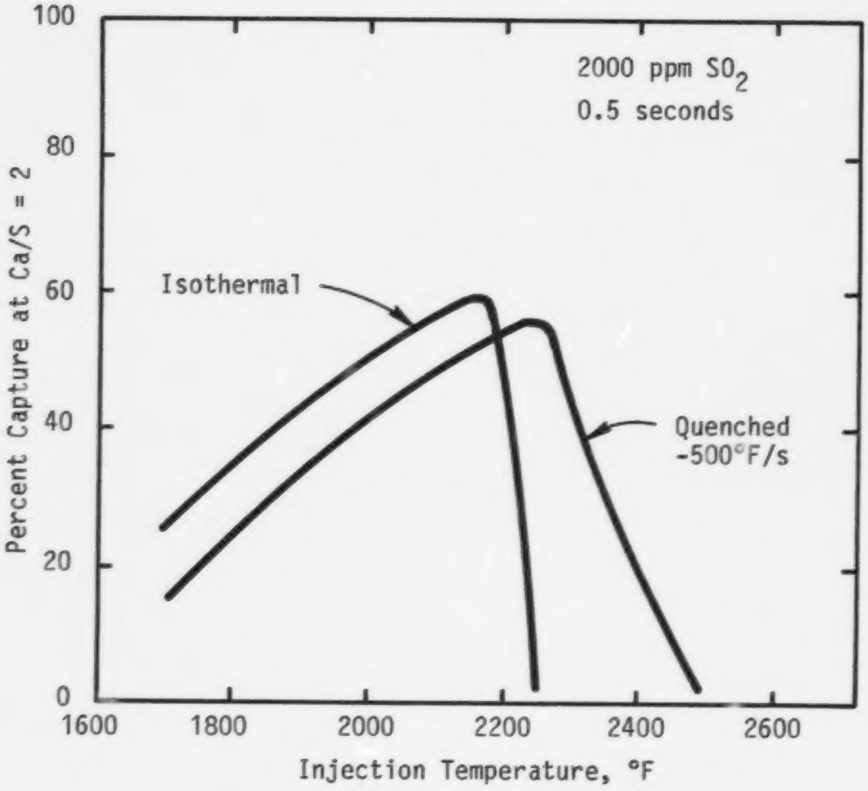

Figure 4-32. Grain model predictions showing the effect of reaction or injection temperature for both isothermal and quenched systems. Sorbent surface area loss was allowed to occur during sulfation due to sintering.

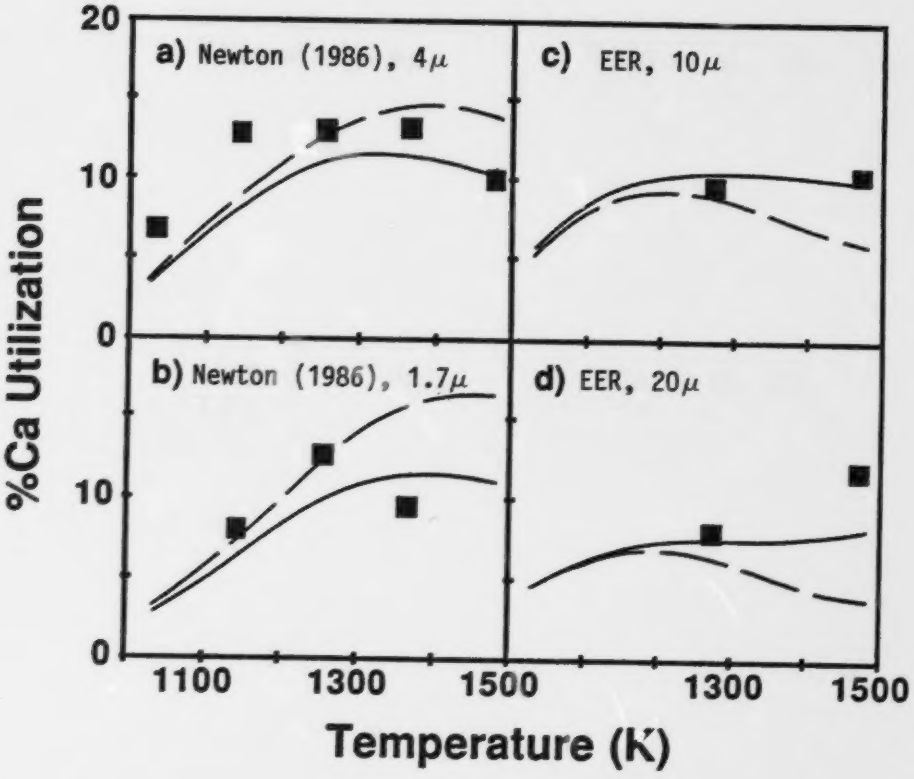

Figure 4-33. Comparison of distributed pore model (with and without sintering) and experimental data (EER data generated under EPA Contract 68-02-3995.

further increases in sulfur capture with increasing temperature. The solid line in Figure 4-33a represents the model predictions for the Longview precalcine with the sintering mechanism included. The model now predicts a much more rapid leveling off in capture and an actual drop in calcium utilization at 1480 K.

The 1.7 μm precalcine, prepared from a sized Linwood atmospheric hydrate, shown in Figure 4-33b has a the smallest mean particle size but the largest mean pore diameter (261 Å) of the sorbents considered. These data again suggest an optimum sorbent temperature of approximately 1250 K. Without the sintering mechanism (dotted line) the model predicts that calcium utilization should increase almost linearly with increasing temperature. These predictions result from the large pore structure which is not susceptible to pore mouth closure under the conditions studied. In the absence of sintering most of the internal surface area is, therefore, available to react for times in excess of 300 ms. Since higher temperatures increase the rates of chemical reaction and product layer diffusion, higher calcium utilization is predicted. When the sintering mechanism is included in the model, predictions above 1200 K are significantly reduced for this precalcine as a result of the lower surface areas brought about by sintering.

Figures 4-33c and 4-33d illustrate experimental data obtained by Cole and Coworkers (1985) for 10 and 20 μm precalcines prepared from limestones (rather than hydrated sorbents) and sulfated 3100 ppm SO_2, 500 ms, and Ca/S = 1. Data for the 10 μm precalcine exhibit a slight increase in sorbent utilization as temperature increases. The solid and dashed lines again represent model predictions with and without the sintering mechanism, respectively. Without sintering, the model predicts that the rate of pore closure will increase as temperature rises and result in a decrease in utilization at higher temperatures. When the sintering mechanism is included in the model, the predictions are greater than for the nonsintering case and more accurately represent the experimental data.

The 20 μm precalcined data actually shows an increase in calcium utilization at the highest temperature examined. The model predictions including sintering (solid line) do not completely predict this increase; however, they are clearly more representative than the predictions without sintering.

Comparison of Figures 4-33a and 4-33b with Figures 4-33c and 4-33d indicate a distinct difference in the high temperature behavior of these materials which may result from their differing pore structure. The 1.7 and 4 μm precalcines prepared from hydrated sorbents have consistently larger pores than the 10 and 20 μm precalcines prepared from the limestones. To illustrate the influence of pore size on sulfur capture, the model was used to compute calcium utilizations for particles with a single mean pore size and with an ideal porosity of $\epsilon = 0.55$, as illustrated in Figure 4-32. The model predicts that for the smallest pores shown, utilization is limited by pore mouth closure to less than 5 percent. As pore diameter increases the rate of pore closure decreases and utilization rises until a maximum is reached at about 220 A where pore closure ceases to occur for this reaction time and temperature (500 ms and 1260 K). Further increases in pore size reduce calcium utilization by reducing particle surface area. (A doubling in pore size reduces the pore surface area by 50% if porosity remains constant.) A calcine with a mean pore size primarily larger than 220 Å will therefore exhibit a decrease in calcium utilization if sintering increases the mean pore diameter. Conversely, sintering of a calcine with a pore structure primarily smaller than 220 Å will tend to increase utilization by slowing the rate of pore mouth closure. Calcines with pore structures in the immediate vicinity of 220 Å may exhibit both types of behavior depending on the exact rate of sintering and experimental conditions.

Therefore, it is not unreasonable that the 1.7 and 4 μm precalcines exhibit behavior distinctly different from the 10 and 20 μm precalcines. The smaller particles derived from hydrates (Figures 4-33a and 4-33b) have mean pore sizes in excess of 220 Å, while the larger particles prepared from limestone (Figures 4-33c and 4-33d) both have mean pore sizes less than 220 Å. In the latter cases sintering may actually increase reactivity of the material because it tends to open the pore structure.

4.3.4 Closure

In conclusion, most of the differential reactor data of Borgwardt and Bruce (1986) can be correlated by simple grain or pore models. However, the extrapolation of this data to conditions of practical interest ($T > 1250$ K, $t < 0.55$) is still somewhat problematical due to a paucity of high temperature, very short time, sulfation and sintering data with well characterized sorbents. However, both the grain and pore models are capable of reproducing the temporal and thermal behavior measured experimentally, if sintering is (empirically) included.

Both models attribute the dramatic decrease in sulfation rate beyond 200 ms to a loss of Ca accessability. In the grain model this is predicted to occur due to CO_2 and H_2O catalyzed thermal sintering; in the distributed pore model it results from the closure (plugging) of small pores and from sulfate promoted sintering. The available experimental data on pore structure clearly indicate that both pore closure and sintering do occur within the first 500 ms (Newton, 1986); however, the data are not sufficiently time resolved to define which process is controlling.

5.0 COUPLED ACTIVATION AND SULFATION

The previous section was devoted to the sulfation of precalcines. This is a subject of research interest because it allows the examination of the sulfation reaction without the interference of concurrent activation. However, most proposed applications of LIMB will use raw sorbents, so the behavior of sorbents during concurrent activation and sulfation is of immediate concern. In this section the data for isothermal sulfation of raw materials is compiled, and the modeling approaches are applied to the data in an effort to resolve apparent discrepancies.

5.1 Compilation of Experimental Results

5.1.1 Time-Resolved Sulfation

The isothermal capture of sulfur has been found to be primarily influenced by sorbent type, temperature, heating rate, particle size, and SO_2 concentration. Figure 5-1 compares data for Vicron 45-3 limestone with that of Linwood atmospheric hydrate in the EER isothermal reactor (Cole et al., 1986). Each plot shows time resolved capture at 1100°C for two heating rates: the venturi precombustor causes the sorbent to approach 1100°C within the order of 7 ms, while the straight precombustor provides mixing in about 30 ms. Three general conclusions are noted from the graph:

1. For the high reactivity conditions, the sulfation takes place at a rapid rate within the first 100 ms, and subsequently at a slower rate.

2. Raw hydrates consistently out perform raw carbonates on a calcium available basis.

3. The higher heating rate yields substantially improved performance for all materials.

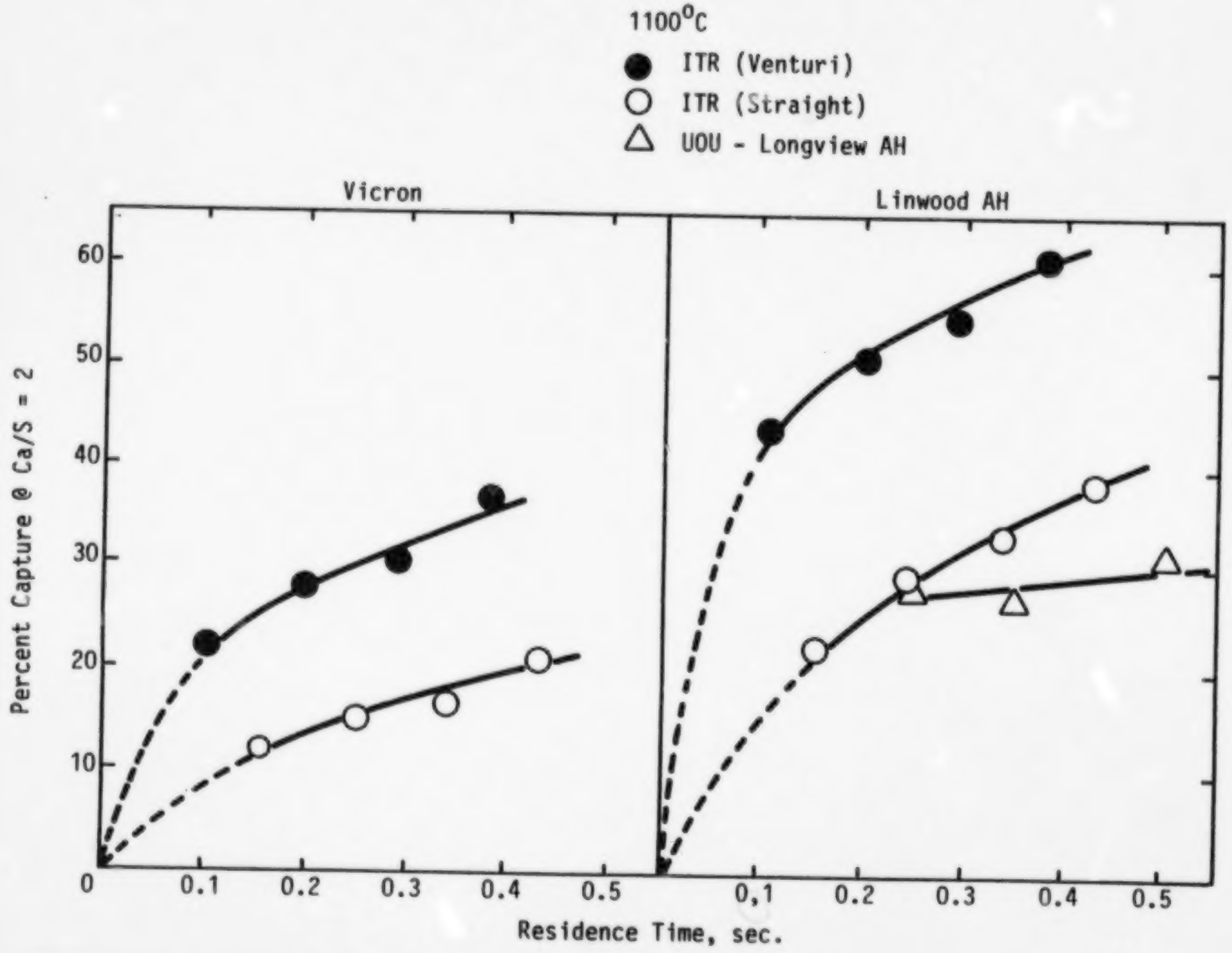

Figure 5-1. Time-resolved SO_2 capture for Vicron 45-3 and Linwood hydrate at 1100°C. Comparison of Straight vs. Venturi precombustors. U of U data added for comparison (Newton, 1986). (EER data generated under EPA Contract 68-02-4239.

Even with hydrates there is a substantial difference in reactivity at all scales. In the next chapter hydrates from various commercial sources will be shown to yield significantly different sulfation behavior in actual bench-scale combustion tests. Also, hydrates prepared from the same parent quicklime can have significant differences in reactivity that can be correlated to the conditions under which they were hydrated. Figure 5-2 shows the calcium utilization resulting when six hydrates were sulfated under identical isothermal circumstances, Table 5-1 identifies the hydration conditions. The results suggest that if hydration can be completed under lower temperatures and shorter times, less grain growth will occur and the hydrate will exhibit more reactivity. This is consistent with the finding that hydrates prepared with excesses of alcohol in the hydration water show superior reactivity under some conditions. The presence of the alcohol moderates the hydration temperature and may control grain growth.

All of the materials in Figure 5-2 showed identical particle size with the exception of Mix 4 (low hydration water stoichiometry), which had a higher particle size. Other means of varying hydrate particle size have included variations in hydrator discharge conditions and parent quicklime size. These also have influences on reactivity, which suggests that hydrate reactivity is made up of a structure component and a size component.

Figure 5-3 compares results at around 1000°C for carbonates. Only the data of Tokuda et al. (1984) show the rapid early utilization noted in the preceding two figures. Results from MIT (Snow, 1985) provide one explanation. Snow's data were obtained on a 45-53 micron size cut of Icelandic Spar limestone. Figure 5-4 shows the time resolved conversion of limestone to sulfate at various temperatures. The data do not generally indicate an early, rapid sulfation rate. However, the large size of the sorbent significantly slows the calcination rate of the particles. Snow (1985) suggests that this effect can be removed by plotting the utilization of the available CaO, and ignoring the non-reactive carbonate component. Figure 5-5 shows results of replotting the data in this manner, which illustrates a rapid utilization of the CaO, as it becomes available. This suggests that the larger particle size used in the EPRI/MHI study may have

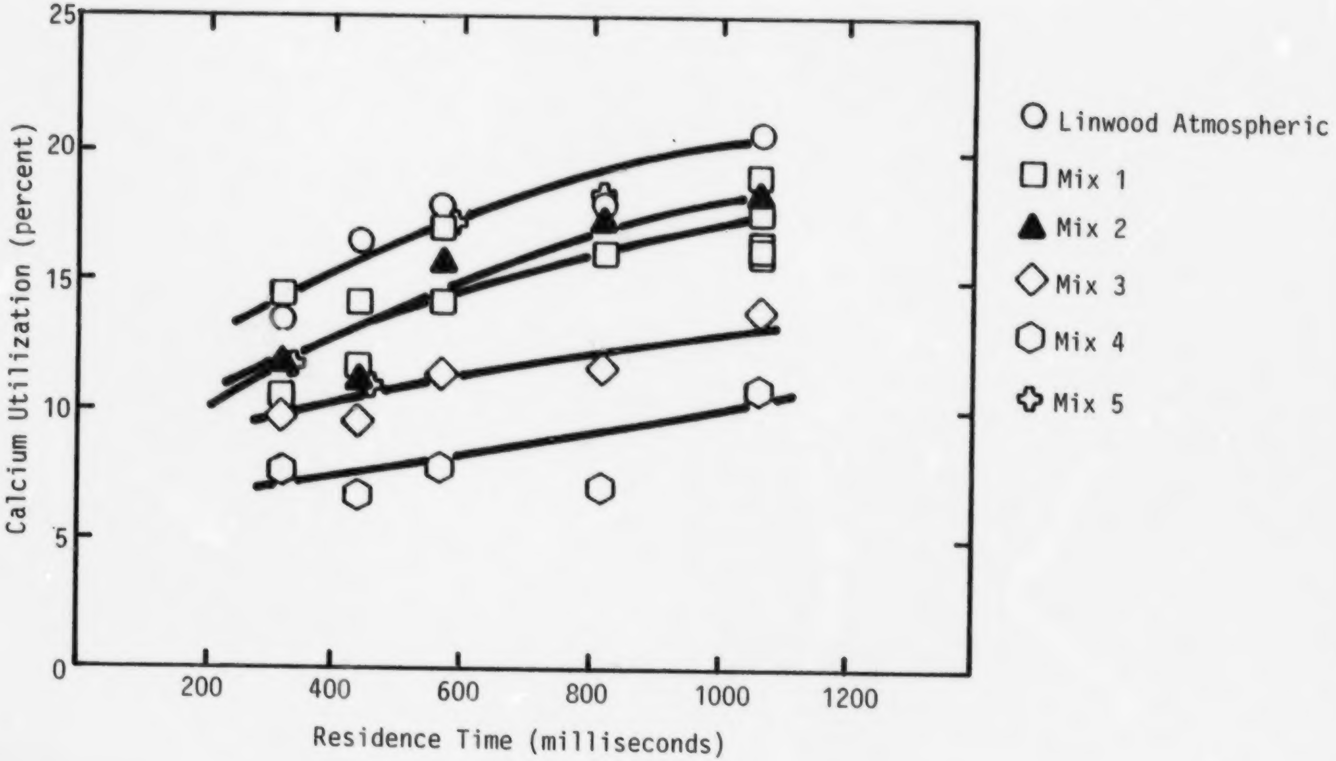

Figure 5-2. Sulfation performance of the various sorbents in the isothermal reactor at 1000°C and 3000 ppm SO_2 (data generated under EPA Contract 68-02-4239.

TABLE 5-1. PRESSURE HYDRATOR CONDITIONS

Designation	Preheat (^oC)	Pressure (psi)	Water/Calcium Stoichiometry
Mix 1	190	150	1.4
Mix 2	240	150	1.4
Mix 3	190	250	1.4
Mix 4	190	150	0.8
Mix 5	90	150	1.4
Mix 9	190	75	1.4

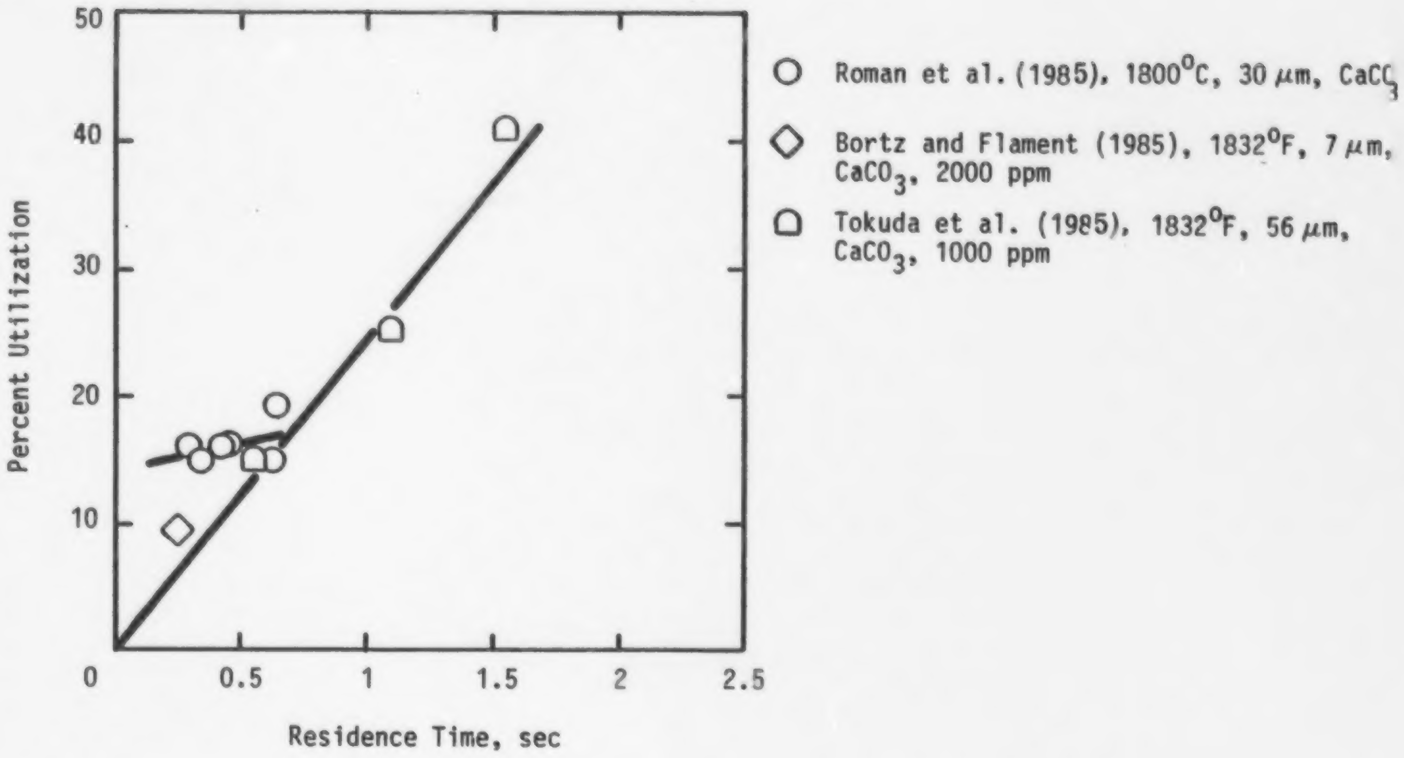

Figure 5-3. Conversion of carbonates to sulfates in various isothermal facilities.

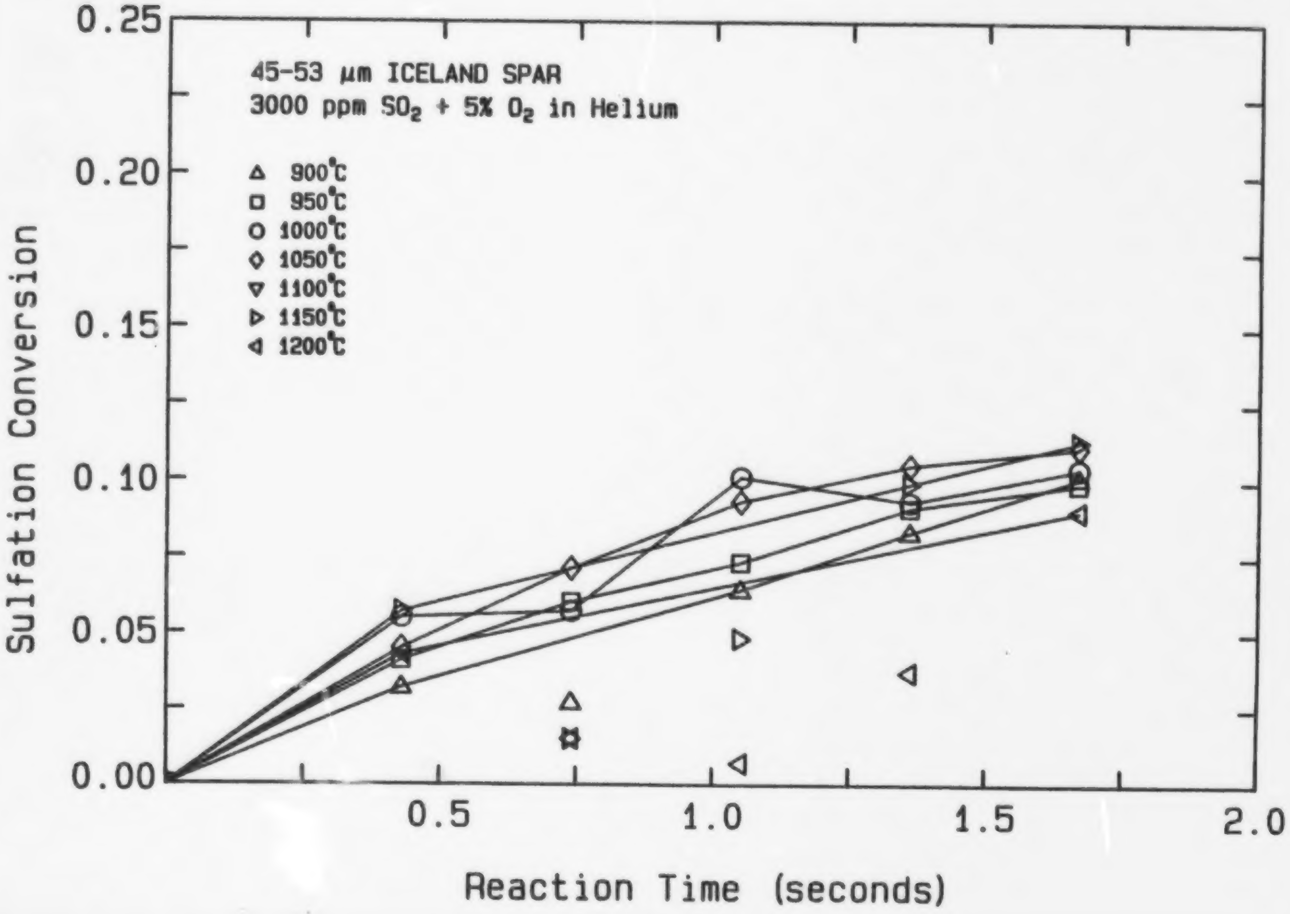

Figure 5-4. High temperature sulfation of limestone (Snow, 1985).

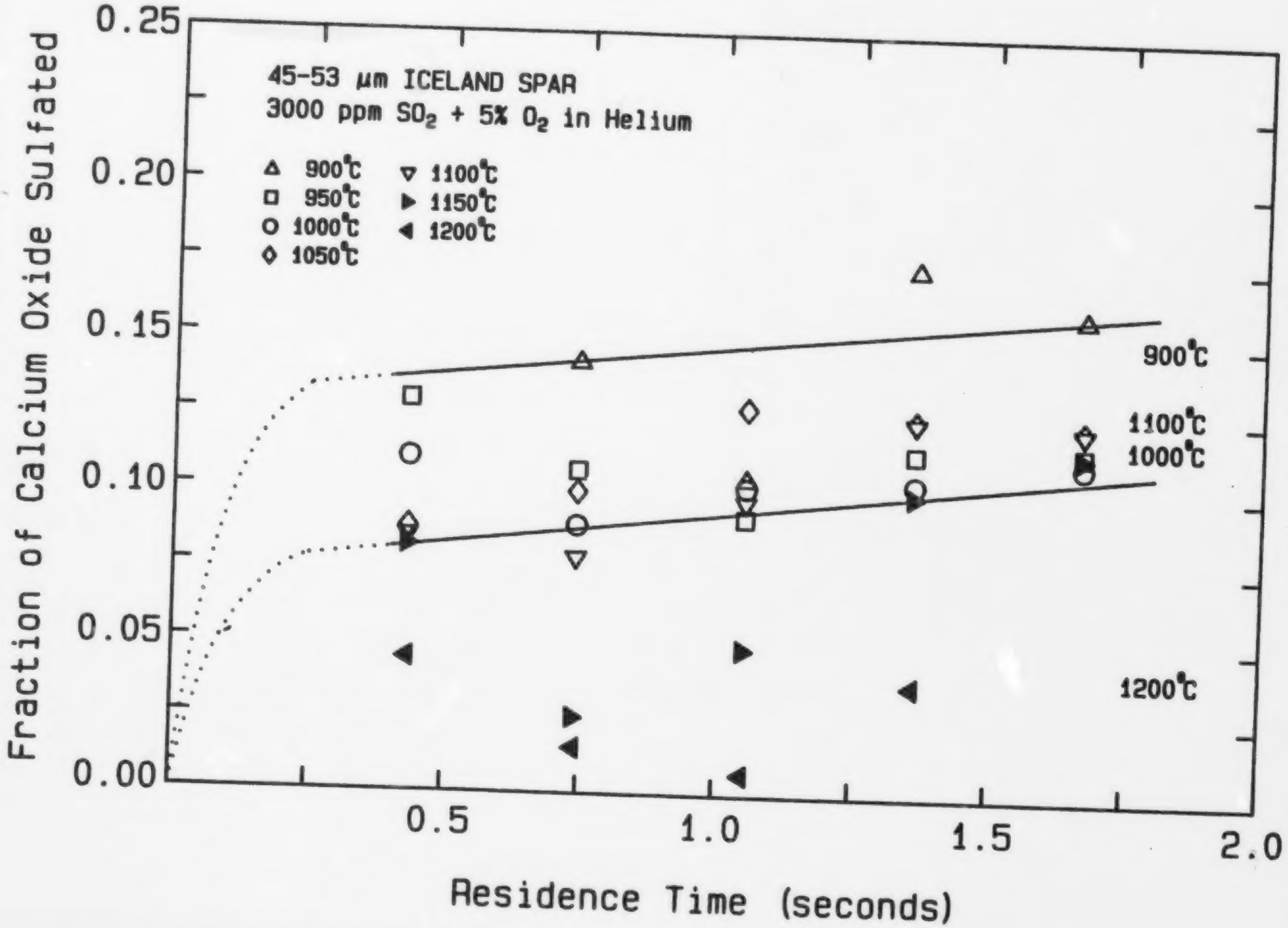

Figure 5-5. High temperature sulfation of limestone: fraction of CaO sulfated (Snow, 1985).

limited the calcination rate, which caused the appearance of a smoothly increasing sulfation extent.

Figure 5-6 compares data from the various facilities for hydrate injection. These data were all obtained for 2 micron sorbents at approximately 1000°C. The results indicate, within the apparent scatter, a certain degree of consistency between the facilities performance. The data also again suggest the existence of a rapid overall sulfation reaction at early times.

Figure 5-7 shows time resolved sulfation data for Longview hydrated lime. The data were generated in the University of Utah isothermal furnace (Newton, 1986) at approximately 1100°C and 2000 ppm SO_2. The results show that almost all of the sulfation reaction has occurred over the first 250 msec, and the second 250 msec results in almost no additional capture.

5.1.2 Particle Size

In Section 4.0 results were presented in which particle size was shown to influence reactivity. The sulfation models suggest that this is due to the improved accessibility of the particle interior via less pore diffusional resistance as particle size is decreased. Section 3.0 suggested that the reactivity of smaller particles is favored by the activation process. This is because the higher calcination rate that accompanies the activation of small particles results in a higher surface area during the earliest sulfation stage. Because of the difficulty in obtaining large amounts of sized materials in the quantities needed for furnace testing, only limited amounts of particle size-resolved data are available on combustion systems.

Figure 5-8 shows data obtained for various size cuts of limestone in the EER isothermal reactor. The material was aerodynamically classified Marblewhite 125 limestone. The results clearly indicate the preference for small particle sizes. Of great interest would be the performance of very fine (order 1 micron or less) size cuts under similar conditions. These

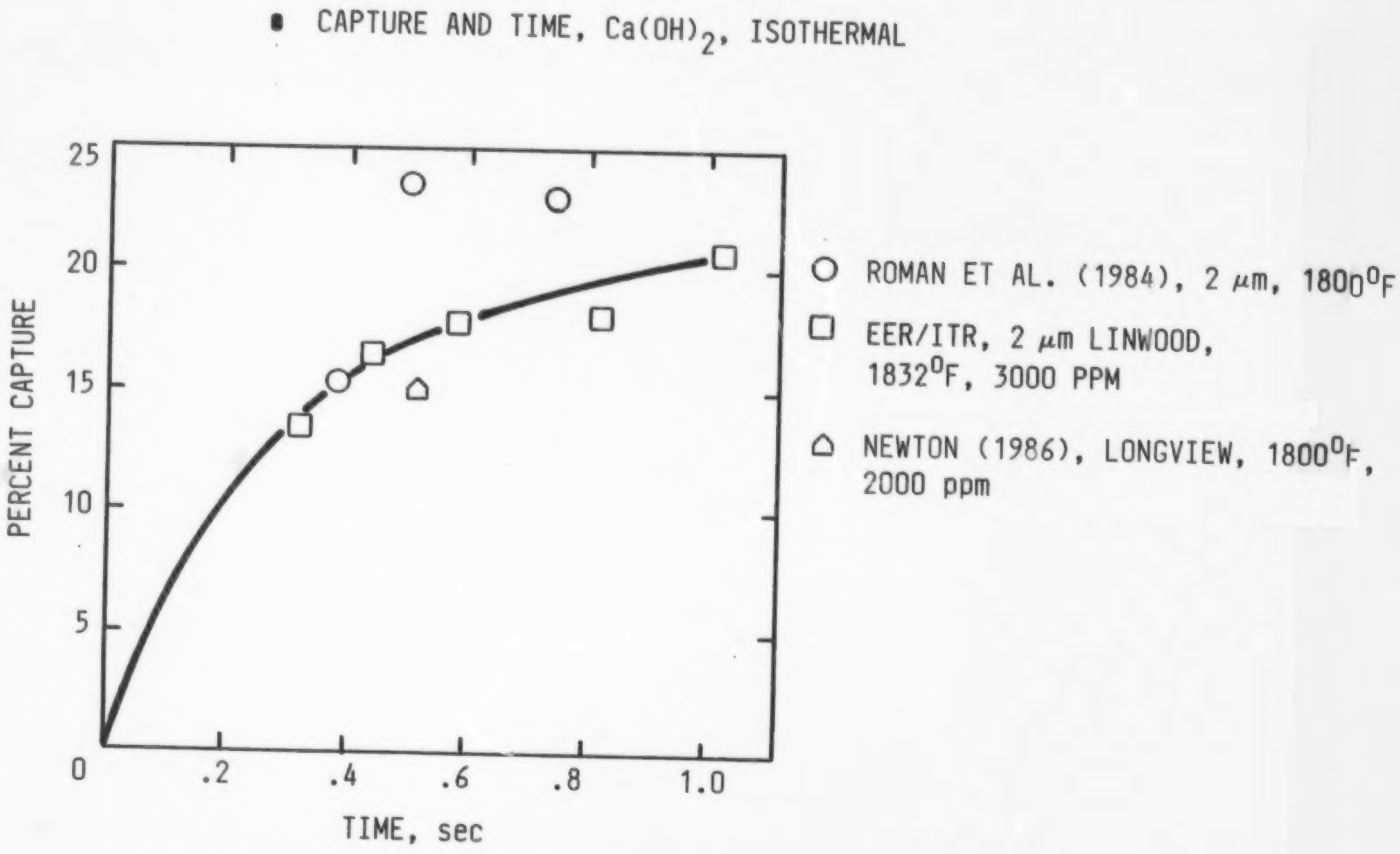

Figure 5-6. Comparison of facilities performance for calcium hydrates. (EER/ITR data generated under EPA Contract 68-02-4239).

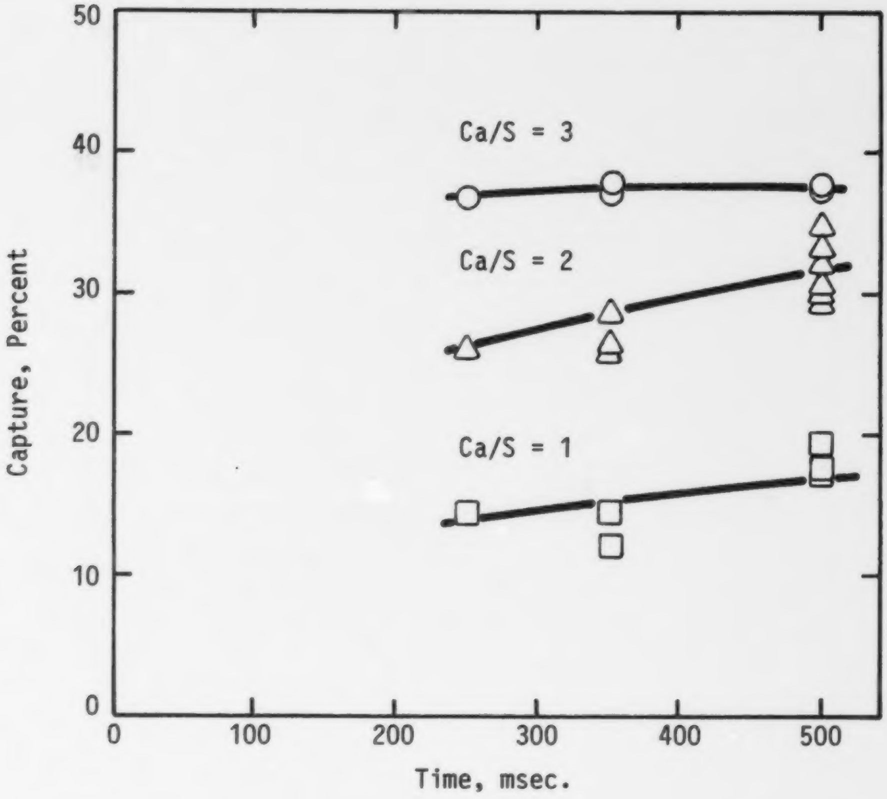

Figure 5-7. Time resolved sulfation data in the University of Utah isothermal reactor at 1100°C and 1950-2118 ppm SO_2 for Longview hydrate (Newton, 1986).

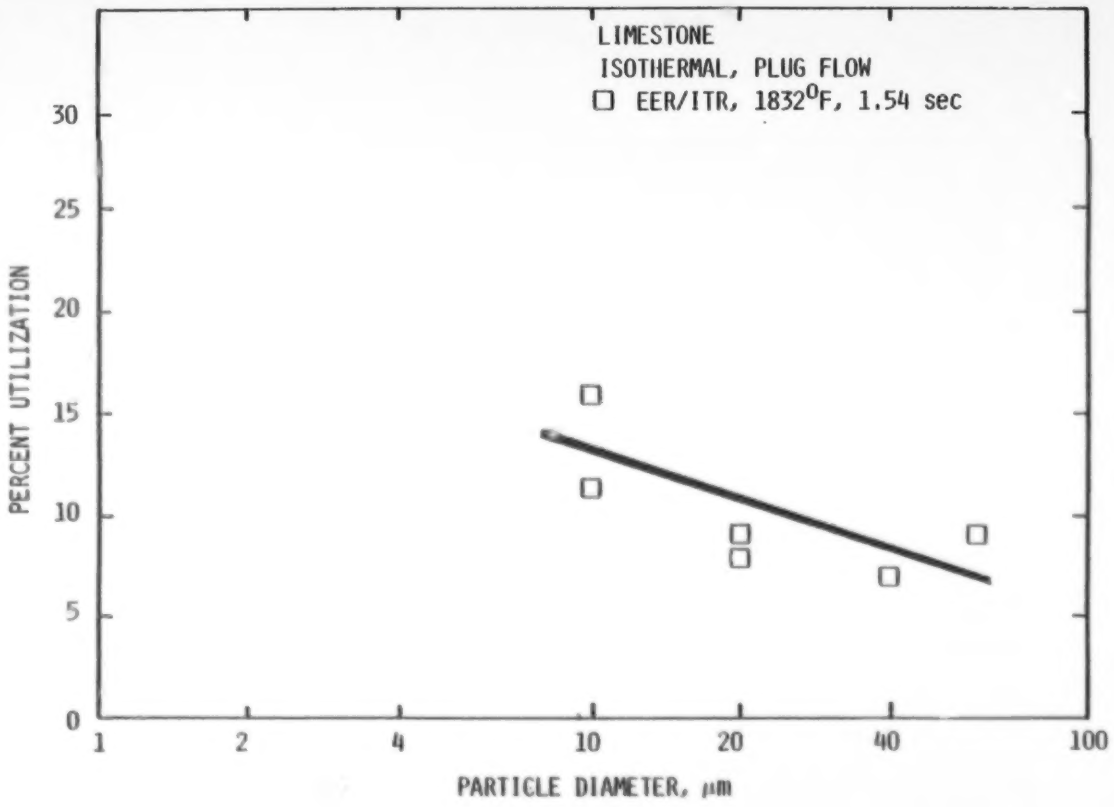

Figure 5-8. Dependence of sorbent utilization on carbonate particle size (data generated under EPA Contract 68-02-3995).

results would suggest if an effort is worthwhile to find an economical means of preparing large quantities of microfine carbonates.

Figure 5-9 shows similar data for hydrates generated at the IRFR (Bortz et al., 1986). Again, the smaller particle size cuts are favored. One key question involves the larger size cuts of hydrate. Extensive work in the characterization of hydrates suggests that fully hydrated materials consist of agglomerates of very small (order 1 micron) elementary hydrate particles. From these microscopic examinations it would appear that a 40-50 micron particle obtained from the air classification of a hydrate would be either (1) a collection dominated by large CaO particles that have resisted hydration, or (2) a collection of hydrate agglomerates. Thus, although the data suggest that finer hydrate are more reactive, a key question must involve what constitutes fineness in a hydrate.

Snow (1985) also examined the effect of limestone particle size on the extent of sulfation. Figure 5-10 reports data from the MIT isothermal furnace on sized Icelandic Spar for two residence times and two furnace temperatures. For these long times the calcination was stated to be essentially complete, so the plot need not consider the adjustment for unreacted carbonate. The results indicate a consistent improvement with decreasing particle size. However, truly significant increases in utilization occur only for the smallest particle sizes. This is because a factor of five reduction in size is needed to double conversion.

5.1.3 Injection Temperature

The influence of temperature on raw sorbent reactivity appears to arise due to several effects. Probably the most fundamental of these is the thermodynamic stability limit for calcium sulfate. Figure 5-11 shows data that were obtained in an effort to define the maximum temperature limit for isothermal sulfation. The data indicate that the observed sulfation touches zero at about 1300°C. In theory the sulfate should be unstable at any temperature above 1225°C. The appearance and survival of the sulfate of slightly higher temperature can be attributed to two factors:

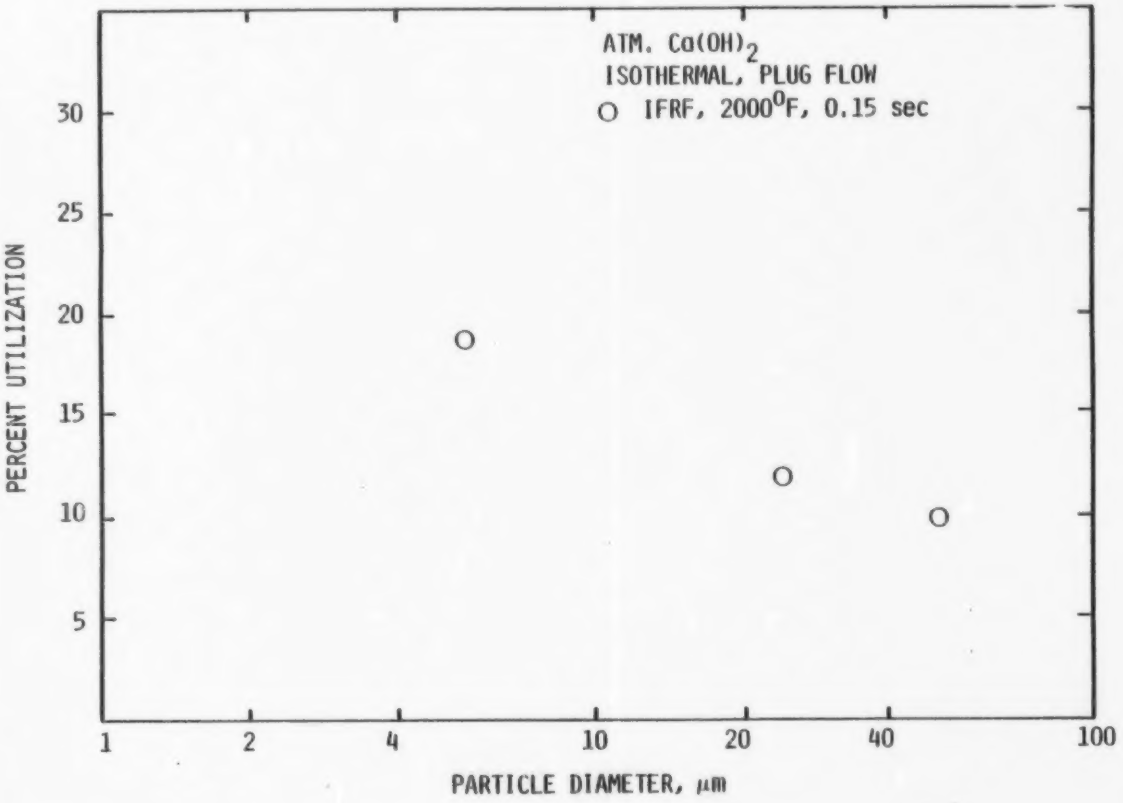

Figure 5-9. Dependence of sorbent utilization on hydrate particle size (Bortz et al., 1986).

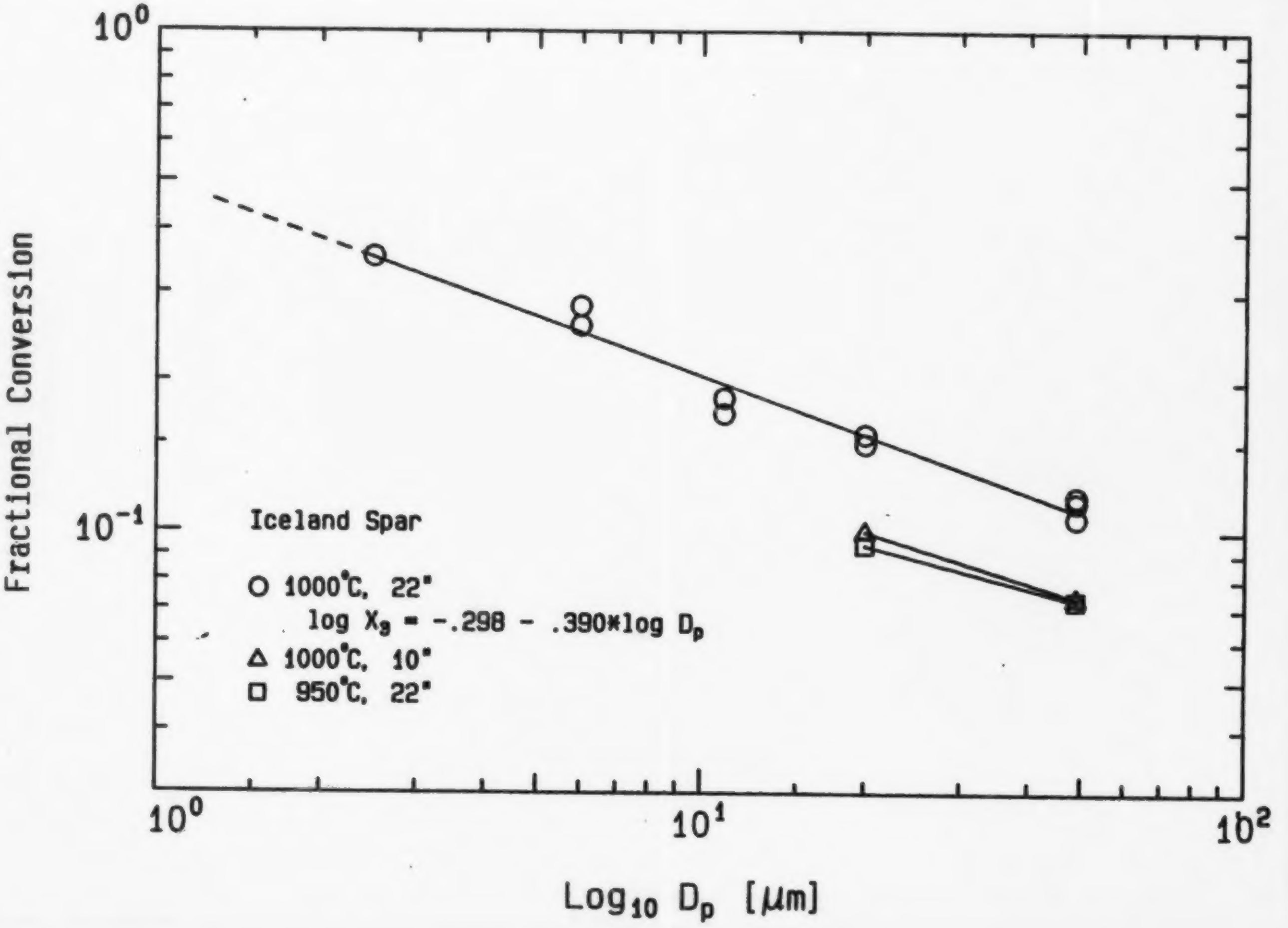

Figure 5-10. Effect of particle diameter on high temperature sulfation (Snow, 1985).

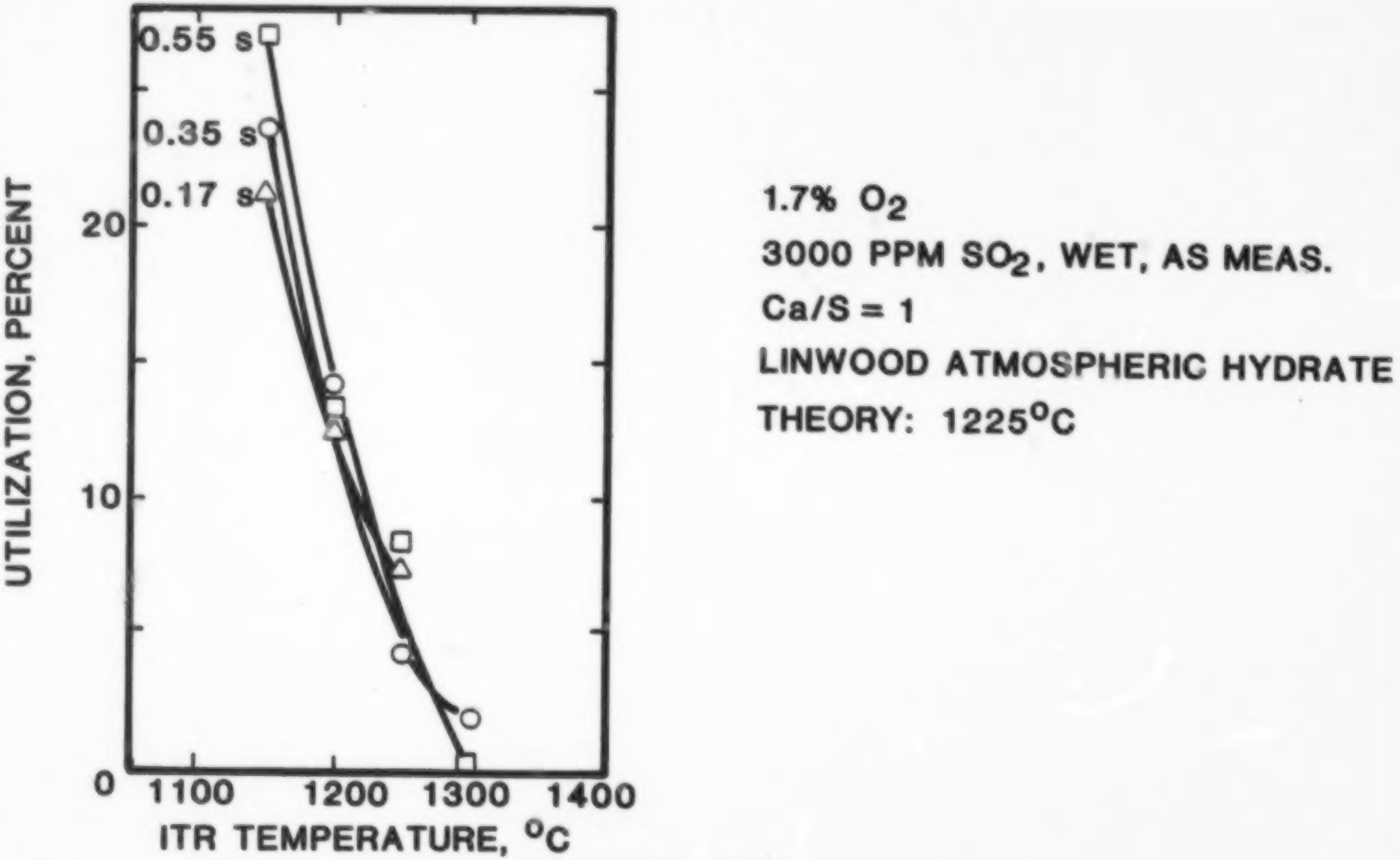

Figure 5-11. Isothermal hydrate conversions near the high temperature limit for sulfation in the EER isothermal reactor (data from Section 7.0).

1. Sorbent sulfation has been shown in previous figures to be sufficiently rapid that it can be expected to occur to a significant extent during sorbent heatup. Thus, the time required for the sorbent to heat to, and above 1225°C may be sufficient to obtain some sulfate formation.

2. In the limit of equilibrium, sulfate is unstable above 1225°C. However, its rate of decomposition is necessarily finite. Thus, the sulfate formed early in the reaction may not have had time to fully decompose.

In addition to the stability limit, other factors may enter into defining the optimum reaction temperature of raw stones under isothermal conditions. These include:

- Loss of reactive surface area due to sintering at higher temperatures.

- Loss of inherent reaction rate, or product layer diffusion rate, at lower temperatures.

- Loss of access to the interior of fine pores due to plugging with product at the surface due to a accelerated rate at higher temperature.

- Loss of reactive calcium due to incomplete carbonate decomposition at low temperatures.

Figure 5-12 presents data on the reactivity of carbonates vs. temperature. Two of these three data sets are consistent with a maximum in utilization around 1000°C, although a more exact maximum is difficult to define. Figure 5-13 shows similar data for hydrates. These data suggest that maximum reactivity occurs at a temperature near 1100°C.

- CAPTURE AND TEMPERATURE, ISOTHERMAL, RAW $CaCO_3$

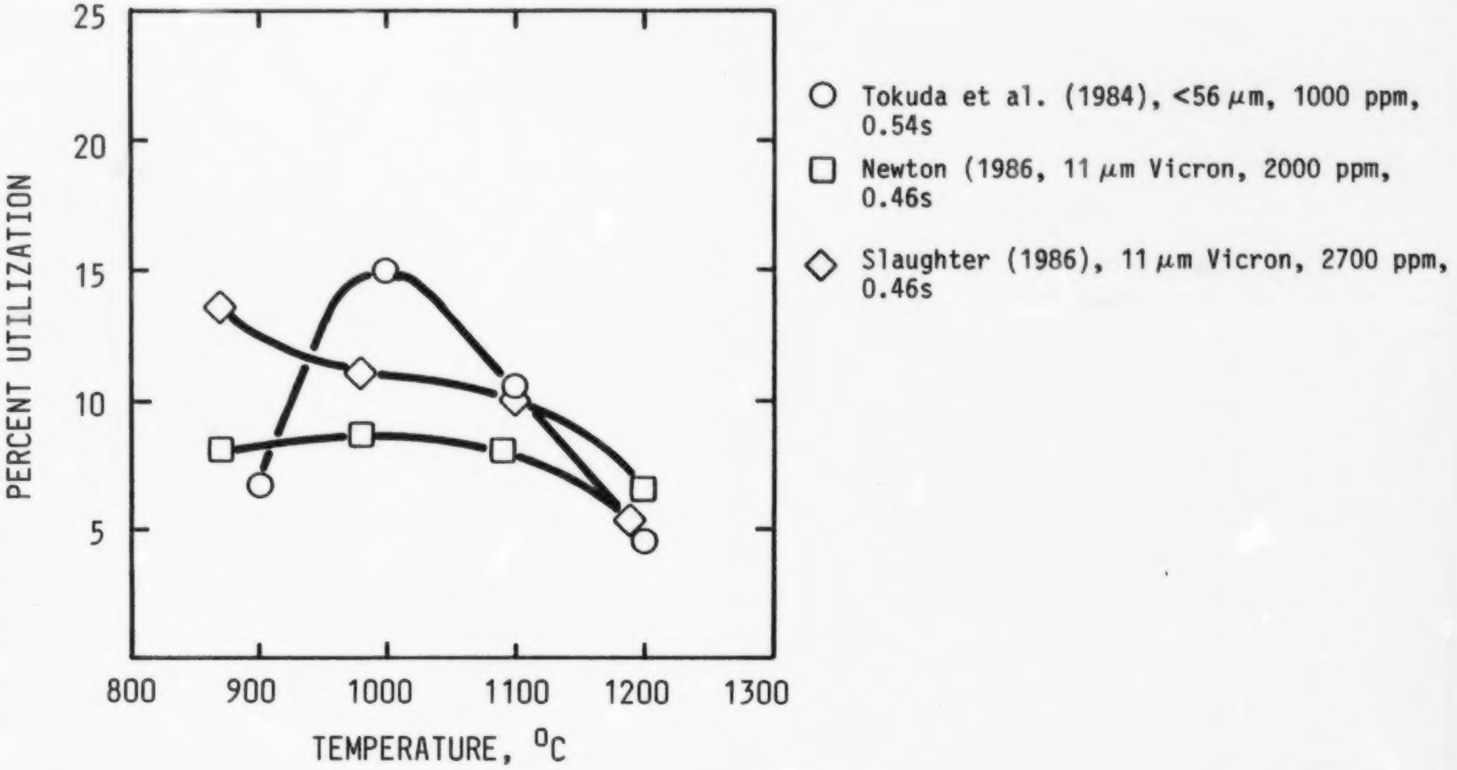

Figure 5-12. Influence of isothermal reactor temperature on the utilization of limestone sorbents.

- INJECTION TEMPERATURE: ATM. $Ca(OH)_2$; ISOTHERMAL
  τ = 0.16 - .58S

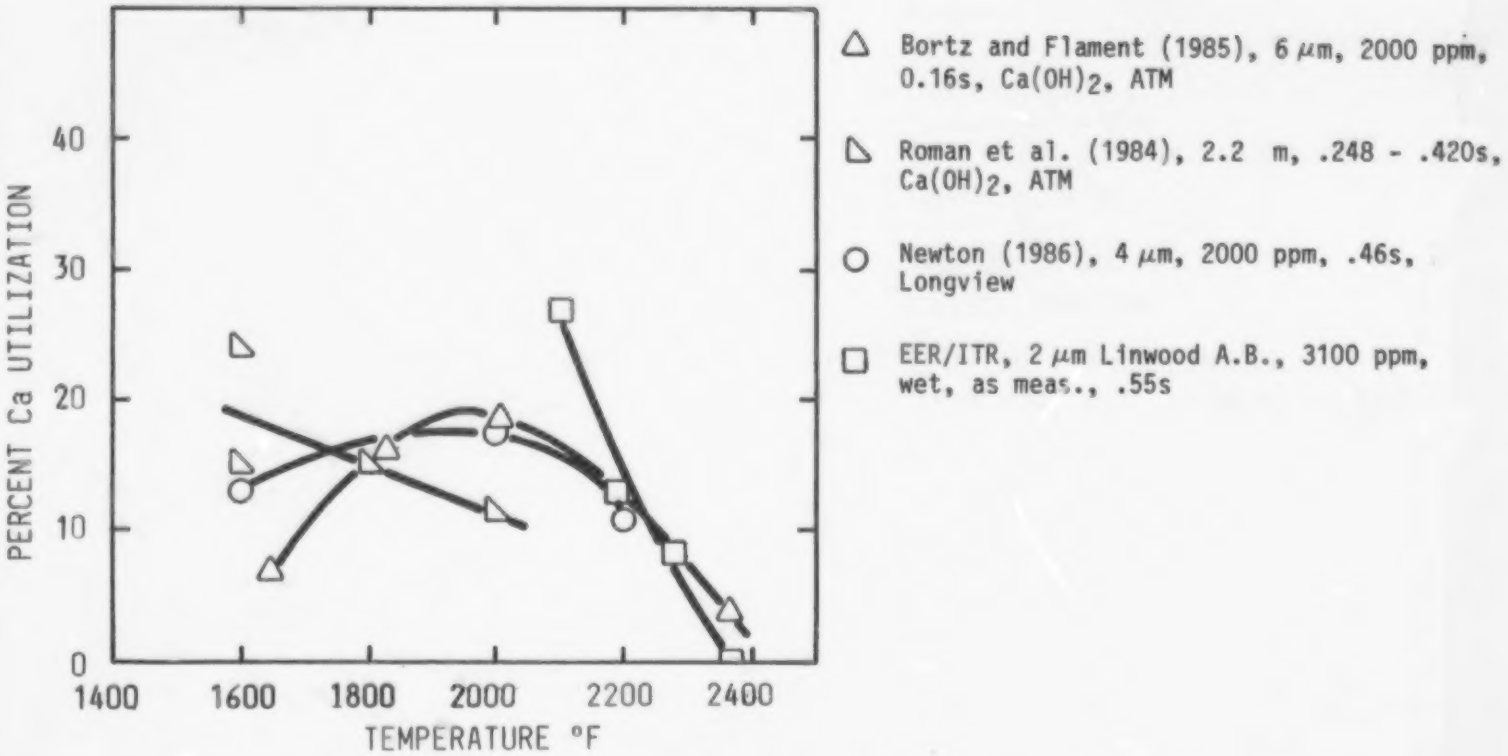

Figure 5-13. Influence of isothermal reactor temperature on the utilization of hydrated sorbents (EER data generated under EPA Contract 68-02-3633.

The MIT isothermal experiment (Snow, 1985) was used to develop a database on the temperature dependence of limestone sulfation. These data are presented for a series of limestones in Figure 5-14. The conversions are based on the available calcium, which ignores the fraction of the original material which has not calcined. To place these data on the same basis as Figure 5-12, the fraction of the original sorbent which had sulfated would have to be normalized to the total calcium present, not just that portion which had calcined. This has the effect of reducing the relative conversions on the low-temperature side of the figure and creating an overall utilization maximum in the 1000-1100°C range.

5.1.4 Closure

The wide variance in data from facility to facility points out several issues to be overcome in generalizing sorbent reactivity data. Firstly, the number of mechanisms that may enter into determining the temperature for optimum reactivity is large. Thus, comparison of any two experiments is likely to involve uncontrolled variation in parameters such as sorbent size, sorbent composition, heating rate to isothermal conditions, and sorbent crystal structure. This can lead to apparently divergent or inconsistent results. Secondly, the problem of obtaining reactivity data free from experimental artifacts in a flowing system is not easy to solve. Setting and holding the sorbent feeding rate and obtaining uniform dispersion in the free stream are both problems that are easy to ignore but which, if not critically evaluated, will influence data quality. Evaluating the extent of reaction is another point where problems can occur. The capture of sulfur by calcium hydrate has been shown to occur to significant extents within the time frame associated with sampling. Thus, the probe and sampling/analysis system must always be viewed as a separate reactor which must be designed to minimize the extent of additional sulfur pickup to known and acceptable bounds. The inability to do this evaluation in sufficient detail from reported data limits the confidence that can reasonably be placed in the results.

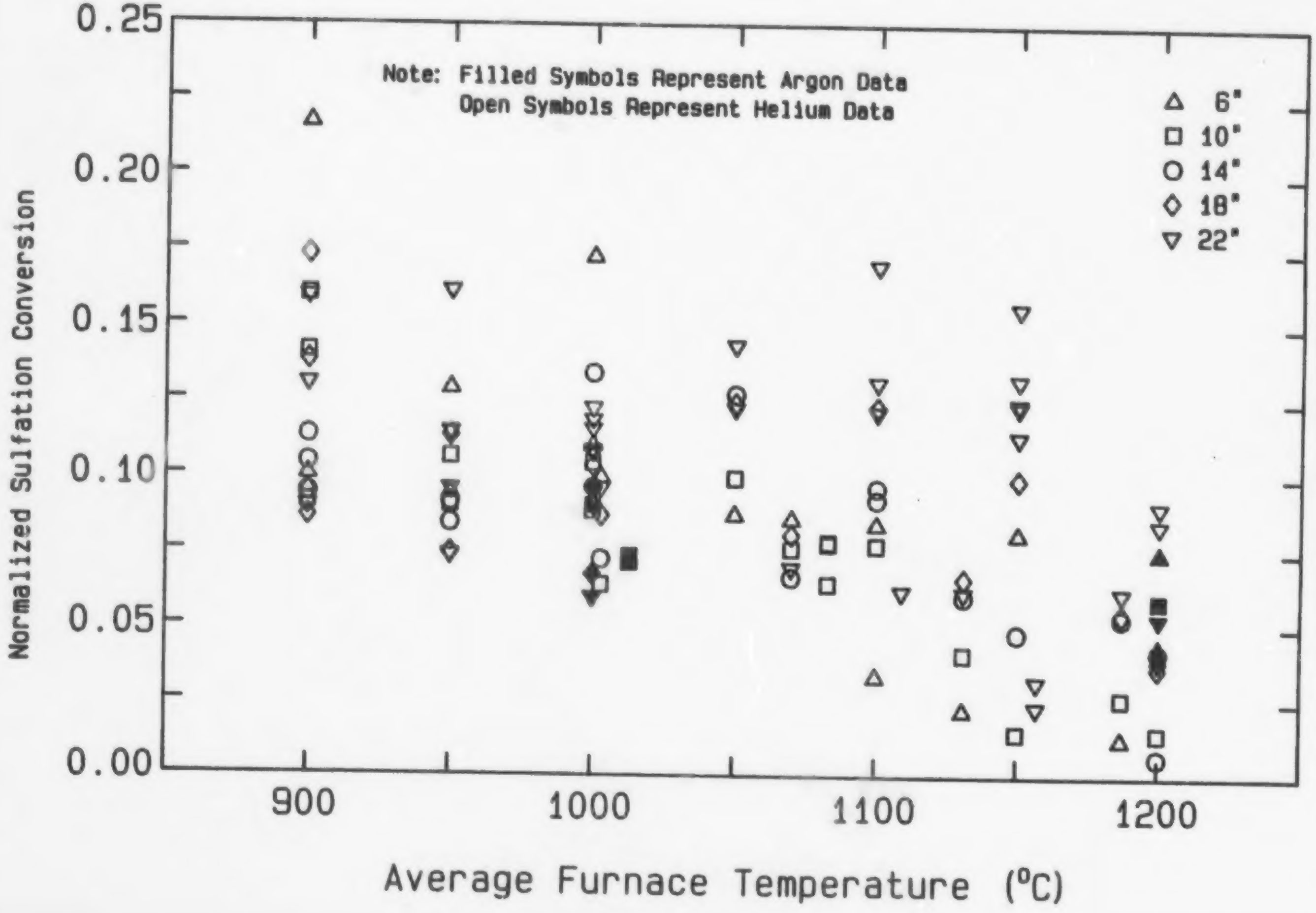

Figure 5-14. High temperature sulfation of limestone: effect of temperature (Argon highlighted) (Snow, 1985).

5.2 Modeling Approaches

Each of the sulfation models require information about the sorbent physical properties (particle size and grain or pore size distribution) at the beginning of the calculation. With precalcines these data can be obtained by direct measurement prior to sorbent injection. With raw carbonates and hydrates, no such data are generally available. Therefore, modeling of raw sorbents has relied on either (1) correlations of experimental results in particle size and surface area based on measurement of solid samples withdrawn from experiments with no SO_2 present or (2) mathematical modeling of the activation processes. Both approaches have merit. Initially the grain model was driven exclusively by an experimental surface area (mean grain size) correlation. More recently the new activation model has been used to set the initial conditions. Experimental pore size distribution data are still used to initialize the distributed pore size distribution model because the activation modeling has not progressed sufficiently to predict pore size distributions.

Two basic approaches to the mathematical modeling of simultaneous sorbent activation and sulfation are discussed in this section. The first involves a simple scheme that uses the activation model discussed in Section 3.0 to initialize the sorbent's surface area prior to sulfation. This initialization approach assumes that the particle does not begin sulfating until calcination is complete and that the particle is of uniform surface area. Predicted sulfur capture results using this approach are discussed below. The second modeling avenue involves allowing the sorbent particle to calcine in shells with sulfation immediately occurring in the newly created shell. The sulfation front progresses through the particle just behind the calcination front. The first approach will be referred to as the initialization model and the second as the progressive shell model.

5.2.1 Initialization Model

The initialization model uses the activation model discussed in Section 3.0 to estimate sorbent surface area upon completion of calcination. The estimated surface area is then used as input for the sulfation model. In the example given below, this approach is used to examine the effects of sorbent type on simultaneous sulfation and activation.

Consider hydrate and carbonate particles with diameters of 1 and 5 μm, respectively. If the particles are calcining at 2000°F under isothermal conditions, the activation model discussed in Section 3 predicts that the hydrate will develop a maximum surface area of 100 m^2/g in less than 1 msec while the carbonate will require 60 msec to develop a maximum of 54 m^2/g. The complete predicted surface area development history for both sorbents is shown in Figure 5-15. The predictions are based upon the assumption that the hydrate calcines 50 times faster than the carbonate. Relative calcination rates can be estimated from the data of Bortz and Flament (1984). Some of their data for 6 μm Ca(OH), and 6 m $CaCO_3$ at 900°C are shown in Figure 5-16. The data show a tremendous difference in the calcination rates of hydrates and carbonates. The tendency for CaO to rehydrate is evidenced in Figure 5-16 by the failure of the $Ca(OH)_2$ to completely calcine. The rehydration probably occurred in the sorbent sampling system.

The maximum surface areas shown in Figure 5-15 were used in conjunction with the sulfation model to obtain the predicted sulfur capture curves shown in Figure 5-17. The predictions are based on an isothermal temperature of 2000°F and a SO_2 concentration of 2000 ppm. The relative sulfur capture levels in Figure 5-17 are in rough agreement with experimental studies and show the usefulness of this simple model of simultaneous sulfation and calcination.

5.2.2 Progressive Shell Model

The progressive shell model of simultaneous sulfation and activation is an extension of the activation model described previously in Section 3.0. The model assumes that as each layer of raw sorbent is calcined, it becomes available for sulfation. The model can be developed at three levels of sophistication. The simplest version is appropriate for conditions where pre diffusional resistances to SO_2 and CO_2 are small. In this case, simplified

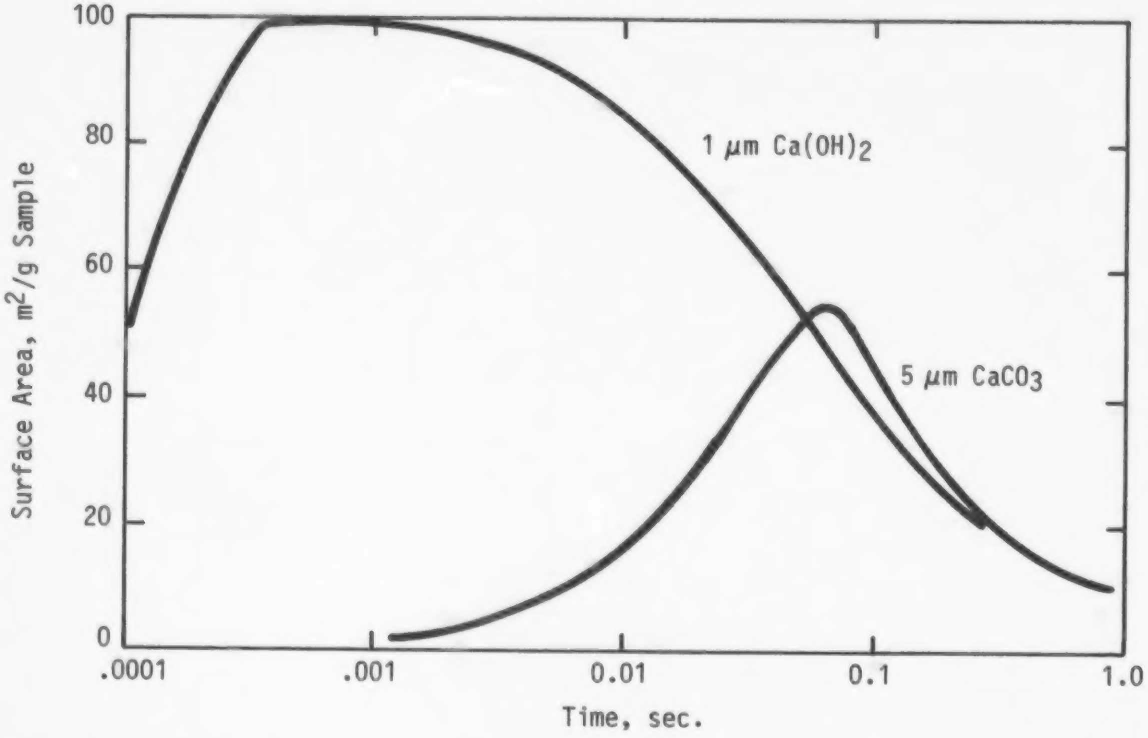

Figure 5-15. The predicted surface area development for 1 μm $Ca(OH)_2$ and 5 μm $CaCO_3$ at an isothermal temperature of 2000°F.

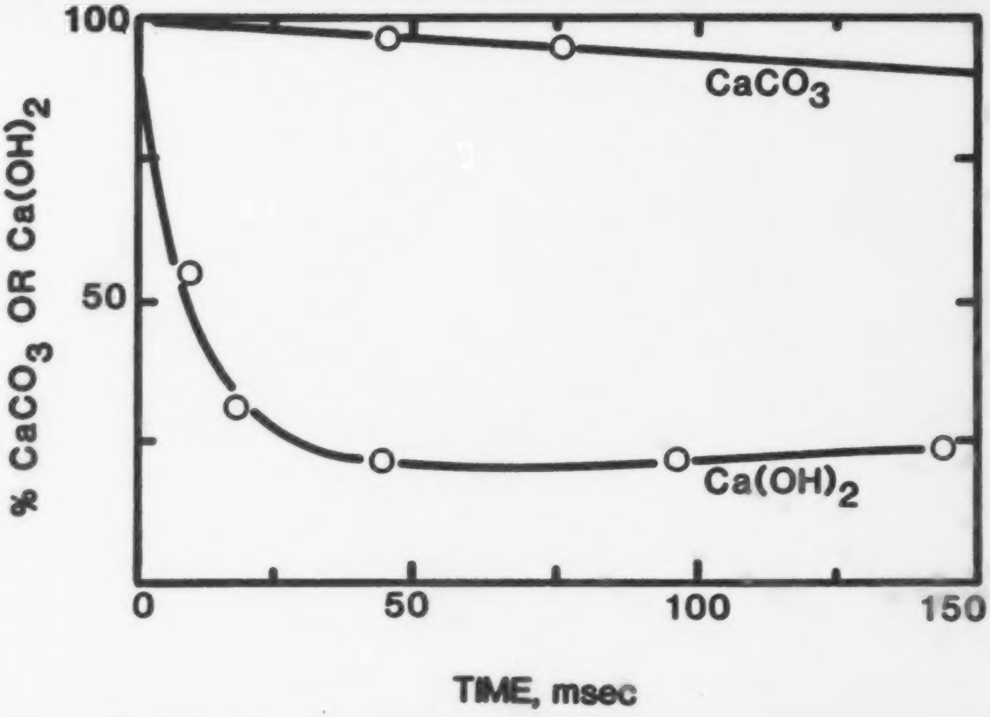

Figure 5-16. The data of Bortz and Flament (1985) showing the relative rates of calcination for 6 μm Ca(OH)$_2$ and CaCO$_3$ at 900°C. The materials were calcined in combustion gases.

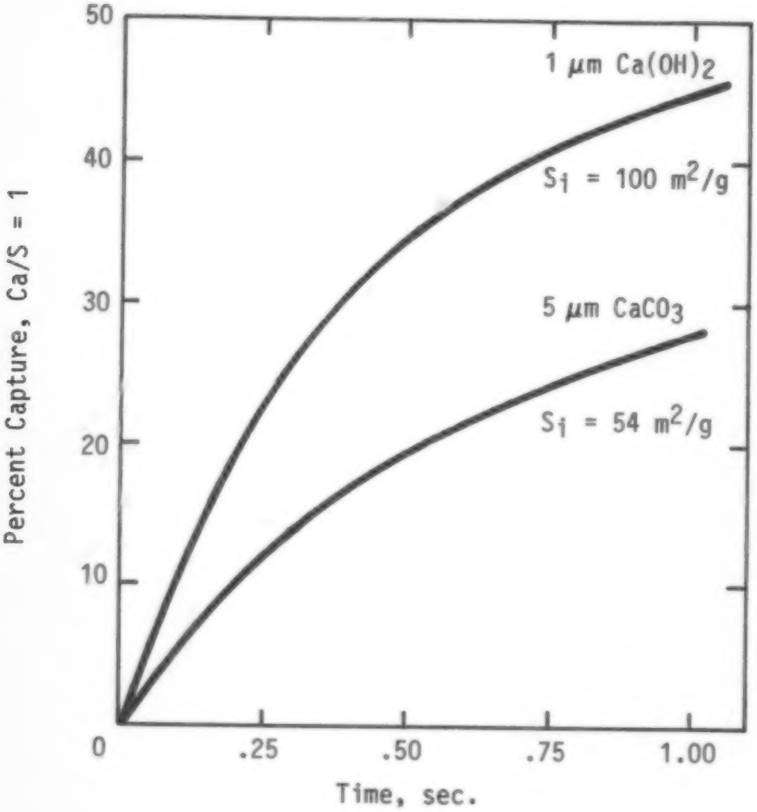

Figure 5-17. Predicted sulfur capture level based on initial surface areas estimated with the activation model. A constant temperature of 2000°F and a SO_2 concentration of 2000 ppm were assumed.

versions of the activation model and the sulfation model can be easily coupled because both models need only consider chemical resistances.

The next level of complexity assumes that pore diffusional resistances are important only for SO_2. If this is the case then the governing equations for diffusion in a spherical particle must be modified to account for the presence of the $CaCO_3$-CaO interface during calcination. The most general model assumes that diffusional resistances to both CO_2 and SO_2 are important. The general model would be a simple extension of the previous one.

Of the models discussed above, only the intialization approach has actually been tested and shown to produce results which agree qualitatively with data. The development of more sophisticated descriptions of the coupled activation - sulfation process might provide improved understanding and help direct experimental efforts. It is doubtful that the development of such models would improve the predictive capabilities of existing approaches. This is not due to any weakness in the models but rather to a lack of understanding of the fundamental physics and chemistry of the activation and sulfation processes. In particular, there are gaps in knowledge in the following areas:

- structure of flash calcined materials,
- mechanisms of surface area development and loss,
- the effect of heating rate on the properties of calcines,
- techniques for sampling flash-calcined sorbents which do not alter the sorbents physical properties
- sulfation kinetics at short times with flash-calcined sorbents.

Until these gaps in knowledge are addressed, it is doubtful that more sophisticated modeling approaches will result in improved predictive capabilities. It is also likely that even if such knowledge were available, its complexity would make necessary an empirical approach.

For these reasons the model of coupled activation and sulfation which is used below to analyze selected experimental results has the following characteristics:

- Calcination is instantaneous.
- The sulfation kinetics are based on the data of Borgwardt and Bruce (1986).
- The rate of surface area loss is based on the activation modeling results described in Chapter 3. This is empirical.
- The initial surface area is chosen so as to enable one to predict a selected set of sulfation results with the grain model.

This approach is applied in Section 5.3 and is more fully discussed in Chapter 9.

5.3 Analysis of Experimental Results

5.3.1 Time-Resolved Predictions

To illustrate the methodology described above, consider the ITR data shown in Figure 5-18. Two sets of capture data were obtained, one with Longview atmospheric hydrate at 2200°, and the other with Linwood pressure hydrate at 1800°F. The solid lines in Figure 5-18 are grain model predictions based on an assumed initial surface area of 40 m^2/g with no surface area loss due to sintering. The model obviously overestimates the effect of temperature. The rate of sulfation increases with increasing temperature. But according to the results of Chapter 3, the rate of surface area loss also increases in an Arrhenius fashion with increasing temperature. Hence, one possible explanation for the ITR results in Figure 5-14, and their apparent insensitivity to temperature, is that sulfation and sintering are occurring simultaneously.

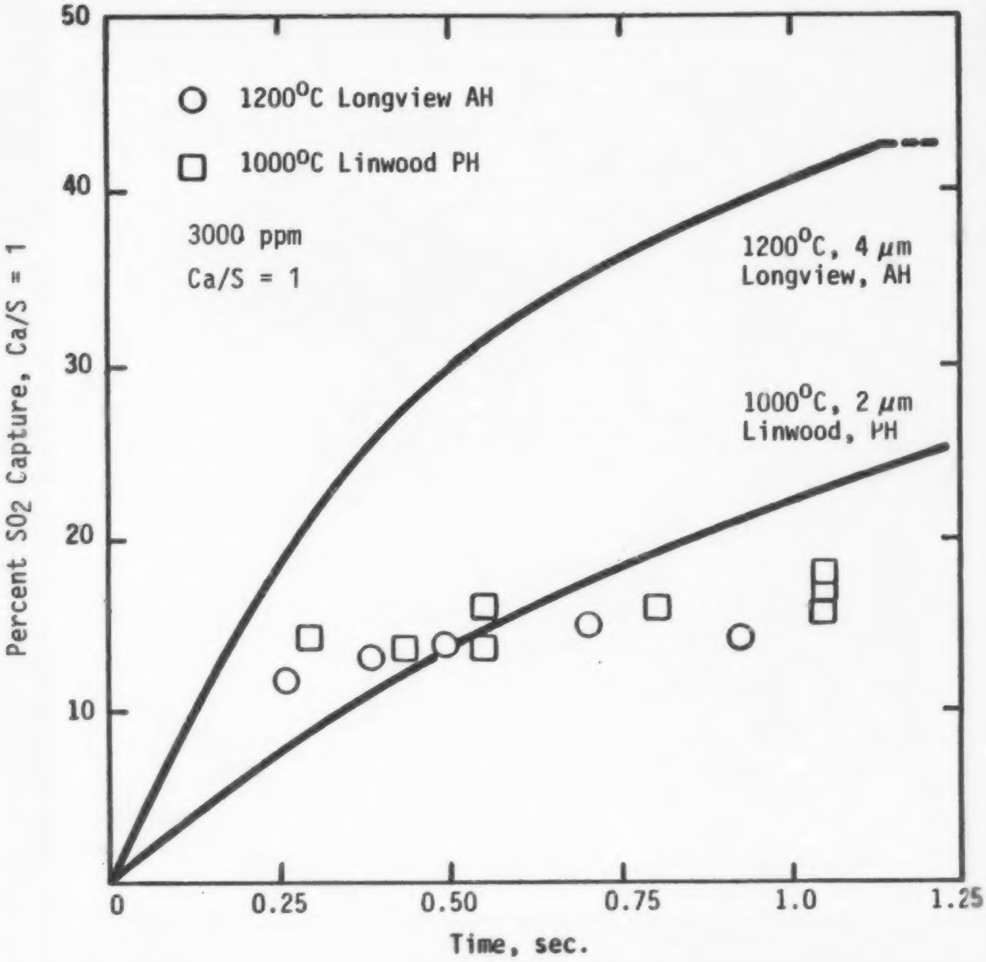

Figure 5-18. Grain model predictions of EER's ITR data. The predictions do not account for surface area loss due to sintering.

Introducing surface area loss due to grain growth into the sulfation model has the effect shown in Figure 5-19. Using an initial surface area of 80 m^2/g and an asymptotic value of 5 m^2/g gives a rate of sintering which compensates for the increased rate of sulfation at 1200°C. An initial surface area of 80 m^2/g was chosen based on bench-scale data obtained in EER's Controlled Temperature Tower (CTT) as described in Chapter 9. Allowing for simultaneous sulfation and surface area loss helps explain the sulfur capture data of Figure 5-19 with its apparent insensitivity to temperature.

The distributed pore model can also be successfully used to predict raw sorbent behavior in isothermal reactors if pore size distribution measurements are available for precalcines derived from the same sorbents. Figure 5-20 shows pore model predictions (made using the pore size distribution from the Longview precalcine) compared to time-resolved sulfation measurements for Longview hydrate in the University of Utah isothermal furnace. (No parameters were adjusted to improve the agreement between the data and the predictions). As with the precalcine results in Chapter 4.0, the marked decrease in sulfation rate beyond 200 ms is due to plugging of small pores.

5.3.2 Influence of Particle Heating Rate

Near the end of this program, new data were obtained in the EER-ITR furnace fitted with a Venturi precombustor which suggested that particle heating rate can be extremely important in determining the overall extent of sulfation. At the present time neither the grain nor the pore models have the ability to explicitly predict the influences of heating rate (or even peak particle temperature) because the necessary solids characterization data are still missing. The models can, however, be used to evaluate potential impacts. Figure 5-21 shows percent SO_2 capture plotted as a function of time for the Linwood atmospheric hydrate. These data correspond directly with the hydrate data shown in Figure 5-18 (obtained without the Venturi precombustor). Note, however, that the capture levels measured with the Venturi in place (Figure 5-21) are almost double those measured and successfully predicted under normal injection conditions (Figure 5-18).

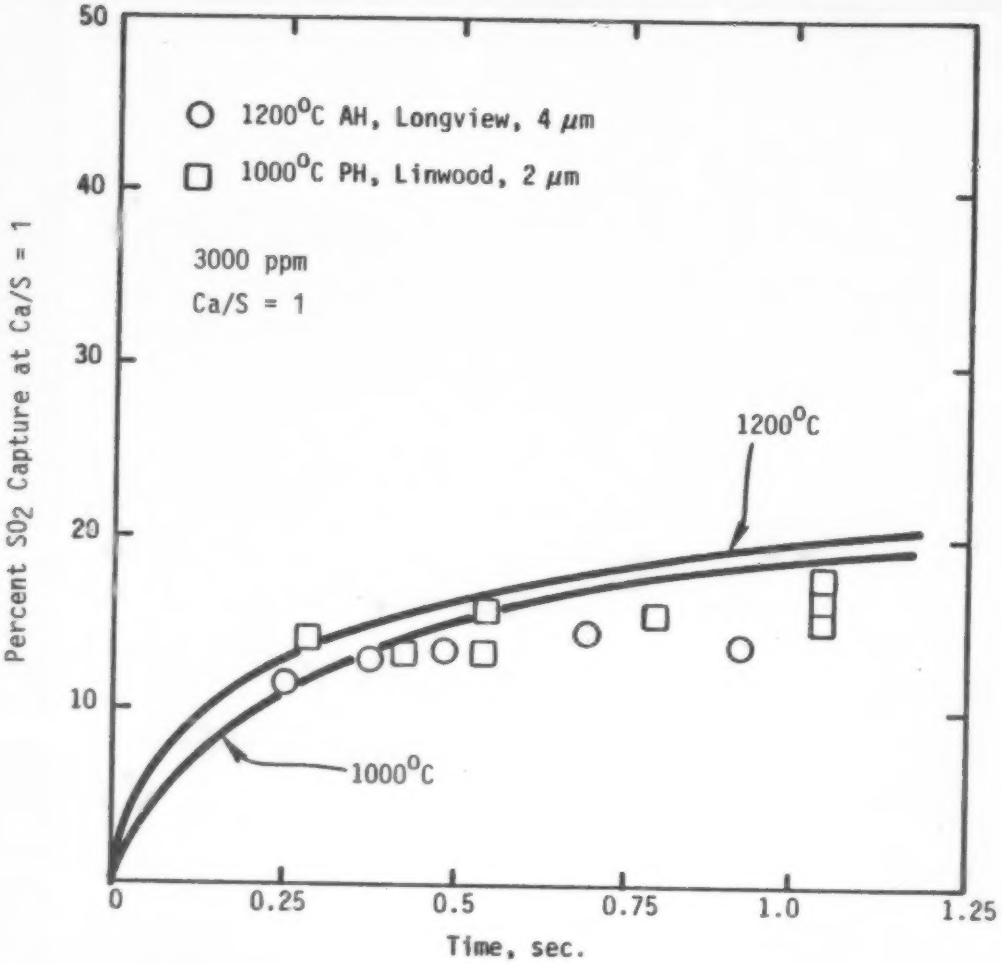

Figure 5-19. Grain model predictions of EER's ITR data. The predictions include the loss of sorbent surface area due to sintering.

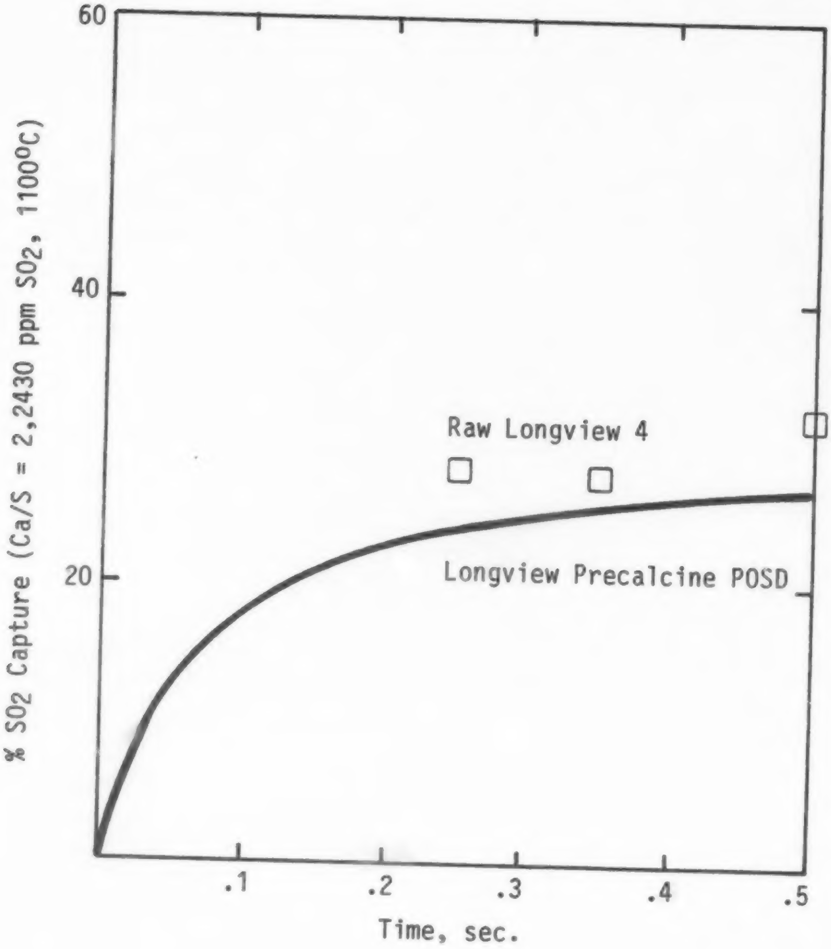

Figure 5-20. Pore model predictions compared to Longview hydrate data; Utah isothermal data.

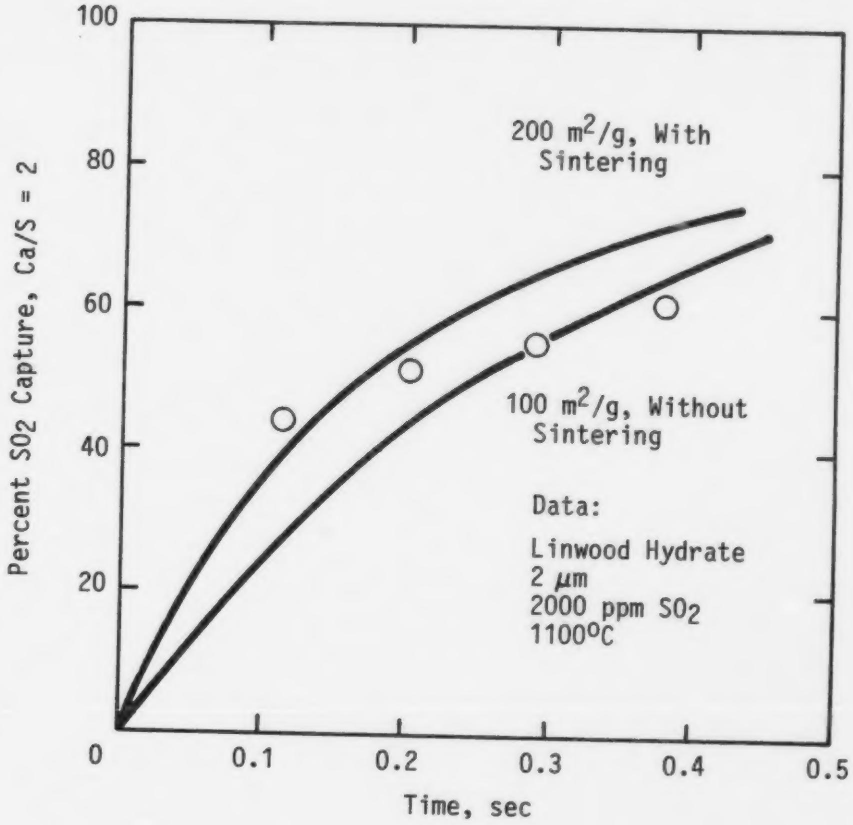

Figure 5-21. Grain model predictions showing the unreasonably high surface areas required to fit EER's ITR data. A uniform grain size was assumed.

Further, the Venturi capture levels are so high that the grain model is incapable of predicting these results except at surface areas which are physically unreasonable. As discussed in Chapter 3, the maximum B.E.T. surface areas obtained from the vacuum calcination of $Ca(OH)_2$ are roughly 130 m^2/g. The initial surface area of 200 m^2/g which is required to fit the data of Figure 5-21 is so high that one is led to conclude that either major particle fragmentation is occurring and producing a profound change in the inherent grain and particle sizes or the intrinsic sulfation kinetics for CaO as determined from the data of Borgwardt and Bruce (1986) are too slow. The latter is not unexpected because the ITR experiment involves flash-calcined sorbents while the Borgwardt differential reactor studies utilized precalcined and sintered CaO. In the differential reactor system of Borgwardt the particles are slowly brought to temperature before reaction begins. In a combustion system, thermal shock may serve to fragment or fracture the sorbent, even if it is already calcined. This is an activation process since it results in increased sorbent surface area.

Figure 5-22 shows distributed pore model comparisons against the same Linwood hydrate data with and without the Venturi precombustor. The normal results can be reasonably approximated with predictions based on pore size distribution data from another calcined hydrate (since actual pore size distribution data were not available for this sorbent). The extremely high capture levels can also be approximated if we assume the development of a large crack network which increases the mean pore size. Simple fragmentation of the particles (without a change in the resulting pore size distribution) does not allow prediction of the high capture levels.

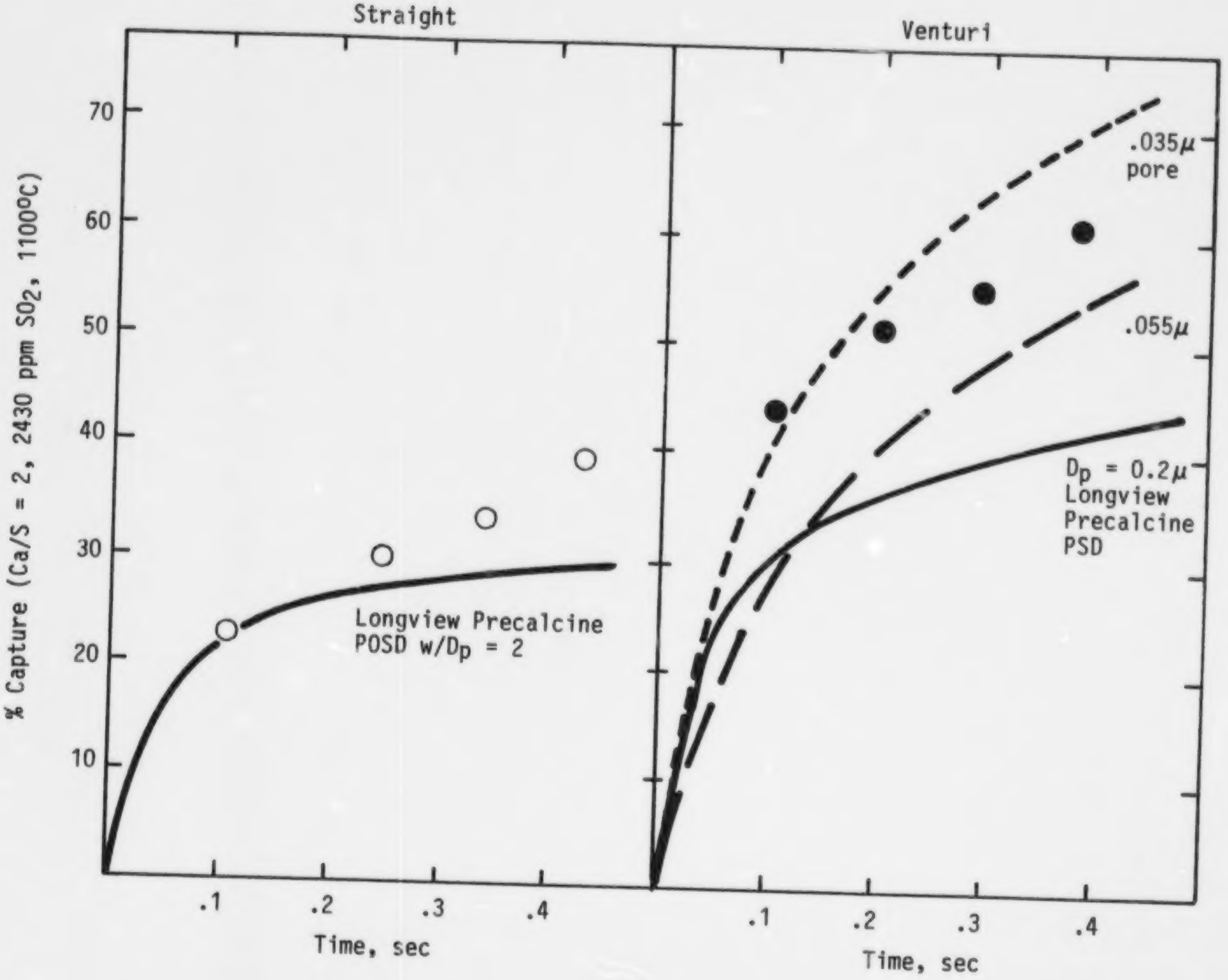

Figure 5-22. Comparison of ITR sulfation data with pore model predictions with and without rapid heating.

EPA. 4808--6

[illegible]

6.0 PROCESS PARAMETER STUDIES: A COMPILATION OF BENCH SCALE RESULTS

The process parameters selected for discussion in this section include sorbent thermal history, sorbent particle size and type, and SO_2 concentration. The parameters which characterize sorbent thermal history include injection temperature, quench rate (i.e., the rate of temperature decrease in the reaction zone), and time. Another parameter affecting the sulfation process is sorbent type. The effect of sorbent type is discussed throughout this section as part of the coverage of the other parameters. However, a study of sorbent effects is complicated by the particle size differences that typically exist between classes of sorbents: $Ca(OH)_2$ particles are generally less than 5 μm in diameter while $CaCO_3$ particles range in size from 10 to 50 μm or more. For this reason, the effect of sorbent type is best studied in conjunction with particle size effects so that comparisons can be made on an equal size basis.

The results presented here were obtained on bench scale reactors at several different research centers. The coal- or natural gas-fired reactors have thermal inputs ranging from 1×10^5 to 6×10^6 Btu/hr. Most of the reactors are fired at 1×10^6 Btu/hr or less and have well characterized temperature profiles.

6.1 Thermal History

The parameters which characterize the sorbent thermal history include injection temperature and quench rate. The results discussed here are plotted with percent SO_2 capture at Ca/S = 2 on the ordinate and injection temperature, quench rate, or time on the abscissa. The inclusion of time as a separate parameter allows the data to be viewed from a different perspective. The results are presented in the order given above.

Before discussing the effects of injection temperature it is important to clearly understand what is meant by this term. Confusion arises because the air used to convey the sorbent into the reactors is typically at room temperature. The amount of conveying air used at the bench scale is generally from 10 to 15 percent of the total air added. A simple energy balance reveals that using such large amounts of conveying air can significantly reduce the reactor gas temperature. Table 6-1 summarizes energy balance calculations based on an initial reactor gas temperature of 2250°F and a conveying air temperature of 80°F. Additional cooling of the gas can be expected from the endothermic decomposition of the sorbent, but this factor was not considered in the energy balance. Two ways of defining injection temperature are possible. The first involves measuring the gas temperature at the injection point in the absence of conveying air and sorbent. The second involves measurement in the presence of conveying air and sorbent. Data obtained as part of this program at EER on the Controlled Temperature Tower (CTT) and the Boiler Simulator Furnace (BSF) are specified in terms of the former definition.

TABLE 6-1. THE EFFECT OF CONVEYING AIR ON REACTANT GAS TEMPERATURE

Initial T, °F	Fraction Added, 80°F	Mixed T, °F
2250	.05	2140
2250	.10	2030
2250	.15	1925

The effect of injection temperature on SO_2 capture for hydrated limes is shown in Figure 6-1 and the plotting symbols are explained in Table 6-2. Observed capture levels range from 25 to 65 percent and the optimum injection temperature appears to be about 2050°F. An absolutely critical point in resolving the optimum injection temperature from the various experiments is evaluating the peak temperature experienced by the sorbent. For example, in some experiments the maximum utilization was obtained at 2300°F, where the temperature was measured in the absence of the sorbent flow. The peak temperature experienced by the sorbent would actually be closer to that obtained by mixing the furnace gas with the sorbent and its carrier gas. In other words, the furnace gas heats the sorbent carrier, and the carrier cools the furnace gas to some mass mean average. The mean temperature most closely represents the peak temperature experienced by the sorbent. All of the

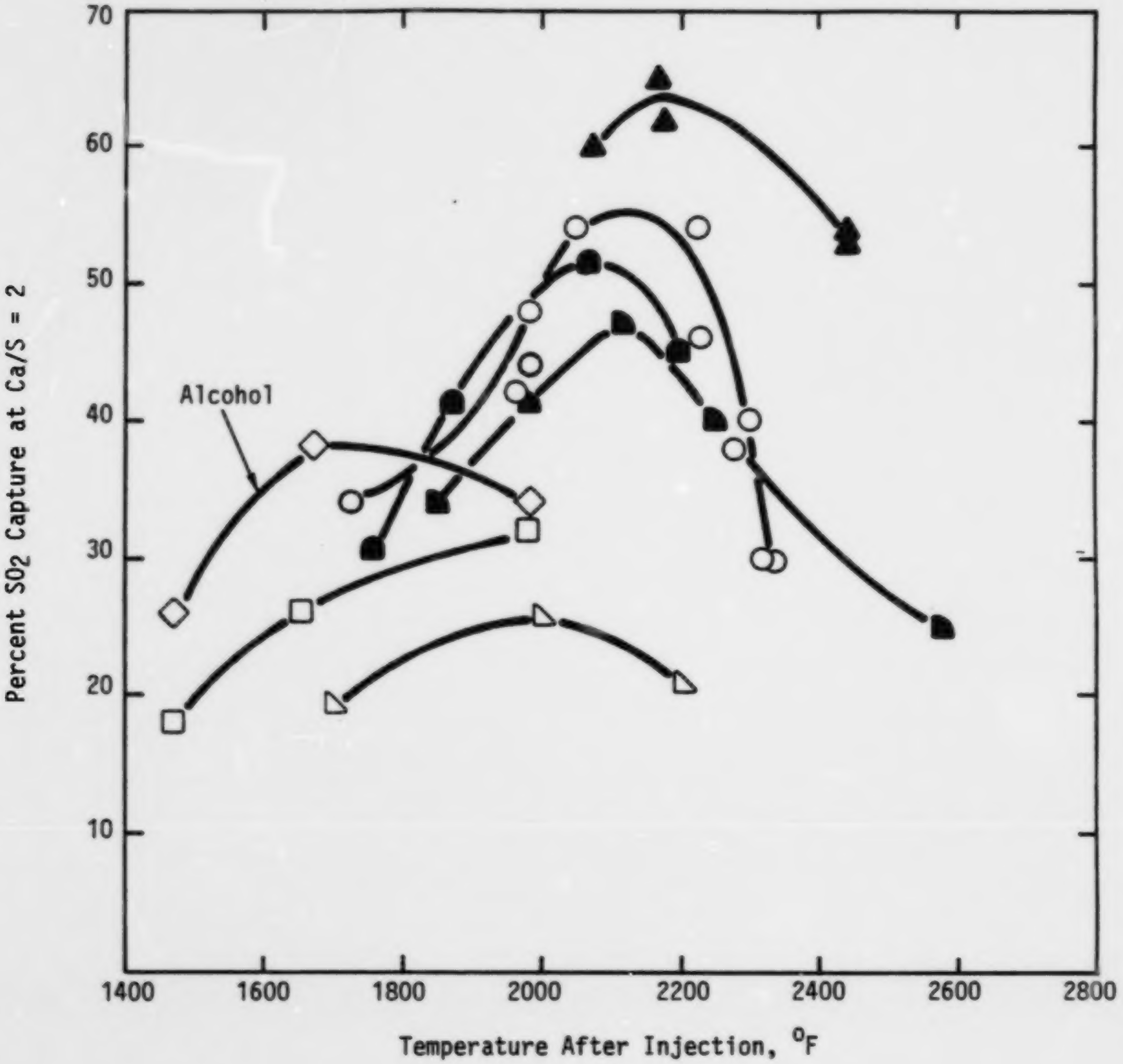

Figure 6-1. The effect of injection temperature on SO_2 capture at Ca/S = 2 for hydrated limes. See Table 6-2 for an explanation of the plotting symbols.

TABLE 6-2. SYMBOL KEY FOR FIGURE 6-1

1. Teixeira, et al. (1986) 1×10^5 Btu/hr, gas fired, -450°F/s, 2500 ppm SO_2, 0.35 s, pressure hydrated dolomitic lime.

2. Muzio, et al. (1986) 1×10^5 Btu/hr, gas fired, -450°F/s, 2500 ppm SO_2, 0.35 s, Colton atmospheric hydrate, 5 μm.

3. Muzio, et al. (1986), atmospheric, alcohol-water hydrate, 2 μm.

4. Beittel, et al. (1986), 1×10^6 Btu/hr, Hallmark coal, -360°F/s, 2200-3200 ppm SO_2, Longview atmospheric hydrate, 2 μm.

5. Newton (1986), 2.2×10^5 Btu/hr, gas fired, -870°F/s, 2000 ppm SO_2, 0.5 s, Linwood atmospheric hydrates, 2 μm.

6. EER-CTT, 9×10^4 Btu/hr, gas fired, -1000°F/s, 2000 ppm SO_2, Linwood atmospheric hydrate, 2 μm (data generated under EPA Contract 68-02-3633).

7. EER-BSF, 1×10^6 Btu/hr, gas fired, -250°F/s, 1800 ppm SO_2, Linwood atmospheric hydrate, 2 μm (data generated under EPA Contract 68-02-3633).

temperature data of Figure 6-1 were adjusted on a "mixed temperature after injection" basis. This allows direct comparison between experiments for which dissimilar sorbent carrier flows were used. Plotted on this basis, the maximum utilization occurs at 2050°F. The only sorbent for which shows a markedly different optimum is an alcohol hydrate; these sorbents are thought to have an additional advantage at lower temperatures due to their high surface area, but they loose this advantage at higher temperatures due to accelerated sintering.

This conclusion is corroborated by the data shown in Figure 6-2 for carbonates. In particular, the carefully controlled experiments of Coutant, et al. (1971) show an optimum injection temperature of about 2000°F. The carbonates appear to be less sensitive to injection temperature than the hydrates. This may be attributable to differences in the rate of calcination for hydrates and carbonates.

The effect of quench rate on SO_2 capture is shown in Figure 6-3 for both hydrates and carbonates. Most of the data indicate that capture depends weakly on the rate of temperature decrease. The results obtained on the CTT with Linwood atmospheric hydrate shown capture decreasing from 60 percent to 43 percent as the quench rate is increased from -350 to -900°F/s. The data of Beittel, et al. (1986) shows an optimum quench rate of roughly -400°F/s. Coutant, et al. (1971) observed no effect of quench rate on capture. Elucidation of the impact that quench rate has on sorbent utilization will require additional experiments.

The effect of residence time on SO_2 capture is illustrated in Figure 6-4 for hydrates and carbonates. These data were obtained at quench rates ranging from -250 to -1200°F/s and for injection temperatures ranging from 2250°F to 2300°F. For a quench rate of -1200°F/s the length of time available for reaction is only about 0.5 sec. The data of Farzan, et al. (1986) show that in 0.5 sec, capture levels of 43 percent are obtained with a dolomitic hydrate at a quench rate of -1200°F/s. Time resolved data obtained on the BSF and the CTT for Linwood atmospheric hydrate show ultimate capture levels of 40 and 65 percent respectively, at Ca/S = 2. The two systems have

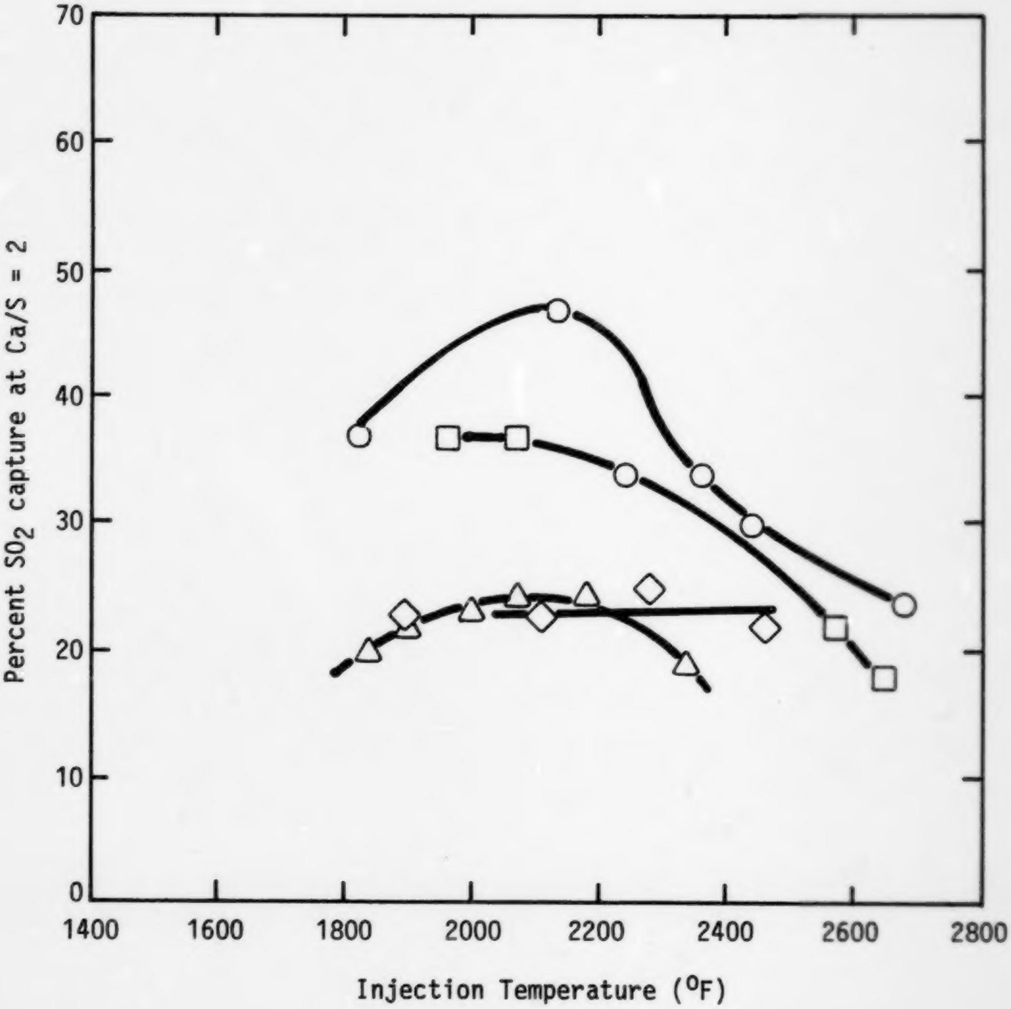

Figure 6-2. The effect of injection temperature on SO_2 capture at Ca/S = 2 for calcium carbonates. See Table 6-3 for an explanation of the plotting symbols.

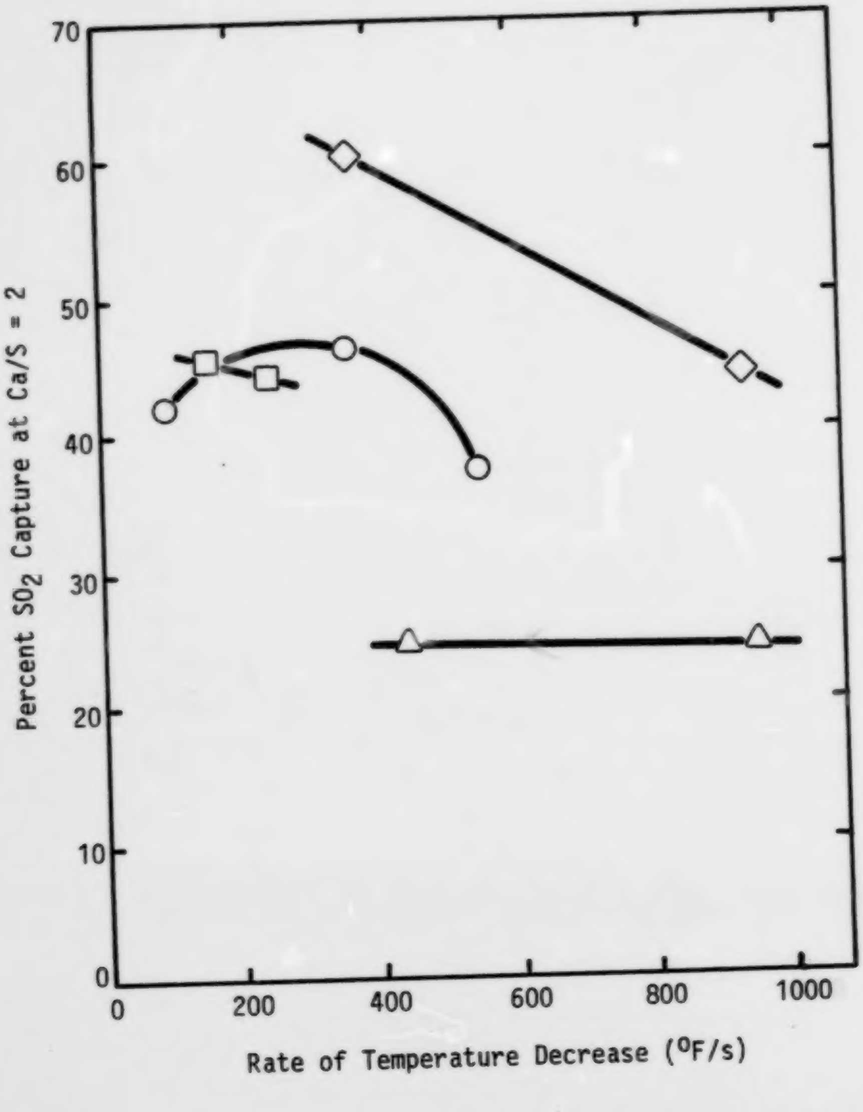

Figure 6-3. The effect of quench rate on SO_2 capture at Ca/S = 2 for hydrates and carbonates. See Table 6-4 for an explanation of the plotting symbols.

TABLE 6-3. SYMBOL KEY FOR FIGURE 6-2

1. Beittel, et al. (1986), 1 x 10^6 Btu/hr, Hallmark, coal, -30oF/s, 2200-3200 ppm SO_2, Mariana limestone, 7 μm.

2. Beittel, et al. (1986), as in (1) except -550°F/s.

3. EER-BSF, 1 x 10^6 Btu/hr, natural gas, -250°F/s, 1800 ppm SO_2, Vicron limestone, 11 μm (data generated under EPA Contract 68-02-3633).

4. Coutant, et al. (1971), 2 x 10^5 Btu/hr, natural gas, -440°F/s, 3000 ppm SO_2, limestone, 50 μm.

TABLE 6-4. SYMBOL KEY FOR FIGURE 6-3.

1. Beittel, et al. (1986), 1 x 10^6 Btu/hr, Hallmark coal, -100 to -550°F/s, 2200-3200 ppm SO_2, Mariana limestone, 6 μm, T_{inj} = 2100°F.

2. EER-BSF, 5 x 10^5 to 1 x 10^6 Btu/hr, natural gas, -160 to -250°F/s, 1800 ppm SO_2, Linwood atmospheric hydrate, 2 μm, T_{inj} = 2100°F (data generated under EPA Contract 68-02-3633).

3. EER-CTT, 9 x 10^4 Btu/hr, natural gas, -370 to -940°F/s, 2000 ppm SO_2, Linwood atmoshperic hydrate, 2 μm, T_{inj} = 2300°F (data generated under EPA Contract 68-02-3633).

4. Coutant, et al. (1971), 2 x 10^5 Btu/hr, natural gas, -440 to -950°F/s, 3000 ppm SO_2, limestone, 50 μm, T_{inj} = 2200°F.

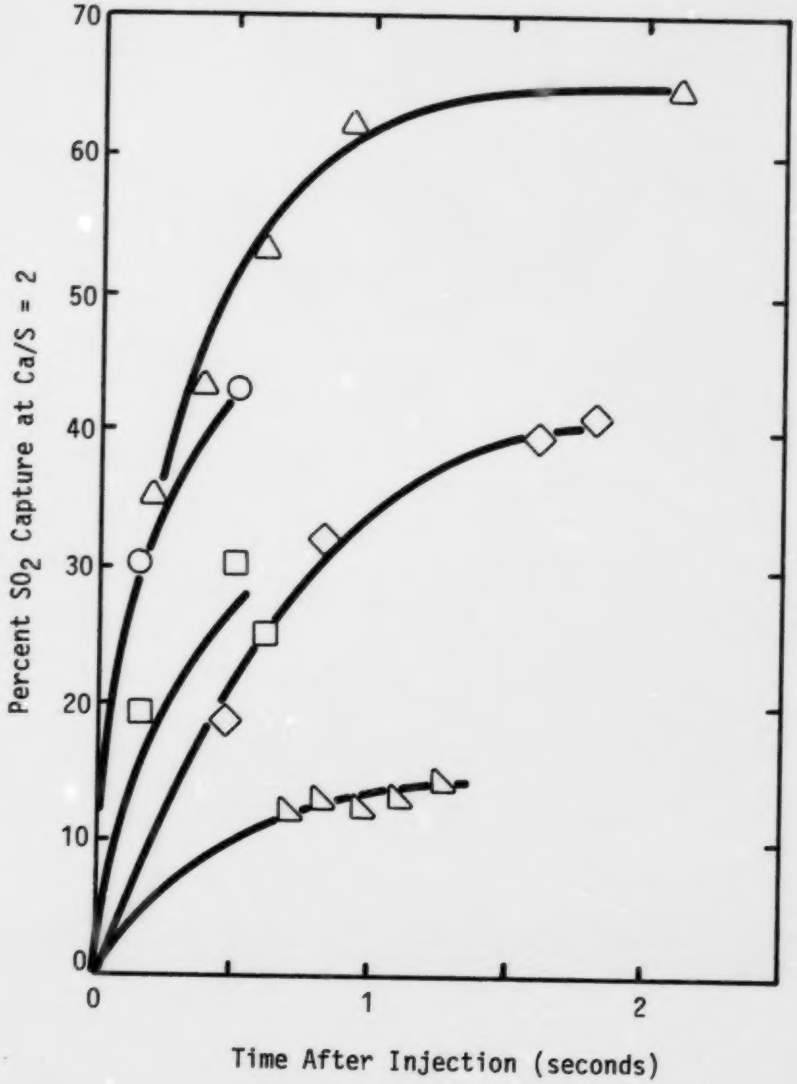

Figure 6-4. The effect of residence time on SO_2 capture at Ca/S = 2 for hydrates and carbonates. See Table 6-5 for an explanation of the plotting symbols.

TABLE 6-5. SYMBOL KEY FOR FIGURE 6-4.

1. Farzan, et al. (1986), 6 x 10^6 Btu/hr, Blacksville coal, 1.8% S, -1200°F/s, Corson atmospheric dolomitic lime, 4 μm, T_{inj} = 2250°F.

2. Farzan, et al. (1986), same as (1) except Longview hydrate, 5 μm, T_{inj} = 2250°F.

3. EER-BSF, 1 x 10^6 Btu/hr, natural gas, -250°F/s, 1800 ppm, Longview atmospheric hydrate, 4 μm, T_{inj} = 2250°F (data generated under EPA Contract 68-02-3633).

4. EER-CTT, 9 x 10^4 Btu/hr, natural gas, -370°F/s, 2000 ppm, Linwood atmospheric hydrate, 2 μm, T_{inj} = 2300°F (data generated under EPA Contract 68-02-3633).

5. Coutant, et al.,(1971) 2 x 10^5 Btu/hr, natural gas, -440°F/s, 1600 ppm SO_2, limestone, 90 μm, T_{inj} = 2300°F.

roughly equal quench rates and injection temperatures. It is possible that the differences in reactivity are related to the rates of sorbent-gas mixing in the two systems.

6.2 Sorbent Particle Size and Type

In general, hydrates are more reactive than carbonates. Inspection of Figure 6-1 and 6-2 shows that for data obtained on the BSF, Linwood atmospheric hydrate is twice as reactive as Vicron limestone. The mass-mean particle diameters for the two sorbents are 2 and 11 μm, respectively. The reactivity difference observed in the BSF is typical of that observed on other facilities. At least part of this difference can be attributed to particle size effects. For this reason, comparisons of the reactivities of hydrates and carbonates should include experiments on particle size effects. Furthermore, given the variability in reactivity of limestones from different quarries, comparisons between hydrates and carbonates ought also to include materials from the same parent limestone.

Figure 6-5 shows CTT reactivity data as a function of both particle diameter and sorbent type. Two limestones and two hydrates were tested. The size fractions were obtained by air-classification techniques and the mass mean diameters were verified using sedimentation and electron microscope techniques. The data show a consistent decrease in reactivity with increasing particle size. For a given particle size the hydrates are roughly twice as reactive as the carbonates. The Linwood atmospheric hydrate (indicated by the circles) and the Linwood carbonate (indicated by the diamonds) are directly comparable because the hydrate was obtained from the carbonate. The pair of Linwood sorbents show that the hydrate is approximately twice as reactive as the carbonate for particle diameters ranging from 2 to 10 μm.

Figure 6-5 also shows that there is considerable variation in reactivity for a given sorbent type. The 5 μm Colton hydrate shows a capture level of 41 percent compared to 54 percent for the Linwood hydrate. The Linwood limestone is also more reactive than the Vicron.

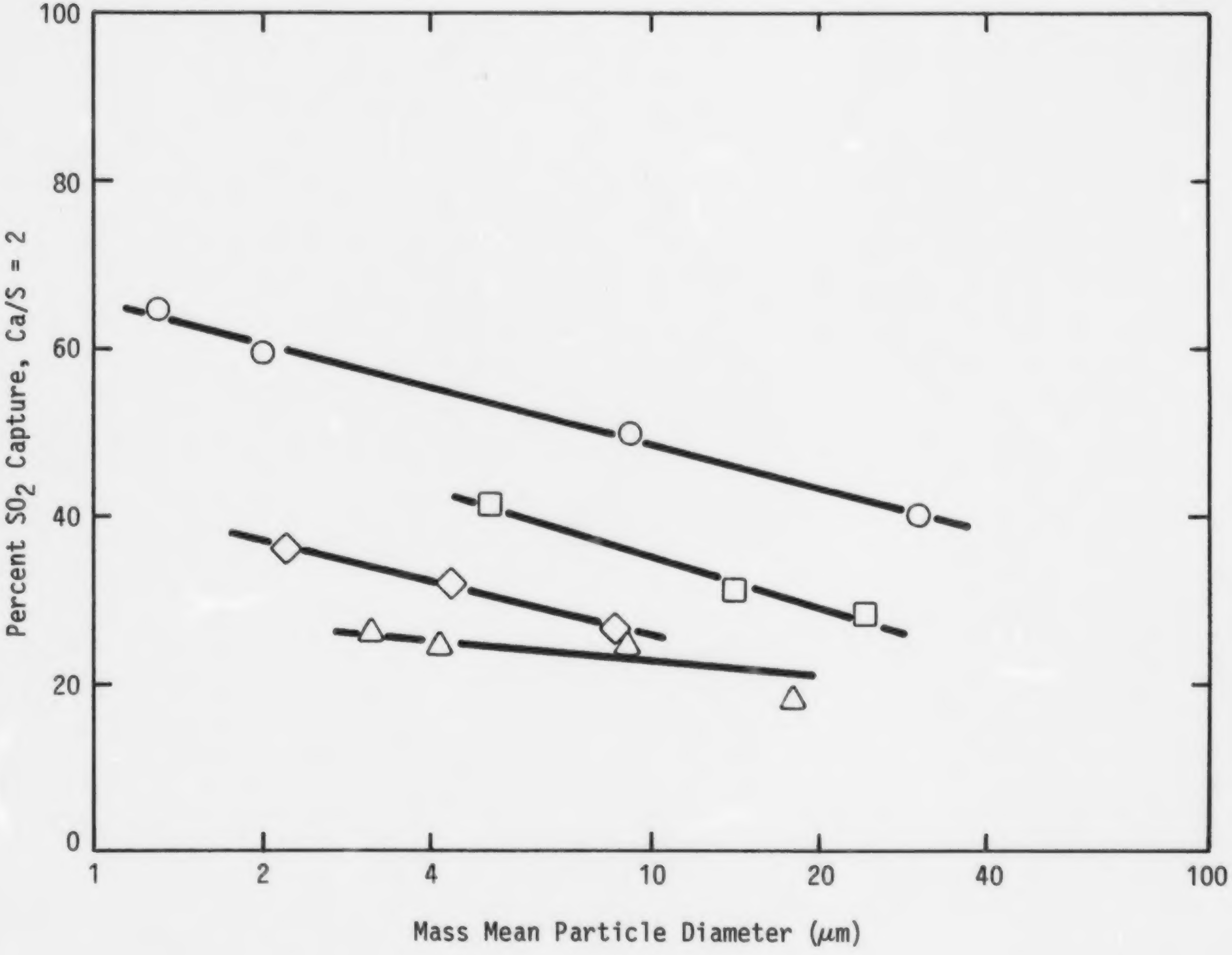

Figure 6-5. The effect of particle size on SO_2 capture at Ca/S = 2 for hydrates and carbonates. See Table 6-6 for an explanation of the plotting symbols.

TABLE 6-6. SYMBOL KEY FOR FIGURE 6-5

1. EER-CTT, 9×10^4 Btu/hr, natural gas, -370°F/s, 2000 ppm, Linwood atmospheric hydrate, $T_{inj} = 2300^\circ$F (data generated under EPA Contract 68-02-3633).

2. EER-CTT, Colton atmospheric hydrate (data generated under EPA Contract 68-02-3633).

3. EER-CTT, Linwood limestone (data generated under EPA Contract 68-02-3633).

4. EER-CTT, Vicron limestone (data generated under EPA Contract 68-02-3633).

6.3 SO_2 Concentration

6-6

Bench-scale results showing the effect of SO_2 concentration on percent SO_2 capture are shown in Figure 6-6 for hydrates and carbonates. Isothermal bench-scale data have been included. The data shown two apparently different trends. Results obtained on the CTT at EER show a very weak dependence on SO_2. The isothermal reactor studies of Newton, et al. (1986) and of Slaughter (1986) also show a weak dependence. In contrast, the data of Coutant, et al. (1971) shows capture levels increasing from 7 percent up to 32 percent as the SO_2 concentration increases from 100 to 10,000 ppm. Based on time-resolved capture studies, Coutant determined a 0.5-order dependence on SO_2. The differential reactor studies of Borgwardt and Bruce (1986) (not shown here) suggest a 0.6-order dependence. The results of Teixeira, et al. (1986) agree with Coutant's in showing a fairly significant increase in capture with increasing concentration.

Detailed examination of the data helps explain the apparent contradiction in trends. All of the data which exhibited a weak dependence on SO_2 were obtained with small, calcitic particles under condition where the model calculations would suggest pore blockage is controlling. In these cases increasing the SO_2 concentration does not increase capture because it enhances pore closure. However, in both "exceptions" to the weak sensitivity, pore blockage is less likely to be the controlling resistance. The Teixeira et al. data were obtained with a dolomitic sorbent. Since the MgO does not react, the pores tend to remain open longer and, therefore, increasing the SO_2 concentration should increase the capture. The Coutant et al. data are for very large particles (90 μm) where the bulk diffusion in the large pores is rate controlling. Here, too, increasing SO_2 should increase capture.

6.4 Conclusions and Key Experimental Issues

The primary conclusions and the key remaining experimental issues, based on examination of the bench-scale data in this section, are summarized below.

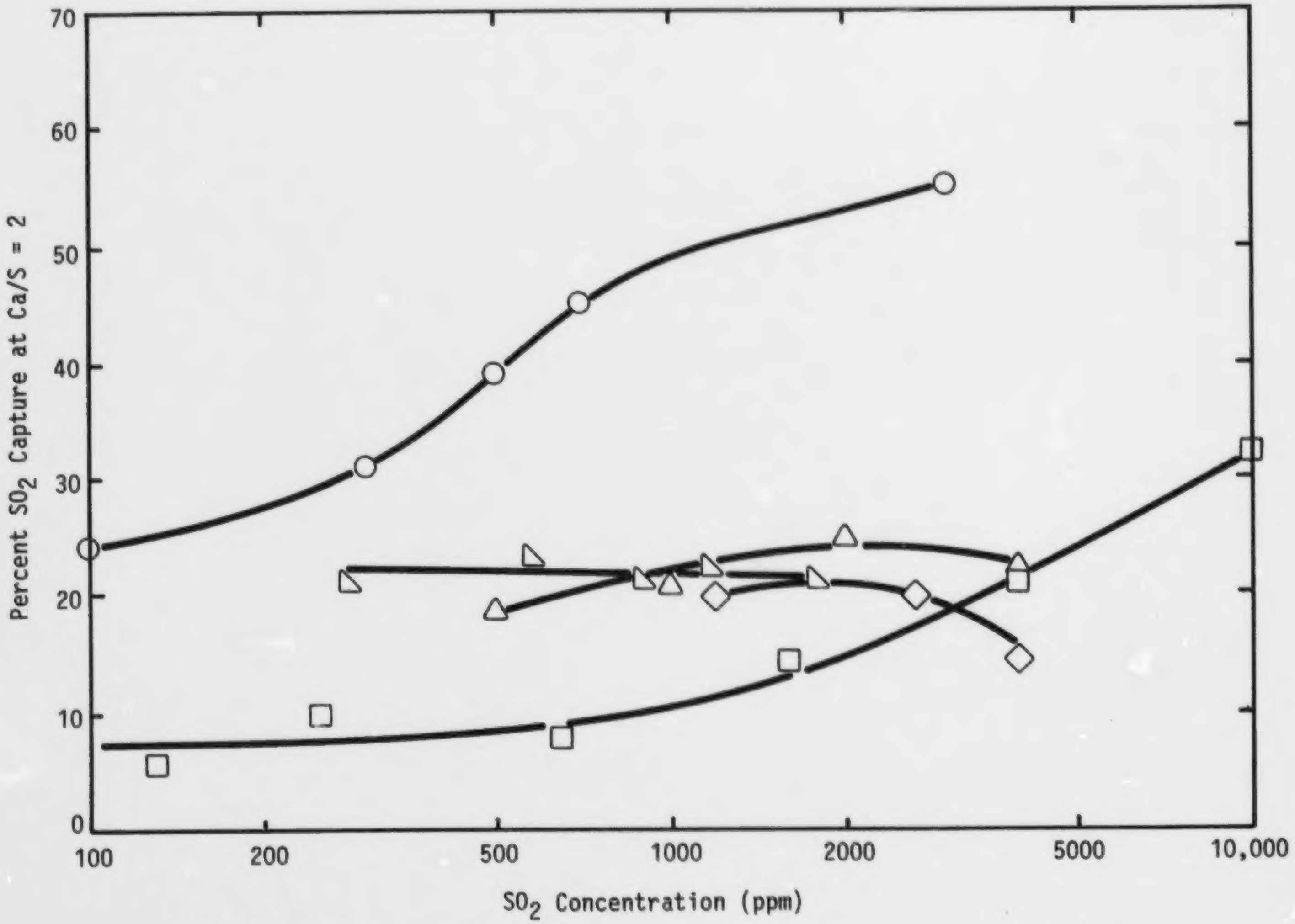

Figure 6-6. The effect of SO_2 concentration on SO_2 capture at Ca/S = 2 for hydrates and carbonates. See Table 6-7 for an explanation of the plotting symbols.

TABLE 6-7. SYMBOL KEY FOR FIGURE 6-6

1. Teixeira, et al. (1986), 1 x 10^5 Btu/hr, natural gas, -450°F/s, 1 sec., pressure hydrated dolomitic lime, T_{inj} = 2000°F.

2. Coutant, et al. (1971), 2 x 10^5 Btu/hr, natural gas, -500°F/s, 1.2 sec., limestone, 90 μm, T_{inj} = 2200°F.

3. Slaughter (1986), 2.2 x 10^5 Btu/hr, natural gas, isothermal, 0.5 sec., Vicron limestone, 11 μm, 2000°F.

4. Newton, et al. (1986), 2.2 x 10^5 Btu/hr, natural gas, isothermal, 1.0 sec., precalcined Linwood atmospheric lime, 2 μm, 1800°F.

5. EER-CTT, 9 x 10^4 Btu/hr, natural gas, -400°F/s, Vicron limestone, 11 μm, T_{inj} = 2200°F (data generated under EPA Contract 68-02-3633).

The effects of thermal history, particle size and type, and SO_2 concentration are included in the discussion.

The thermal environment can be described in terms of injection temperature, quench rate, and time. The primary conclusions regarding these variables include the following.

- The optimum injection temperature is 2050°F for most sorbents. This temperature is defined as that the maximum temperature resulting when the carrier gas is mixed into the furnace gas; this is a reasonable representation of the true peak sorbent temperature.

- Hydrates appear to be more sensitive to injection temperature than carbonates. This may reflect differences in the activation or calcination process. Carbonates calcine more slowly than hydrates which probably results in the production of unreacted CaO over longer periods of time. This could be significant in a quenched system in which the sorbent particles are falling from higher to lower temperatures.

- Clear conclusions regarding the effect of quench rate are impossible to formulate based on the available data. Results obtained on the CTT show capture levels falling from 60 percent down to 43 percent (at Ca/S = 2 with Linwood hydrate) as the quench rate is increased from -350°F/s to -950°F/s. Data obtained on other facilities show a weak dependence on quench rate.

- Time-resolved capture studies at the bench scale demonstrate that capture levels of 30 percent at Ca/S = 2 can be achieved with hydrates in less than 200 msec.

The key experimental issues regarding the effects of thermal history are discussed below. Suggestions are included for resolving these issues.

- Experiments show that capture is sensitive to injection temperature but the optimum sorbent injection temperature is still unclear. Greater care needs to be taken in the measurement of injection temperature. The rate with which the sorbent jet mixes with the bulk gases is also an important parameter which clearly has an effect on the sensitivity of capture to injection temperature. The rate of mixing can be estimated by injecting tracers with the conveying air.

- The effect of quench rate is unclear. Much of the uncertainty is probably due to the complicating effects of mixing. Related to this is the uncertainty introduced by conveying the sorbent with a large volume of cold air.

The principle conclusions regarding the effects of particle size and sorbent type are listed below.

- For a given particle size, hydrates are roughly twice as reactive as carbonates. This conclusion is based on CTT studies performed with sorbent obtained from the same percent limestone.

- Increasing particle size decreases sorbent reactivity.

Unresolved experimental issues include the differences in reactivity between hydrates and carbonates. In particular, can a determination be made of the differences in the CaO obtained from $Ca(OH)_2$ and the CaO from $CaCO_3$?

Finally, the overall reaction order with respect to SO_2 concentration is less than one and is probably greater than zero. Experiments designed to distinguish between the various postulated sulfation mechanisms might be useful but are of secondary importance compared to the experimental issues discussed above.

EPA. 4208 FINAL RPT (7)

7.0 EXPERIMENTAL RESULTS - THIS PROGRAM

In order to resolve some of the experimental issues discussed in Section 6.4, a series of experiments were designed and conducted in a range of combustion facilities at EER. This section first describes the characteristics of the combustion facilities and the experimental techniques employed. The results obtained are subsequently presented to address the two key data gaps, i.e., the influence of thermal history and the impacts of sorbent properties on sorbent utilization.

7.1 Experimental Facilities

7.1.1 Isothermal Reactor, Control Temperature Tower and Boiler Simulator Furnace

Three experimental facilities were used in this program: a laboratory scale Isothermal Reactor (ITR); a bench scale Control Temperature Tower furnace (CTT), and a pilot scale Boiler Simulator Furnace (BSF).

The ITR is shown in Figure 7-1. This reactor was centered in a 21 kW (72 kBtu/hr), 1500°C (2700°F) three-zone Lindberg furnace. The heated zone was 0.9μm long and could hold a 10-cm reaction tube. Three independently controlled heating zones, separated by baffles, ensured that a flat temperature profile was maintained over the heated length.

The ITR was downfired by a precombustor assembly coupled with a sliding burner, as shown in Figure 7-2. There are two main features to this assembly: a sliding burner and a venturi. The sliding burner was a premixed, water cooled, flat-flame burner in a square stainless steel chimney. Due to heat losses through the chimney, variance of the burner position allowed downstream temperature control independent of the gas velocity and burner stoichiometry. The venturi, located immediately downstream of the sorbent injector/flow straightener, created turbulence which enhanced sorbent dispersion in the flame gases. The gradually

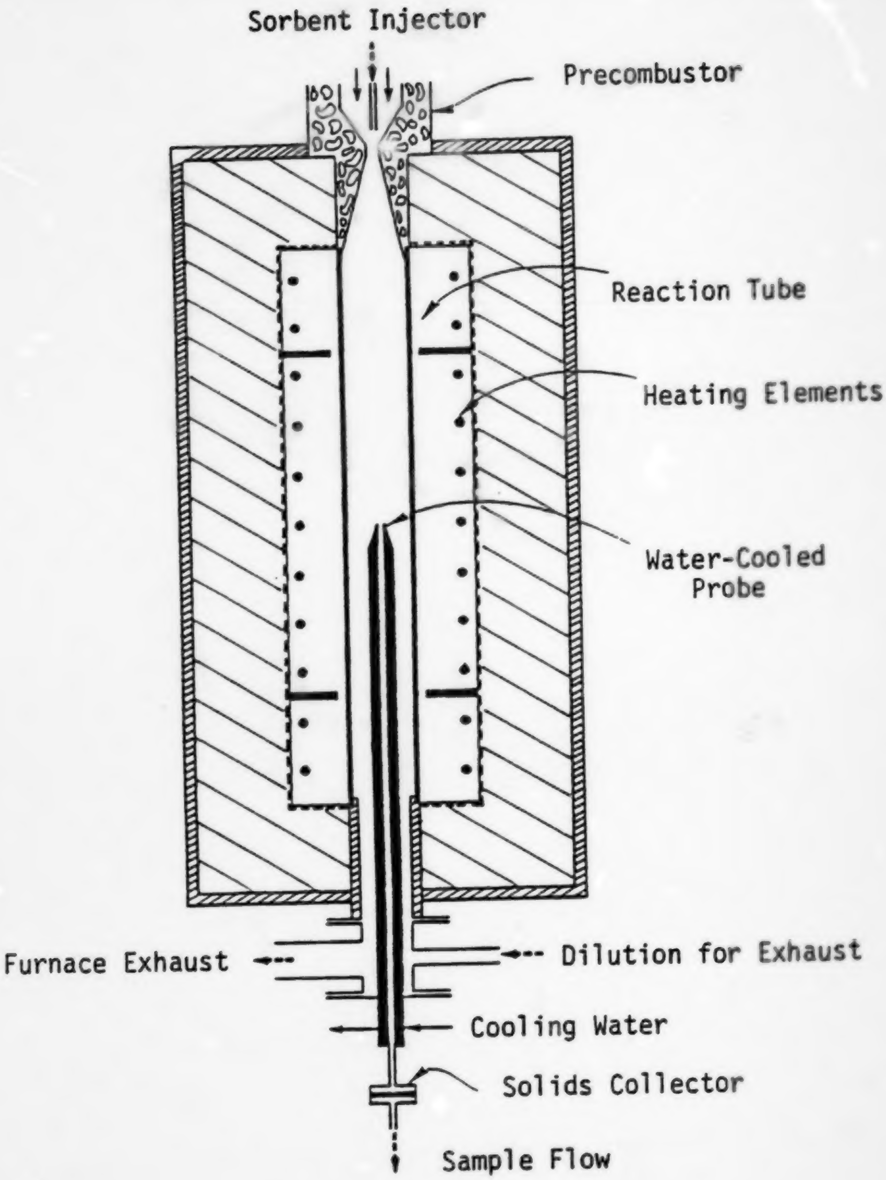
Sorbent Injector
Precombustor
Reaction Tube
Heating Elements
Water-Cooled Probe
Furnace Exhaust
Dilution for Exhaust
Cooling Water
Solids Collector
Sample Flow

Figure 7-1. Schematic of the isothermal reactor (ITR).

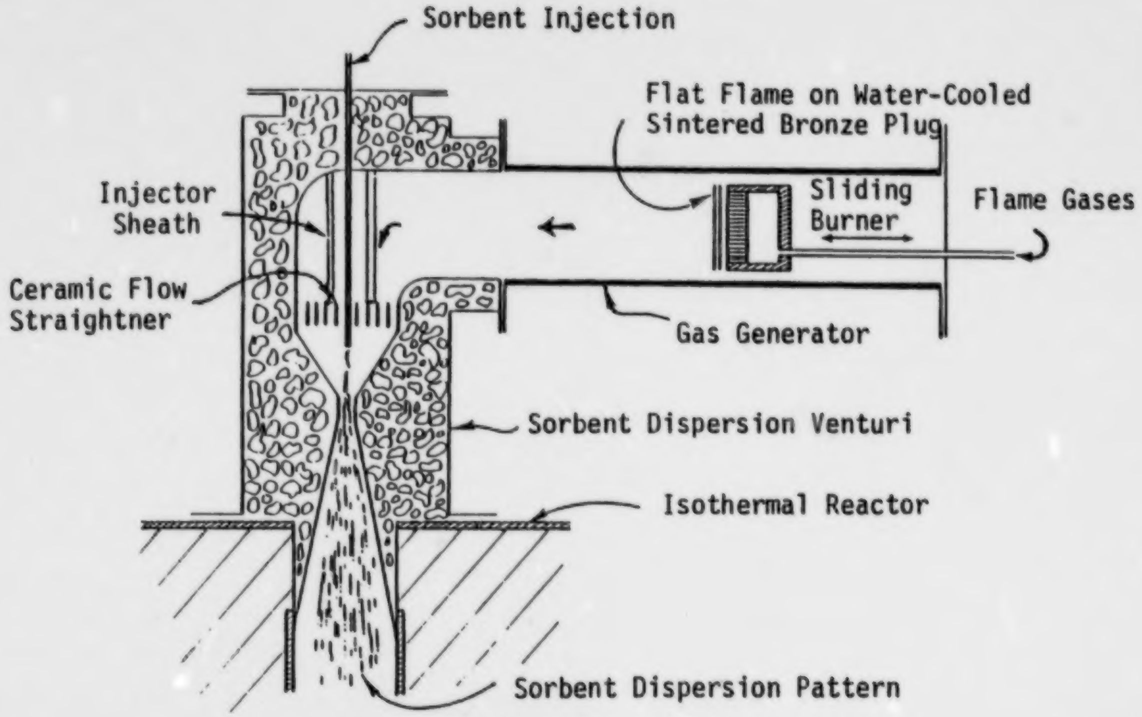
Sorbent Injection
Flat Flame on Water-Cooled Sintered Bronze Plug
Injector Sheath
Sliding Burner
Flame Gases
Ceramic Flow Straightner
Gas Generator
Sorbent Dispersion Venturi
Isothermal Reactor
Sorbent Dispersion Pattern

Figure 7-2. Schematic detail of the precombustor/sliding burner assembly.

divergent section after the venturi throat prevented backmixing and promoted a flat velocity profile.

Sorbent was injected via an injector which used swirl air to aid sorbent dispersion. Solid or gas sampling probes were inserted axially at the exhaust end of the reactor. Complete documentation on the ITR facility can be found in a report by Cole (1985).

An overall diagram of the 18 kW (60 kBtu/hr) Control Temperature Tower furnace (CTT) is presented in Figure 7-3. The reactor entry (top section) included a 45.7 cm long quarl that diverged from 5.1 cm to 20.3 cm. The long quarl provided flame stabilization as well as establishing a one-dimensional flow pattern. Numerous ports located along the axis of the reactor enabled supplementary equipment, i.e., zone separation chokes, cooling coils, and fuel, air, and sorbent injectors, to be placed in the reactor.

The time-temperature profile was manipulated by firing one or both of the back-fired heating sections (second and fourth sections from the top). The back-fired sections employed natural gas burners which were fired in the opposite direction of the main combustion gas. The back-fired effluent passed through channels in the refractory walls surrounding the main combustion zone (see the radial cross-sectional view in Figure 7-3). Backfiring in this manner minimized the temperature decay of the combustion products in the main combustion zone. Additional alteration of the temperature profile could be accomplished by inserting cooling coils in the main combustion chamber.

Detailed information on the CTT can be found in a report by Greene (1984).

The Boiler Simulator Furnace (BSF) is illustrated in Figure 7-4. The facility, which was fired at 147 kW (500 kBtu/hr), consisted of two main sections; a refractory-lined vertical radiant tower and a horizontal convective section containing air-cooled heat exchangers. The radiant tower had an ID of 0.6μm and an OD of 1.0μm and consisted of eight modular sections

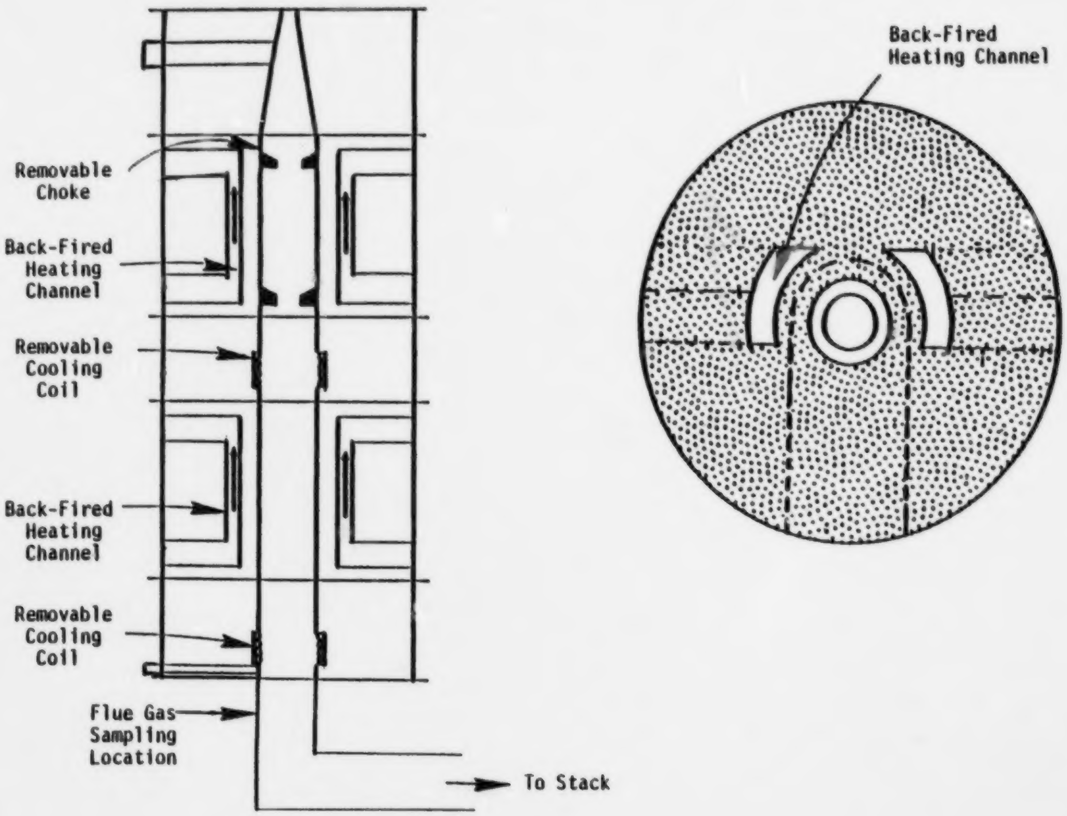
Removable Choke
Back-Fired Heating Channel
Removable Cooling Coil
Back-Fired Heating Channel
Removable Cooling Coil
Flue Gas Sampling Location
To Stack
Back-Fired Heating Channel

Figure 7-3. Cross-sectional views of the control temperature tower.

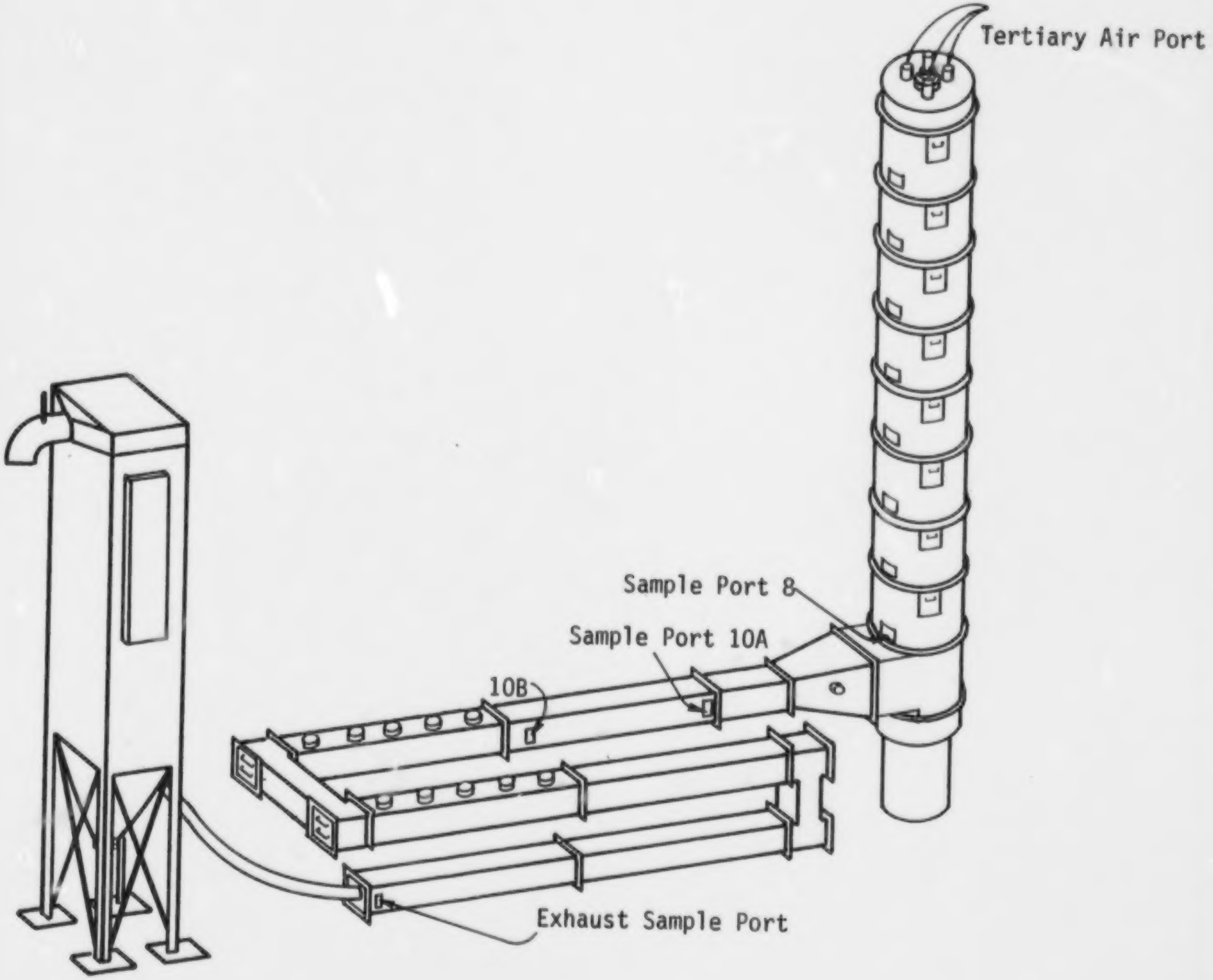
Tertiary Air Port
Sample Port 8
Sample Port 10A
10B
Exhaust Sample Port

Figure 7-4. Boiler simulator furnace (BSF).

with multiple access ports. The BSF time/temperature profile was manipulated by positioning water-cooled panels or rods appropriately in the furnace. The horizontal convective section contained air-cooled tube bundles that simulated the superheaters, economizers and air heaters in a boiler. Cooling air was supplied by a forced draft fan with a damper to control flow.

The furnace was equipped with a versatile DMB (Distributed Mixing Burner) modeled after the EPA prototype burner. Two secondary air streams supplied the burner and the air swirl could be controlled by modifying the swirl and axial air flow rates. The burner had four external staging air ports supplied with separately metered tertiary air. The burner was designed to fire coal or natural gas.

Complete documentation on the BSF facility and fundamental sorbent injection work can be found in an earlier report (Overmoe, 1984).

7.1.2 Measurement Systems and Analytical Methods

Exhaust gas samples were taken in the ITR, CTT and BSF with a stainless-steel, water-jacket probe and analyzed using standard continuous instrumentation for O_2, CO and CO_2. The schematic of the sampling system is shown in Figure 7-5. The gas stream was sampled separately for SO_2 analysis. SO_2 samples were carried via a heated sample line to a permeation dryer and on to a DuPont non-dispersive ultraviolet SO_2 analyzer. Figure 7-6 shows the schematic of the SO_2 sampling system. Furnace temperature profiles were characterized with a suction pyrometer in the CTT & BSF. In the laboratory scale ITR, temperature measurements were made with type-S thermocouple wires.

The principal technique used for particle size analysis of the sorbents was measurement on a Sedigraph Analyzer. This instrument operates on the principles of gravity sedimentation as defined by Stoke's law. The mass of particles settling from suspension at a given rate is measured by their attenuation of a collimated X-ray beam. The attenuation and the settling rate are converted into a cumulative plot of mass fraction vs. diameter. Scanning electron microscopy (SEM) was relied upon to provide certainty of

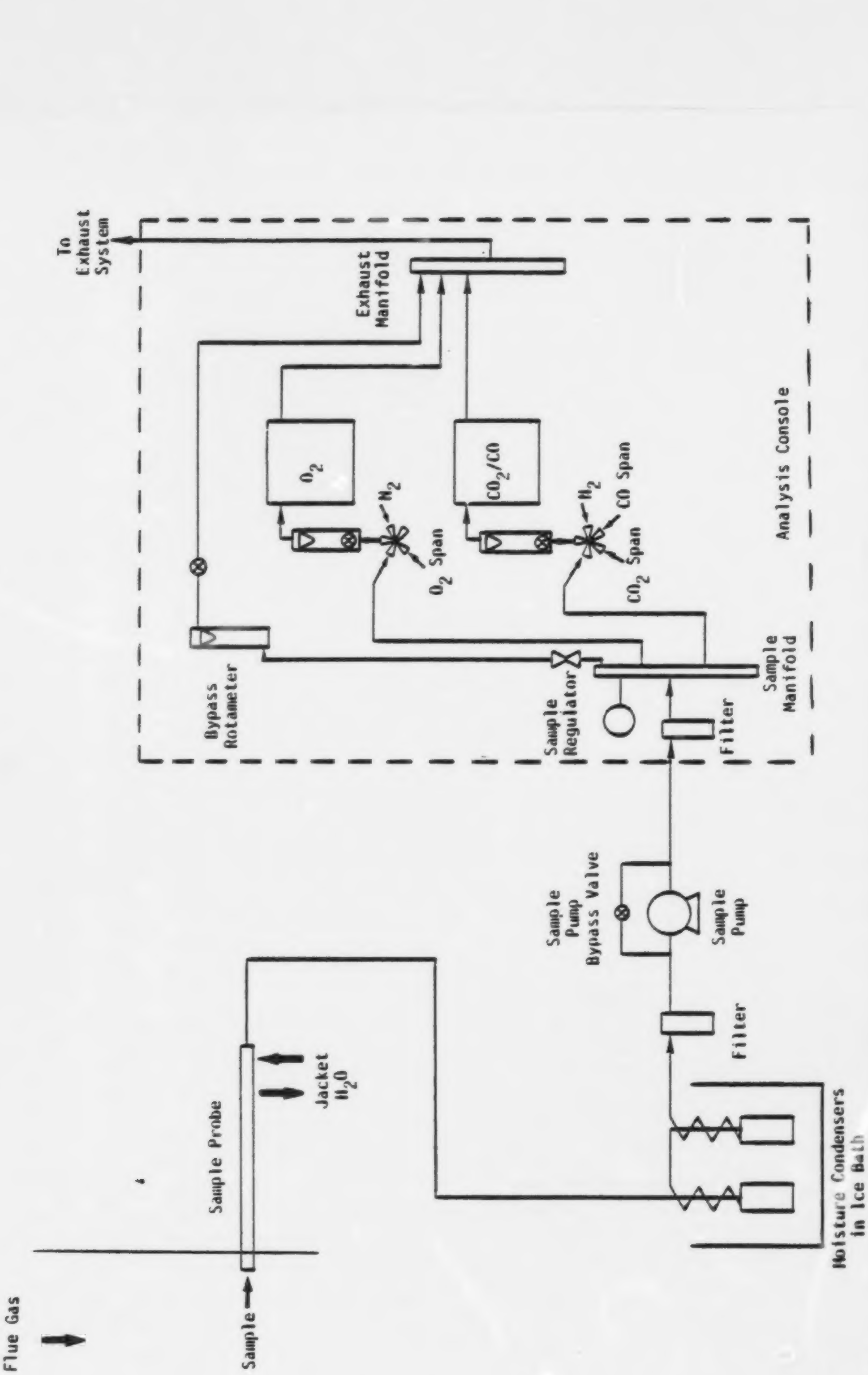
Flue Gas
Sample
Sample Probe
Jacket H_2O
Moisture Condensers in Ice Bath
Filter
Sample Pump Bypass Valve
Sample Pump
Filter
Sample Regulator
Sample Manifold
Bypass Rotameter
O_2 Span
N_2
O_2
CO_2 Span
CO Span
N_2
CO_2/CO
Analysis Console
Exhaust Manifold
To Exhaust System

Figure 7-5. Continuous monitoring sampling system.

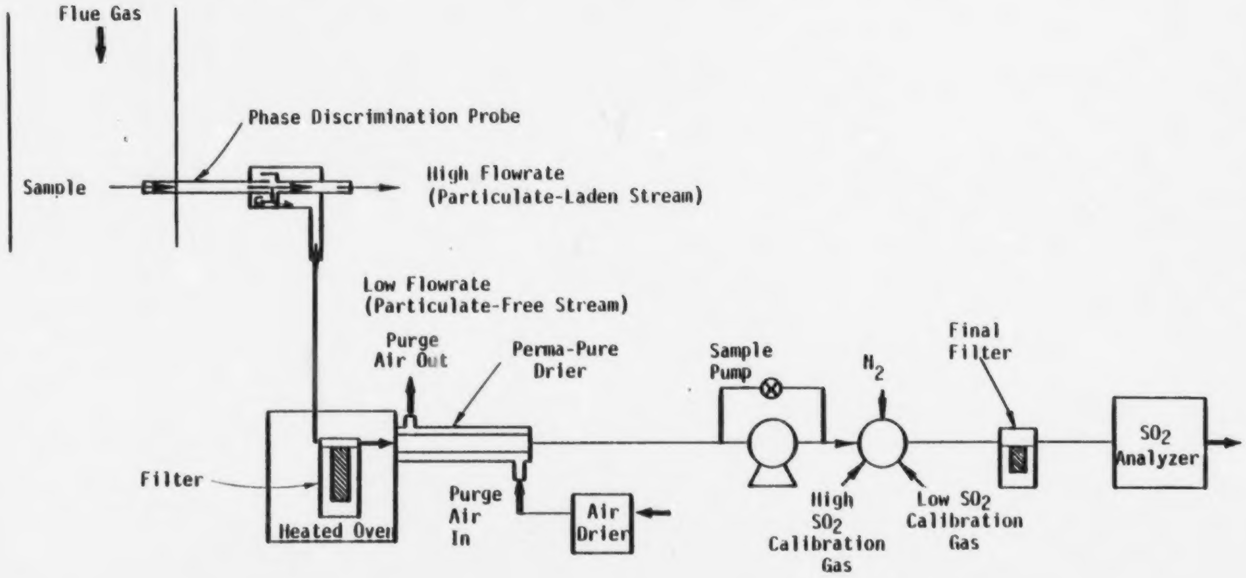
Flue Gas
Phase Discrimination Probe
Sample
High Flowrate
(Particulate-Laden Stream)
Low Flowrate
(Particulate-Free Stream)
Purge
Air Out
Perma-Pure
Drier
Filter
Heated Oven
Purge
Air
In
Air
Drier
Sample
Pump
N_2
High
SO_2
Calibration
Gas
Low SO_2
Calibration
Gas
Final
Filter
SO_2
Analyzer

Figure 7-6. SO_2 continuous monitoring system.

the particle size as determined by the Sedigraph and to provide information on the morphology of the sorbent particles.

In-house analyses were performed on sorbents to determine surface area, and calcium, hydrogen and carbon content. Specific surface area was determined on a Quantachrome Quantasorb unit. The measurements followed the BET model of nitrogen absorption isotherms at 77 K. Calcium was determined in solid samples following ASTM procedure D2795. Carbon and hydrogen (as CO_2 and H_2O) were determined in solid samples on a Perkin-Elmer 240B elemental analyzer.

7.1.3 Sorbents and Fuels

The properties of the high calcium limestones and hydrated limes used in this study are shown in Table 7-1. These sorbents, as well as their respective aerodynamic size classifications, were tested for reactivity. Information on the size cuts tested, and a more thorough look at size distribution data, will be presented in Section 7.3.2, devoted specifically to particle size effects on sorbent reactivity.

Natural gas was used as the fuel for all of the tests conducted. The gas contained 90 percent methane, six percent ethane and one percent propane by volume. Combustion air was doped with H_2S to provide SO_2 levels similar to those generated by common coals.

7.1.4 Sorbent Injection Technique

For sorbent injection, a primary concern was a rapid mixing rate between the sorbent and combustion gases. Due to the small diameters of the ITR and CTT, mixing times were relatively short for the injection schemes employed: the ITR used a venturi section immediately downstream of a swirl air injector; the CTT used an injector which produced a divergent cone concurrent to the furnace flow. With an SO_2 tracer in the sorbent transport air, measurements at residence times less than 300 msec showed a well mixed, uniform flow in the facilities. However, the comparatively large diameter of

TABLE 7-1. PROPERTIES OF SORBENTS

Sorbent	Linwood Limestone	Vicron Limestone	Linwood Atmospheric Hydrate	Colton Atmospheric Hydrate
Surface Area (m^2/gm)	1.1		16.0	15.2
Median Particle Size (μm)	13.3	9.8	2.2	4.0
Ca (weight %)	38.6	39.2	51.6	51.4
Mg	0.60	0.33	0.97	0.25
Na	0.01	0.01	0.00	0.01
K	0.03	0.01	0.00	0.05
Fe	0.17	0.06	0.27	0.10
Si	0.38	0.09	0.66	3.30
Al	0.12	0.02	0.18	0.21

the BSF required the development of an injection system which enhanced rapid mixing. A schematic of the injector developed is presented in Figure 7-7. Sorbent was injected counter to the furnace flow through multiple jets at 30 and 60 degrees from vertical. When SO_2 was injected at the main burner, a plug flow was observed at the sorbent injection location. With SO_2 injected through the sorbent injector using the proper amount of sorbent transport air, the concentration profile was relatively flat at 400 msec. Data at three residence times is shown in Figure 7-8. Only a minimal upstream penetration of the sorbent jets was observed.

To show the deviation between good and poor mixing, an injector which produced an axial jet with the same velocity as the furnace flow was also tested. This injection method generated the worst mixing case possible in the facility. A comparison of the furnace profile for the optimal (radial) and axial injectors is shown in Figure 7-9.

With an SO_2 concentration of approximately 2000 ppm (dry, 0% O_2) in the combustion gases, Linwood atmospheric hydrate was injected at 1230^o (2250^{o}F). The results are presented in Figure 7-10. At a molar calcium to sulfur ratio of two, a relative increase of 23 percent was observed when faster mixing was employed. This effect could be due to the contacting between the SO_2 and sorbent particles, as well as the heating rate/peak temperature of the particles.

7.2 Influence of Thermal History

Overall sorbent utilization is directly influenced by the thermal history experienced by sorbent particles. The thermal history can be described with three parameters:

- particle heating rate
- peak particle temperature, and
- thermal profile within the sulfation zone, i.e., quench rate.

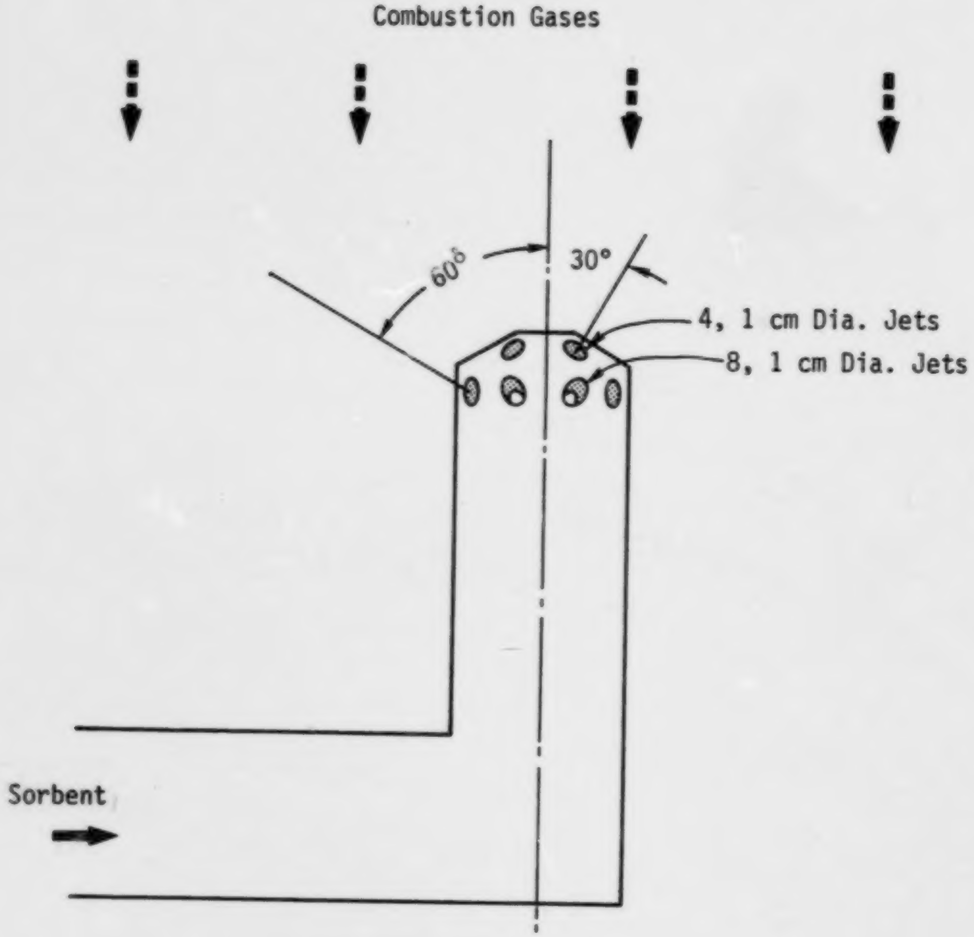
Combustion Gases
60°
30°
4, 1 cm Dia. Jets
8, 1 cm Dia. Jets
Sorbent

Figure 7-7. BSF sorbent injector.

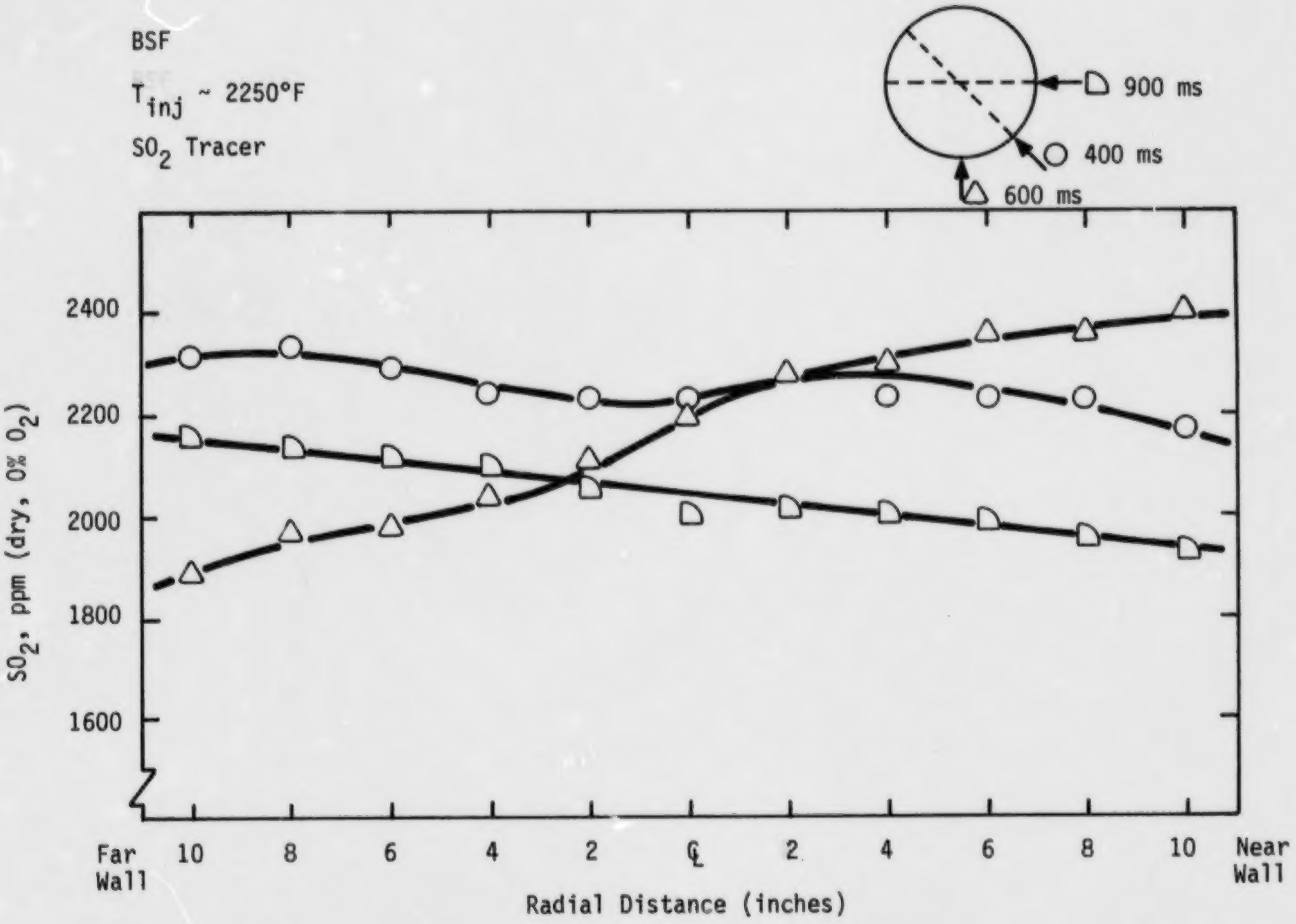

Figure 7-8. Mixing for BSF sorbent injector.

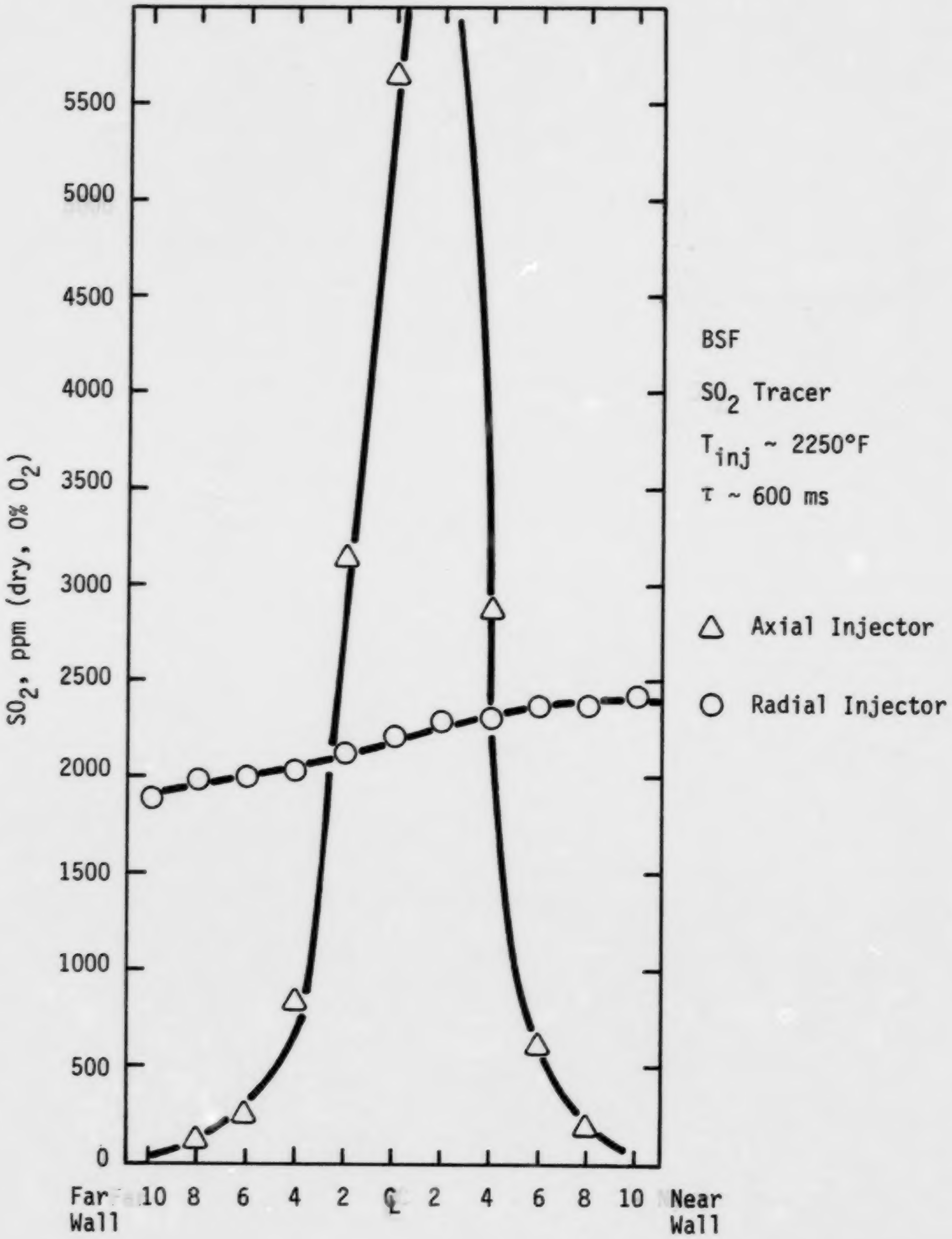

Figure 7-9. Comparison of mixing for radial and axial injectors.

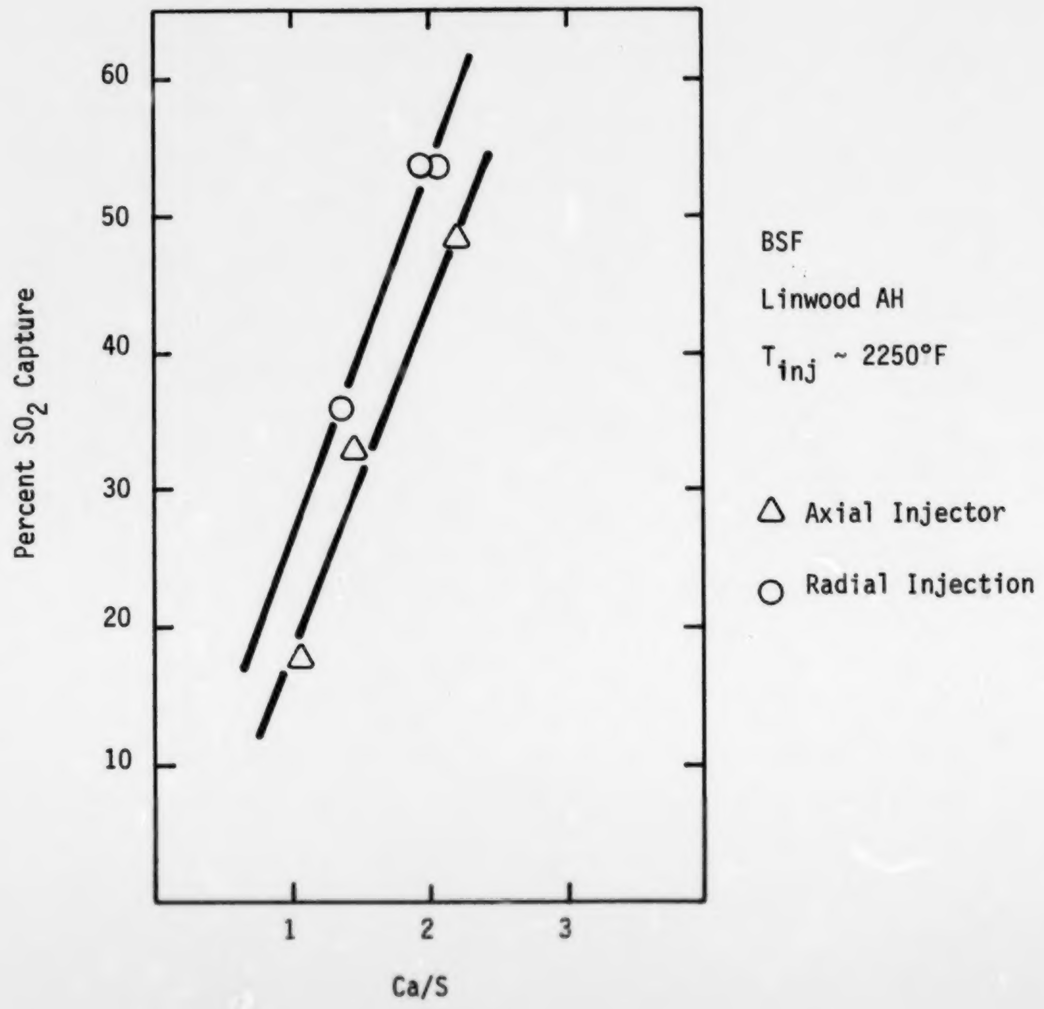

Figure 7-10. Influence of sorbent mixing on SO_2 capture.

After injection, sorbent particles rapidly heat up to the temperature of surrounding gas; thus in a boiler the particle heating rate is controlled by the rate of mixing of the sorbent jet. At the present time, the influence of heating rate on sorbent reactivity is not completely clear. In contrast, the temperature to which the particle is ultimately heated (as determined by the sorbent injection location) and the quench rate within the sulfation zone in the boiler are of major importance because they determine the ultimate utilization of the sorbent.

7.2.1 Injection Temperature

Temperature can influence the sulfation process in several manners. High temperatures favor the reaction kinetics of sulfation, but excessive temperatures hinder the process due to $CaSO_4$ instability and sintering or hard-burning of the sorbent particles. The influence of the sorbent injection temperature on sulfur capture was investigated in the BSF which was configured with a slow quench rate environment to minimize the differences between the temperatures at injection locations and peak particle temperatures. In these experiments the term injection temperature refers to the bulk gas temperature in the absence of sorbent transport air. Figure 7-11 shows the data for Linwood hydrate and Vicron at a calcium to sulfur ratio of two. Both sorbents exhibited an optimum injection temperature of approximately 1200°C (1100°C peak particle temperature) with capture levels decreasing as temperature deviated from the optimum.

At temperatures below the optimal value capture was decreased due to reduced reaction rates and less time in the sulfation window. In Figure 7-12, the SO_2 capture measured at sequential residence times for two injection temperatures is presented. The data, obtained with Linwood hydrate, imply that reaction rates increased with temperature. The temperature profiles downstream of the injection points, shown in Figure 7-13, indicate that the sorbent experienced a similar quench rate in each case, but had substantially longer time in the sulfation window (1230-980 C) when the injection temperature was elevated. The temperature data also suggest that the particles never exceed 1100°C in the optimum case.

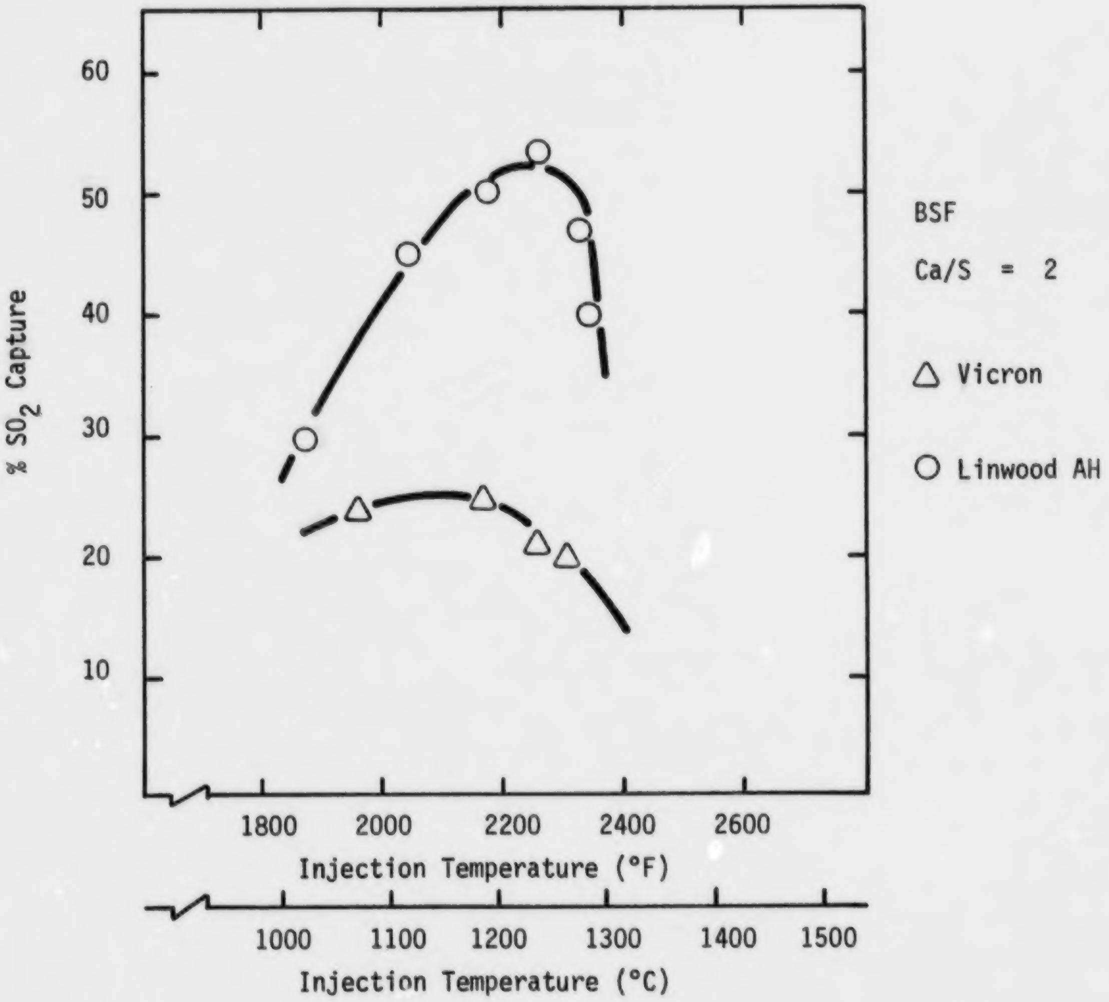

Figure 7-11. Influence of injection temperature on SO_2 capture.

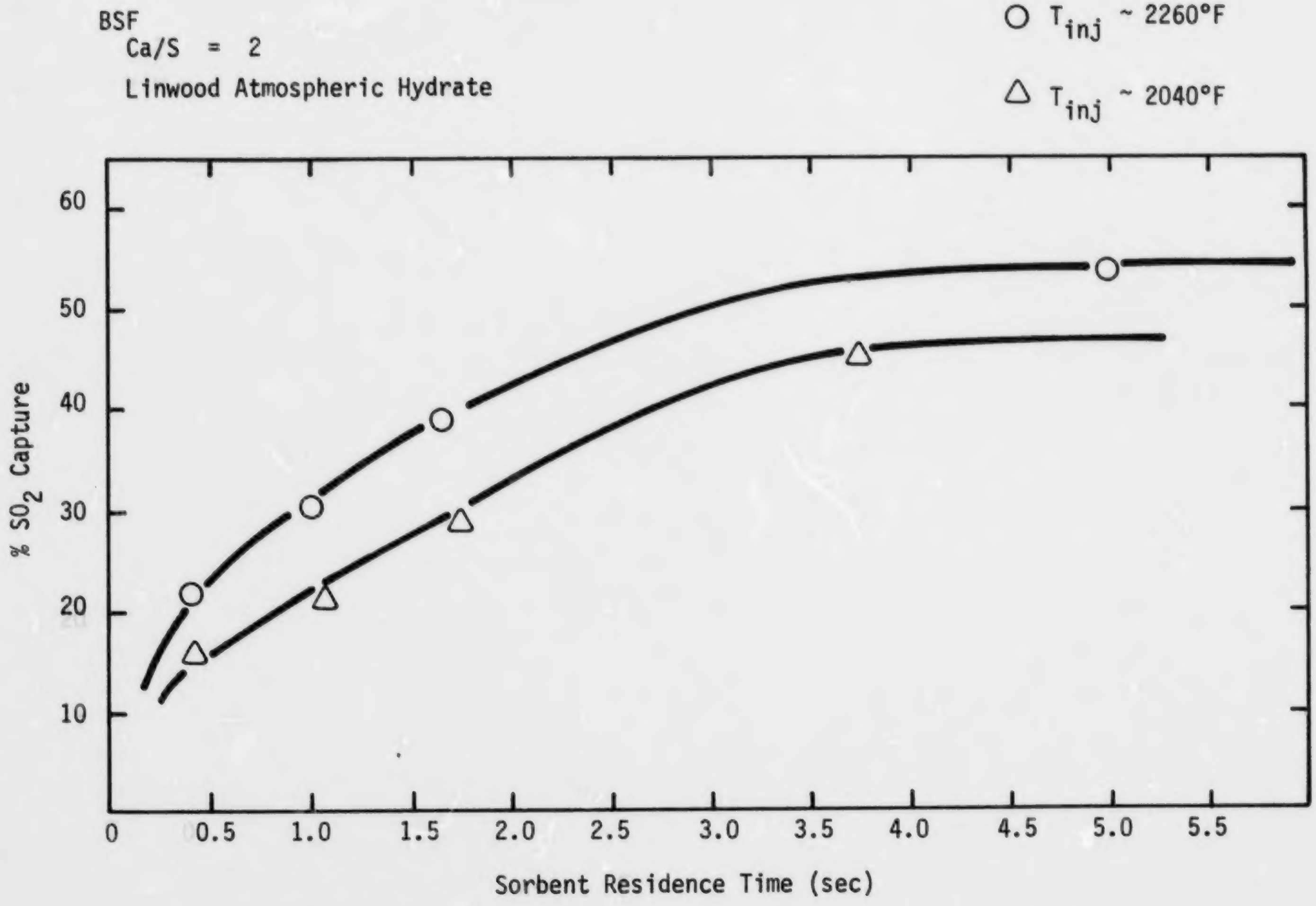

Figure 7-12. Influence of injection temperature on time resolved capture.

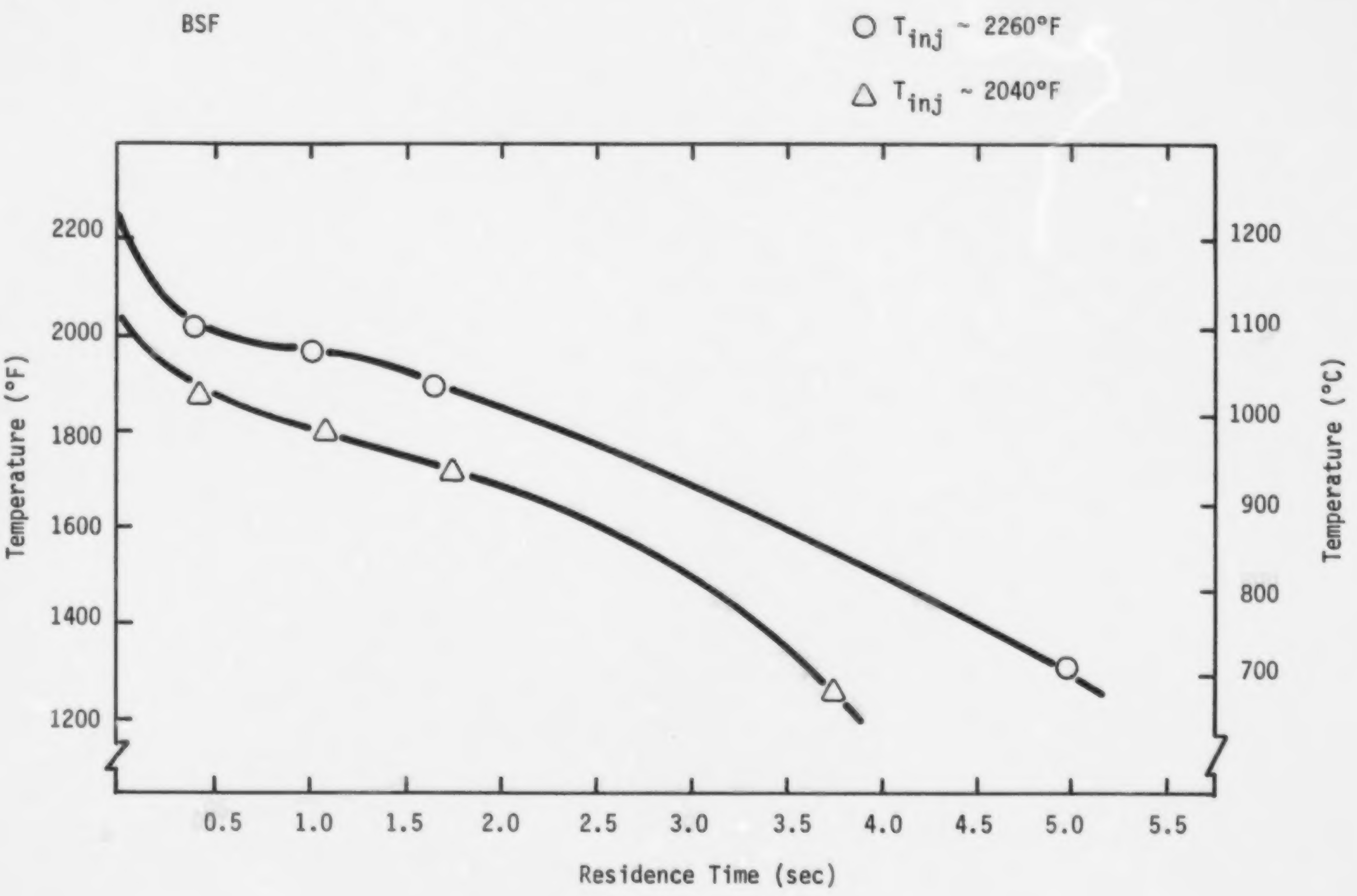

Figure 7-13. Furnace temperature downstream of sorbent injection.

At temperatures higher than the optimum level, the capture decreased due to sorbent particle sintering (McClellan, 1970) and $CaSO_4$ instability. At temperature in excess of 1230°C (2250°F) $CaSO_4$ is thermodynamically unstable, but due to the heating rate of the particles and the quench rate in the furnace, this temperature is probably not attained. Data obtained on the ITR at high temperatures, shown in Figure 7-14, indicate that the higher temperatures greatly reduced the capture potential of the sorbent. Since a constant temperature was maintained in the ITR, the sorbent reached a higher temperature than it did in the BSF. Accordingly, the decrease in reactivity began at a lower temperature (even below 1230°C), and the effect of sintering was evident.

7.2.2 Quench Rate

The previous section has described the influence of injection temperature on the reactivity of the sorbent. However, the injection temperature does not fully describe the time-temperature history that the sorbent experiences. In any practical boiler system the sulfur laden gas stream cools as it flows through the boiler furnace and convective passes. The resulting temperature quench rate impacts the sorbent reactivity and the rate of SO_2 pickup through two competing factors:

- The quench rate determines the time in which the sorbent is exposed to high temperatures which can accelerate sintering and reduce surface area;

- The quench rate also determines the time within the range of temperatures that allow the sulfation reaction to take place.

To investigate the impact of quench rate on sorbent reactivity two temperature profiles were established in the CTT and testing of ultimate and time-resolved sulfur capture was performed with atmospheric hydrates and carbonates. The temperature profiles from the sorbent injection point onward are presented in Figure 7-15. The baseline condition consisted of a firing rate of 17.6 kW (60,000 Btu/hr) at a stoichiometric ratio of 1.25 and

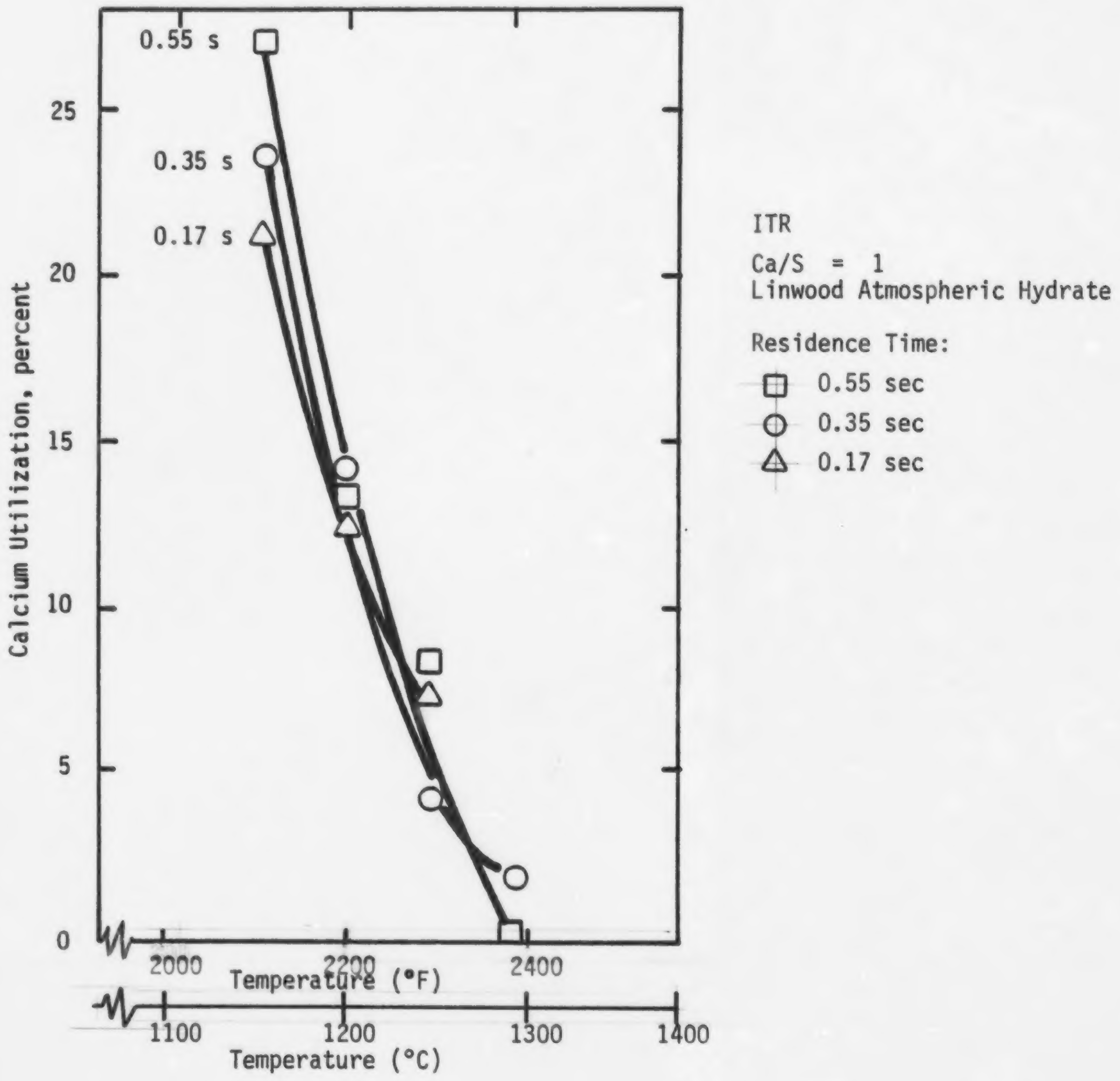

Figure 7-14. Capture at elevated injection temperatures.

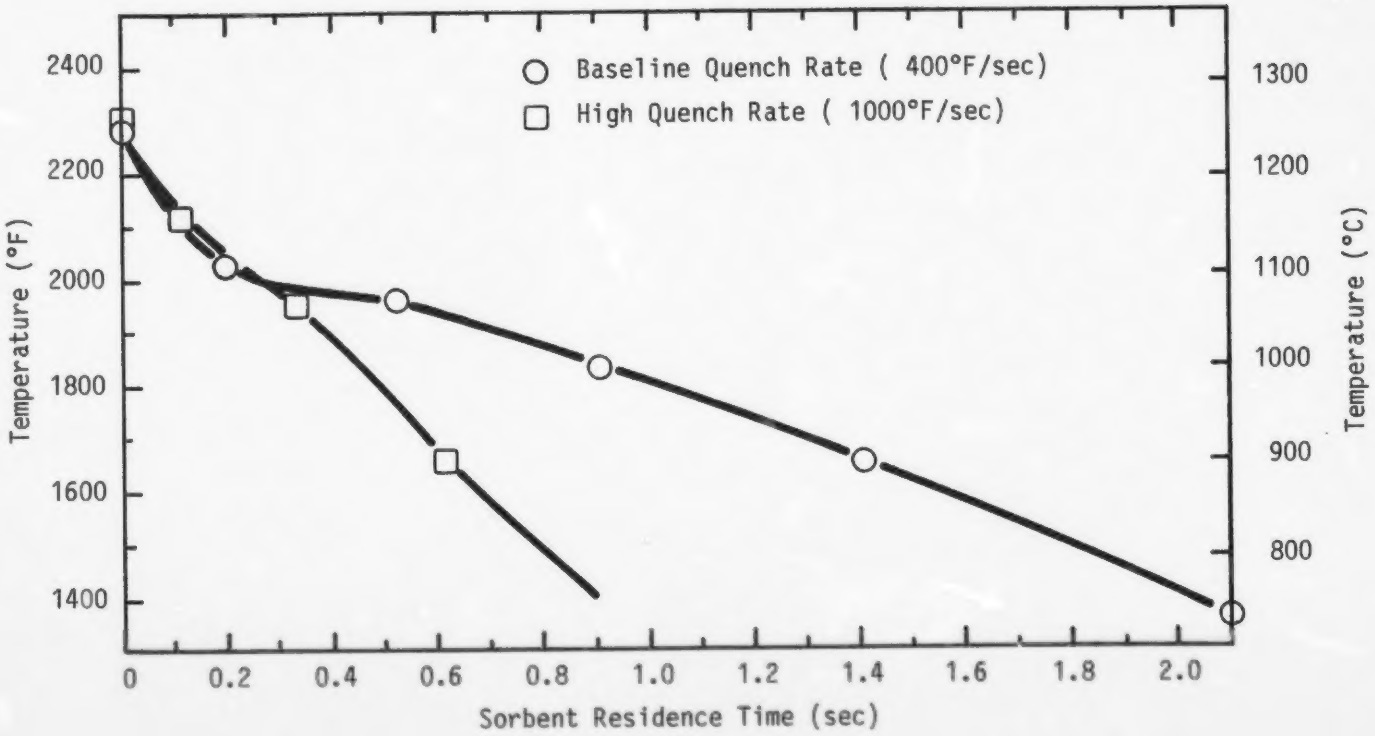

Figure 7-15. Temperature profiles experienced by the sorbent in the CTT when injecting near a temperature of 1260°C (2300°F).

injection of sorbent at 65 cm (25.5 inches) downstream from the burner. The high quench rate condition was established by increasing the firing rate to 28.6 kW (90,000 Btu/hr) at the same stoichiometry and inserting a set of cooling coils 132 cm (52 inches) away from the burner. Also, to match as closely as possible to the baseline injection temperature, the sorbent injection location was moved to 69 cm (27 inches) from the burner.

Notice that over the first 0.3 seconds the temperature profiles are essentially the same before splitting into very distinct quench rates. This is due to a dilution effect of the sorbent transport nitrogen flow (49.3 ℓ/min (1.74 scfm) for both cases). At the lower firing rate of the baseline condition, the diluent nitrogen has a greater quenching effect than at the high quench rate condition since it is a larger portion of the exhaust gas flow.

Using 982°C (1800°F) as the lower cutoff temperature for the sulfation reaction, sorbent injected into the baseline quench rate has approximately twice the residence time within the sulfation reaction zone as the high quench rate case (1.0 seconds compared to 0.5 seconds). Measurement of time-resolved capture was performed to help distinguish whether the slower quench rate impacted sulfur capture through increasing the reaction time or by somehow altering the initial calcination and formation of surface area.

Figure 7-16 presents sulfur capture as a function of Ca/S molar ratio for Linwood hydrate, Colton hydrate and Vicron carbonate under both baseline and high quench rate conditions. An injection temperature of approximately 1260°C (2300°F) was used for each case. The baseline results have been previously reported by Overmoe et al. (1986).

Both the Linwood and Colton hydrate results showed a considerable increase in capture under the baseline quench rate compared to the high quench rate; 58 percent compared to 44 percent capture for the Linwood and 40 percent compared to 32 percent capture for the Colton at Ca/S = 2. Vicron results, however, showed no measurable difference between quench rates (21 percent capture at Ca/S = 2). To better understand the capture process and

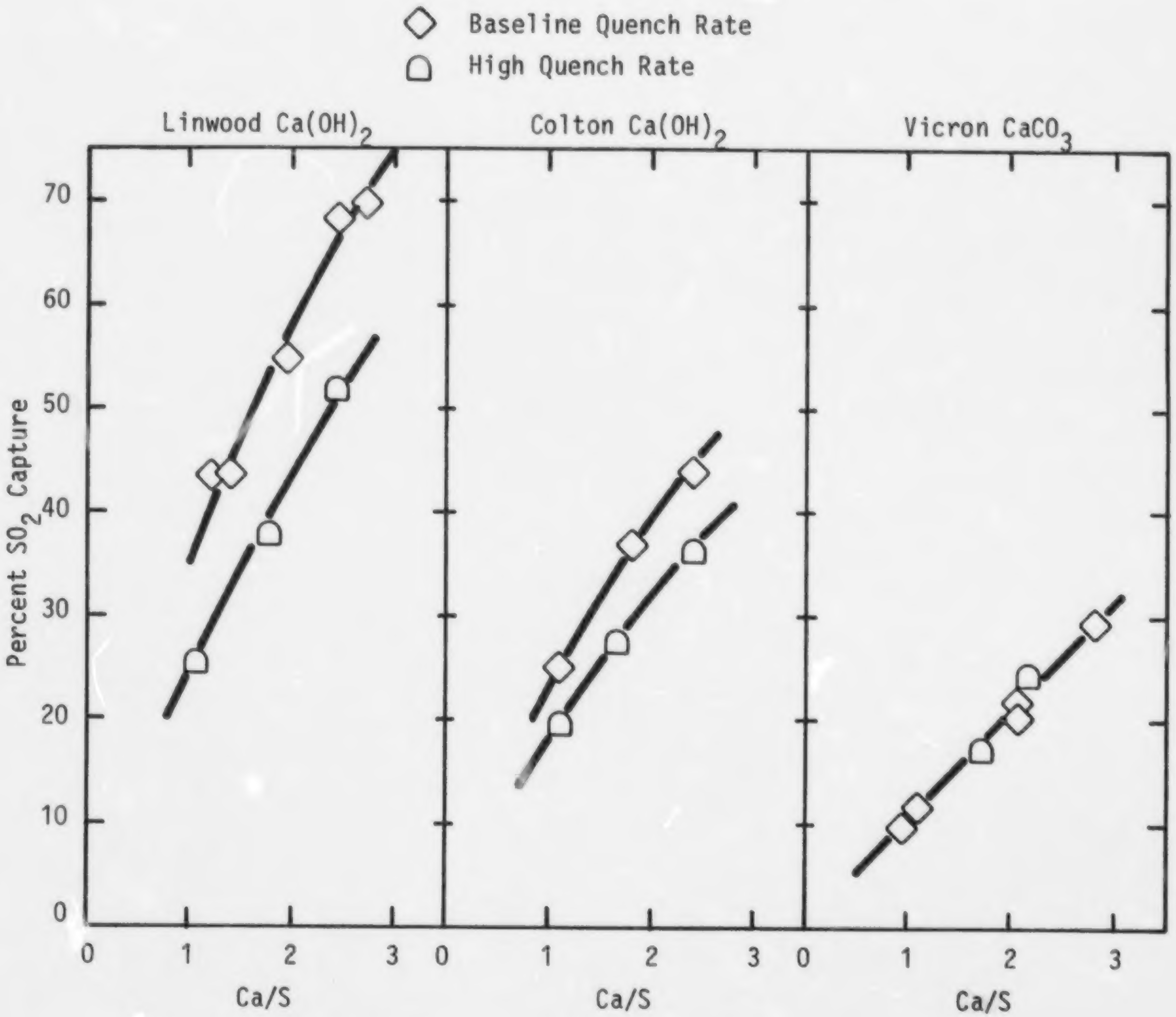

Figure 7-16. Sulfur capture for three sorbents under two different furnace quench rate conditions (Tinj = 1260°C (2300°F) for each case).

to help determine why the hydrates responded different than the carbonate to the two quench rates, time-resolved measurements were made at selected conditions.

The time-resolved measurements were performed by taking gas-phase samples at available ports along the length of the reactor. At short residence times SO_2 capture was measured at four points across the furnace diameter (20 cm) to avoid skewed data due to non-uniform mixing and to assure a reasonable average for the capture at each port.

Figure 7-17 presents the time-resolved results for Linwood hydrate. The initial capture rate was very fast for both quench rate conditions. Over the first 0.3 to 0.4 seconds, the capture behavior was quite similar (50 percent capture), with slight differences due to a higher Ca/S ratio in the high quench rate case. After 0.4 seconds in the high quench rate case the sorbent no longer captured any additional sulfur -- corresponding fairly well to the 982 C (1800°F) sulfation window cutoff. For the baseline conditions the reaction continued until about a 1.0 second residence time which again is consistent with the lower end of the sulfation window at 982°C (1800°F). These data suggest that the sorbent was of similar reactivity in both cases, but that the additional residence time at sulfation temperatures resulted in additional capture for the baseline quench rate case.

The time-resolved measurements of Vicron resulted in somewhat different findings. As Figure 7-18 shows, the capture of SO_2 using Vicron was very similar for both quench rate conditions. Again, the initial capture rate was very high, but stopped abruptly after about 0.2 seconds. The Vicron does not continue to react in the baseline case after the initial capture even though the thermal environment is favorable for continued SO_2 pick up. This is believed to be caused by all of the readily available surface area being utilized within the first 0.2 - 0.3 seconds. These results demonstrate that the impact of quench rate on capture is sorbent dependent and that the initial reactivity of the sorbent is critical to its ultimate utilization.

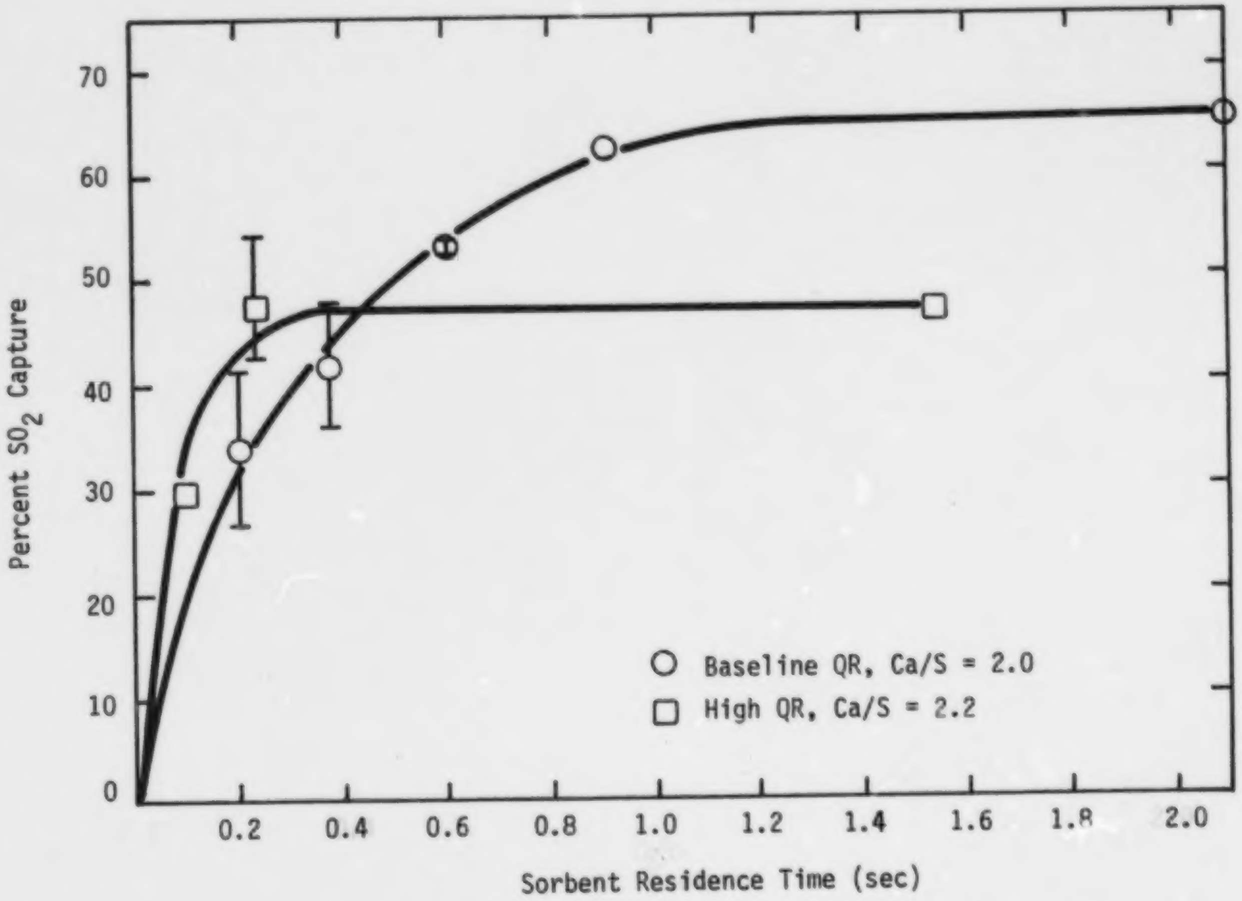

Figure 7-17. Time-resolved capture for Linwood atmospheric hydrate when injected into the CTT at 1260°C (2300°F) under two different quench rates.

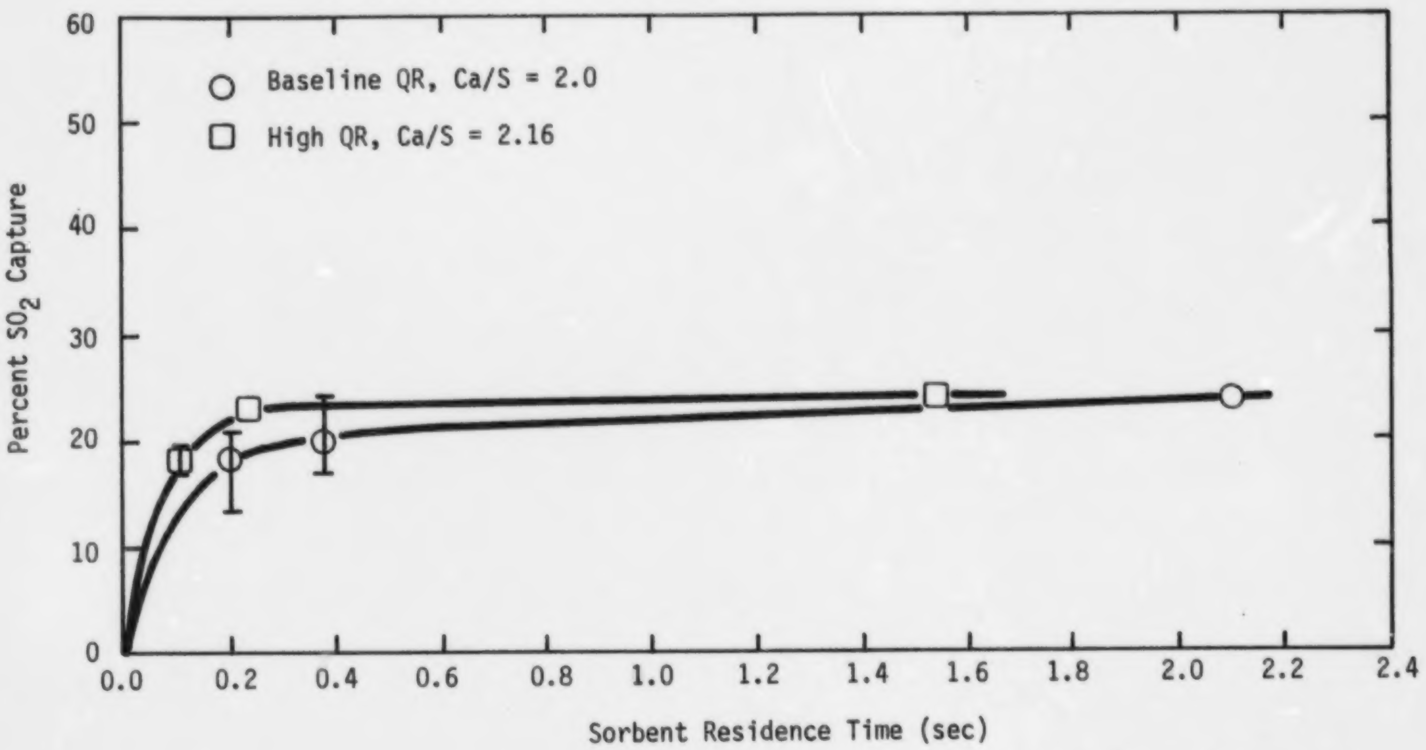

Figure 7-18. Time-resolved capture for Vicron carbonate when injected into the CTT at 1260°C (2300°F) under two different quench rates.

The effect of quench rate also impacts the influence of sorbent injection temperature on sulfur capture. Figure 7-19 presents capture versus injection temperature for the high quench rate conditions in the CTT compared to the low quench rate conditions in the BSF. Both Linwood hydrate and Vicron carbonate were used to compare the impact of quench rate on optimum injection temperature. A comparison of the two temperature profiles at similar injection temperatures is presented in Figure 7-20.

Figure 7-19 shows once again that a higher peak capture can be obtained with a slower quench rate. The BSF profile provides an exceptionally long time in the sulfation window (about 2.2 seconds). It can be seen that the optimum injection temperature is lower for the BSF because the slow quench rate results in peak particle temperatures that are closer to the injection temperature.

The reduction in capture as the injection temperature is increased beyond about 1260°C (2300°F) is partially due to the reduced stability of $CaSO_4$ at high temperatures as presented in the previous section, and, in part, to increased particle sintering. Note that the low quench rate capture (BSF) drops off more sharply at high injection temperature. This is believed to be due to a longer residence time at temperatures which promote sintering, reducing surface area and resulting in a less reactive sorbent.

Vicron follows the same trends as Linwood hydrate. However, Figure 7-19 shows that the sorbent is much less sensitive to injection temperature and the optimum injection temperature is shifted to lower temperatures for both quench rates. The lower optimum injection temperature for Vicron may be due to a lower susceptibility to fragmentation than the Linwood hydrate.

In summary, the thermal history which a sorbent experiences determines the initial reactivity of the material and establishes the temperature/ residence time experienced by the sorbent as it reacts with SO_2 to form calcium sulfate. In general, lower quench rates are more favorable for improved sulfur capture, but may not produce any improvement in ultimate capture if the sorbent reactivity is low. The optimum injection temperature

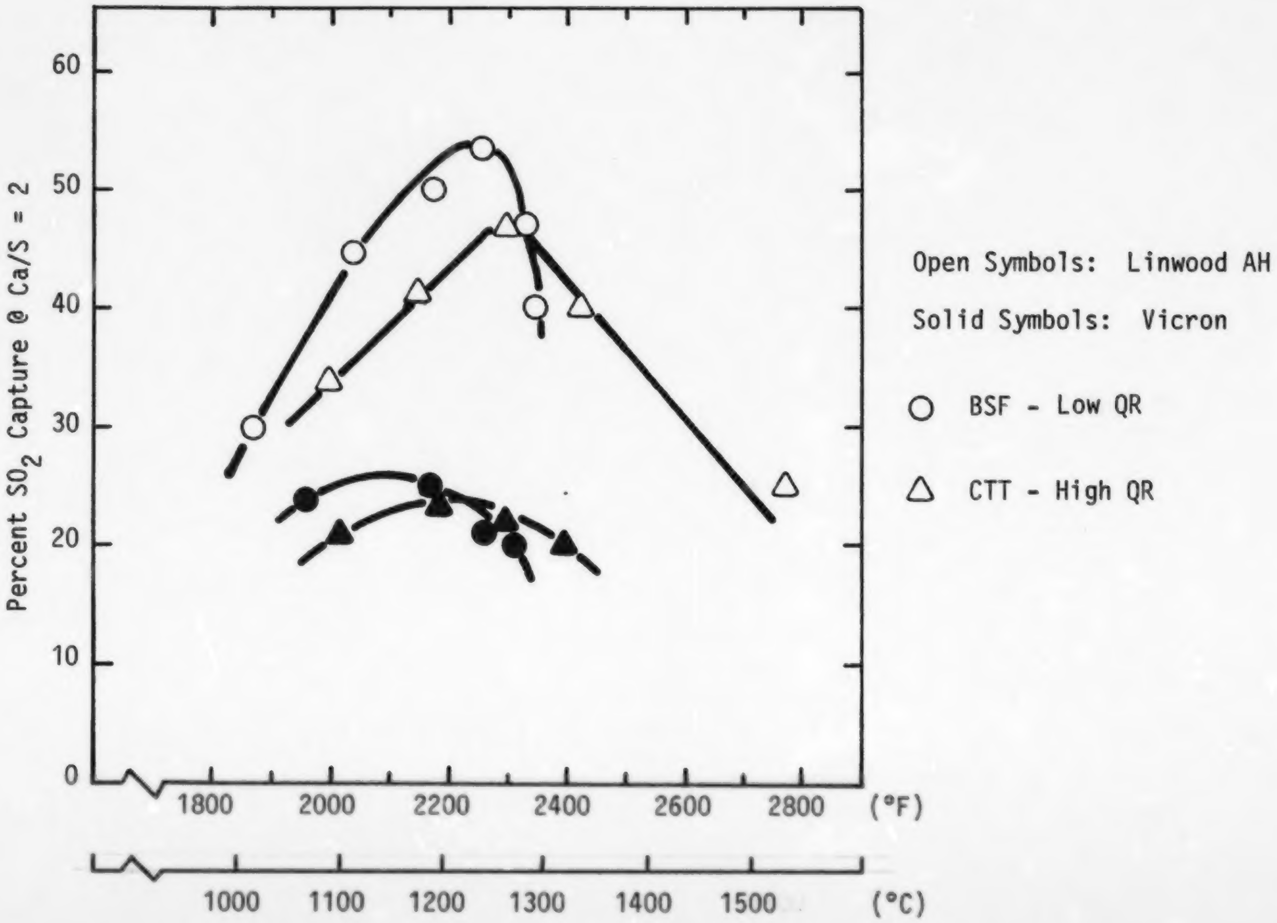

Figure 7-19. Comparison of the impact of quench rate on sorbent injection temperature for Linwood hydrate and Vicron carbonate.

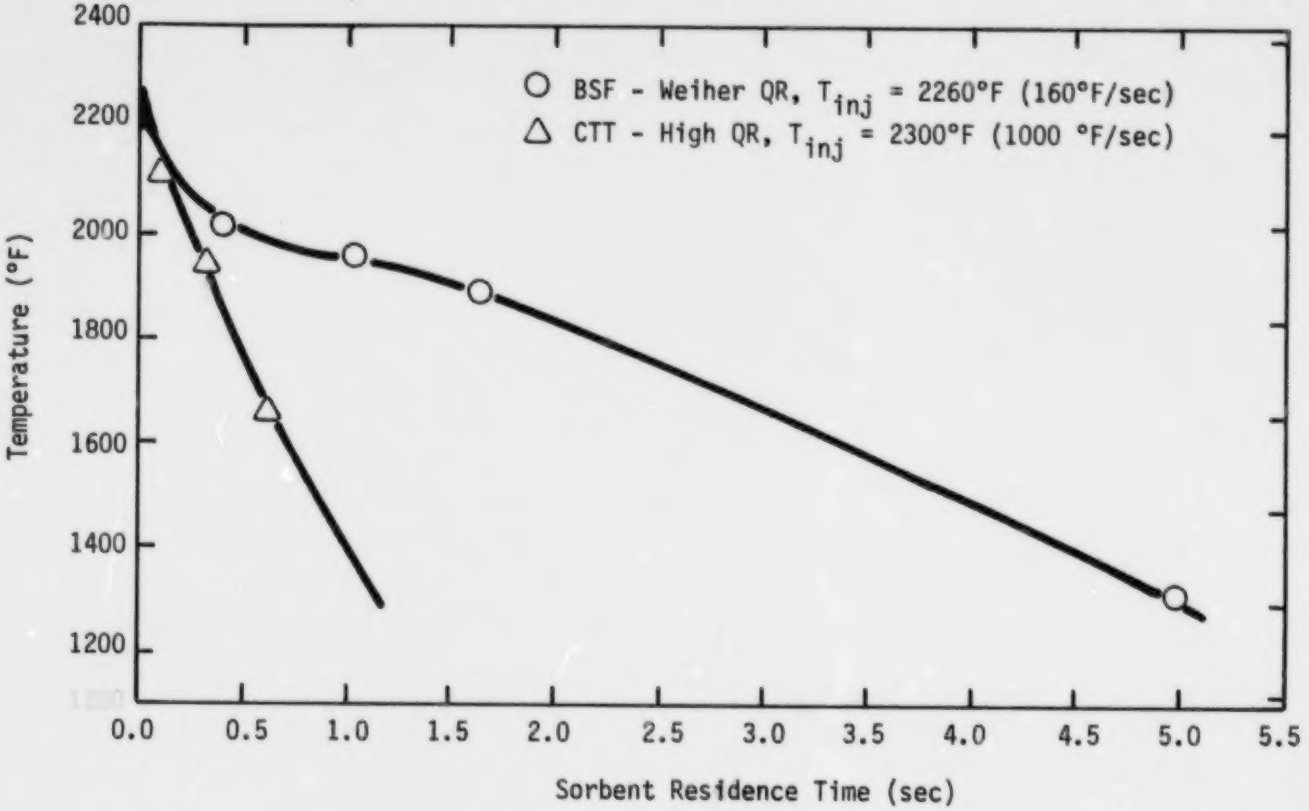

Figure 7-20. Examples of temperature profiles from the BSF and CTT at similar injection temperatures.

varies slightly with the quench rate. Lower quench rates require lower injection temperatures to avoid excessive sintering. Vicron (limestone) appears to be less sensitive to the thermal environment compared to the more reactive Linwood hydrate.

7.3 Influence of Sorbent Properties

It has been shown that the thermal environment in which a sorbent is exposed is critical to establishing the reactivity and the ultimate SO_2 capture of the material. Another important issue that will be addressed in this section is how sorbent properties can impact sulfur capture.

7.3.1 Sorbent Type

Two carbonates and two hydrates were tested under the CTT baseline conditions with the objective of explaining the obvious differences in the reactivity of different sorbent types. As shown in Figure 7-21, the hydrates (Linwood and Colton) were much more effective sorbents than the carbonates (Linwood and Vicron). These data were obtained in an earlier EPA program at EER and were originally reported by Overmoe et al. (1986).

Within the same sorbent classification, Linwood hydrate provided significantly higher capture than Colton (58 percent compared to 40 percent at Ca/S = 2), and Linwood carbonate gave better results than Vicron (26 percent compared to 21 percent at Ca/S = 2). The same trend was observed when Linwood hydrate and Colton hydrate were tested under the high quench rate conditions (see Figure 7-16).

7.3.2 Particle Size

Past researchers have suggested that differences in particle size between different sorbent types and brands was the single most important property controlling sorbent reactivity and ultimate sulfur capture. The argument is that reactivity depends on developed surface area, that specific surface area is primarily a function of particle size, and that, once

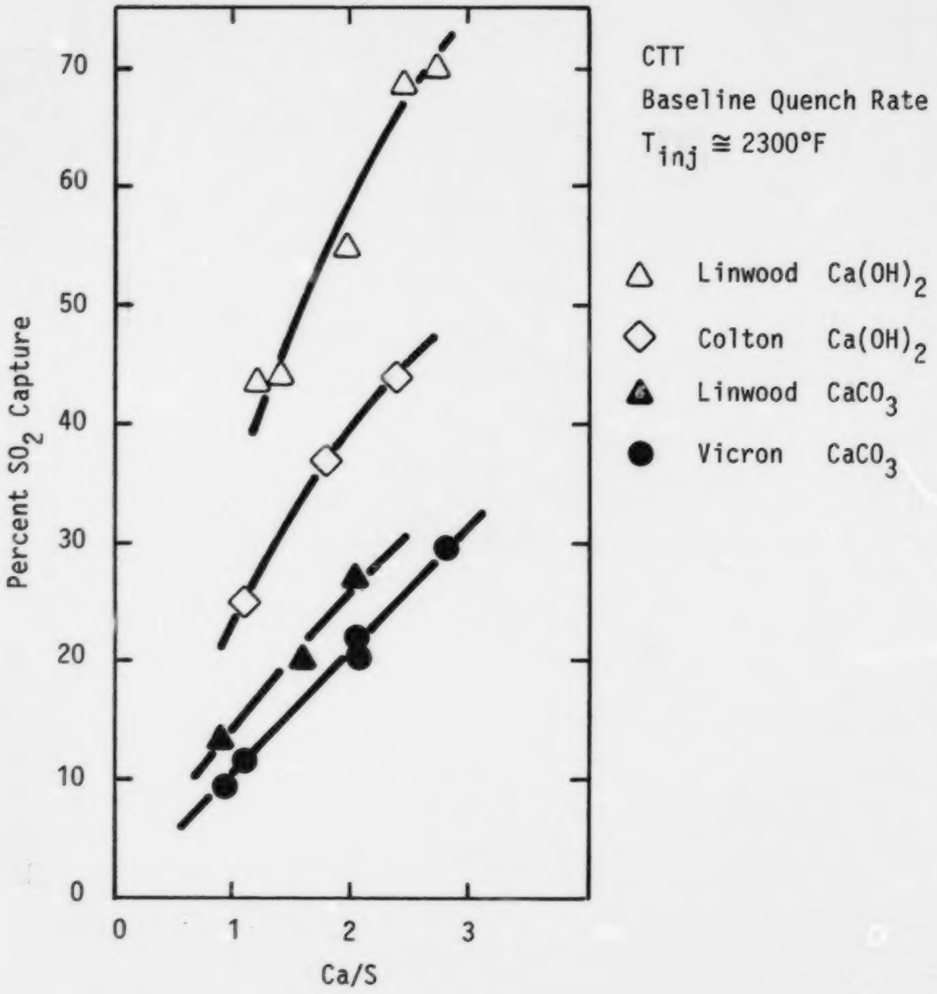

Figure 7-21. Comparison of sulfur capture capability for four different sorbent materials (Overmoe et al., 1986).

calcined, particles of the same size are of similar reactivity regardless of type, i.e., CaO from a hydrate is identical to CaO from a carbonate.

In reviewing the analyses of each of the four sorbents tested, the most obvious physical difference between sorbents is, indeed, their particle size distributions. Sedigraph size analysis was performed on each material and the resulting size distributions are presented in Figure 7-22. The sorbents rank, from the largest to the smallest as follows: Linwood $CaCO_3$ (13.3 μm), Vicron (9.8 μm), Colton (4.0 μm) and Linwood $Ca(OH)_2$ (2.2 μm). In general, smaller sized sorbent obtains higher sulfur capture levels. However, it is difficult to make a comparison of sorbent types or draw informed conclusions without testing the materials on a common size basis. To this end, all four materials were air classified into a number of narrow size bands. Testing of a number of size cuts for each material allowed comparison of the sorbents at the same size and helped establish capture trends as a function of particle size.

Materials with mean particle sizes ranging from 1.3 to 26 μm were tested, including four sizes of Linwood hydrates, three of Colton hydrate, three of Linwood carbonate, and four of Vicron carbonate. Figure 7-23 summarizes these results. Each size cut sorbent was tested under identical conditions: the baseline quench rate firing SO_2-doped natural gas, with an injection temperature of 2300°F.

The majority of the data show a similar trend of improved sulfur capture at smaller mean particle sizes. However, although the data are of similar slope over wide ranges of particle size, the capture magnitudes are displaced according to the type of material. At the same size, Linwood hydrate is much more reactive than Colton hydrate and Linwood carbonate is significantly more reactive than Vicron carbonate. In each case, a summation of the capture using weighted averages for discreet size ranges corresponded well (within 5 percent absolute) to capture results using the parent material.

The trend towards higher capture at smaller particle size is consistent with what is expected based on theoretical considerations, i.e., that the calcined, particles of the same size are of similar reactivity regardless of type, i.e., CaO from a hydrate is identical to CaO from a carbonate.

In reviewing the analyses of each of the four sorbents tested, the most obvious physical difference between sorbents is, indeed, their particle size distributions. Sedigraph size analysis was performed on each material and the resulting size distributions are presented in Figure 7-22. The sorbents rank, from the largest to the smallest as follows: Linwood $CaCO_3$ (13.3 μm), Vicron (9.8 μm), Colton (4.0 μm) and Linwood $Ca(OH)_2$ (2.2 μm). In general, smaller sized sorbent obtains higher sulfur capture levels. However, it is difficult to make a comparison of sorbent types or draw informed conclusions without testing the materials on a common size basis. To this end, all four materials were air classified into a number of narrow size bands. Testing of a number of size cuts for each material allowed comparison of the sorbents at the same size and helped establish capture trends as a function of particle size.

Materials with mean particle sizes ranging from 1.3 to 26 μm were tested, including four sizes of Linwood hydrates, three of Colton hydrate, three of Linwood carbonate, and four of Vicron carbonate. Figure 7-23 summarizes these results. Each size cut sorbent was tested under identical conditions: the baseline quench rate firing SO_2-doped natural gas, with an injection temperature of 2300°F.

The majority of the data show a similar trend of improved sulfur capture at smaller mean particle sizes. However, although the data are of similar slope over wide ranges of particle size, the capture magnitudes are displaced according to the type of material. At the same size, Linwood hydrate is much more reactive than Colton hydrate and Linwood carbonate is significantly more reactive than Vicron carbonate. In each case, a summation of the capture using weighted averages for discreet size ranges corresponded well (within 5 percent absolute) to capture results using the parent material.

The trend towards higher capture at smaller particle size is consistent with what is expected based on theoretical considerations, i.e., that the

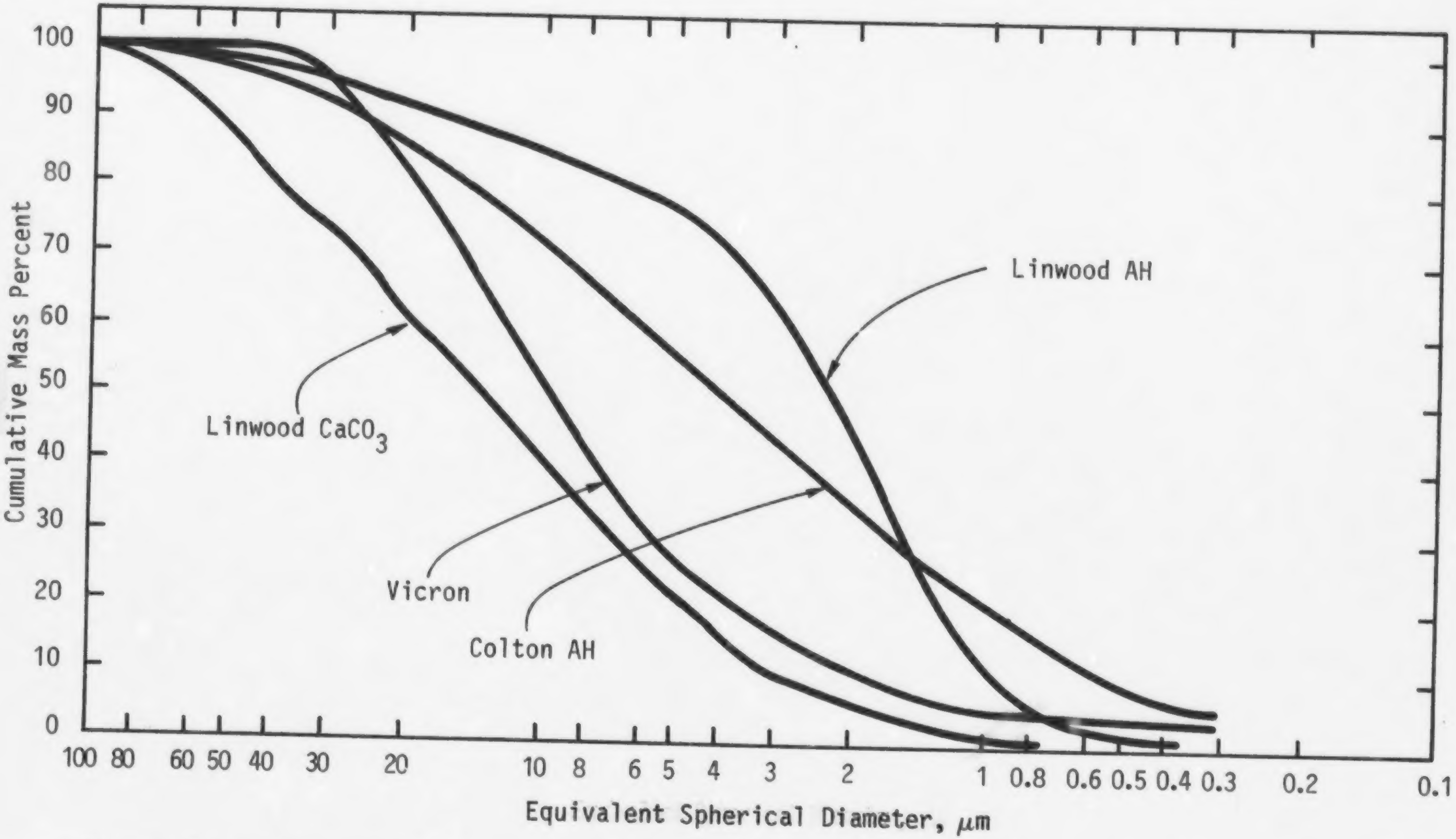

Figure 7-22. Comparison of sorbent size distributions as measured by sedigraph technique

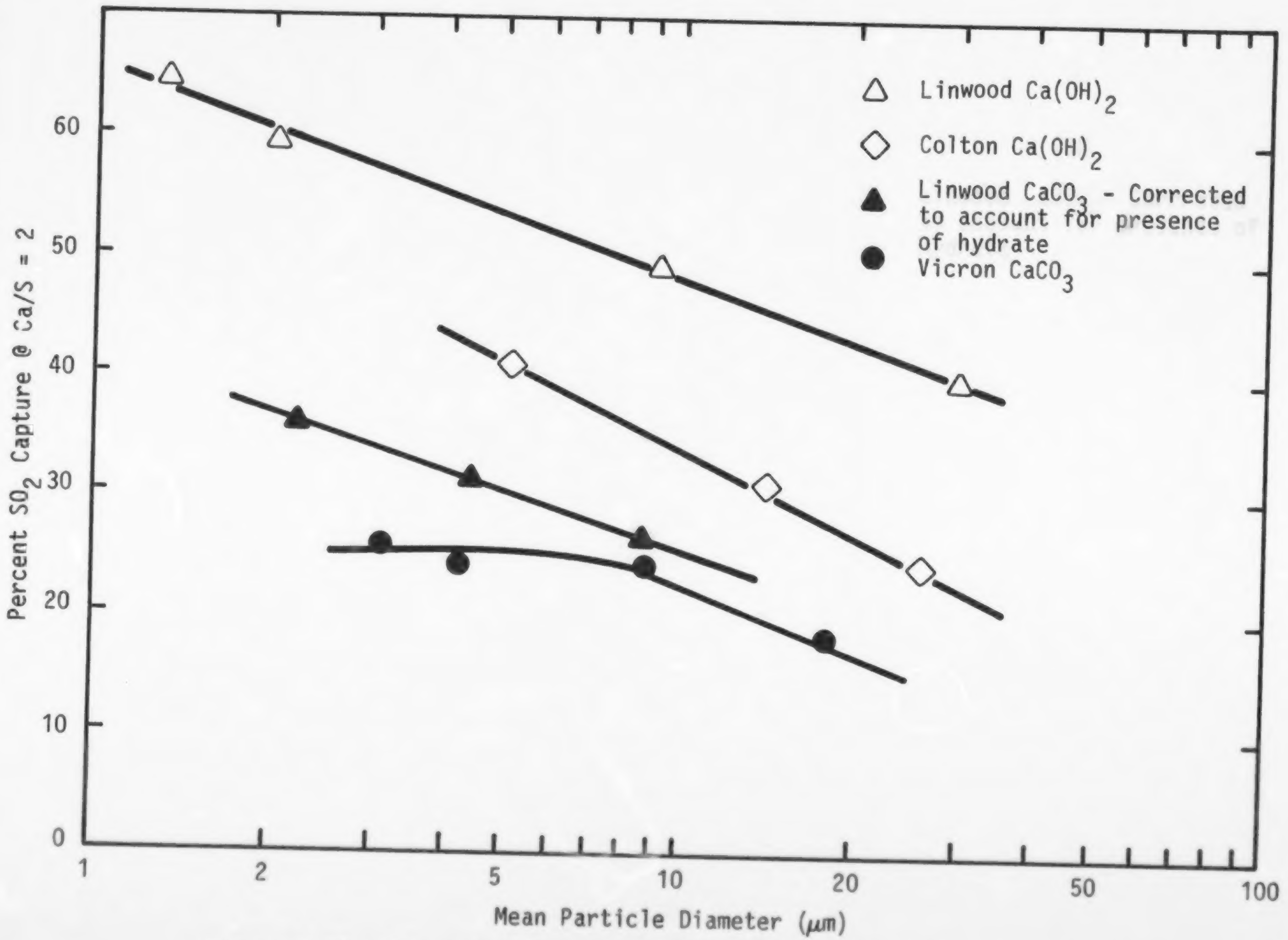

Figure 7-23. Comparison of sulfur capture for four different sorbents as particle size is varied.

specific surface area increases as the sorbent size decreases. Also, the slope of the data is fairly consistent to a compilation of carbonate data presented by Borgwardt and Bruce (1986). However, the fact that each material has a different, innate reactivity when compared at the same particle size is in opposition to conclusions drawn by Borgwardt and Bruce.

Figure 7-24 presents the same capture data plotted against specific surface area for the raw materials. The trend is for carbonates as expected, the higher the raw surface area the higher the measured SO_2 capture. But again, there is no clear correlation between raw surface area and sulfur capture for hydrates. Potentially, good correlation could be achieved using surface areas of the calcined sorbent material, but reliable sampling and handling techniques have not yet been established for this measurement.

Scanning electron microscopy (SEM) analysis has indicated a tremendous difference in physical structure between Linwood and Colton hydrates and noticeable differences between Linwood and Vicron carbonates. Figure 7-25 presents a highly magnified view of Linwood hydrate size cut to a mean diameter of 2.0 μm. Notice that the material appears to be clusters of 0.5 μm diameter nodules. These nodules are present throughout the entire Linwood hydrate size distribution, giving the appearance that the large particles would be easily fragmented when exposed to thermal or mechanical stress. The Colton, on the other hand, looks like larger agglomerates. Figure 7-26 presents a size cut of Colton with a mean diameter of 5.1 μm. The surface of the particles look extremely porous, but the body of the particles appear to be held rigidly together by webbed connections. This webbing is probably due to the high silicon content in the Colton sorbent (3.30 wt percent Si compared to 0.66 percent for Linwood hydrate). At the same size, Linwood looks much more susceptible to fragmentation upon injection at furnace temperatures compared to the Colton sorbent.

The Vicron carbonate showed a tendency to cease increasing in capture as the particle size decreased below about 9 μm. This trend is consistent with previous nonpublished data obtained at EER using air classified Marblewhite carbonate at slightly different test conditions. This implies that efforts

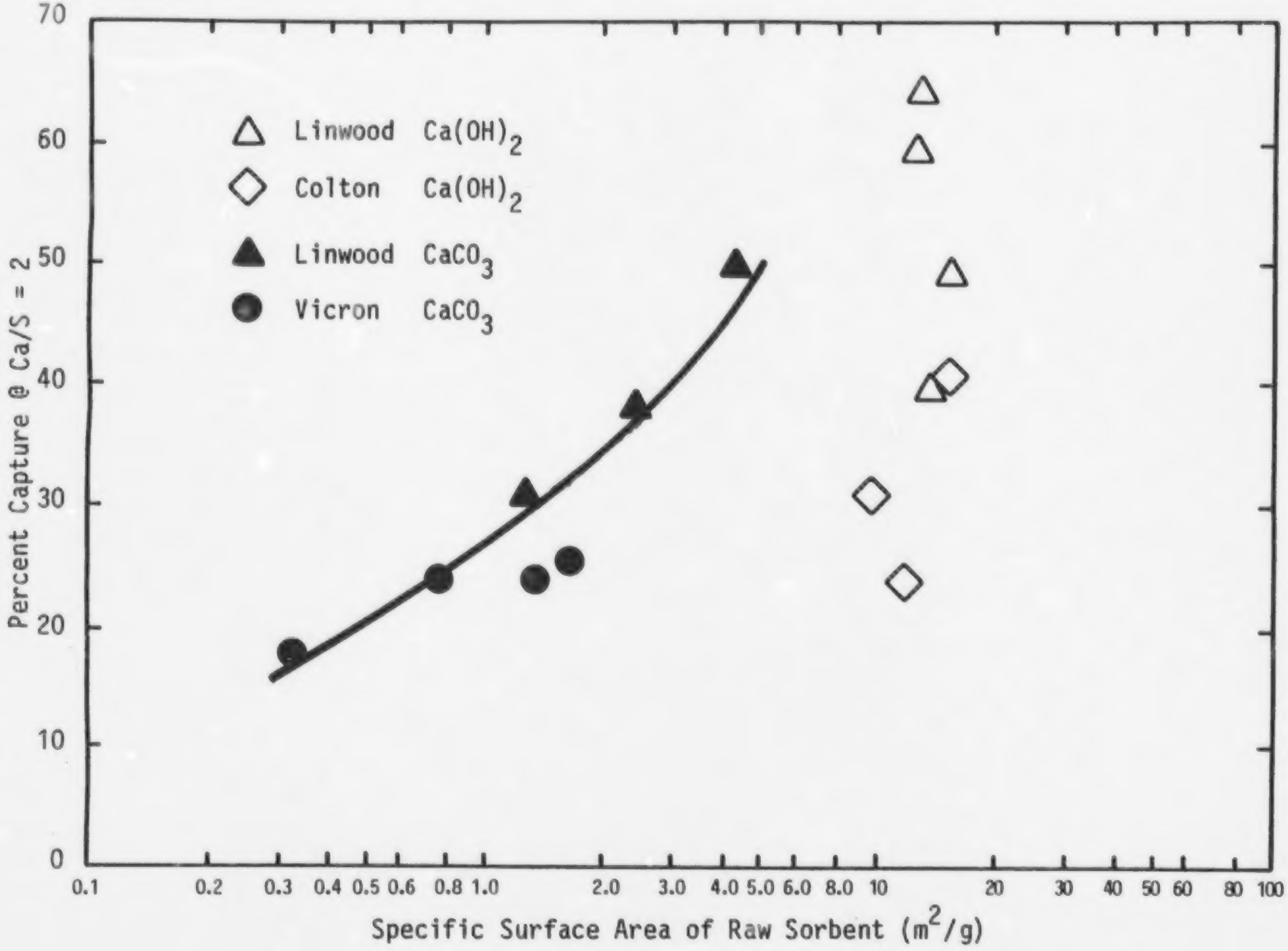

Figure 7-24. Comparison of sulfur capture for four different sorbents at varied specific surface areas.

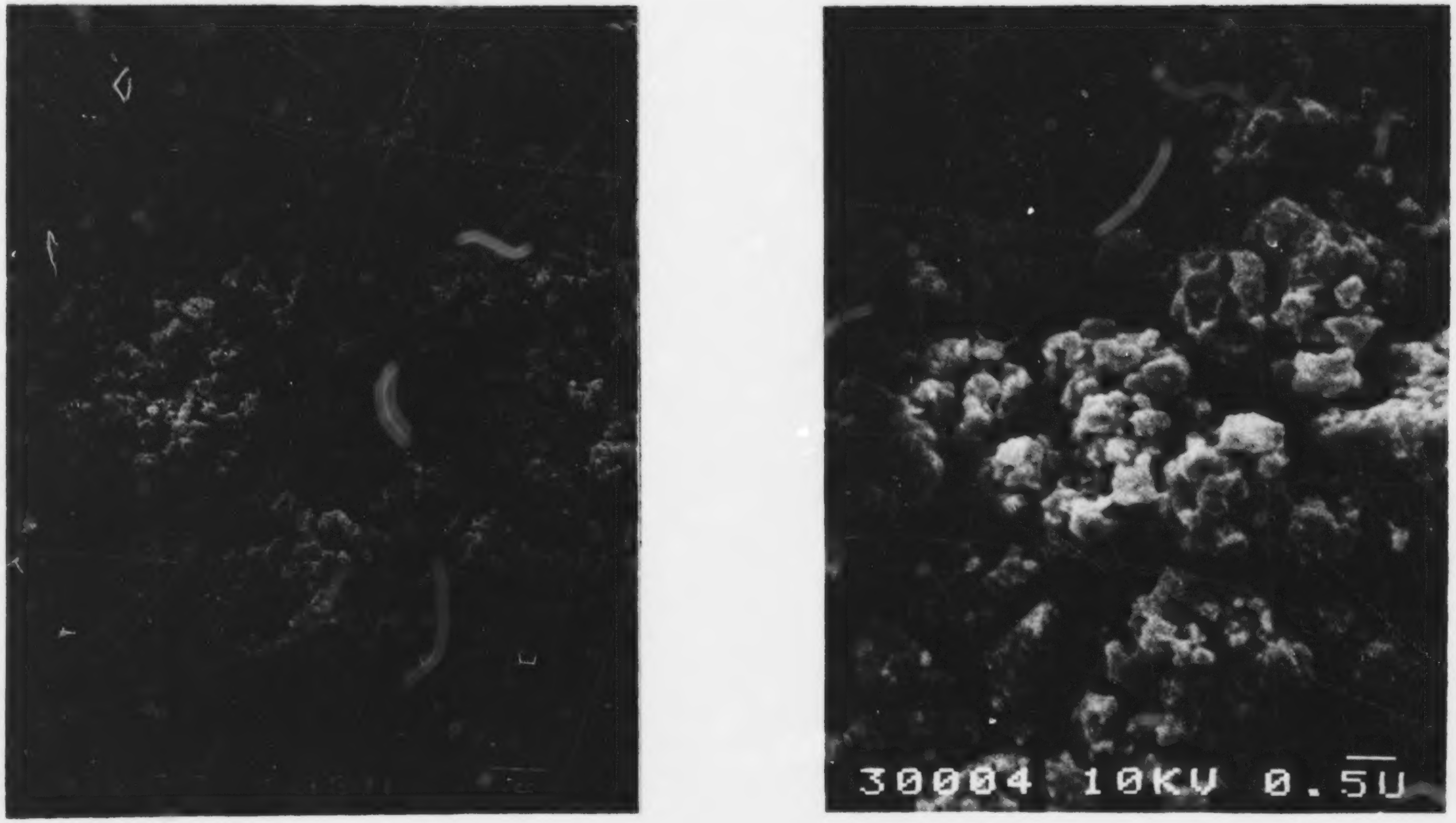
30004 10KV 0.5U

Figure 7-25. Linwood hydrate (2.0µm size cut).

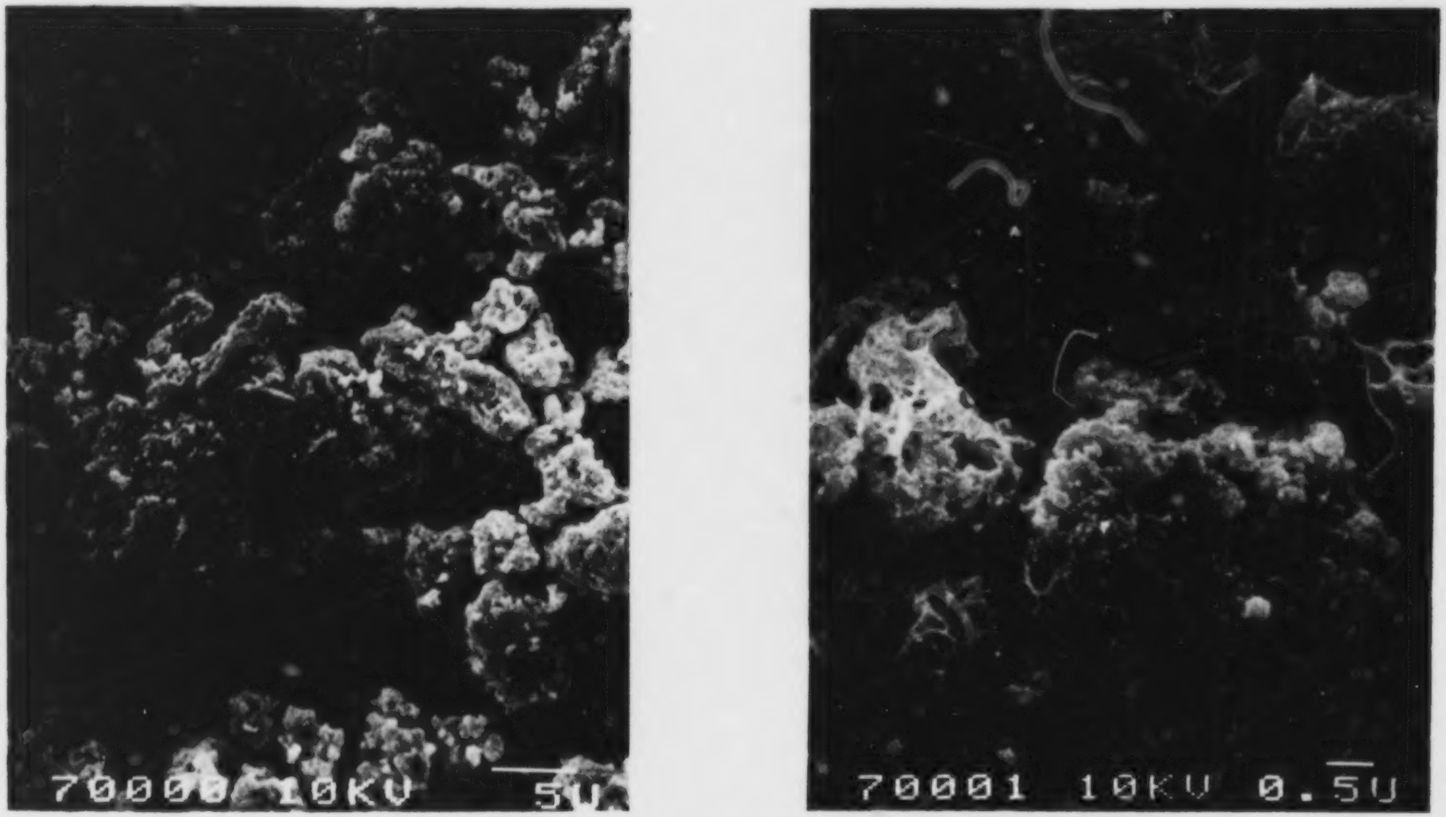
70000 10KV 5U
70001 10KV 0.5U

Figure 7-26. Colton hydrate (5.1µm size cut).

to decrease calcium carbonate size by increased pulverization will not result in drastically improved sulfur capture.

When testing the Linwood carbonate, it initially acted quite differently from other carbonates. Its performance increased drastically as the particle size decreased. Elemental analyses for carbon and hydrogen were performed on the size cut Linwood carbonate revealed high levels of hydrogen in the fine sized particles, indicating hydrate contamination in the fines. The smaller the size distribution the more hydrogen was present. The amount of calculated calcium hydroxide increased from 10 percent (by mole) at a mean size of 8.6 μm to 41 percent at a mean size of 2.2 μm. The data in Figure 7-23 present the measured values corrected for the amount of capture attributed to the hydrate in the mixture, so that capture from the carbonate itself is presented. The correction calculation is based on the amount of hydrogen measured in the size cut material, the respective Ca/S ratios for both carbonate and hydrate, and the hydrate capture capability drawn from the size cut data using pure Linwood hydrate. Without considering the effect of the presence of hydrate, the fine sized Linwood carbonate would have given results that were misleadingly high. Figure 7-27 shows an SEM comparison of the fine Linwood carbonate and pure Linwood hydrate. The small clustered particles of the carbonate look similar to the hydrate particles.

Table 7-2 presents a break down of the molar percentage of hydrate versus carbonate for each size cut material and their parent sorbent. Notice that the fine size cut Vicron has essentially no hydrate in it at all and that the Linwood hydrate has a small amount of carbonate. The larger the Linwood hydrate, the more carbonate is present. The existence of carbonate in the parent hydrate sorbent is thought to be dependent on the efficiency of the calcination process, whereas the presence of hydrate in the parent carbonate sorbent is due to the natural occurrence of hydrate in the carbonate as it exists at the mine site.

A comparison between the two carbonates by SEM also reveals some visual differences. Figure 7-28 shows that the Vicron is very angular. Its sharp corners give it a "hard" appearance. The Linwood, on the other hand, has

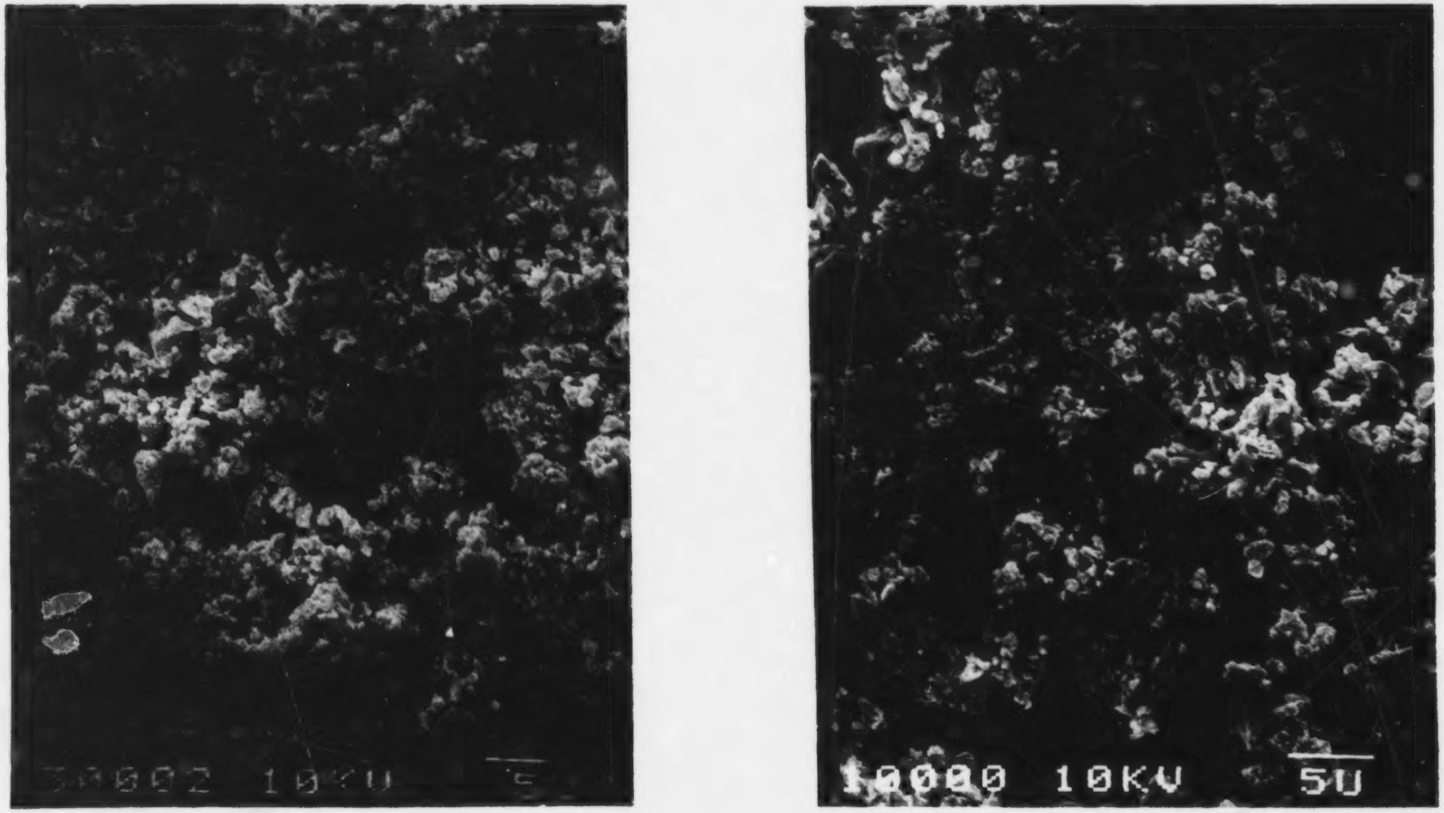
10000 10KV 5U

Figure 7-27. Linwood hydrate (2.0μm) vs. Linwood carbonate (2.2μm).

TABLE 7-2. CALCULATED DISTRIBUTION BETWEEN HYDRATE AND CARBONATE FOR FOUR DIFFERENT SORBENTS AND THEIR SIZE CUT COUNTERPARTS.

Sorbent Type	Size Range 10-90% by wt (μm)	Mean Particle Size (μm)	$CaCO_3$ (% by mole)	$Ca(OH)_2$ (% by mole)
Linwood $Ca(OH)_2$ (Parent)	0.95-16.0	2.2	2.2	97 .8
Linwood $Ca(OH)_2$	0.78- 2.2	1.3	9.5	90 .5
Linwood $Ca(OH)_2$	0.96- 6.8	2.0	8.0	92 .0
Linwood $Ca(OH)_2$	1.1 - 7.6	2.4	9.2	90 .8
Linwood $Ca(OH)_2$	1.1 -19.0	9.1	12.3	87 .7
Linwood $Ca(OH)_2$	19 -52.0	30.0	16.3	83 .7
Colton $Ca(OH)_2$ (Parent)	0.54-24.0	4	7.2	92 .8
Colton $Ca(OH)_2$	1.5 -11.0	5.1	5.9	94 .1
Colton $Ca(OH)_2$	8.6 -21.0	14.0	4.7	95 .3
Colton $Ca(OH)_2$	15.5 -42.0	26.0	6.8	93 .2
Linwood $CaCO_3$ (Parent)	2.8 -55.0	13.3	92.8	7 .2
Linwood $CaCO_3$	1.1 - 4.4	2.2	58.9	41 .1
Linwood $CaCO_3$	1.8 - 7.2	4.4	76.6	23 .4
Linwood $CaCO_3$	4.6 -14.0	8.6	89.5	10 .5
Vicron $CaCO_3$ (Parent)	1.9 -24.0	9.8	96.1	3 .9
Vicron $CaCO_3$	0.6 - 2.0	1.1	99.0	1 .0
Vicron $CaCO_3$	1.3 - 6.4	3.1	99.0	1 .0
Vicron $CaCO_3$	1.9 - 7.0	4.2	97.6	2 .4
Vicron $CaCO_3$	4.8 -14.0	8.8	99.0	1 .0
Vicron $CaCO_3$	11.0 -29.0	18.0	99.0	1 .0

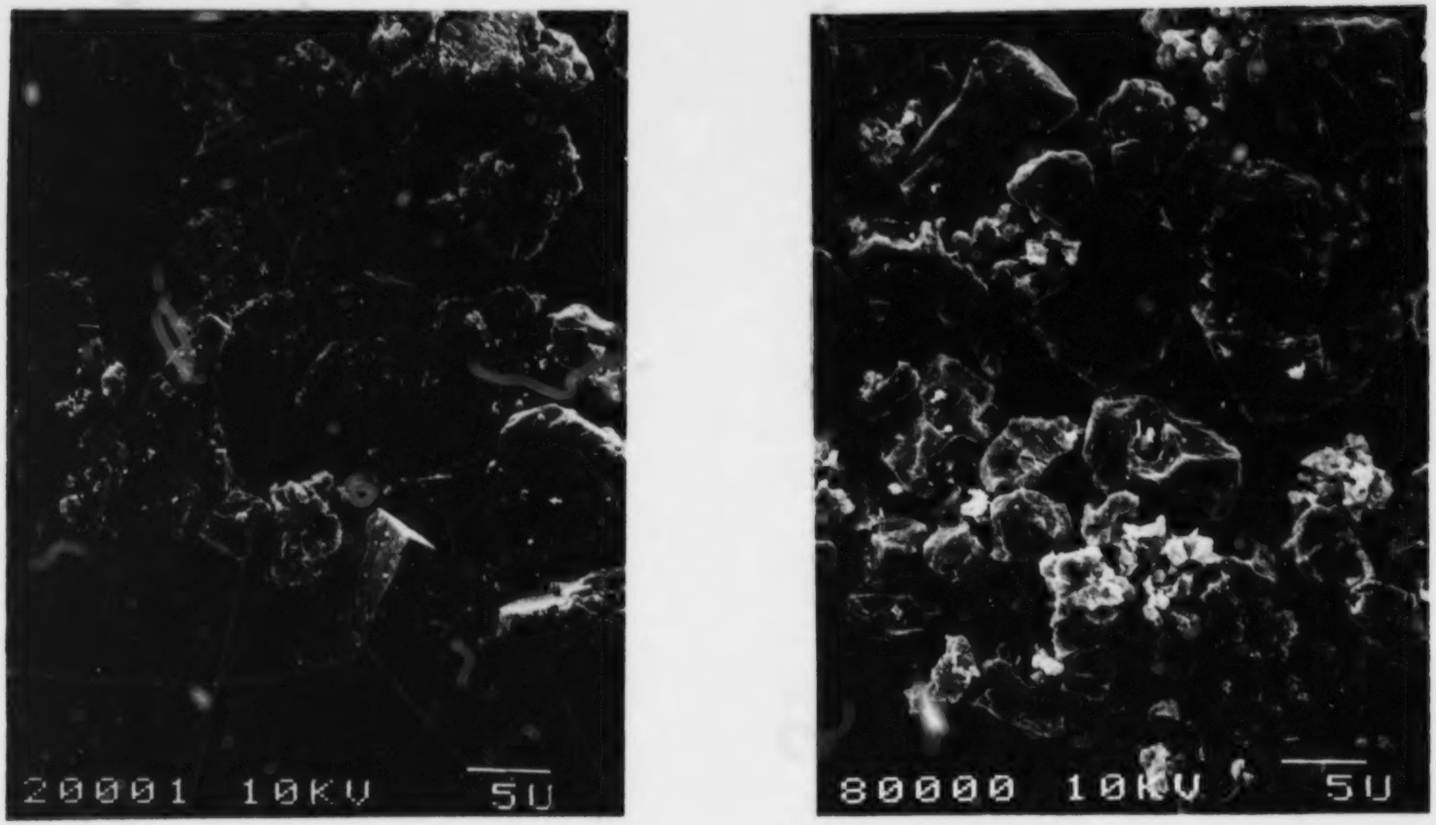
20001 10KV 5U
80000 10KV 5U

Figure 7-28. Carbonate comparison: Vicron (8.8μm) vs. Linwood (8.6μm).

much more rounded edges and a "softer" appearance. It is not known why the Linwood carbonate is so much more reactive than the Vicron, but it may be tied to the presence of hydrate in the Linwood carbonate -- either by some form of carbonate enhancement process or just as an indication of the reactivity of the Linwood material.

In conclusion, sorbent properties have a tremendous influence on SO_2 capture. When compared at the same size, hydrates are much more reactive than carbonates. Even within the same classification some sorbents are more reactive than others (e.g., Linwood and Colton hydrates). Physical differences in morphology and composition can cause these variations in reactivity. In particular, the presence of a small amount of hydrate in a predominatly carbonate sorbent can produce unexpectedly high capture results.

(GEN. 4208 F/R (8))

8.0 ANALYSIS OF PROCESS PARAMETERS

The process parameters selected for analysis in this section include sorbent thermal history, sorbent particles size, and SO_2 concentration. The parameters which characterize sorbent thermal history include injection temperature, quench rate, and time. The analytical treatment given below is an attempt at predicting the general trends seen in the bench-scale sulfation results presented in Section 6. In doing so, the grain model is used with parameters whose values are chosen to roughly match those of practical interest. For example, the particles size and SO_2 concentration calculations are performed for a quench rate of -600°F/s.

The grain model selected for the calculations includes grains of uniform size and it allows the grains to grow with time so as to simulate sintering. Unless otherwise specified, the model parameters are as follows:

- SO_2 concentration = 1500 ppm, wet, as measured,
- Injection temperature = 2200°F,
- Collection temperature = 1600°F,
- Particle diameter = 2μm,
- Initial surface area = 80m^2/g,
- Completely sintered surface area = 5m^2/g,
- Initial sorbent porosity = 0.5,
- Quench rate = -600°F/s,
- Oxygen mole fraction = 0.05.

Consideration of the effects of mixing are not included and the particles are assumed to be monosized.

8.1 Thermal History

The parameters which characterize the thermal history experienced by the particle include the quench rate and the injection temperature. Sorbent residence time is also discussed explicitly. The predictions are plotted with percent SO_2 capture at Ca/S = 2 on the ordinate and injection temperature or time on the abscissa.

Figure 8-1 shows the predicted effects of injection temperature and quench rate on SO_2 capture. The quench rates range from -200 to -1000°F/s. The family of curves shows an optimum injection temperature of about 2200°F. The location of the optimum is determined by the thermodynamic limits on the stability of $CaSO_4$ which is, in turn, dependent on the SO_2 concentration. This explains the slight shift to higher optimum injection temperatures as the capture levels fall with increasing quench rate. The precise location of the thermodynamic limits is unknown due to uncertainties in the equilibrium data. The data reported by Reid (1971) on the $CaSO_4$ system are representative of those used in this study. General expressions for the calculation of the equilibrium constant, K, and the equilibrium partial pressure of SO_2, P_{SO_2}, are given below for the reaction $CaO + SO_2 + 1/2\ O_2 = CaSO_4$:

$$K = \exp\left(\frac{61200}{T} - 37.0 + 0.00263T\right)$$

and

$$P_{SO_2}\ (\text{atm}) = P_t^{2/3} / (K \cdot P_{O_2}^{1/2})$$

where P_t is the total pressure in atmospheres and the temperature, T, is in degrees Kelvin.

The calculations shown is Figure 8-1 indicate that capture levels decrease if the optimum injection temperature is exceeded. This results from the sintering of CaO in the absence of sulfation. Figure 8-2 is a schematic showing the progress of the reaction for a case where the sorbent has been injected at a temperature in excess of the equilibrium temperature. In this instance the course of the reaction is divided into two zones, sintering without sulfation and sintering with sulfation. The first zone decreases the

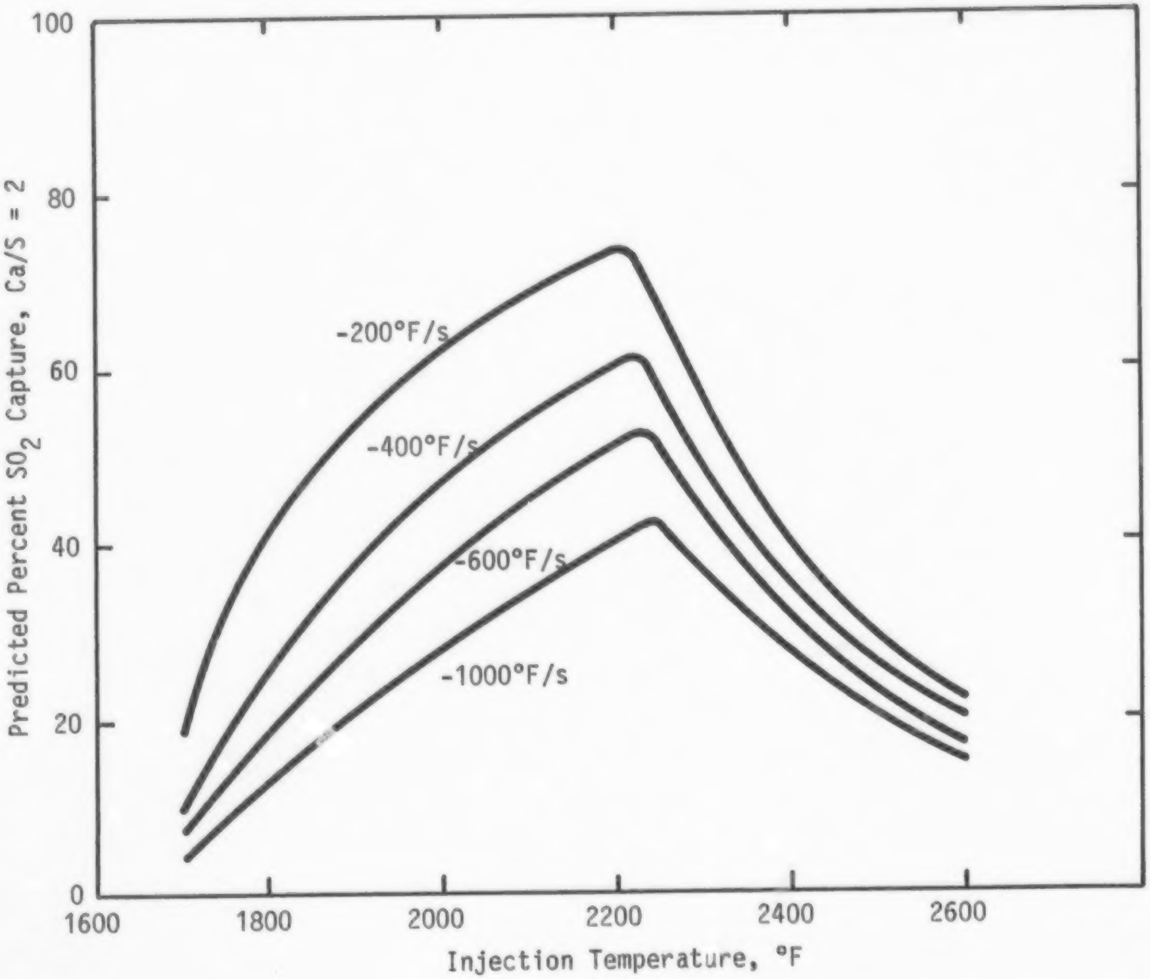

Figure 8-1. Grain model predictions showing the effect of injection temperature and quench rate assuming initial and asymptotic surface areas of 80 and $5m^2/g$, a SO_2 concentration of 1500 ppm (wet, as meas.), and particle size of 2μm.

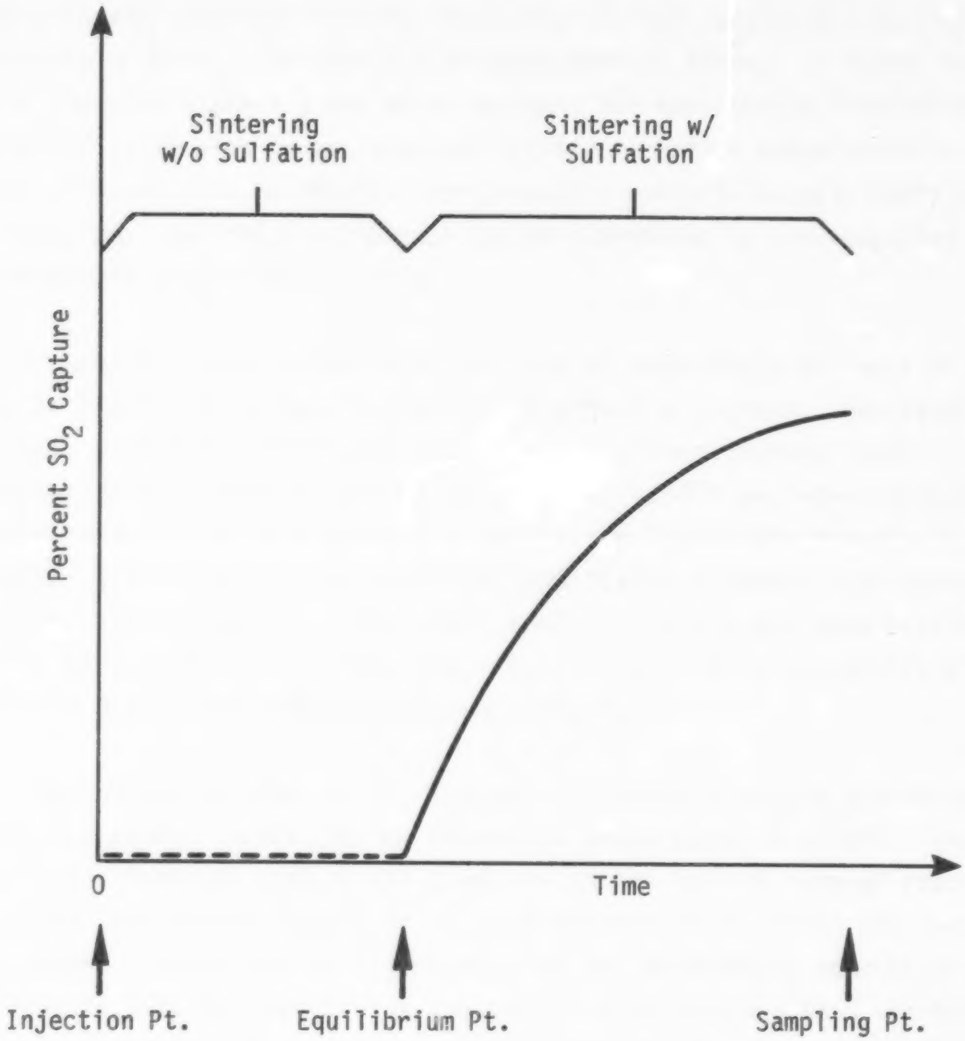

Figure 8-2. A schematic of the progress of the sulfation reaction for sorbent injected at temperatures in excess of the stability limit of $CaSO_4$.

reactivity of the sorbent before it has a chance to react with SO_2. Hence, the overall capture is lower.

Comparison of Figure 8-1 with Figure 6-1 shows that the grain mode predicts the general trends observed in the bench-scale, injection temperature data. The data can be understood in terms of a sulfation model which includes sintering and which accounts for equilibrium constraints. As discussed in Section 6, the observed optimum injection temperature is in the range of from 1800 to 2000°F. The predicted value is roughly 200°F higher. At least part of this difference can be attributed to uncertainties in the thermodynamic properties of $CaSO_4$.

Figure 8-1 also shows that the rate of temperature decrease or quench rate is predicted to have a significant effect on capture. The bench-scale CTT data presented in Figure 6-3 show 60 percent capture (Ca/S = 2) at a quench rate of -350°F/s and 43 percent for -950°F/s. The corresponding predicted values from Figure 8-1 (at T_{inj} = 2300°F) are roughly 50 and 36 percent, respectively. The predicted sensitivity to quench rate agrees with that observed on the CTT. The other results in Figure 6-3 show little or no effect of quench rate. This insensitivity cannot be reconciled with the model and may be attributable to mixing effects.

The effect of time on SO_2 capture is shown in Figure 8-3 for several different quench rates and an injection temperature of 2200°F. The model predictions indicate that at all quench rates the initial rate of reaction is rapid and that capture levels of 30 to 36 percent occur within 200 msec after injection. Comparison of Figure 8-3 with the bench-scale results of Figure 6-4 reveals that the same trends are exhibited by both and that the data also shows a rapid initial reaction rate. The data of Farzan, et al. (1986) and the CTT results both show capture levels of 30 percent, 200 msec after injection.

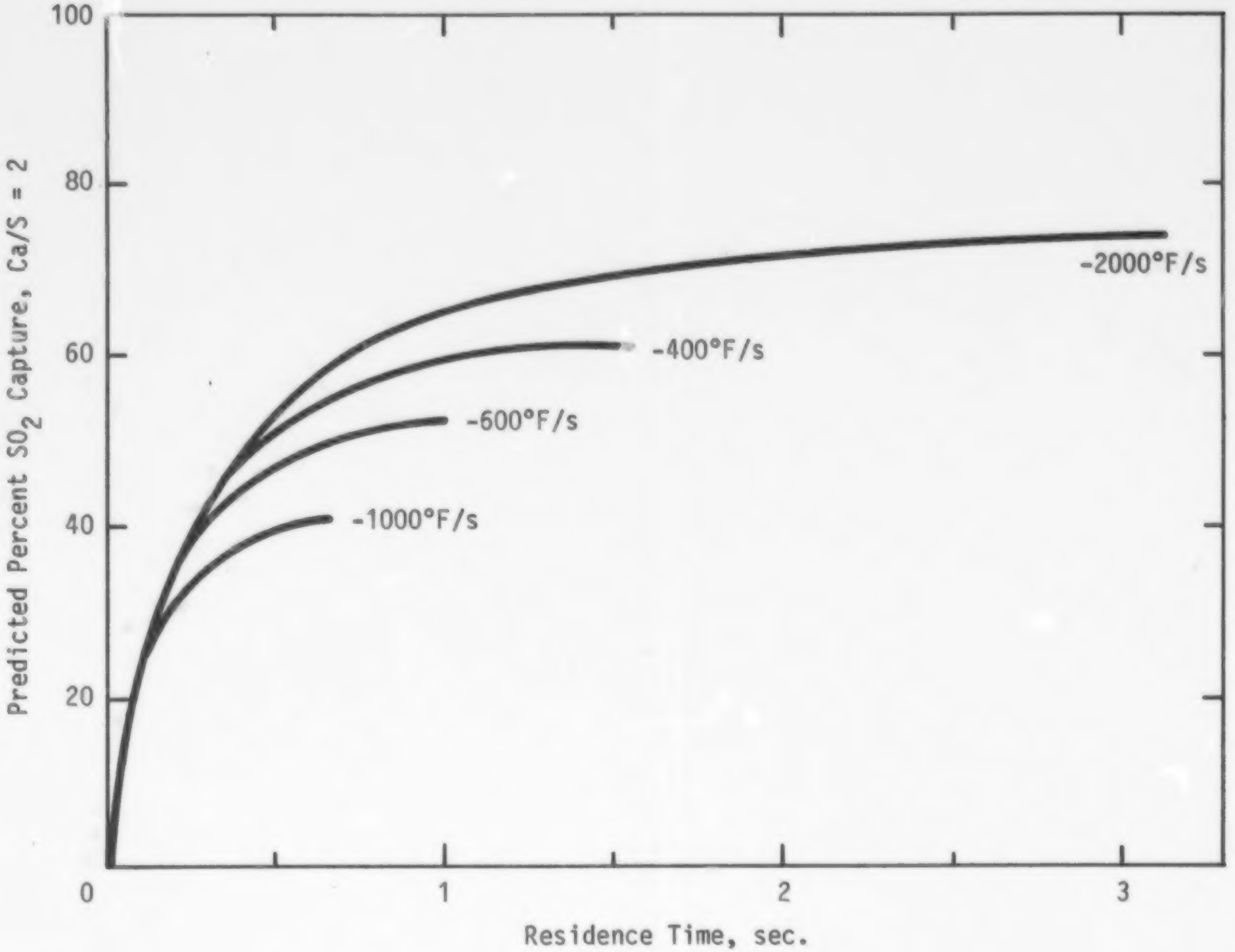

Figure 8-3. Grain model predictions showing the effect of residence time at different quench rates assuming an injection temperature of 2200°F and a sampling point temperature of 1600°F.

8.2 Particle Size

The predicted influence of sorbent particle size on SO_2 capture is illustrated in Figure 8-4 for initial sorbent surface areas of 20, 40, and 80 m^2/g. The calculations show a strong effect of particle diameter on capture. The sensitivity to diameter increases with increasing initial surface area. For large particles the rate of the reaction is completely dominated by pore diffusion so that increasing the surface area correspondingly decreases the rate of pore diffusion. Hence, no net increase in reactivity occurs. This can be seen in Figure 8-4 for particle diameters in excess of 20 μm.

The model also suggests that below a certain diameter threshold the sorbent utilization becomes independent of further reductions in particle size. This occurs because when the particle size becomes sufficiently small that pore diffusion resistance becomes negligible and the entire particle is uniformly accessible to SO_2. The data of Figures 6-5 and 7-23 do not show this "flatening" with decreasing size, which suggests that the threshold for pore diffusion resistance may be lower than that predicted by the model. Otherwise, the general trend of increasing capture with smaller particle size is consistent between model and data.

8.3 SO_2 Concentration

The predicted influence of SO_2 concentration on capture is shown in Figure 8-5. The grain model incorporates a 0.55 order dependence on SO_2, based on the fundamental studies of Borgwardt and Bruce (1986). Comparison of Figure 8-5 with the bench-scale results of Figure 6-6 shows that the model agrees with some of the data but that in general the data show a weaker dependence on SO_2. The 0.55 order used in the model may not be appropriate for describing data obtained under more practical conditions than those used by Borgwardt and Bruce.

Also shown in Figure 8-5 are predictions using the distributed pore model described in Section 4.2.4. The distributed pore model predicts a much weaker dependence on SO_2 concentration than the grain model and therefore

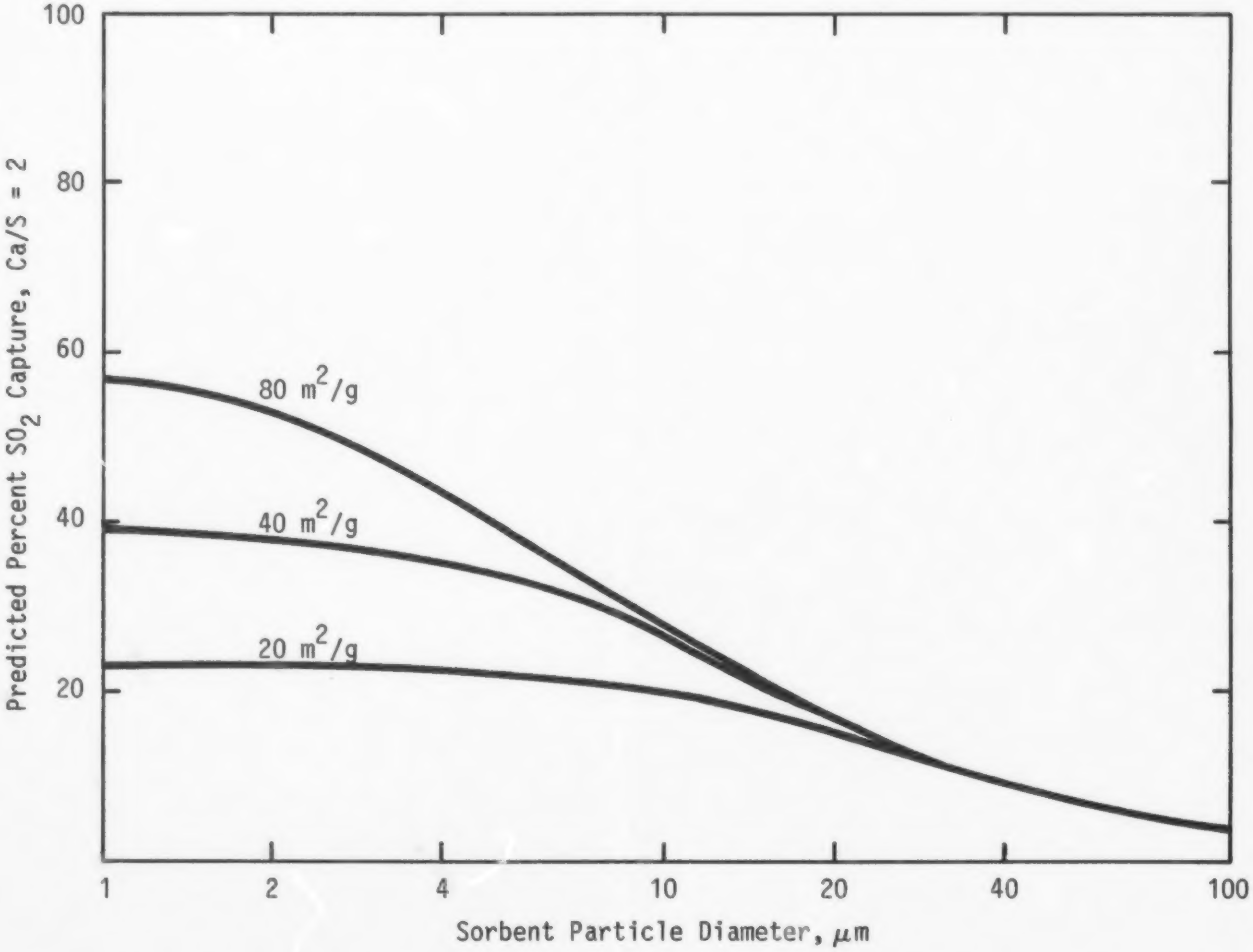

Figure 8-4. Grain model predictions showing the effect of particle diameter for different initial surface areas. A SO_2 concentration of 1500 ppm (wet, as meas.), an injection temperature of 2200°F, and a quench rate of -600°F/s were assumed.

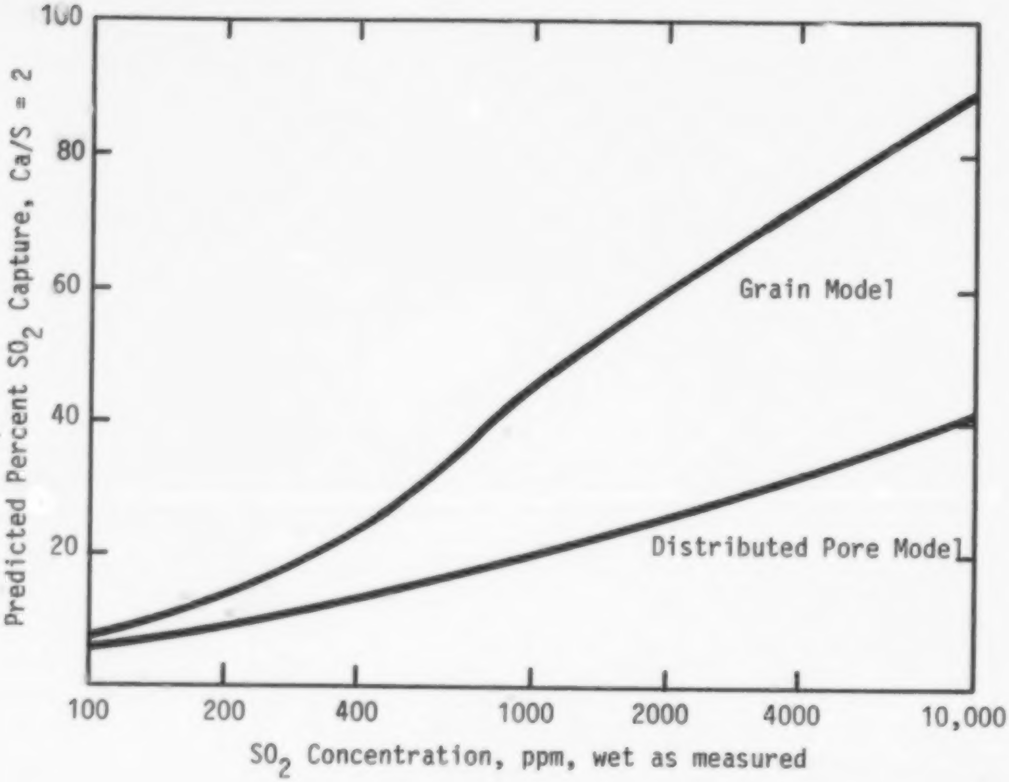

Figure 8-5. Grain model predictions (assuming initial and asymtotic surface areas of 80 and 5 m^2/g) and distributed pore model predictions showing the effect of SO_2 concentration. An injection temperature of 2200°F, a quench rate of -600°F/s, and a particle diameter of 2 μm were used in the calculations.

shows better agreement with the data plotted in Figure 6-6. The weak dependence on SO_2 concentration results not from from the order of chemical reaction (a first order dependence issued), but from the pore closure mechanism. As SO_2 concentration is increased the rate of pore closure at the particle surface increases, thus negating the increased rates of chemical reaction and diffusion within the particle.

8.4 Conclusions

In conclusion, the analysis of key process parameters in this section shows that from both an analytical and an experimental viewpoint, there is basic agreement on the importance and impact of injection temperature, quench rate, residence time, particle diameter, and SO_2 concentration. The analytical treatment of sulfation described here is capable of duplicating most of the experimentally observed trends and demonstrates significant understanding of the sulfation process.

GEN. 1208 F/R (9)

9.0 LARGE-SCALE TEST RESULTS

Large-scale test results from a variety of pilot- and full-scale facilities are summarized in this section. The pilot-scale facilities were fired with coal at rates ranging from 50 to 100 million Btu/hr. Sulfur capture data for full-scale boilers as large as 330 MW are presented. Because of the large size of these facilities it is difficult to characterize the sorbent injection process in terms of key parameters such as injection temperature, quench rate, and the rate of sorbent jet mixing. Nevertheless, conclusions regarding the effects of boiler load, sorbent type, and injection location are possible.

9.1 Compilation of Experimental Results

Full scale sorbent injection tests were performed on the TVA Shawnee steam plant in the late sixties and early seventies by Womble, et al. (1970). A schematic of the Shawnee Unit 10 is shown in Figure 9-1 with the elevations and locations of the sorbent injectors as indicated. When operating at full load (140 MW) the unit's approximate quench rate over the temperature extending from 2200°F down to 1700°F is -550°F/s. At reduced load (75 MW) the quench rate is roughly -380°F/s. The boiler is wall-fired and optimum sulfur capture results were obtained by injecting sorbent in the plane of the boiler arch or nose. At full load the approximate temperature in this plane is 2100°F. Temperature profiles for the plane including the arch and for the plane including the lower rear rear injectors are shown in Figure 9-2.

Three sorbents were tested at Shawnee: an aragonite, a marl, and Fredonia limestone with mass-mean diameters of 15, 6, and 9 μm, respectively. Averaged results for all three sorbents at full load and low load are presented in Figure 9-3. The marl and the Freidonia are of equal reactivity and are somewhat more reactive that the aragonite. This difference may be due to the large mean diameter of the aragonite. Decreasing the furnace load resulted in a small improvement in sorbent utilization. In general, the Shawnee capture levels are slightly lower than those obtained in other large-

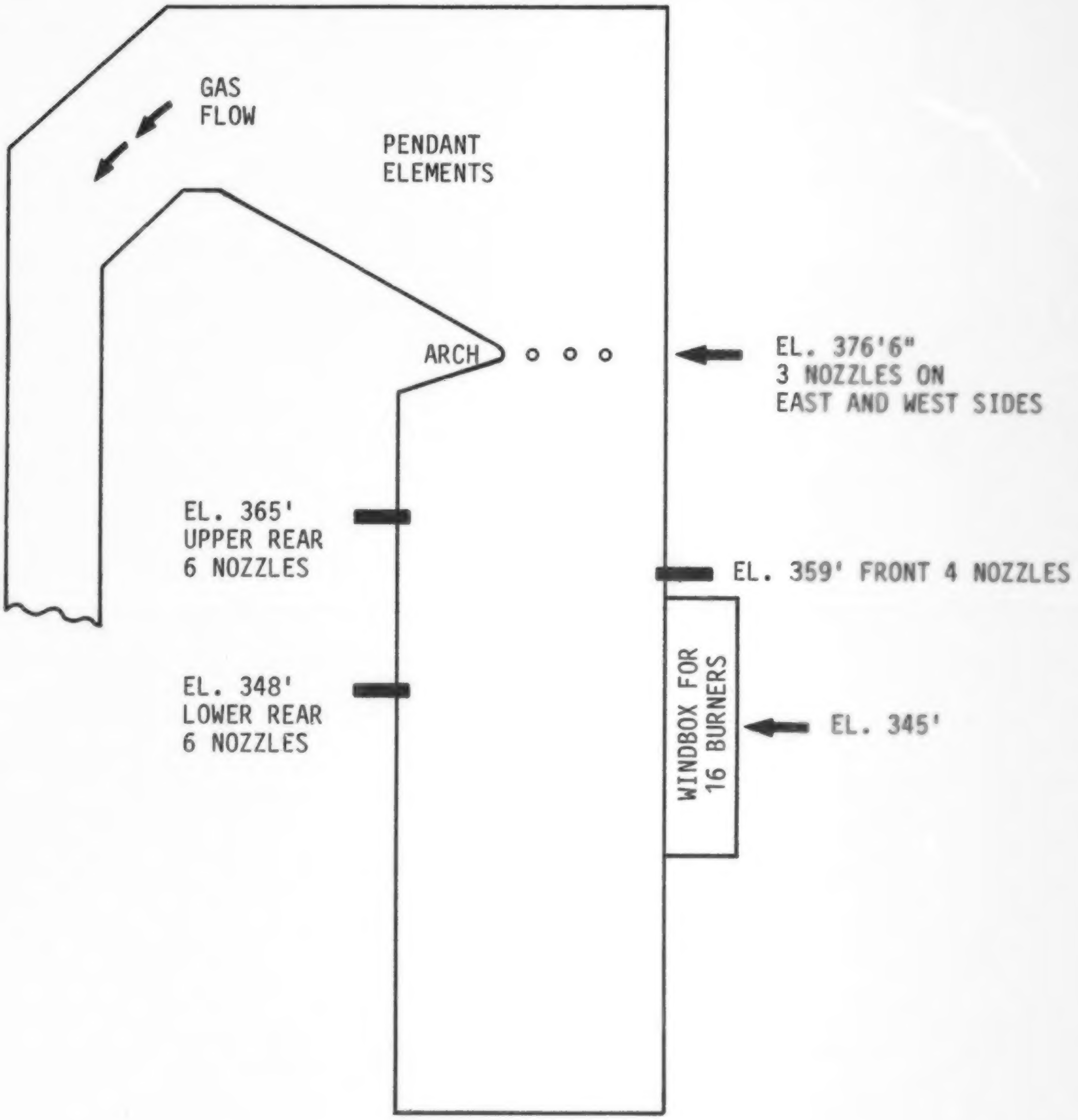
GAS
FLOW
PENDANT
ELEMENTS
ARCH
EL. 376'6"
3 NOZZLES ON
EAST AND WEST SIDES
EL. 365'
UPPER REAR
6 NOZZLES
EL. 359' FRONT 4 NOZZLES
WINDBOX FOR
16 BURNERS
EL. 345'
EL. 348'
LOWER REAR
6 NOZZLES

Figure 9-1. Schematic of Shawnee Unit 10 showing injection locations.

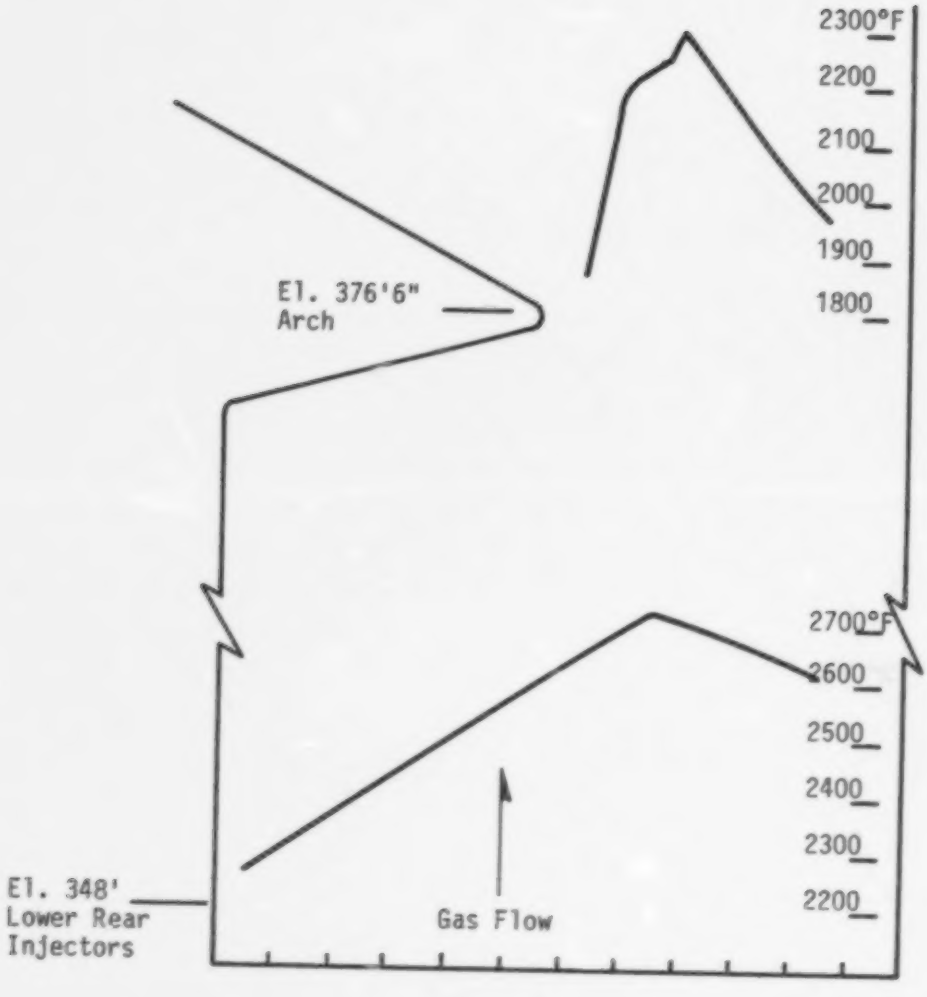

Figure 9-2. Measured temperature profiles for the planes including the Shawnee unit's arch and lower rear injectors.

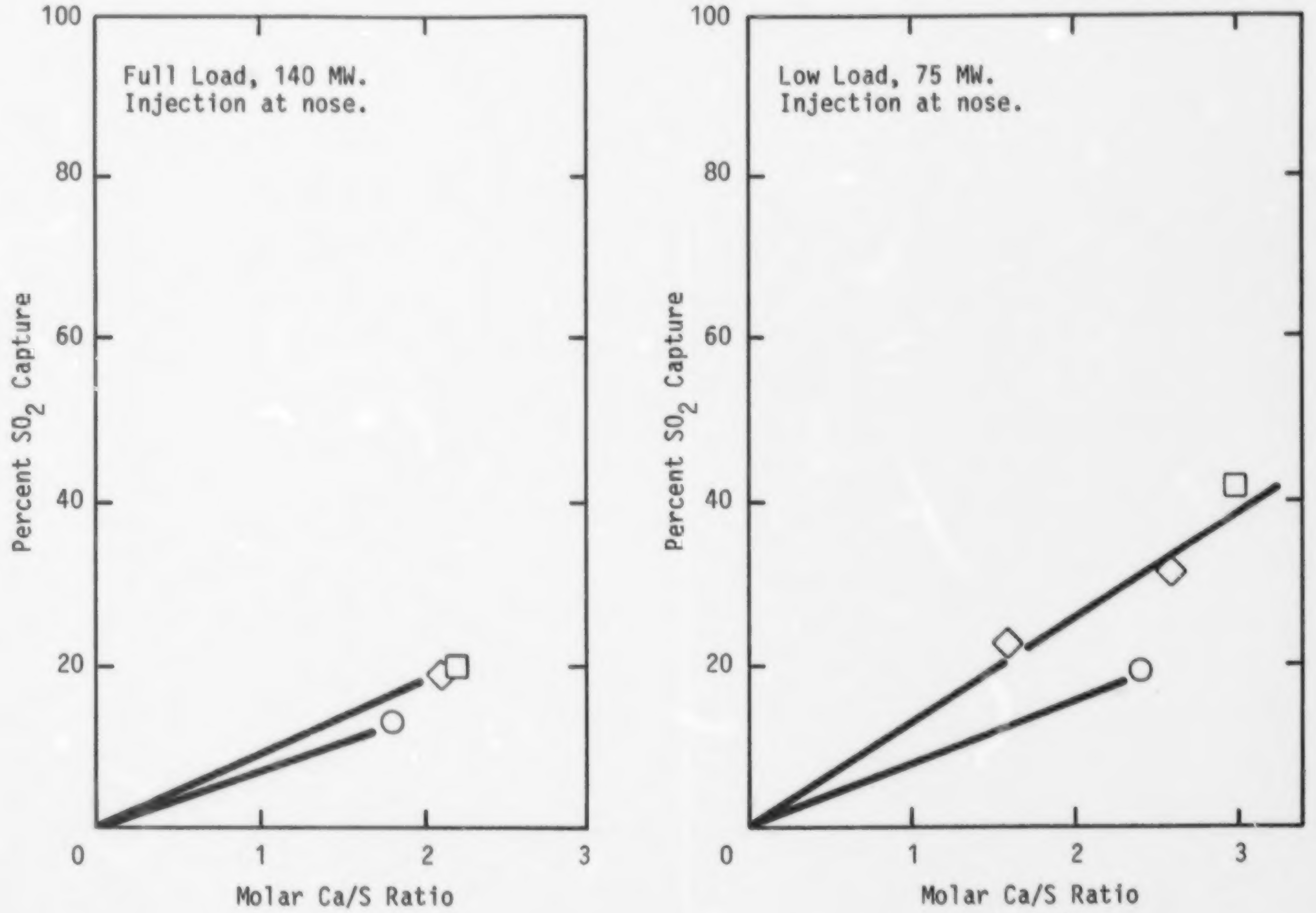

Figure 9-3. Average SO_2 capture levels for three sorbents at the Shawnee steam plant: aragonite (○), marl (□), and Fredonia limestone (◇). At full load the temperature at the nose is roughly 2100°F.

scale and bench-scale facilities with limestone. This may be attributable to mixing effects and/or to the unit's high quench rate.

Full-scale sorbent injection tests were performed by EER (Reese, et al. (1985)) at Hoot Lake. The Hoot Lake boiler is shown schematically in Figure 9-4. The tangentially fired boiler has a gross load of 44 MW and a reduced load of 34 MW. The flue gas contained 750 ppm SO_2 on a dry basis corrected to zero percent oxygen. The calculated temperature distribution at the furnace center plane is shown in Figure 9-5. The predicted temperatures are from EER's boiler heat transfer code. The estimated quench rate is -450°F/s.

Two sorbents were tested, a high calcium hydrate and a dolomitic hydrate. Only the results for the high calcium hydrate are reported below. The mass mean diameters of both sorbents were approximately 4 μm. Sulfur capture data for the high calcium hydrate are shown in Figure 9-6. These results were obtained with injection at level 3 or 4 and with boiler operation at full or reduced load. The effect, of changing injection load appear to be small. Capture levels obtained with the calcium hydrate are roughly 35 percent at a molar Ca/S ratio of 2. However, additional tests not shown here, involving injection on several levels at once, resulted in sorbent utilizations as high as 31 percent. This utilization corresponds to 62 percent capture at Ca/S of 2.

Vatsky and Schindler (1985) summarize large-scale tests on two facilities, a 50 x 10^6 Btu/hr test facility at Ishikawaja-Harima Industries (IHI) in Japan and a 110,000 pounds/hr boiler at a DuPont plant in Virginia. The IHI facility has a single burner with two levels of overfire air and is shown schematically in Figure 9-7. The DuPont plant is front-wall fired with four burners and is shown schematically in Figure 9-8.

The IHI tests utilized a western Pennsylvanian bituminous coal. The sorbent was a powdered limestone with a mass-mean diameter of 50 μm. A series of tests were performed at IHI. Initial tests involved injecting the sorbent with the coal. The SO_2 capture levels at Ca/S = 2 for this method

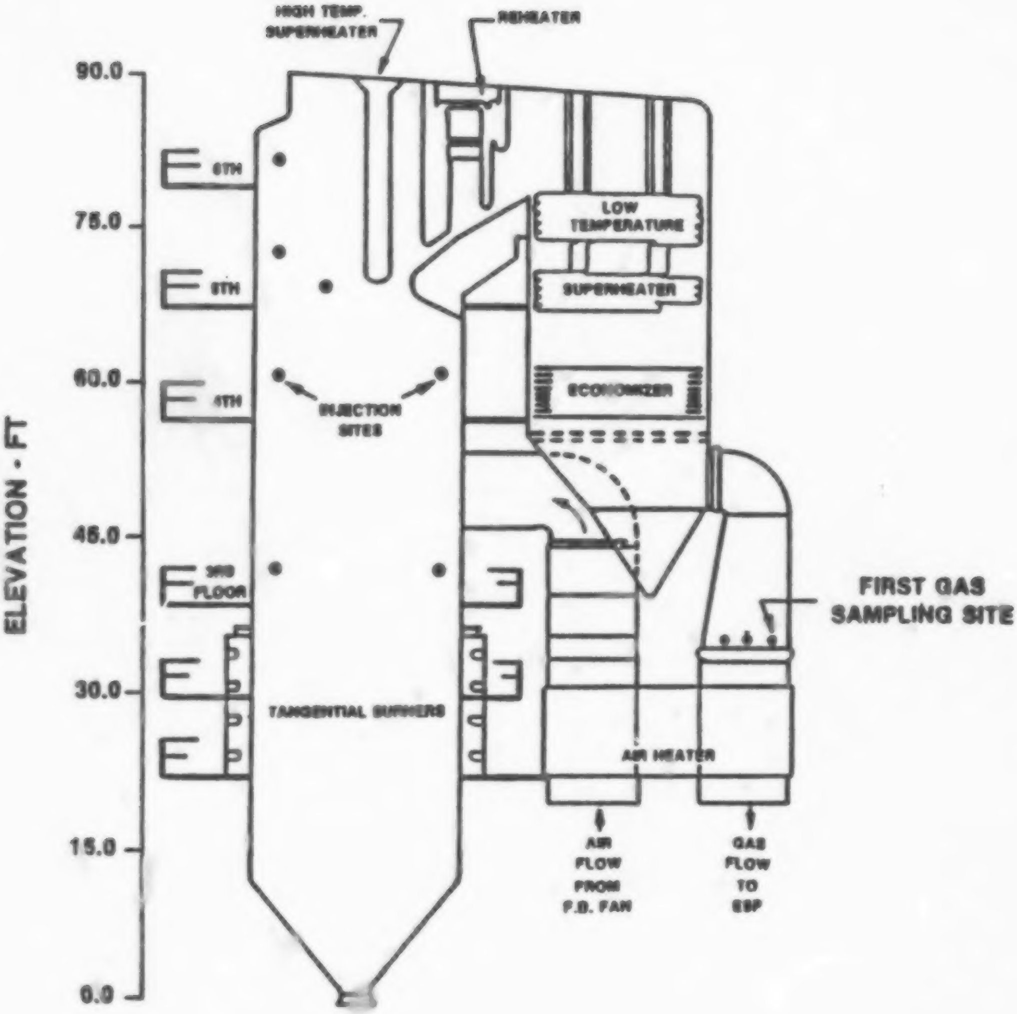
HIGH TEMP. SUPERHEATER
REHEATER
90.0
75.0
60.0
45.0
30.0
15.0
0.0
ELEVATION - FT
6TH
5TH
4TH
3RD FLOOR
LOW TEMPERATURE
SUPERHEATER
ECONOMIZER
INJECTION SITES
FIRST GAS SAMPLING SITE
TANGENTIAL BURNERS
AIR HEATER
AIR FLOW FROM F.D. FAN
GAS FLOW TO ESP

Figure 9-4. A schematic of the Hoot Lake boiler showing the location of the sorbent injectors.

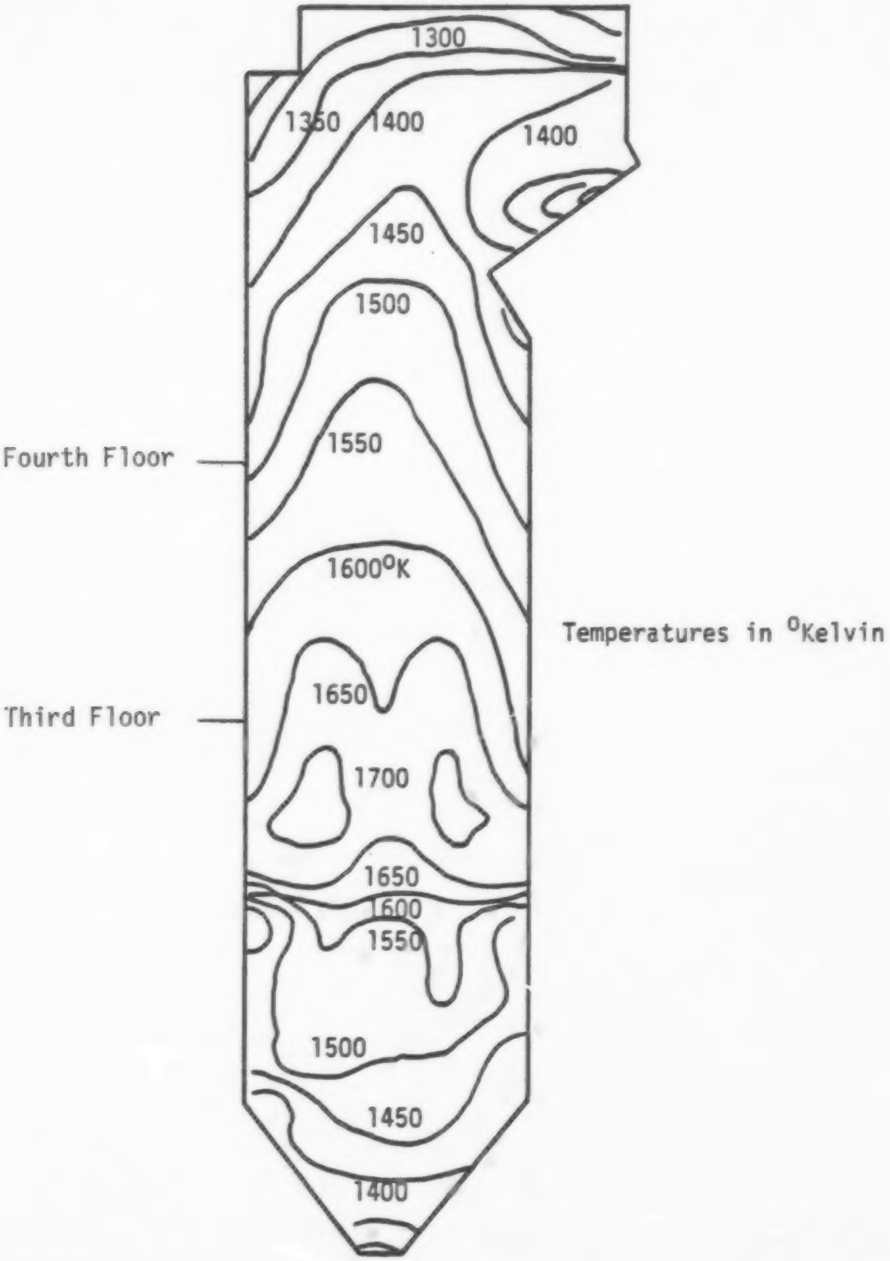
1300
1350
1400
1400
1450
1500
1550
Fourth Floor
1600°K
Temperatures in °Kelvin
1650
Third Floor
1700
1650
1600
1550
1500
1450
1400

Figure 9-5. Temperature distribution at furnace center plane for the Hoot Lake boiler as predicted by EER's boiler heat transfer code.

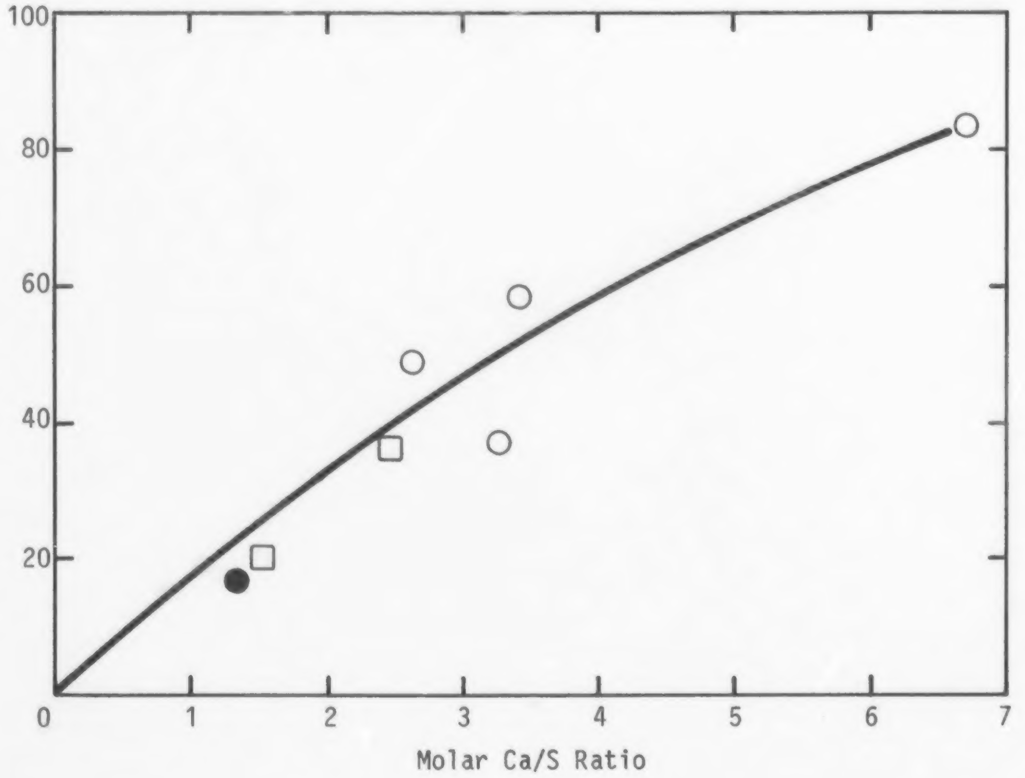

Figure 9-6. SO_2 capture measurements for high-calcium hydrate at Hoot Lake for two injection levels and two boiler loads: floor 4 at full load (○), floor 4 at reduced load (●), and floor 3 at full load (□).

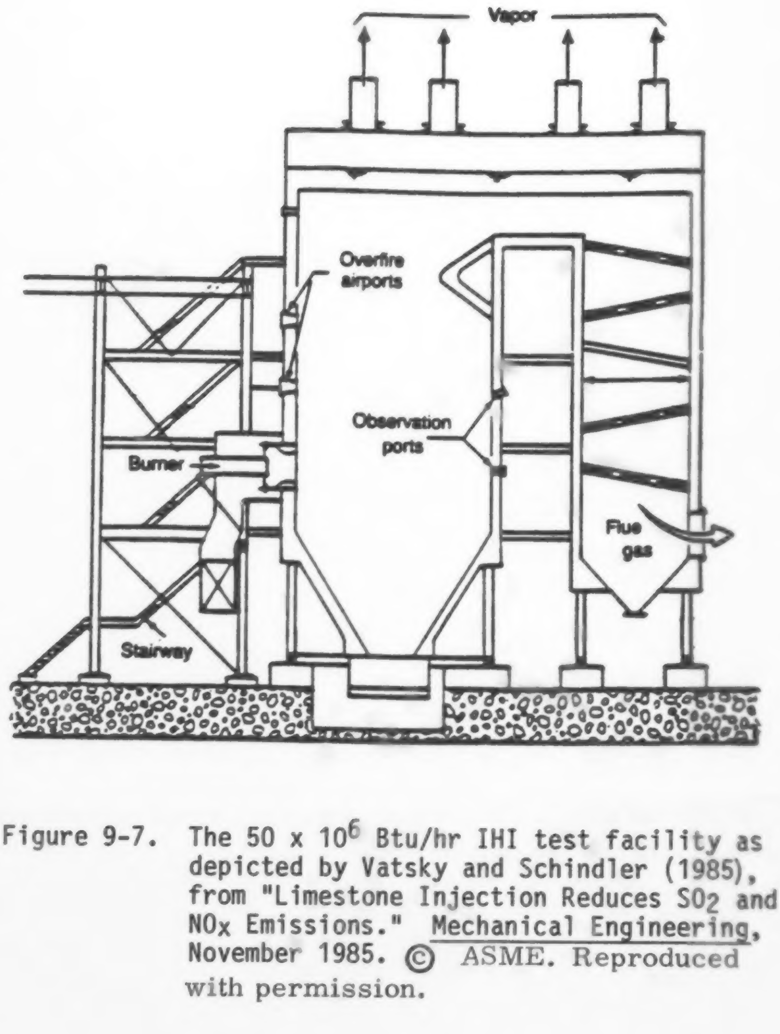
Vapor
Overfire airports
Observation ports
Burner
Flue gas
Stairway

Figure 9-7. The 50 x 10^6 Btu/hr IHI test facility as depicted by Vatsky and Schindler (1985), from "Limestone Injection Reduces SO_2 and NO_x Emissions." Mechanical Engineering, November 1985. © ASME. Reproduced with permission.

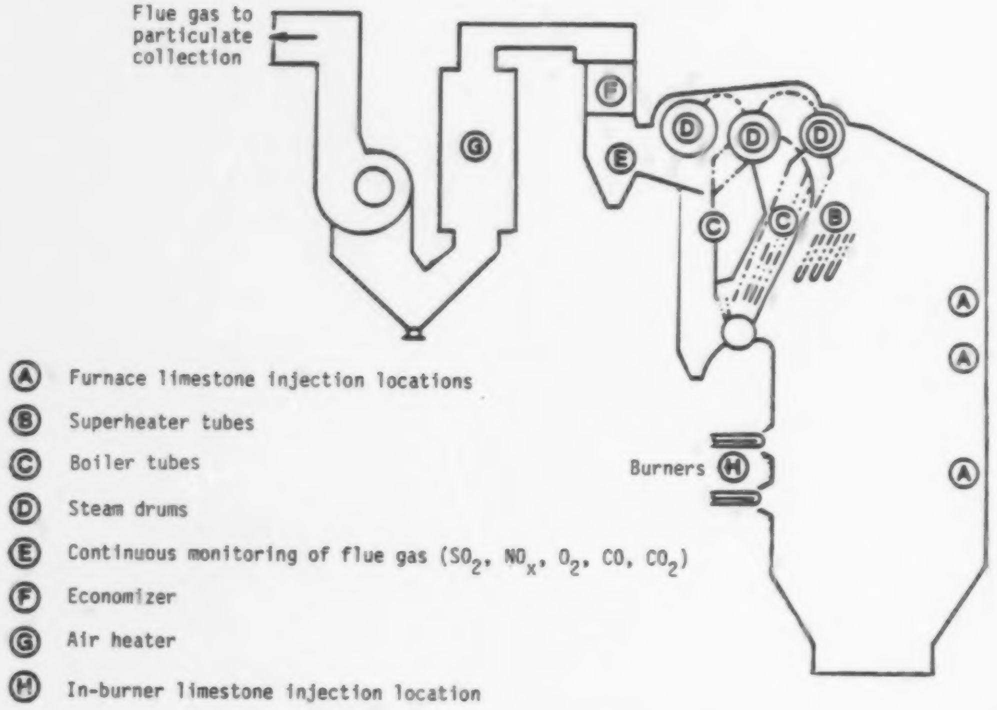
Flue gas to particulate collection
F
D
D
D
G
E
C
C
B
A
A
Burners
H
A
A Furnace limestone injection locations
B Superheater tubes
C Boiler tubes
D Steam drums
E Continuous monitoring of flue gas (SO_2, NO_x, O_2, CO, CO_2)
F Economizer
G Air heater
H In-burner limestone injection location

Figure 9-8. The 110,000 lbs/hr DuPont boiler as depicted by Vatsky and Schindler (1985), from "Limestone Injection Reduces SO_2 and NO_x Emissions." Mechanical Engineering, November 1985. © ASME. Reproduced with permission.

are 20 percent. Additional tests included sorbent injection with the secondary burner air, resulting in 40 percent SO_2 capture at Ca/S = 2. Injection with the overfire air also gave 40 percent capture but upper furnace injection gave poor results.

The DuPont boiler tests also utilized pulverized limestone with a mean size of roughly 50 μm. Injection of the sorbent with the secondary burner air resulted in 50 percent SO_2 capture at Ca/S = 2.6. Upper furnace injection gave lower capture levels than secondary burner air injection except when operating the boiler at 20 percent below full load. The pilot- and full-scale tests are summarized in Figure 9-9. Compared to results obtained on other pilot- and full-scale facilities, the limestone utilization levels reported by Vatsky and Schindler are high.

The design and testing of a retrofit, dry sorbent injection system for a 300 MW, tangentially-fired boiler is described by Cameron and Arnott (1986). The pulverized fuel boiler is owned by Ontario Hydro. The tests were performed with a bituminous coal from Ohio with a sulfur content of 1.7 percent. The uncontrolled SO_2 concentration was 1500 ppm at 3 percent O_2.

A schematic of the boiler is given in Figure 9-10 with the location of the sorbent injectors indicated by arrows. The calculated gas temperature at the injection point is approximately 2500°F, at 250 MW. The estimated residence time from the point of injection to the first tube bank is 1.2 seconds.

Two sorbents were tested, a pulverized limestone and $Ca(OH)_2$. The limestone was 95 percent $CaCO_3$ and 90 percent by weight was less than 45 μm in diameter. The size of the hydrate is unknown but a typical value is about 4 μm.

The results of sorbent injection tests are summarized in Figure 9-11 for two sorbents and at boiler loads of 220 and 290 MW. The carbonate was tested at two loads, 220 and 290 MW, with capture levels of 27 and 20 percent, respectively, at Ca/S = 2. The hydrate was tested at 220 MW and capture

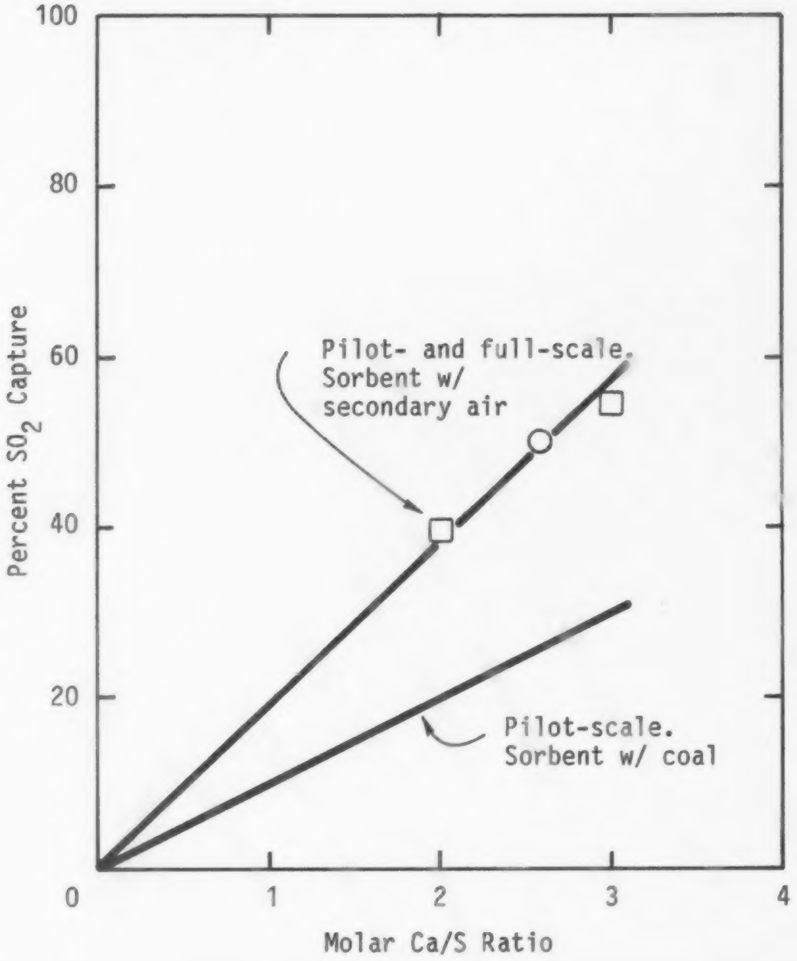

Figure 9-9. Pilot- (□) and full-scale (○), limestone injection results as reported by Vatsky and Schindler (1985, from "Limestone Injection Reduces SO_2 and NO_x Emissions." Mechanical Engineering, November 1985. © ASME. Reproduced with permission.

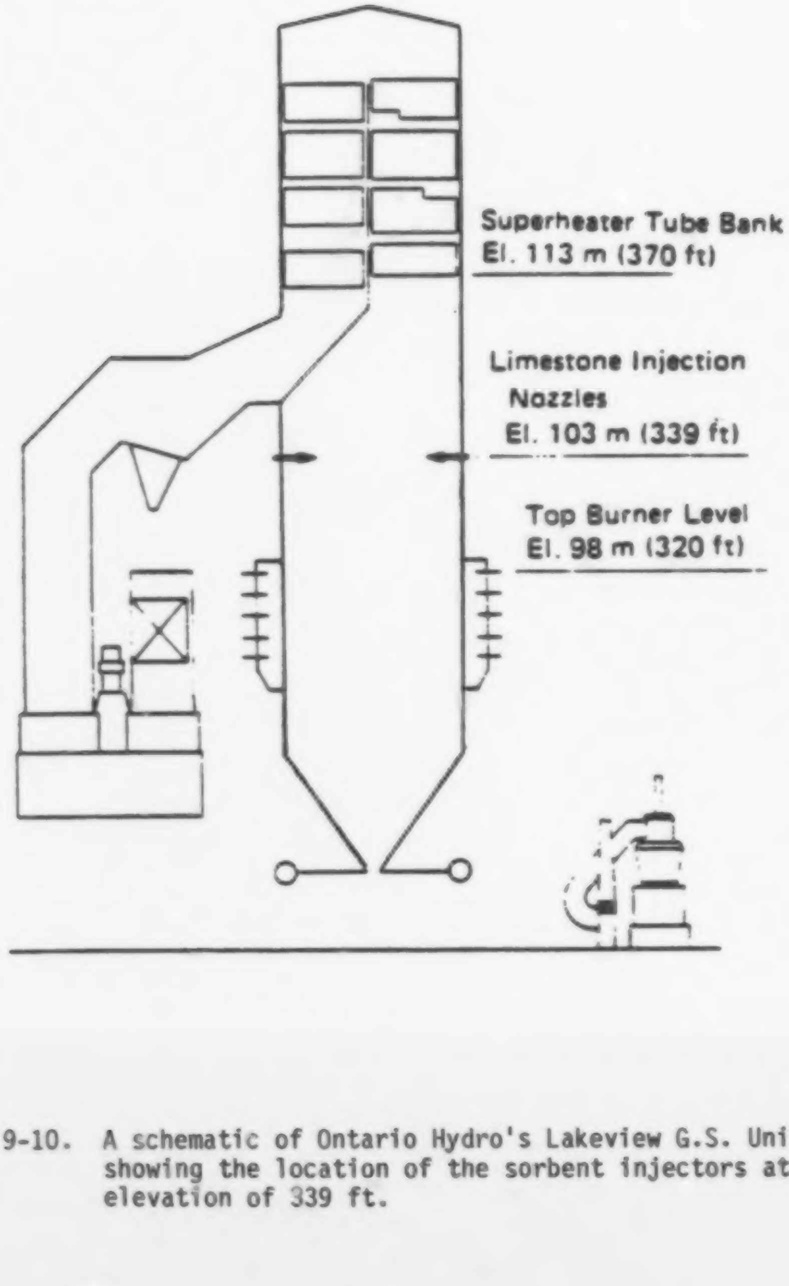
Superheater Tube Bank
El. 113 m (370 ft)
Limestone Injection
Nozzles
El. 103 m (339 ft)
Top Burner Level
El. 98 m (320 ft)

Figure 9-10. A schematic of Ontario Hydro's Lakeview G.S. Unit 4 showing the location of the sorbent injectors at an elevation of 339 ft.

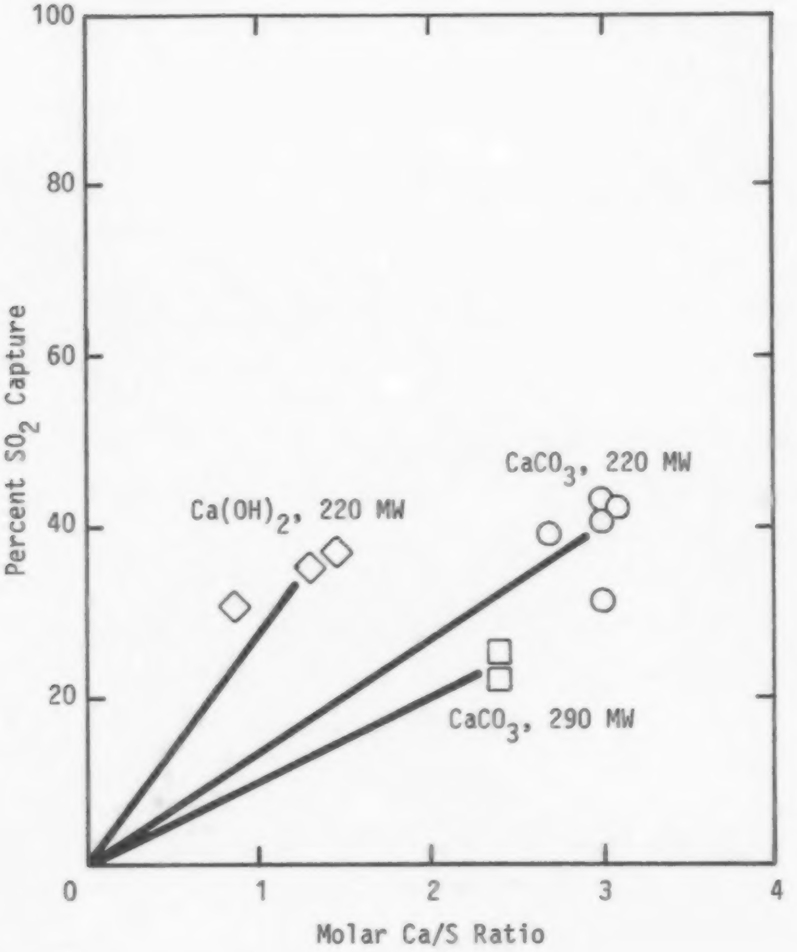

Figure 9-11. The SO_2 capture results of Cameron and Arnott (1986) for $Ca(OH)_2$ and $CaCO_3$ at two different loads.

levels of 36 percent at Ca/S = 1.4 were observed. The hydrate is approximately twice as reactive as the carbonate and the overall capture levels are in agreement with typical pilot- and full-scale results.

Testing performed by EER at Tiefstack, West Germany is discussed by Reese, et al. (1986). The Tiefstack boiler is fired tangentially with coal at 352,000 lbm/hr of steam. The quench rate in the upper furnace region is roughly -250°F/s and the residence time in the sulfation zone (1700-2200°F) is about 2.5s. One or two nozzles were used for sorbent injection. The observed capture levels were insensitive to the number of injectors. A schematic of the Tiefstack boiler is shown in Figure 9-12. The time-temperature profile is shown in Figure 9-13 and is based upon measured temperatures as well as EER's 3-D heat transfer model.

The Tiefstack sulfur capture results are summarized in Figure 9-14 for two sorbents and at two boiler loads. At full load and at a molar Ca/S ratio of 2 the observed capture levels are 22 and 42 percent for pulverized limestone and atmospheric $Ca(OH)_2$, respectively. At low load (250,000 lb/hr) the carbonate captured 27 percent of the SO_2 with Ca/S = 2. The temperature at the injection point was roughly 2280°F. In view of the very favorable Tiefstack thermal profile, the capture levels reported seem somewhat low. However, the limestone was not thoroughly and uniformly pulverized resulting in the injection of some millimeter-sized stones.

Additional full-scale tests have been performed in Austria. Staudinger and Schrofelbauer (1986) have summarized field experience with several Austrian boilers. One of these, the Voitsberg No. 3 is discussed here. The Voitsberg No. 3 unit is tangentially fired and has a maximum load of 330 MW. Two sorbents were tested, a powdered limestone and a powdered dolomite. Both sorbents were 90 percent by weight smaller than 60 μm and 50 percent smaller than 15 μm. The results of the injection tests are summarized in Figure 9-15. For the dolomite and the limestone the capture levels at a molar Ca/S ratio of 2 are 40 and 30 percent, respectively. The temperature at the injection point is unknown. The data were obtained at a normal load of 330 MW.

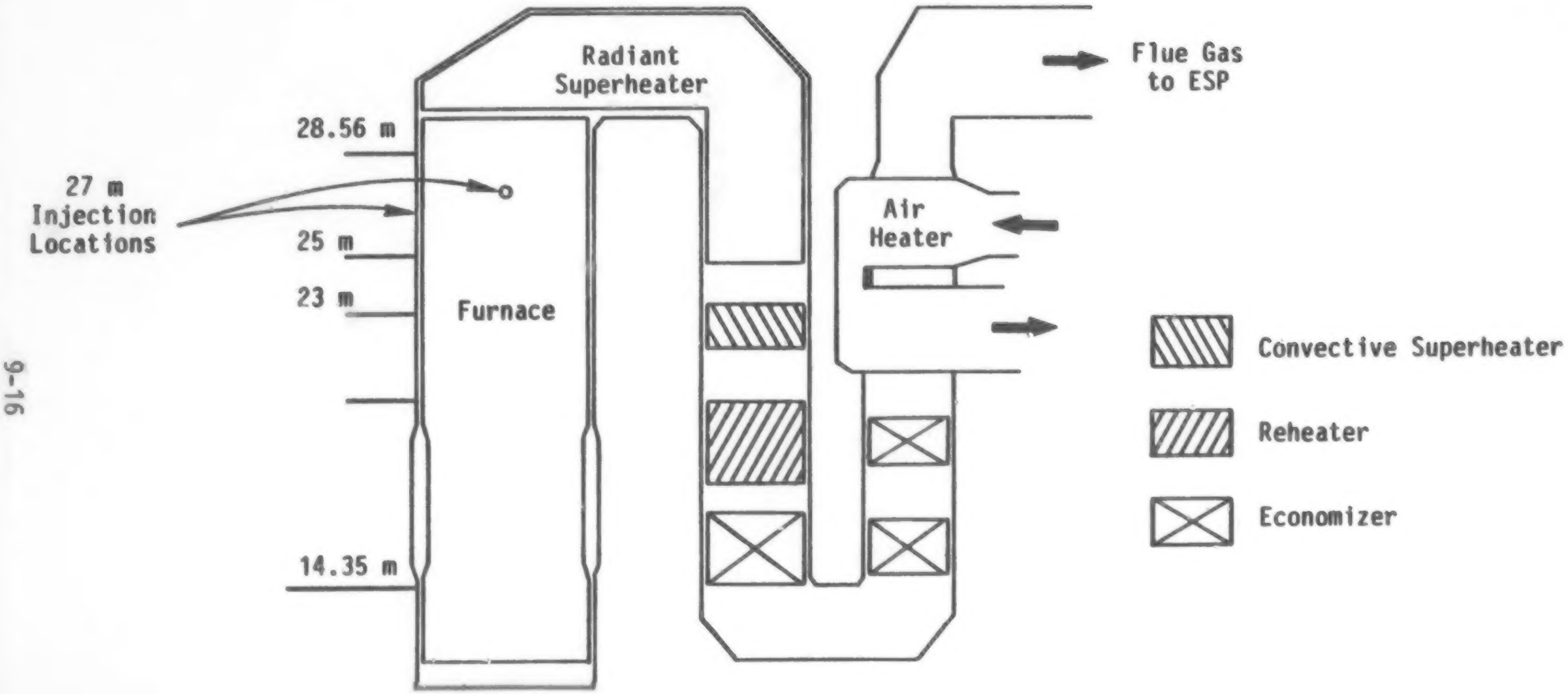
Radiant Superheater
Flue Gas to ESP
28.56 m
27 m Injection Locations
25 m
23 m
Furnace
14.35 m
Air Heater
Convective Superheater
Reheater
Economizer

Figure 9-12. A schematic of the Tiefstack boiler 6.

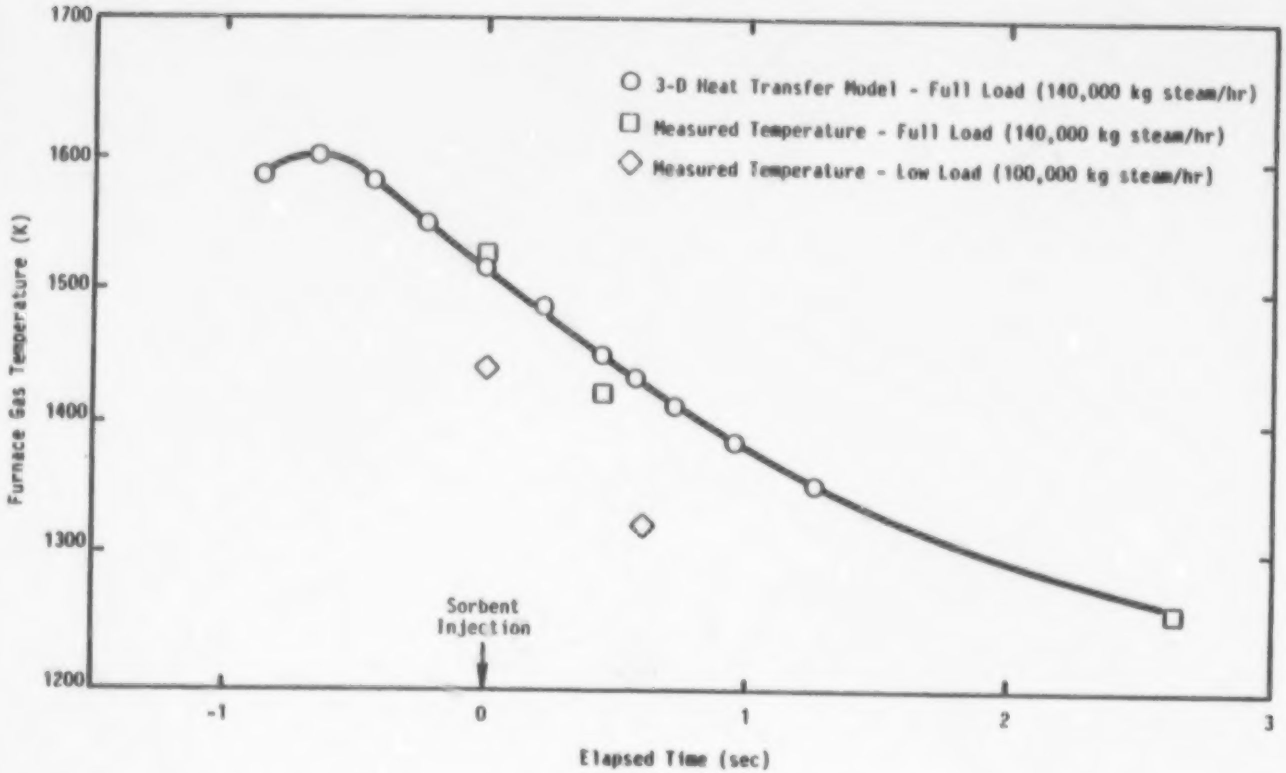

Figure 9-13. The time-temperature profile for the Tiefstack boiler based upon 3-D heat transfer calculations and on measurements.

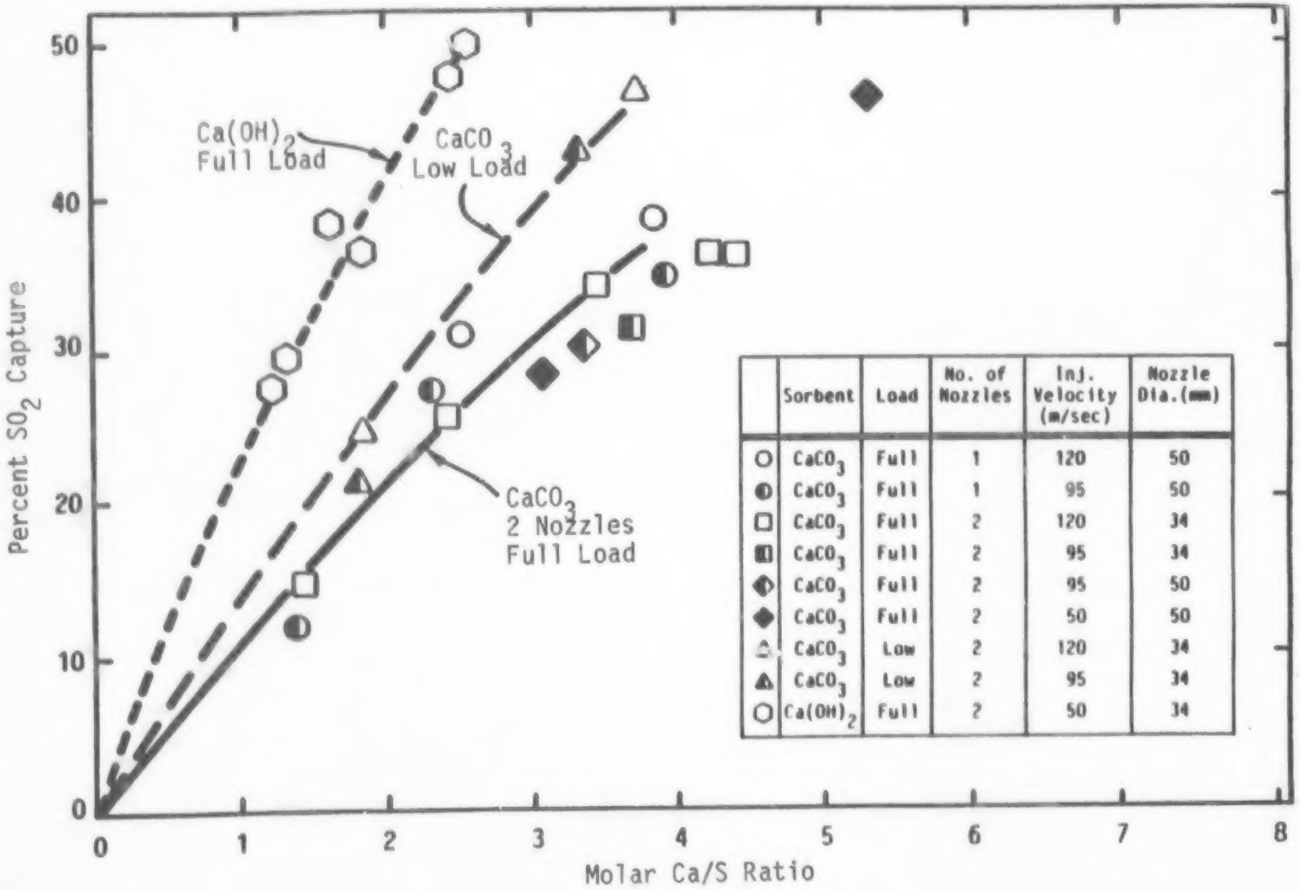

	Sorbent	Load	No. of Nozzles	Inj. Velocity (m/sec)	Nozzle Dia. (mm)
○	$CaCO_3$	Full	1	120	50
◐	$CaCO_3$	Full	1	95	50
□	$CaCO_3$	Full	2	120	34
◧	$CaCO_3$	Full	2	95	34
⬖	$CaCO_3$	Full	2	95	50
◆	$CaCO_3$	Full	2	50	50
△	$CaCO_3$	Low	2	120	34
▲	$CaCO_3$	Low	2	95	34
⬡	$Ca(OH)_2$	Full	2	50	34

Figure 9-14. Sulfur capture results for the Tiefstack boiler.

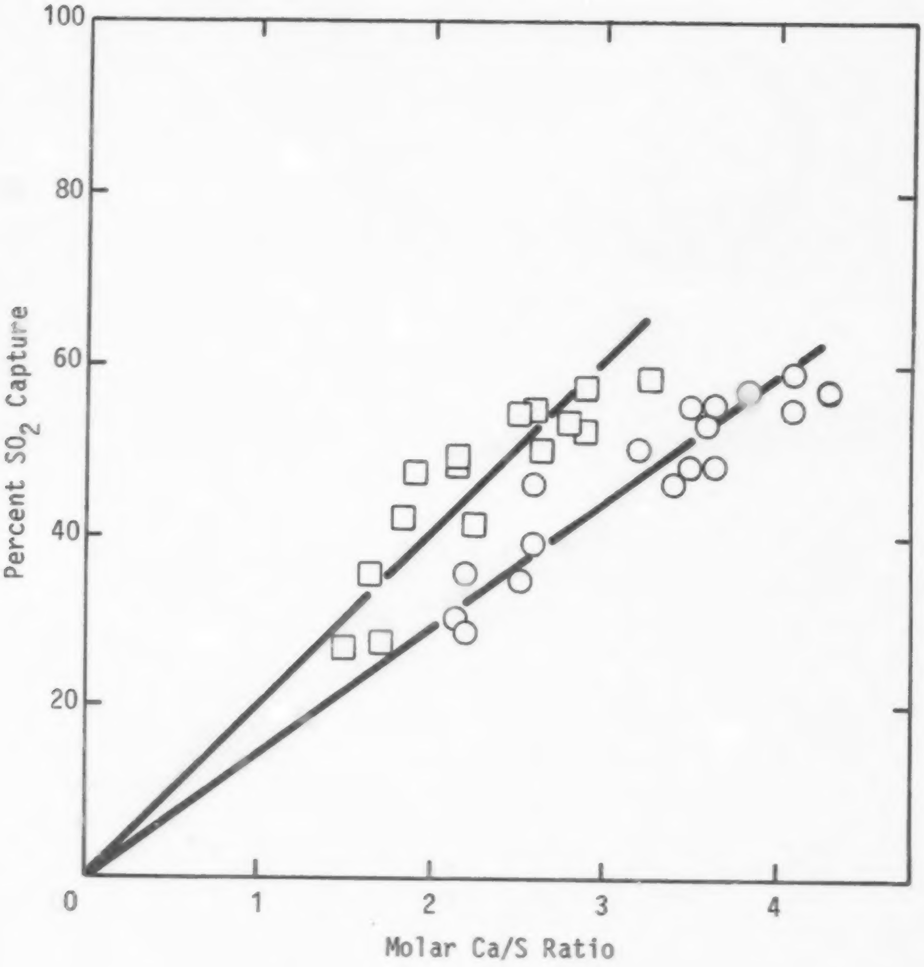

Figure 9-15. Sulfur capture data reported by Staudinger and Schrofelbauer for pulverized limestone (○) and dolomite (□). The data were obtained on the Voitsberg No. 3 boiler at a normal load of 330 MW.

Large-scale test results obtained on EER's large water tube simulator (LWS) are shown in Figure 9-16. A schematic of the LSW is shown in Figure 9-17. The LWS was fired with Utah coal at 100 x 10^6 Btu/hr. The uncontrolled SO_2 concentration was 600 ppm on a dry basis, corrected to zero percent O_2. The results presented in Figure 9-16 are averages of several sets of data obtained with different burners.

Two different sorbents were injected, Vicron limestone with a mass mean size of 11 μm and Colton hydrate with a mean size of 4 μm. The two sorbent injection methods examined included injecting sorbent with the coal and injecting sorbent with the tertiary air. Referring to Figure 9-16, it appears that the injection method has little effect on sorbent utilization. However, there is a significant difference in reactivity between the hydrate and the carbonate. Sulfur capture levels for the hydrate and carbonate at Ca/S = 2 are 44 and 32 percent respectively.

Table 9-1 summarizes the large-scale results discussed above. Included in Table 9-1 are bench-scale results from EER's Controlled Temperature Tower (CTT) and from the Boiler Simulator Furnace (BSF). The capture levels for limestones at Ca/S = 2 range from 14 to 40 percent. However, most of the facilities obtained SO_2 capture of roughly 25 percent with limestone. Capture levels for hydrates range form 35 to 54 percent with most of the investigators reporting about 40 percent. The bench-scale results from EER tend to be slightly higher than the large-scale results but in general, the data from both scales agree fairly well. The higher capture levels at bench-scale may be attributable to the relative ease with which the sorbent can be mixed with the combustion gases.

The effect of load on sorbent utilization appears to be moderately important. The Shawnee, Lakeview, and Tiefstack data all show significant effects from changing load. The optimum injection temperature is difficult to ascertain from large scale data. The limited results from Shawnee suggest that the optimum temperature is 2100°F which agrees well with the bench-scale results discussed in Section 6.

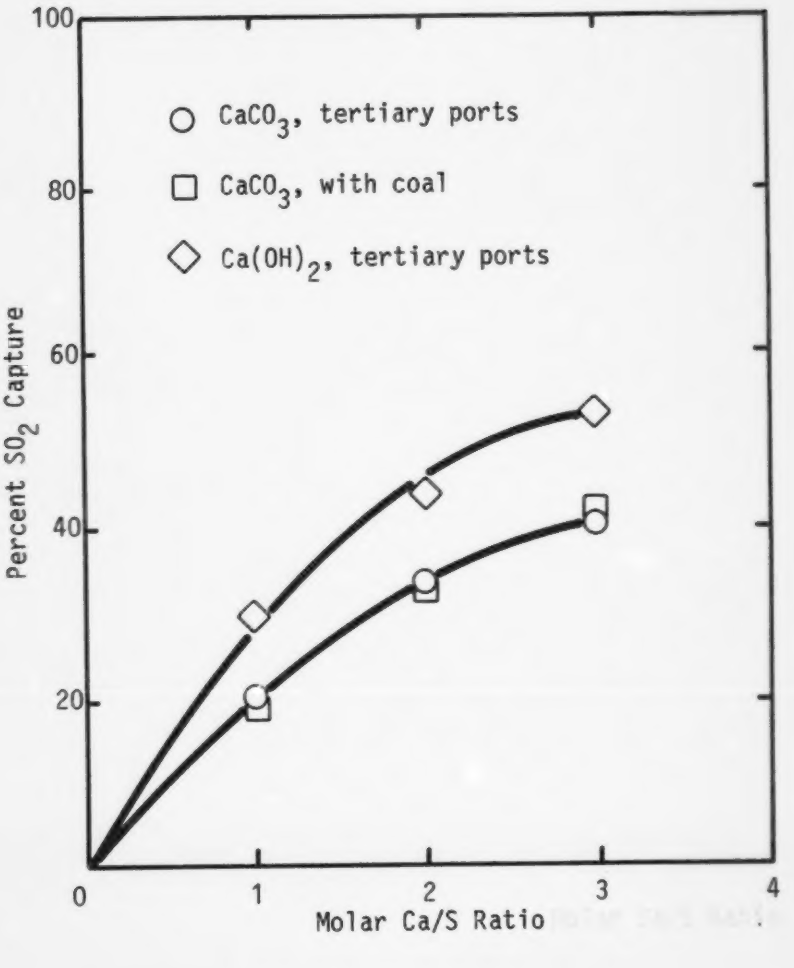

Figure 9-16. SO_2 capture results obtained on EER's Large Water Tube Simulator (LWS).

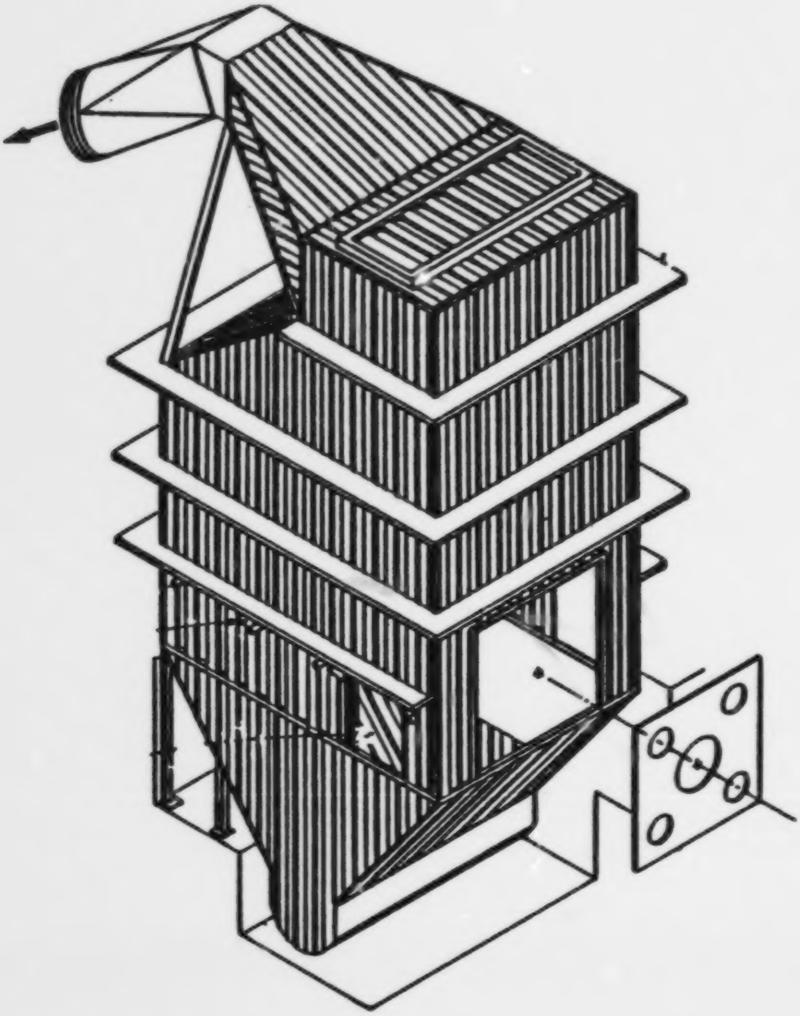

Figure 9-17. A schematic of the LWS with the burner plate detached. The firing depth is 22 feet, the width is 16 feet, and the overall height is 50.5 feet.

TABLE 9-1. LARGE-SCALE FACILITY COMPARISON

Facility	Load	Type	Percent(1) Capture w/$CaCO_3$	Percent(1) Capture w/$Ca(OH)_2$	Optimum Injection T, °F
Shawnee	140 MW	Wall-fired	14-18	--	2100
Shawnee	75 MW	Wall-fired	16-26	--	--
Hoot Lake	44 MW	T-fired	--	35-50	--
Hoot Lake	34 MW	T-fired	--	35	--
IHI	50x10^6Btu/hr	Wall-fired	40	--	--
Dupont	110,000 lb/hr	Wall-fired	40	--	--
Lakeview	290 MW	T-fired	20	--	--
Lakeview	220 MW	T-fired	27	--	--
Lakeview	220 MW	T-fired	--	54	--
Tiefstack	352,000 lb/hr	T-fired	22	42	--
Tiefstack	250,000 lb/hr	T-fired	27	--	--
Voitsberg	330 MW	T-fired	29	--	--
LWS	100x10^6Btu/hr	Wall-fired	32	44	--
Bench/CTT	1x10^5Btu/hr	Down-fired	21-26	40-58	2000
Bench/BSF	1x10^6Btu/hr	Down-fired	26	54	2000

(1) AT CA/S = 2

(2) ESTIMATED FROM CAPTURE AT CA/S = 1

9.2 The Overall Sulfation Modeling Approach

Three methods of estimating SO_2 capture for large-scale are currently being used or are being developed. The first involves direct extrapolation from bench-scale data. This method requires bench-scale data which have been obtained at conditions similar to those in the full-scale system. The second approach utilizes a complete mathematical description of the boiler including fluid mechanics, combustion kinetics, heat transfer, and sulfation kinetics. The third approach uses data to calibrate a semi-empirical sulfation model. The model can then be used to extrapolate data to new conditions. The grain model described in Section 4.0 is sufficiently general for this purpose and it includes provisions for examining the effects of jet heat-up and dilution. The third approach is the one which was in this program and which will be reviewed in this section. It will be discussed in the context of predictions made for the Edgewater boiler which includes the effects of jet mixing. Finally, in Section 9.3 the third approach is used to predict the Tiefstack results presented in Section 9.1.

The bench-scale data selected for the calibration of the grain model are shown in Figure 9-18 along with the fit obtained. The data were collected on the CTT. The jet heat-up and dilution rates for the Edgewater boiler were calculated using the jet model JICFIS. The complicated flow and temperature field in the Edgewater boiler was approximated by a uniform flow and temperature field. Figure 9-19 is a schematic of the modeling procedure for sulfur capture in jets. As indicated by the figure the actual upper furnace flow is straightened while still maintaining the same overall residence time.

The jet concentration and temperature histories are obtained by applying mass and energy balances in conjunction with jet entrainment rates and furnace flue gas temperature histories. From these calculations one obtains the SO_2 concentration and temperature histories of the sorbent within the boundary of the jet. These histories are then used as input for the sulfation model. Because the jet contains all of the sorbent within its boundary, the sulfation calculation provides an estimate of the overall sulfur capture of the jet system being considered.

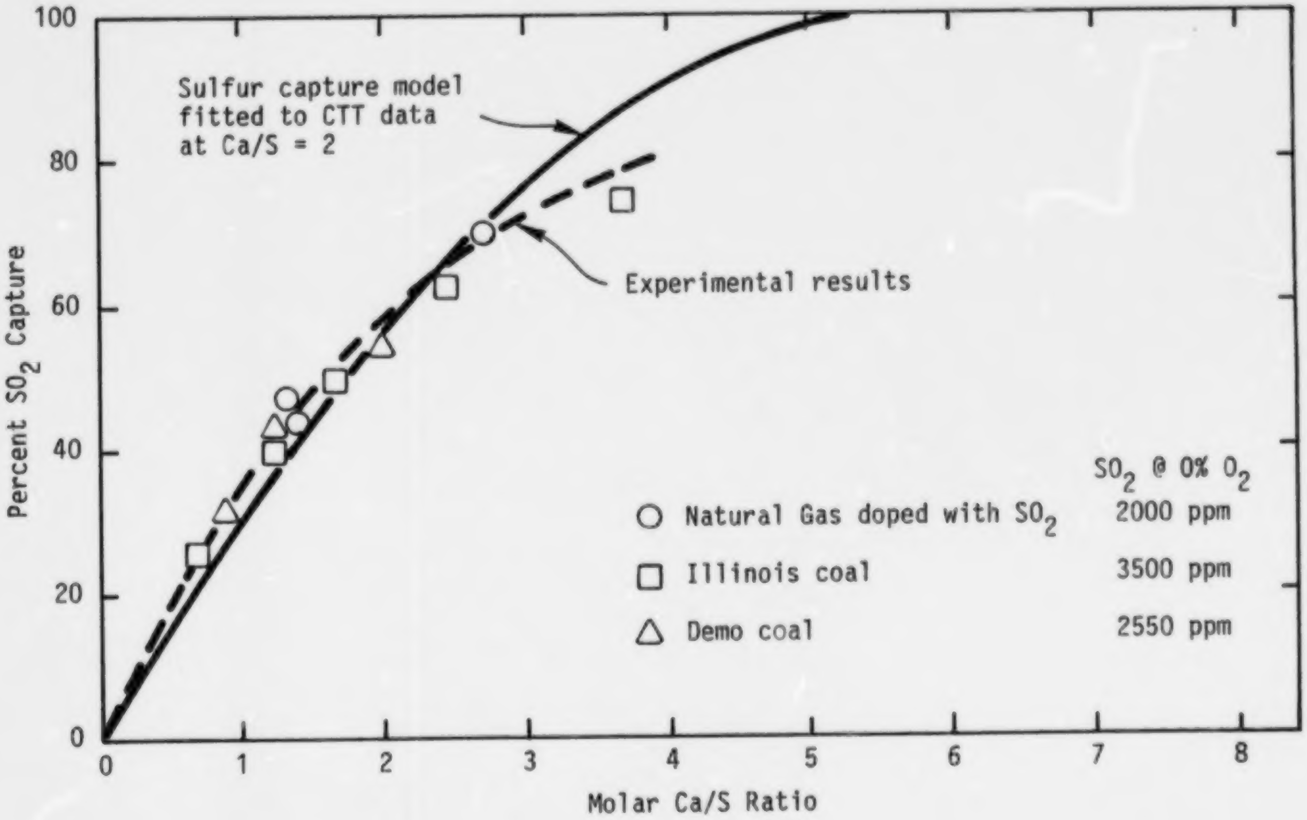

Figure 9-18. Controlled Temperature Tower (CTT) data obtained with Linwood atmospheric hydrate for three different fuels. The data were used to calibrate the sulfation model as indicated by the solid line.

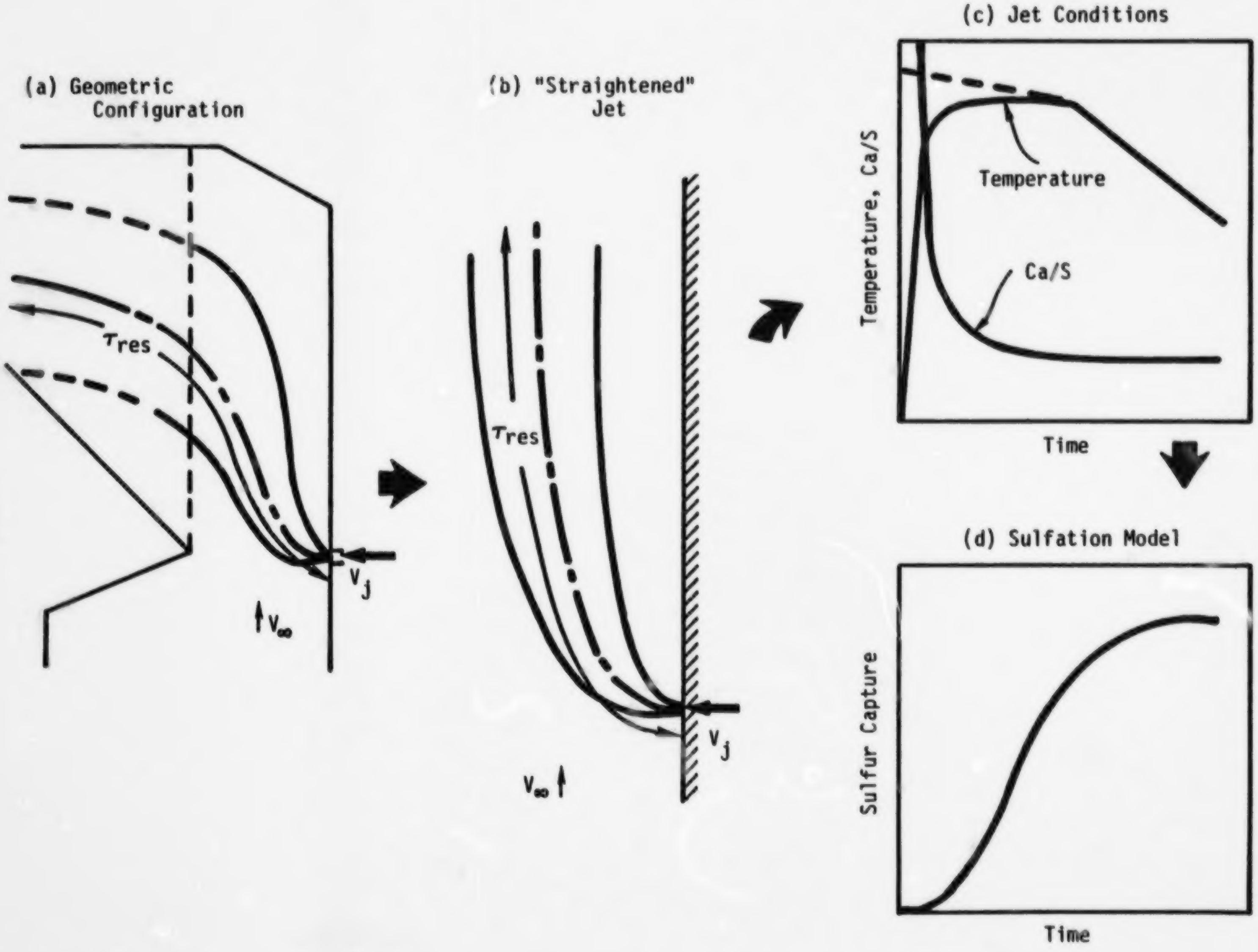
(a) Geometric Configuration
τ_{res}
V_j
V_∞
(b) "Straightened" Jet
τ_{res}
V_∞
V_j
(c) Jet Conditions
Temperature, Ca/S
Temperature
Ca/S
Time
(d) Sulfation Model
Sulfur Capture
Time

Figure 9-19. Schematic of procedure for sulfur capture modeling for jets in crossflow.

Typical results showing the sulfur capture predicted by this procedure are given in Figure 9-20. The calculations are based on injection through eight, 3.5 inch jets on a single plane with a momentum flux ratio of J=100. The upper graph in Figure 9-20 shows the temperature history of the jet along with the molar calcium to sulfur ratio. The dashed line in the upper figure indicates the temperature of the bulk furnace gas. Note that the sorbent jet never attains the peak gas temperature of 2400°F. The lower graph in Figure 9-20 shows the sulfation history of the sorbent as it is carried along by the jet. The initial rate of sulfation is slow due to the low jet temperature and the low SO_2 concentration. The dashed portion of the sulfation curve marks the time during which the jet temperature exceeds the equilibrium decomposition temperature of $CaSO_4$. No capture can occur under these conditions until the jet temperature falls below the equilibrium temperature. It is likely that sulfur capture would be increased if the peak sorbent temperature were just below the equilibrium temperature which in this case is roughly 2150°F.

The grain model predictions in Figure 9-20 are based on the JICFIS model calculations which assume that the sorbent jets completely mix with the bulk gas. However, because of the uncertainties involved in this approach, it is prudent to examine the effect of departing from this assumption. Two predicted sulfur capture curves are shown in Figure 9-21 as functions of calcium to sulfur ratio. The uppermost curve is based on the assumption of complete mixing. According to Figure 9-20, complete mixing occurs in just over 0.5 seconds. The lower curve in Figure 9-21 shows the effect of never allowing the mixing to proceed beyond being 90 percent complete. This lowers the predicted percent capture at Ca/S = 2 from 50 down to 43. The choice of allowing the sorbent to mixing with only 80 percent of the flue gas is based on isothermal flow modeling studies of the Edgewater boiler. Hence, the predicted SO_2 capture for Linwood atmospheric hydrate injection at these conditions in the Edgewater boiler is 43 percent at Ca/S = 2. Using this same approach with the JICFIS model, the grain model, and isothermal modeling, one can predict the effects of angled jets, lower injection temperatures, and multi-level injection schemes.

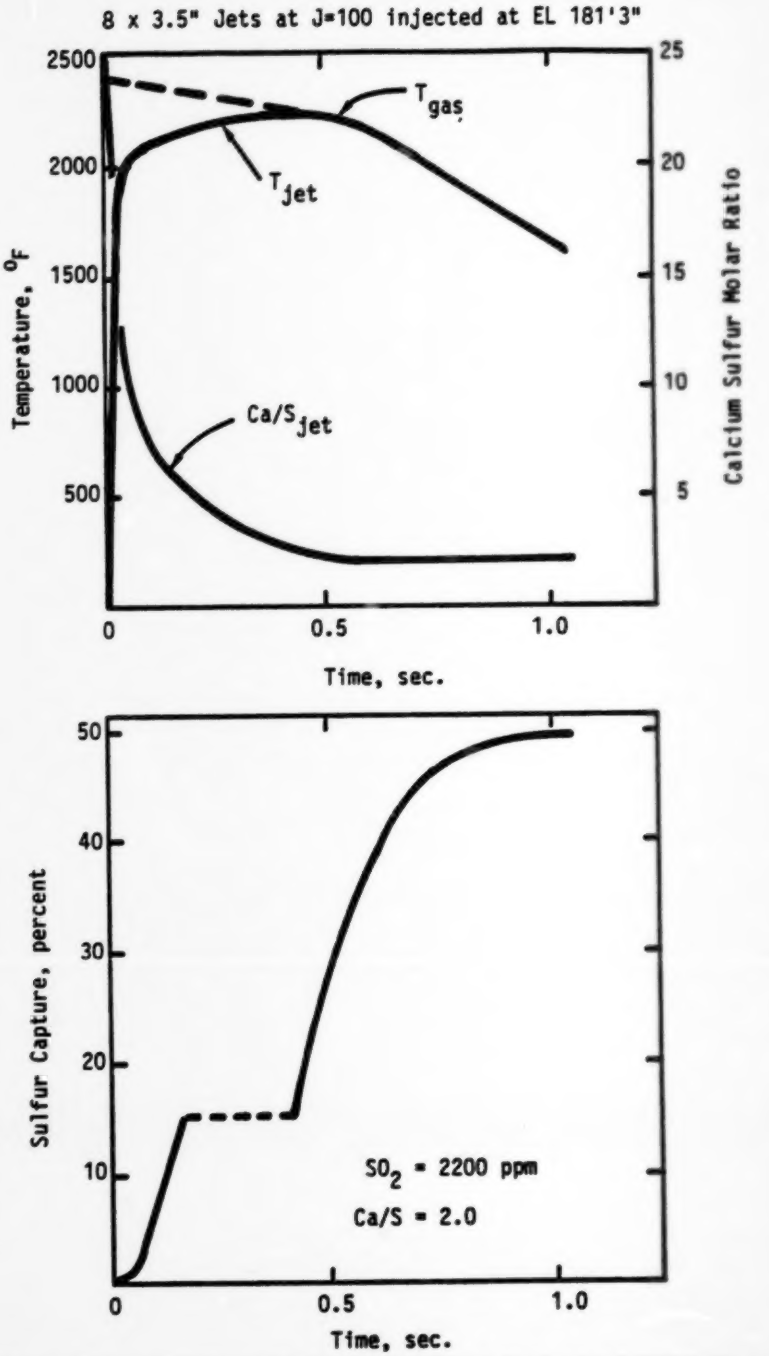

Figure 9-20. Jet and sulfation model calculations showing sorbent jet properties and the corresponding overall sulfur capture levels.

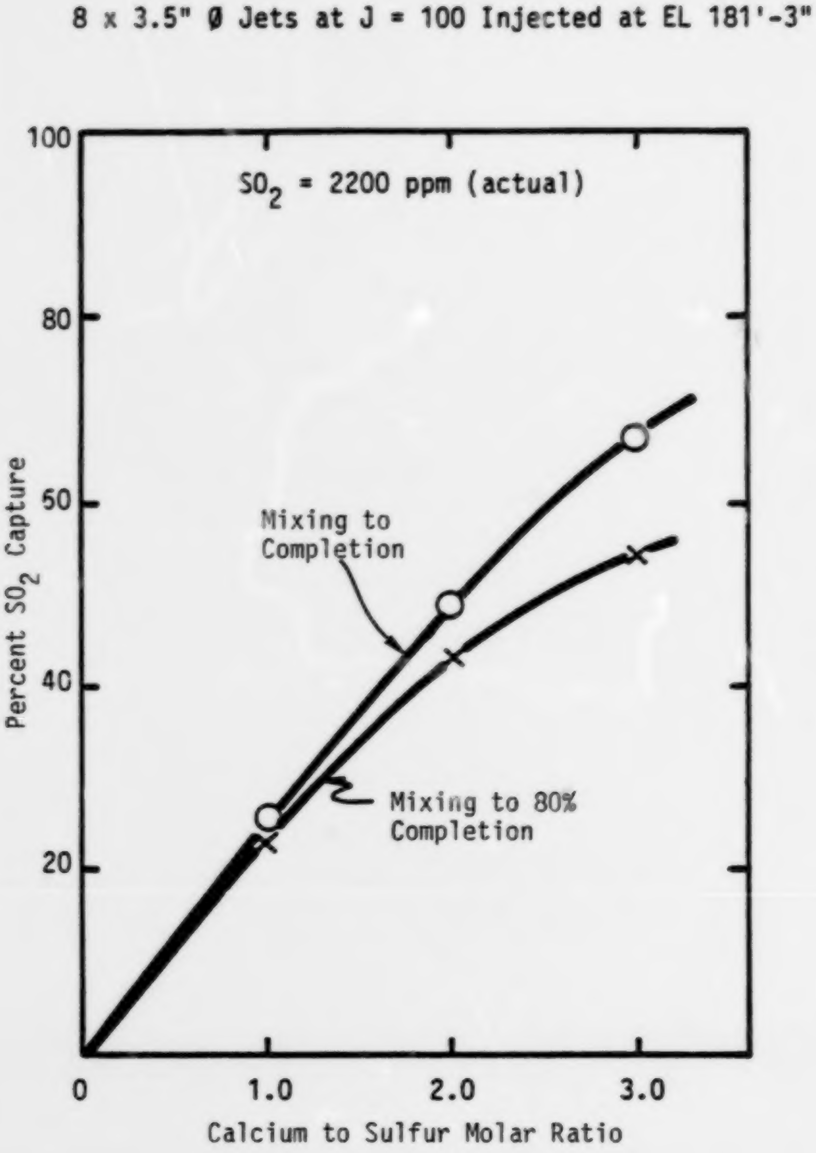

Figure 9-21. Sulfur capture predictions for Edgewater boiler using JICFIA and grain models showing the effect of incomplete mixing of the sorbent jet with the bulk furnace gases.

9.3 Comparison

To demonstrate the sulfation modeling approach outlined above, the grain model was used in conjunction with bench-scale CTT data to predict the large-scale CTT data to predict the large-scale Tiefstack results of Figure 9-14. The CTT data selected for calibrating the grain model are the Linwood hydrate results shown in Figure 9-18. The same data are given in Figure 7-16. The baseline thermal profile for these data is plotted in Figure 7-15.

The bulk gas temperature in the CTT at the injection point was 2280°F. However, because of the large volume of cold air used to convey sorbent into the CTT, the peak sorbent jet temperature never exceeded 2100°F. For this reason the grain model was calibrated against the bench-scale data of Figure 7-16 using a modified version of Figure 7-15. The modification consisted of reducing the temperature at time zero from 2280°F to 2100°F. With this modification, the initial sorbent surface area required to fit the CTT data was 80 m^2/g.

Included in the grain model is a provision for sorbent surface area loss. The rate of surface area loss is determined by an Arrhenius-type expression as described in Section 4.0. The fit to the CTT data was not obtained by varying the sintering rate. Only the initial sorbent surface area was adjusted.

The thermal profile for the Tiefstack boiler is shown in Figure 9-13. The peak temperature at the injection point is 2280°F. The actual SO_2 concentration is 600 ppm. Because of the relatively small volume of air used to convey sorbent into the boiler, and because Tiefstack is tangentially fired, the sorbent was assumed to mix rapidly with the bulk gas and to attain a peak temperature of 2280°F instantaneously. The predicted SO_2 capture for Tiefstack, which is based upon these assumptions and data, is shown in Figure 9-22. The good agreement between the model and the data demonstrates the usefulness of this approach. However, these predictions are based on capture data for Linwood atmospheric hydrate. Had we used the Colton hydrate data of Figure 7-16 a very different result would have been obtained. If

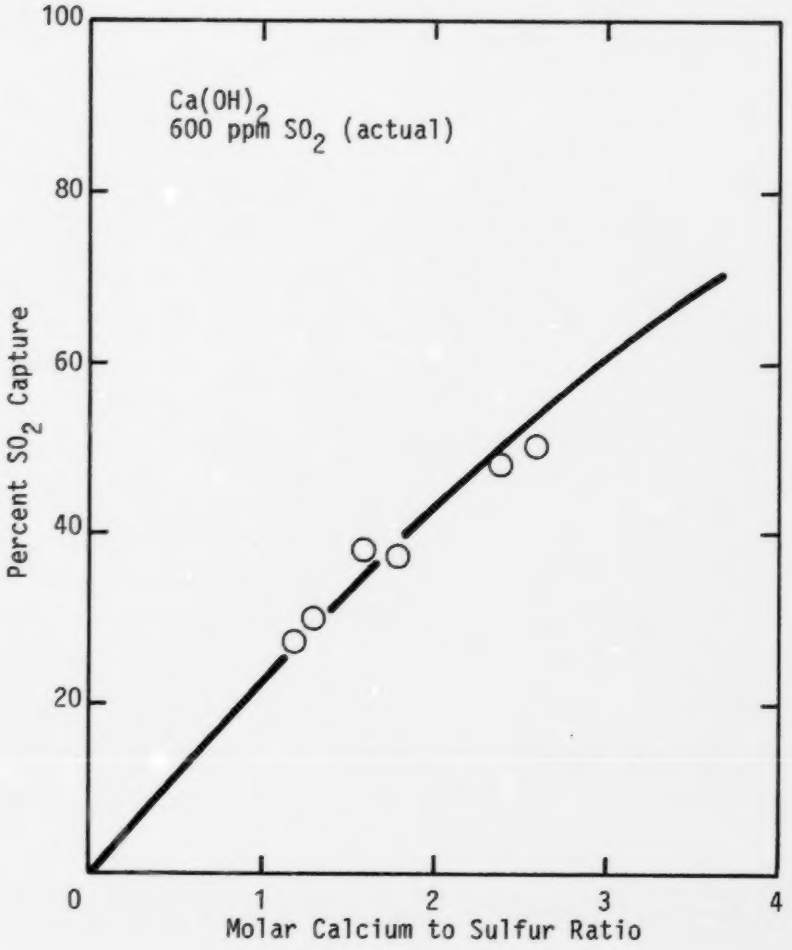

Figure 9-22. A comparison of SO_2 capture results from Tiefstack (see Figure 9-14) with grain model predictions. The grain model was calibrated against the bench-scale data of Figure 9-18 and then used to extrapolate to the Tiefstack conditions.

possible, the procedure outlined above should use only one sorbent for both the bench- and full-scale experiments.

GEN. 4208 F/R (10)

10.0 CONCLUSION

The overall conclusion from this study of combustion system similarity is that the available experimental data are, on the whole, reasonably consistent and most of the apparent discrepancies are the result of differences in experimental system design, sorbent characteristics, terminology, and actual test conditions. Unfortunately, SO_2 control by dry sorbent injection is an extremely complex physical/chemical process so that simple comparison of experimental results is difficult. Non-linear computer modeling of the overall process is required to fully evaluate experimental data from complex systems because no single process is rate limiting. In fact, the overall calculational procedure must include consideration of:

- calcium availability (initial surface area and Ca/S ratio)
- sintering (grain/pore growth)
- intrinsic chemical reaction
- pore diffusion
- product layer diffusion
- product layer buildup (reduced calcium accessibility)
- mixing of sorbent particles and bulk gas
- particle thermal history.

Not all of these process steps are important under all conditions, but at the present time none can be safely ignored.

Detailed activation and sulfation models were developed as part of this overall program. The distributed grain size model including catalyzed thermal sintering is capable of predicting temporal and overall sulfur capture for carbonate and hydrate sorbents in laboratory, bench-, and full-scale applications if at least one set of bench-scale calibration data are available for the sorbent of interest. This calibration process is required because at the present time in-situ sorbent characteristics can not be fully predicted based on fundamental considerations alone. Additional basic rate data are needed to characterize the development and loss of particle porosity (surface area, pore size distribution) as a function of thermal conditions and raw sorbent parameters before complete independent calculations will be possible.

The detailed technical conclusions regarding the overall sulfation process are as follows:

1. The initial sulfation rate is very rapid; as much as eighty percent of the overall calcium utilization may occur within the first 200 milliseconds after sorbent injection. Subsequently, the sulfation rate decreases dramatically and in a well-mixed system the increase in calcium utilization beyond 200 milliseconds is relatively small. The temporal behavior can be accurately predicted by both the distributed grain and distributed pore models. The models attribute the dramatic reduction of sulfation rate at longer times to a combination of sintering, particularly at high reaction temperatures, and pore mouth closure which results in a loss of available calcium sites. The physical property data available from analysis of extracted solid samples also confirm the potential importance of both sintering and pore closure.

2. The optimum sorbent injection temperature depends on the amount of sorbent transport air and, to a lesser extent, the downstream quench rate. In general, both the fundamental and bench-scale results suggest that injection systems should be designed to produce a peak particle temperature of approximately 2000°F. Thus, in instances where high transport air flow rates are used, the sorbent should be injected into a bulk gas stream of approximately 2200°F. Hydrates appear to be somewhat more sensitive to particle injection temperature than carbonates. Under very high quench rate conditions the injection temperature should be increased slightly (Ca 50°F) and the maximum SO_2 capture possible can be expected to decrease, particularly with hydrated sorbents. Theoretical calculations suggest that the influence of quench rate is somewhat mitigated by the competing effects of reduced residence time within

the sulfation window and reduced sintering rates as quench rate increases.

3. Calcium utilization increases as the mean particle size of the sorbent is decreased; for a typical hydrate sorbent a 5 percent increase in calcium utilization can be achieved by reducing the mean diameter from eight microns to four microns. Model calculations suggest that this increase is directly attributable to decreased internal diffusion resistance; a higher percentage of the overall calcium is available near the particle surface and, therefore, less likely to be shut off by subsequent sulfation. Theoretical calculations of particle size effects are complex because internal pore structure may change as external diameter changes.

4. Calcium utilization is relatively insensitive to gas phase sulfur concentration above 1000 ppm SO_2 under the conditions of practical interest in a typical utility boiler application. Increasing the SO_2 concentration increases the diffusional and intrinsic chemical rates; however, these effects are somewhat mitigated by increased pore mouth closure and/or non-linearities in the adsorption/reaction steps.

5. Commercial hydrates are significantly superior to commercial carbonates on an equal calcium basis. The available large scale test results and associated model predictions suggest that optimized injection of high reactivity limestones will produce 25 ± 5 percent SO_2 control at Ca/S = 2. Similar results with atmospheric hydrates indicate that capture levels of approximately 45 ± 5 percent can be achieved under optimized conditions in full-scale applications. This improved performance with hydrates appears to be associated with:

   - smaller inherent sorbent particle size

- significantly more rapid calcination (dehydration) and the associated development of higher local surface areas and more optimum internal porosity distribution during the first, critical 200 milliseconds.

11.0 REFERENCES

Beittel, R., S. J. Bortz, G. R. Offen, and D. C. Drehmel. "Effects of Injection Temperature and Quench Rate on Sorbent Utilization." In: Proceedings: 1986 Joint Symposium on Dry SO_2 and Simultaneous SO_2/NO_x Control Technologies, Vol. 1, EPA-600/9-86-029a (NTIS PB87-120465), October 1986.

Beruto, D. and A. W. Searcy. "Calcium Oxides of High Reactivity." Nature, 263, 221, 1976.

Beruto, D., L. Barco, A. W. Searcy, and G. Spinolo. "Characterization of Porous CaO Particles Formed by Decomposition of $CaCO_3$ and $Ca(OH)_2$ in Vacuum." J. of the American Ceramic Society, 63, 439, 1980.

Bhatia, S. K. and D. D. Perlmutter. "The Effect of Pore Structure on Fluid-Solid Reactions: Application to the SO_2-Lime Reaction." AIChE Journal. 27:226, 1981.

Borgwardt, R. H. Personal Communication, 1984.

Borgwardt, R. H. "Calcination Kinetics and Surface Area of Dispersed Limestone Particles." AIChE Journal, 31, 103, 1985.

Borgwardt, R. H. "Kinetics of the Reaction of SO_2 with Calcined Limestone." Envr. Sci. Tech. 4, 59, 1970.

Borgwardt, R. H., and K. R. Bruce. "Effect of Specific Surface Area on the Reactivity of CaO with SO_2." AIChE J., 32, 239, 1986.

Borgwardt, R. H., K. R. Bruce, and J. Blake. "EPA Experimental Studies of the Mechanisms of Sulfur Capture by Limestone." In: Proceedings: First Joint Symposium on Dry SO_2 and Simultaneous SO_2/NO_x Control Technologies, Vol. 1, EPA-600/9-85-020a (NTIS PB85-232353), July 1985.

Borgwardt, R. H. N. F. Roache, and K. R. Bruce. "Method for Variation of Grain Size in Studies of Gas-Solid Reactions Involving CaO." Ind. Eng. Chem. Fundam. 25, 165, 1986.

Bortz, S. J. and P. Flament. "Recent IFRF Fundamental and Pilot Scale Studies on the Direct Sorbent Injection Process." In: Proceedings: First Joint Symposium on Dry SO_2 and Simultaneous SO_2/NO_x Control Technologies, Vol. 1, EPA-600/9-85-020a (NTIS PB85-232353) July 1985.

Bortz, S. J., V. P. Roman, R. J. Yang, P. Flament, and G. R. Offen. "Precalcination and its Effect on Sorbent Utilization During Upper Furnace Injection." In: Proceedings: 1986 Joint Symposium on Dry SO_2 and Simultaneous SO_2/NO_x Control Technologies, Vol. 1, EPA-600/9-86-029a (NTIS PB87-120465), October 1986.

Cameron, D. and J. A. Arnott. "Design and Testing of a Retrofit Dry Sorbent Injection System on a 300 MW Pulverized Fuel Boiler." In: Proceedings: 1986 Joint Symposium on Dry SO_2 and Simultaneous SO_2/NO_x Control Technologies, Vol. 2, EPA-600/9-86-029b (NTIS PB87-120457), October 1986.

Campbell, F. R., A. W. D. Hills, and A. Paulins. "Transport Properties of Porous Lime and Their Influence on the Decomposition of Porous Compacts of Calcium Carbonate." Chemical Engineering Science, 25, 929, 1970.

Cole, J. A., J. C. Kramlich, W. R. Seeker, G. D. Silcox, G. H. Newton, D. J. Harrison, and D. W. Pershing. "Fundamental Studies of Sorbent Reactivity in Isothermal Reactors." In: Proceedings: 1986 Joint Symposium on Dry SO_2 and Simultaneous SO_2/NO_x Control Technologies, Vol. 1, EPA-600/9-86-029a (NTIS PB87-120465), October 1986.

Coutant, R. W., R. Simon, B. E. Campbell, and R. E. Barrett. Investigation of the Reactivity of Limestone and Dolomite for Capturing SO_2 from Flue Gas. EPA report APTD 0802 (NTIS PB204385), October 1971.

Darroudl, T. and A. W. Searcy. "Effect of CO_2 Pressure on the Rate of Decomposition of Calcite." J. Phys. Chem., 85, 3971, 1981.

Farzan, H., L. Rodger, G. Maringo, and G. Offen. "Application of Upper-Furnace Sorbent Injection for SO_2 Control in Coal-Fired Cyclone-Equipped Boilers." In: Proceedings: 1986 Joint Symposium on Dry SO_2 and Simultaneous SO_2/NO_x Control Technologies, Vol. 1, EPA-600/9-86-029a (NTIS PB87-120465), October 1986.

Hartman, M. and R. W. Coughlin. "Reaction of Sulfur Dioxide with Limestone and the Influence of Pore Structure." Ind. Eng. Chem. Process Develop. 13, 248, 1974.

Hartman, M. and R. W. Coughlin. "Reaction of Sulfur Dioxide with Limestone and the Grain Model." AIChE J. 22, No. 3. 490 (1976).

Hyatt, E. P., I. B. Cutler, and M. E. Wadsworth. "Calcium Carbonate Decomposition in Carbon Dioxide Atmosphere." J. of the American Ceramic Society, 41, 70, 1958.

Ishihara, Y. "Kinetics of the Reaction of Calcined Limestone with Sulfur Dioxide in Combustion Gases." Presented at the Dry Limestone Injection Process Symposium, June 22-26, 1970, Gilbertsville, KY.

Luss, D. "On the Pseudo Steady State Approximation for Gas-Solid Reactions." The Canadian Journal of Chemical Engineering, 46, 154, 1968.

McClellan, G. H. Physical Characterization of Calcined and Sulfated Limestones. Presented at the Dry Limestone Injection Process Symposium, Gilbertsville, Ky., June 1970.

Muzio, L. J., G. R. Offen, A. A. Boni, and R. Beittel. "The Effectiveness of Additives for Enhancing SO_2 Removal with Calcium Based Sorbents." In: Proceedings: 1986 Joint Symposium on Dry SO_2 and Simultaneous SO_2/NO_x Control Technologies, Vol. 1, EPA-600/9-86-029a (NTIS PB87-120465), October 1986.

Newton, G. H. "Sulfation of Calcium-Based Sorbents in a Combustion Environment." Ph.D. Dissertation, Department of Chemical Engineering, University of Utah (1986).

Newton, G. H., D. Harrison, G. D. Silcox, and D. W. Pershing. "Control of SO_x Emissions by In-Furnace Sorbent Injection: Carbonates vs. Hydrates." Environmental Progress, Vol. 5, No. 40 (May 1986).

Overmoe, B. J., S. L. Chen, L. Ho, W. R. Seeker, M. P. Heap, and D. W. Pershing. Boiler Simulator Studies on Sorbent Utilization for SO_2 Control. In: Proceedings: First Joint Symposium on Dry SO_2 and Simultaneous SO_2/NO_x Control Technologies, Volume 1, EPA-600/9-85-020a (NTIS No. PB85-232353), July 1985.

Overmoe, B. J., J. M. McCarthy, S. L. Chen, W. R. Seeker, and D. W. Pershing. Reactivity Study of SO_2 Control with Atmospheric and Pressure Hydrated Sorbents, EPA-600/7-86-040 (NTIS PB87-129250), November 1986.

Pigford, R. R. and G. Sliger. "Rate of Diffusion-Controlled Reaction Between a Gas and a Porous Solid Sphere." Ind. Eng Chem. Process Des. Develop. 12, 85, 1973.

Reese, J. L., R. Payne, and Y. Chughtai. "Evaluation of Sorbent Injection Test at Tiefstack, West Germany." In: Proceedings: 1986 Joint Symposium on Dry SO_2 and Simultaneous SO_2/NO_x Control Technologies, Vol. 2, EPA-600/9-86-029b (NTIS PB87-120457), October 1986.

Reid, W. T. "Basic Factors in the Capture of Sulfur Dioxide by Limestone and Dolomite." Journal of Engineering for Power: Transactions of the ASME, January 1970.

Roman, V. P., L. J. Muzio, M. W. McElroy, K. W. Bowers, and D. T. Gallaspy. "Flow Reactor Study of Calcination and Sulfation." In: Proceedings: First Joint Symposium on Dry SO_2 and Simultaneous SO_2/NO_x Control Technologies, Vol. 1, EPA-600/9-85-020a (NTIS PB85-232353), July 1985.

Searcy, A. W. and D. Beruto. "Kinetics of Endothermic Decomposition Reactions. 2. Effects of the Solid and Gaseous Products." J. Phys. Chem. 82, 163, 1978.

Silcox, G. D. "Analysis of the SO_2-Lime Reaction: Mathematical Modeling and Experimental Studies with Emphasis on Stoker Applications." Ph.D. Dissertation, Department of Chemical Engineering, University of Utah, 1985.

Slaughter, D. M. "Formation and Control of Nitrogen and Sulfur Oxides in Suspension Coal Combustion," Ph.D. Dissertation, Department of Chemical Engineering, University of Utah, 1986.

Snow, M. J. H. "The Sulfation of Limestone and Calcium Oxide: Direct and Series Reaction," Ph.D. Dissertation, Department of Chemical Engineering, Massachusetts Institute of Technology, 1985.

Staudinger, G. and H. Schrofelbauer. "Field Experience with Commercial Furnace Limestone Injection." In: Proceedings: 1986 Joint Symposium on Dry SO_2 and Simultaneous SO_2/NO_x Control Technologies, Vol. 2, EPA-600/9-86-029a (NTIS PB87-120457), October 1986.

Teixeira, D. P., T. A. Lott, and L. J. Muzio. "Dry Sorbent SO_2 Control for New Power Plants Burning Low Sulfur Western Coals." In: Proceedings: 1986 Joint Symposium on Dry SO_2 and Simultaneous SO_2/NO_x Control Technologies, Vol. 1, EPA-600/9-86-029a (NTIS PB87-120457), October 1986.

Tokuda, K., M. Sakai, T. Sengoku, N. Murakami, M. W. McElroy, and K. Mouri. "Evaluation of SO_2 Removal by Furnace Limestone Injection with Tangentially Fired Low-NO_x Burner." In: Proceedings: First Joint Symposium on Dry SO_2 and Simultaneous SO_2/NO_x Control Technologies, Vol. 1, EPA-600/9-85-020a (NTIS PB85-232353), July 1985.

Vatsky, J. and E. S. Schindler. "Limestone Injection Reduces SO_2 and NO_x Emissions." Mechanical Engineering, Vol. 107, No. 11, November 1985.

Womble, T. D., et al. "Presentation of Full-Scale Dry Limestone Injection Project at Shawnee Steam Plant." Presented at the Dry Limestone Injection Process Symposium, Gilbertsville, Ky., June 22-26, 1970.

Appendix A. Descriptions of Various Experimental Systems

A.1 Bench Scale Facilities

A.1.1 The Controlled Temperature Tower

The Controlled Temperature Tower (CTT) is a plug flow reactor designed to study pollutant formation and control associated with coal combustion. A schematic of the reactor is shown in Figure A-1. The top section of the reactor includes an 18 inch long quarl that diverges from 2 to 8 inches. The reactor inside diameter is 8 inches and at a firing rate of 90,000 Btu/hr the Reynolds number is roughly 1400. Numerous ports along the reactor axis permit the insertion of sorbent injectors and sampling probes. The temperature profile of the CTT can be manipulated by firing one or both of the back-fired heating channels shown in Figure A-1. The channels are heated with natural gas burners.

Sorbent injection in the CTT is performed using a radial multi-hole injector positioned on the axis of the reactor. Of the total air flowing into the CTT, 10 to 15 percent is used to convey the sorbent.

A.1.2 The Boiler Simulator Furnace

The Boiler Simulator Furnace (BSF) was designed to simulate the time-temperature history of a full scale utility boiler. Accordingly, the BSF includes a flame zone, a radiant zone, convective passages, and a baghouse. The BSF is shown schematically in Figure A-2. The inside diameter of the radiant and post flame sections is 22 inches and at a firing rate of 1 x 10^6 Btu/hr the Reynolds number is approximately 5000. Ports located along the furnace's axis permit the insertion of sampling probes, sorbent injectors, and cooling tubes. The time-temperature history can be adjusted by changing the firing rate and by the insertion of cooling tubes.

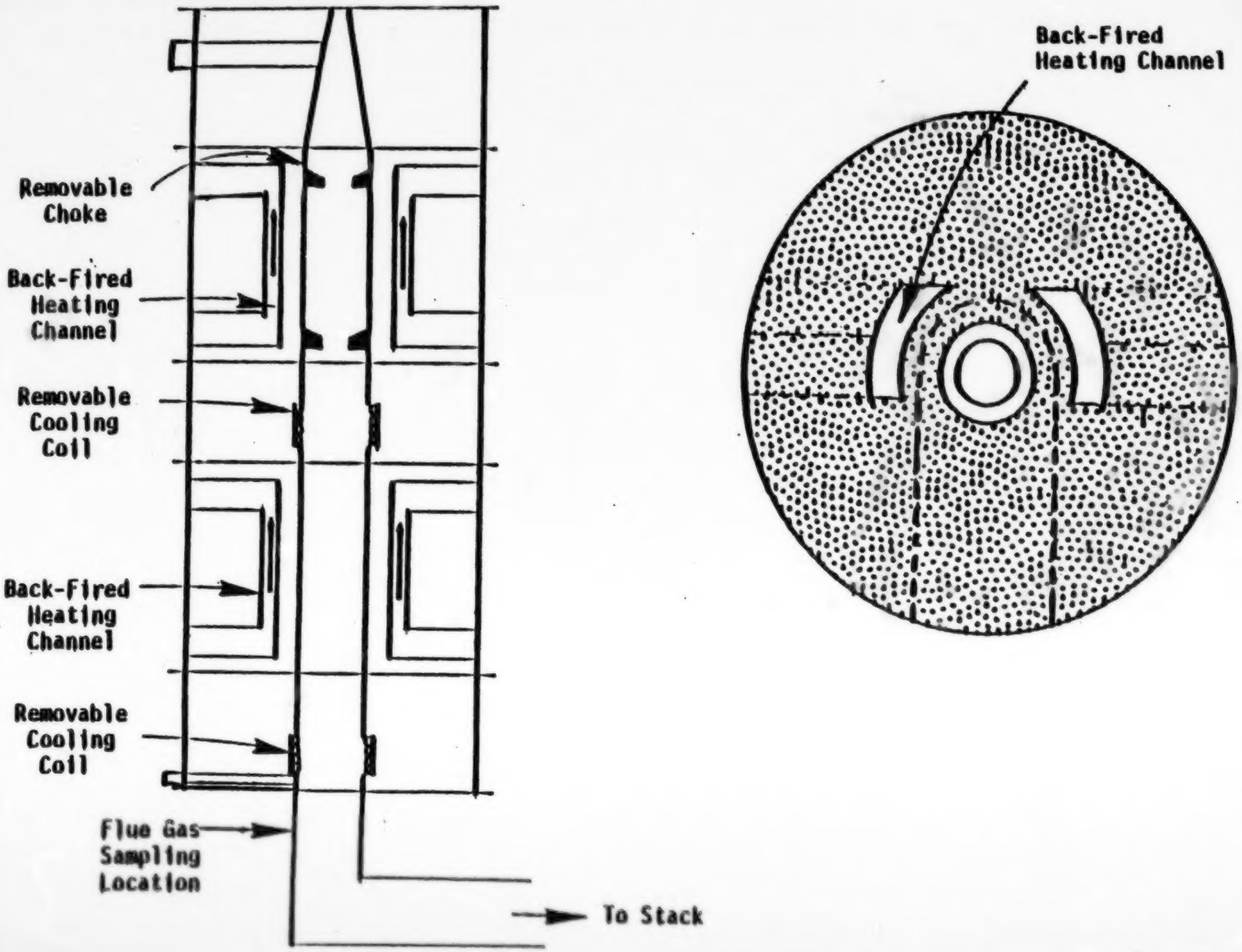
Removable Choke
Back-Fired Heating Channel
Removable Cooling Coil
Back-Fired Heating Channel
Removable Cooling Coil
Flue Gas Sampling Location
To Stack
Back-Fired Heating Channel

Figure A-1. Cross-sectional views of the control temperature tower.

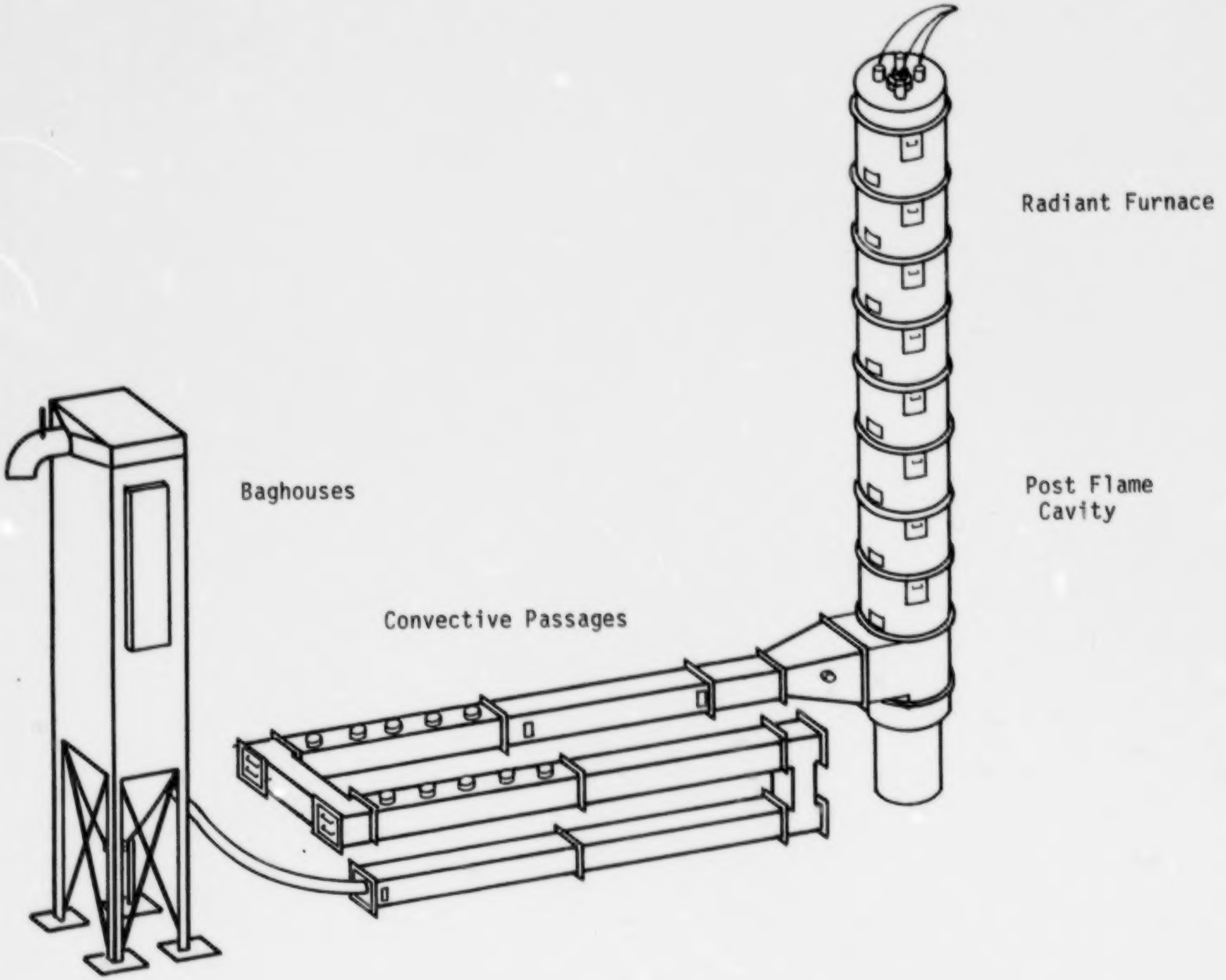
Radiant Furnace
Post Flame
Cavity
Baghouses
Convective Passages

Figure A-2. A schematic of the BSF.

Sorbent injection in the BSF is accomplished using a radial, multi-hole injector positioned on the axis of the furnace. Of the total air supplied to the BSF, 10 to 15 percent is used to convey the sorbent.

A.1.3 The Combustor of Teixeira, et al. (1986)

The vertical, down-fired reactor burns natural gas which has been doped with SO_2. A schematic of the combustor is shown in Figure A-3. The precombustor section of the reactor is 30 inches long with a diameter of 7 inches. The sorbent is injected in a narrow throat that expands into the 6 inch diameter test section.

Nominal operating conditions include a firing rate of 1×10^5 Btu/hr, a gas velocity of 9 ft/s, residence times ranging from 0.05 to 1.3 seconds, and a Reynolds number of 2000 at 2010°F. At nominal load the temperature in the reactor decreases at roughly 450°F/sec.

A.1.4 The Intermediate Scale Combustor of Muzio, et al. (1986)

The intermediate scale combustor of Muzio, et al. (1986 is identical to that described in Section A.1.3.

A.1.5 The Pilot Combustor System of Beittel, et al. (1986)

A schematic of the pilot combustor system of Beittel, et al. (1986) is shown in Figure A-4. The refractory walled combustor is fired with coal at 1×10^6 Btu/hr. The down-fired system has an inside diameter of 30 inches and an overall length of 10 feet. The refractory lined walls can be replaced with water-cooled panels to provide additional cooling. The firing rate can also be varied to provide different thermal environments. The various system configurations and corresponding quench rates are summarized in Table A-1.

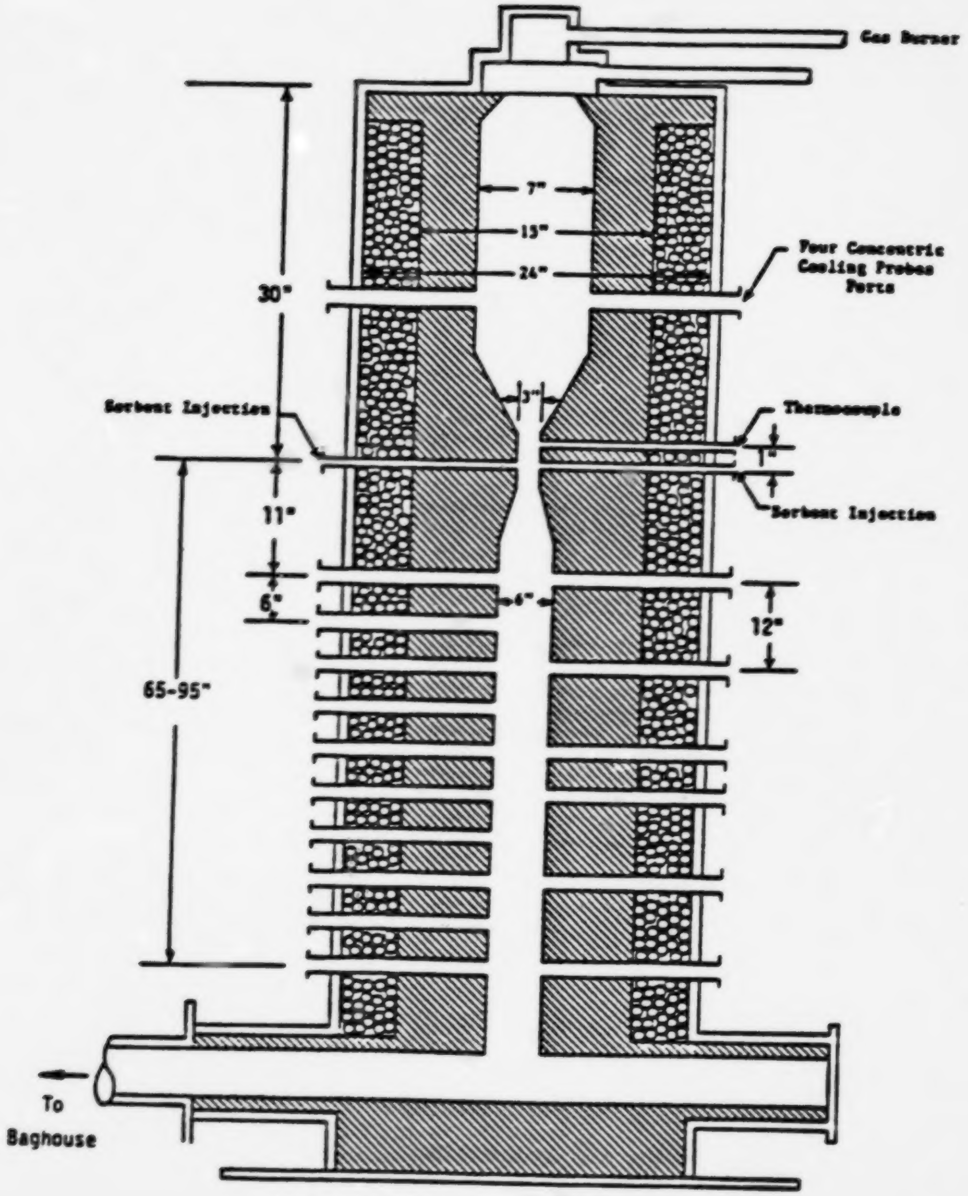
Gas Burner
7"
13"
24"
30"
Four Concentric Cooling Probes Ports
3"
Sorbent Injection
Thermocouple
1"
Sorbent Injection
11"
6"
4"
12"
65-95"
To Baghouse

Figure A-3. A schematic of the reactor used by Teixeira, et al. (1986).

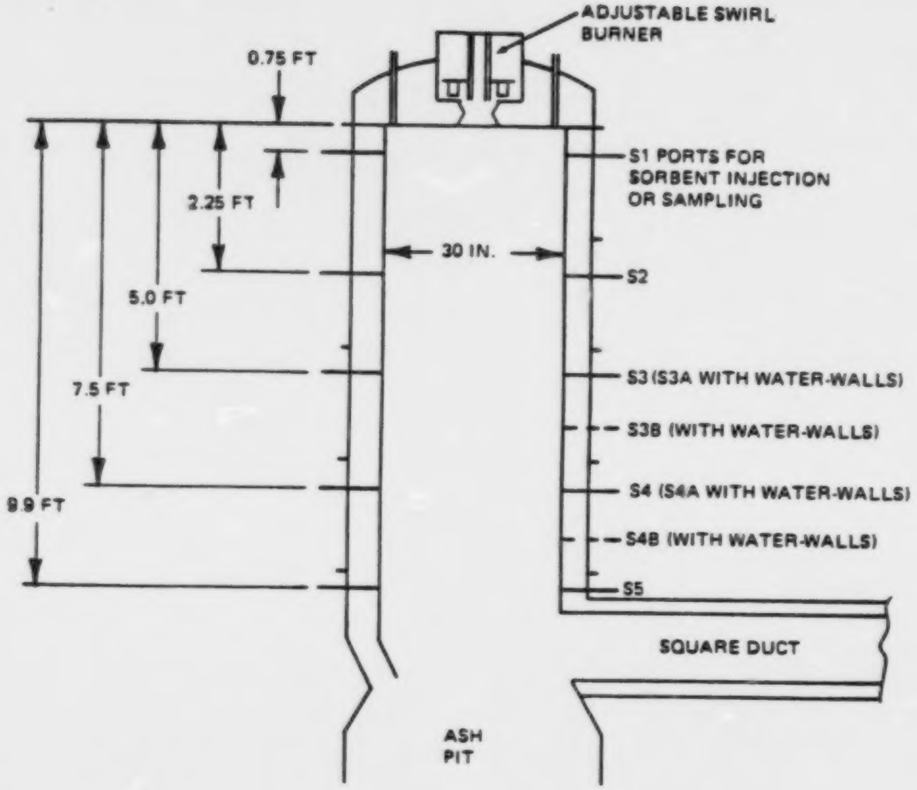
ADJUSTABLE SWIRL BURNER
0.75 FT
2.25 FT
5.0 FT
7.5 FT
9.9 FT
30 IN.
S1 PORTS FOR SORBENT INJECTION OR SAMPLING
S2
S3 (S3A WITH WATER-WALLS)
S3B (WITH WATER-WALLS)
S4 (S4A WITH WATER-WALLS)
S4B (WITH WATER-WALLS)
S5
SQUARE DUCT
ASH PIT

Figure A-4. A schematic of the pilot combustor system of Beittel, et al. (1986).

TABLE A-1. SYSTEM CONFIGURATIONS AND QUENCH RATES

Configuration	Firing Rate, 10^6 Btu/hr	Quench, °F/s
All refractory	0.6	-100
All refractory	1.0	-360
Water wall	1.0	-550
Water wall	1.3	-620

A.1.6 The Small Boiler Simulator of Forzan, et al. (1986)

A schematic of the 6×10^6 Btu/hr small boiler simulator (SBS) is shown in Figure A-5. The pulverized coal fired simulator has inside dimensions of 5 x 7 feet. The superheat sections are 2 x 4 feet. The furnace is refractory lined and water cooled tube banks simulate the cooling found in full-scale convective passages. The tube bank simulation includes sootblowers and observation ports. The quench rate is -1100°F/s. Capture levels were a function of the sootblowing cycle. Capture levels were lowest immediately after sootblowing. Sorbents were injected at the furnace exit at 2250°F.

A.1.7 The Tower Reactor of Slaughter (1986) and Newton (1986)

The tower reactor of Slaughter (1986) and Newton (1986) is shown schematically in Figure A-6. The overall length is 8 feet and the inside diameter is 6 inches. A $2 \times 2 \times 10^5$ Btu/hr, natural gas burner provided the combustion environment while two 1.0×10^5 Btu/hr auxiliary burners in annular channels surrounding the main reaction chamber provided a nearly isothermal (± 20°F) environment. The reactor is refractory lined and can be operated in either an isothermal or a non-isothermal model. The residence time is nominally 0.5 seconds and the non-isothermal configuration is quenched at the rate of 870°F/s.

A.1.8 The Dispersed-Phase Reactor of Coutant, et al. (1971)

A schematic of the reactor of Coutant et al. (1971) is shown in Figure A-7. The reaction zone is 14 feet in length and 11 inches in diameter and is lined with alundum tubing. The gas velocity is roughly 5 ft/s and at 2500°F the Reynolds number is 1800. A gas fired burner at the bottom of the reactor provides hot combustion gases. Particles of limestone injected into the gas stream are carried upward. The nominal quench rate is 440°F/s but quench rates as high as 950°F/s are obtainable.

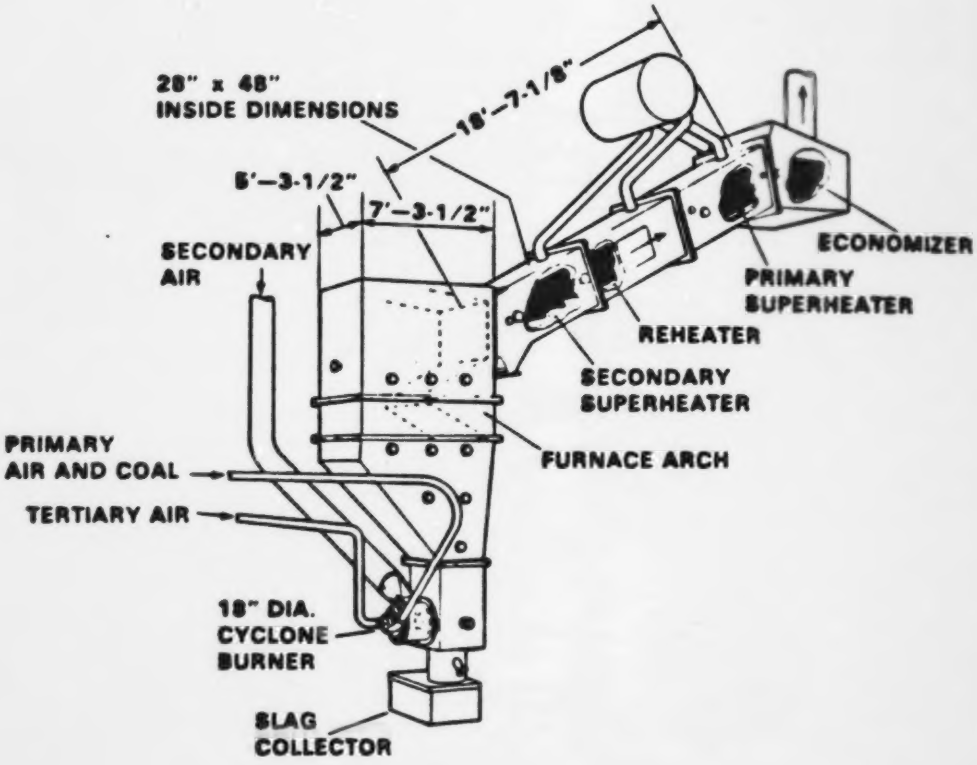
28" x 48"
INSIDE DIMENSIONS
18'—7-1/8"
5'—3-1/2"
7'—3-1/2"
SECONDARY AIR
ECONOMIZER
PRIMARY SUPERHEATER
REHEATER
SECONDARY SUPERHEATER
FURNACE ARCH
PRIMARY AIR AND COAL
TERTIARY AIR
18" DIA. CYCLONE BURNER
SLAG COLLECTOR

Figure A-5. A schematic of the small boiler simulator.

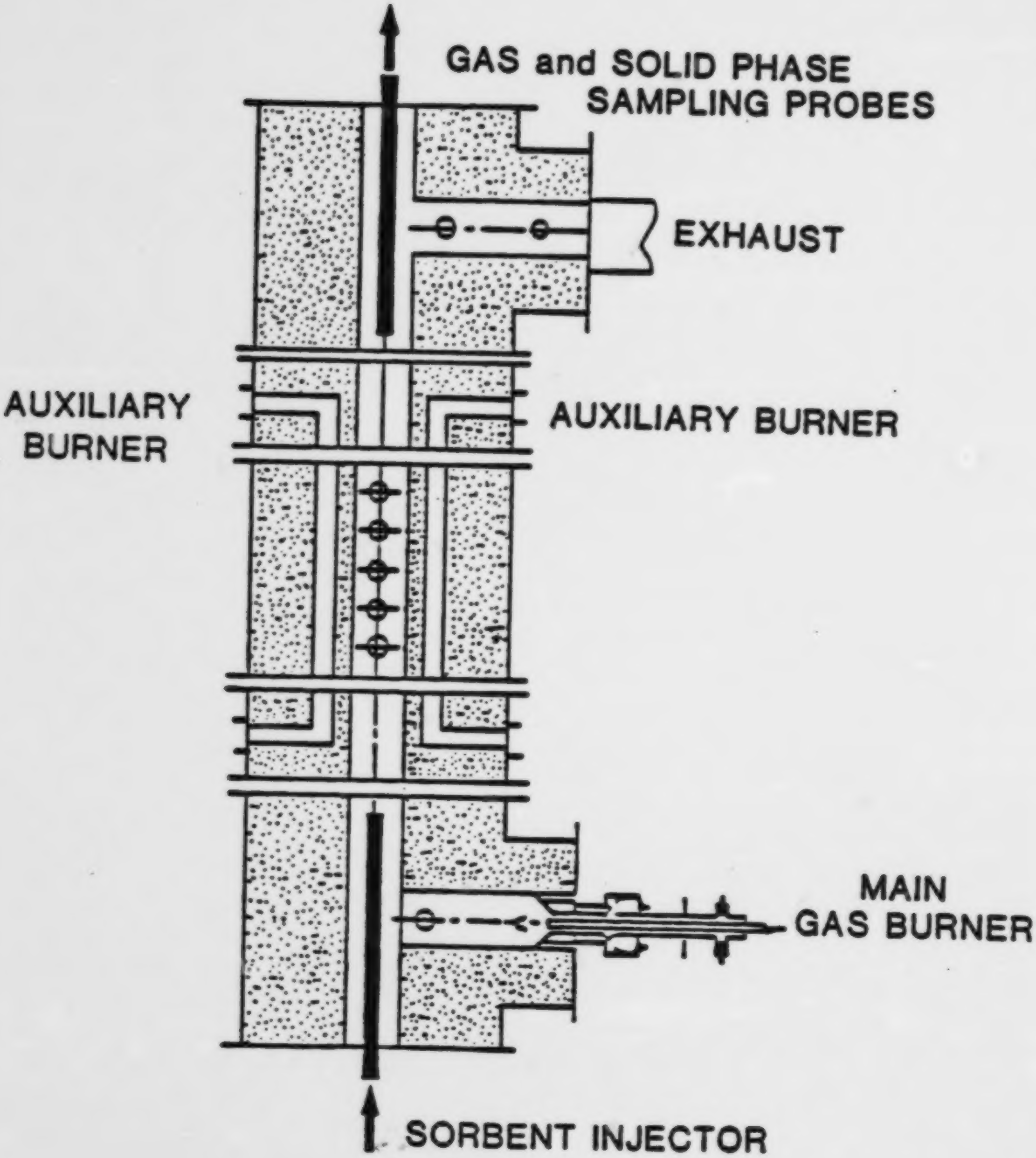
GAS and SOLID PHASE
SAMPLING PROBES
EXHAUST
AUXILIARY
BURNER
AUXILIARY BURNER
MAIN
GAS BURNER
SORBENT INJECTOR

Figure A-6. A schematic of the tower reactor.

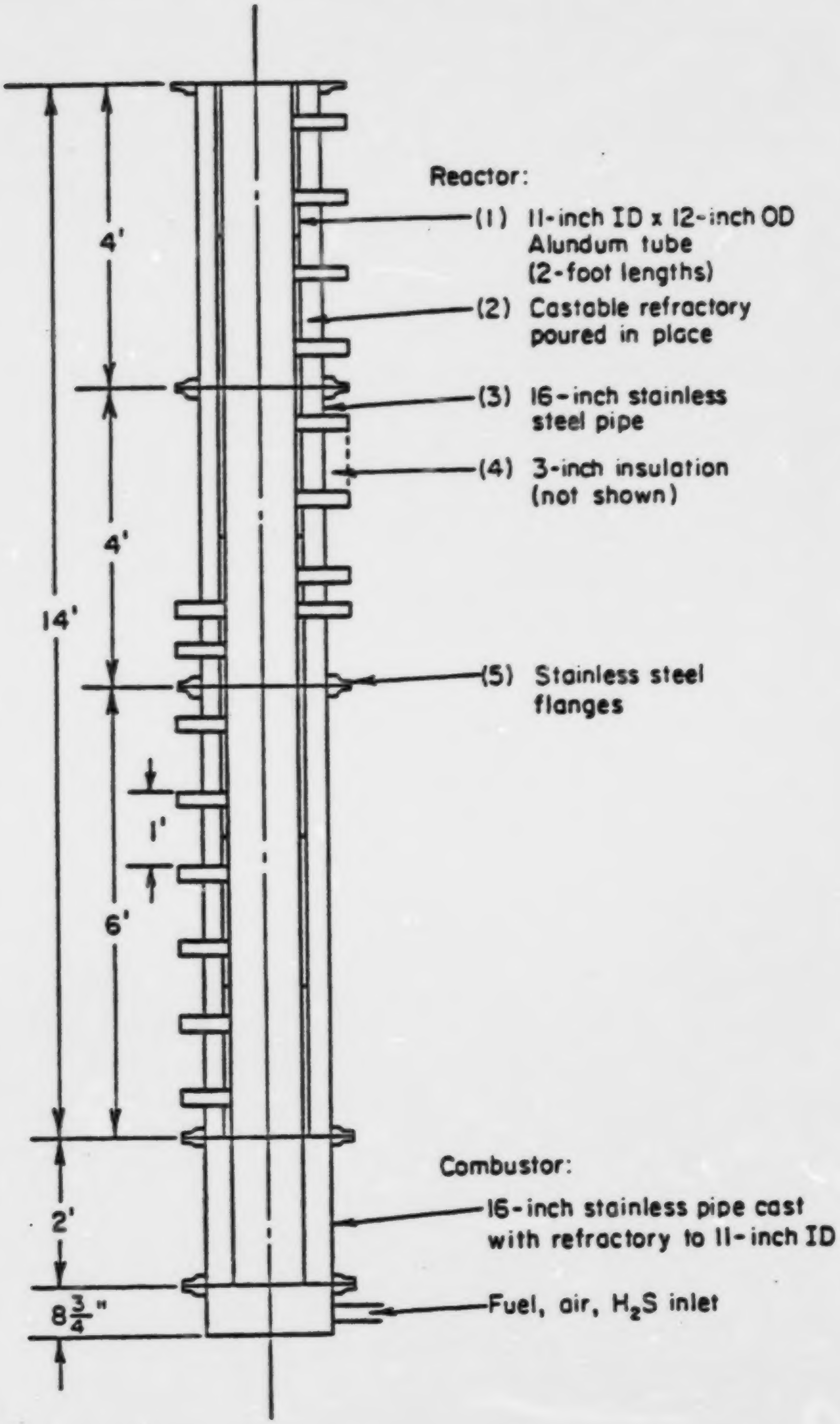
Reactor:
(1) 11-inch ID x 12-inch OD Alundum tube (2-foot lengths)
(2) Castable refractory poured in place
(3) 16-inch stainless steel pipe
(4) 3-inch insulation (not shown)
(5) Stainless steel flanges
Combustor:
16-inch stainless pipe cast with refractory to 11-inch ID
Fuel, air, H_2S inlet
4'
4'
14'
1'
6'
2'
$8\frac{3}{4}$"

Figure A-7. A schematic of the flow reactor of Coutant, et al. (1971).

Appendix B.
DETAILED DESCRIPTIONS OF VARIOUS COMPUTER MODELS

B.1 The Grain Model

A mathematical formulation of the grain model is presented here and the numerical solution is outlined. Figure B-1 shows the main features of the grain model. The porous CaO particle is represented as a conglomerate of small grains. As the sulfation reaction proceeds each grain is surrounded by a layer of $CaSO_4$ indicated in the figure by the heavy black band encircling an unreacted core of CaO. As the reaction progresses the pores between the grains are gradually blocked by the accumulation of $CaSO_4$. The blockage occurs because the ratio of the molar volumes, $V(CaSO_4)/V(CaO)$, is 2.7.

The modeling of the sulfation reaction by Hartman and Coughlin (1976) is used as a starting point for the present work. The reaction is analyzed by considering that the SO_2 must undergo the following:

- Diffusion from the bulk gas to the particle's surface
- Pore diffusion to the particle's interior
- Solid-state diffusion through the product layer
- Reaction at the product-lime interface or at the gas-product interface

The exact mechanism of the reaction is not known and a discussion of various possibilities is given in Section 4.0. The following additional assumptions are made in the development of the model.

- The lime particles are fully calcined
- The reaction is irreversible
- The sole sulfation product is $CaSO_4$
- Excess oxygen is present and its concentration is constant
- The lime particles and grains are spherical

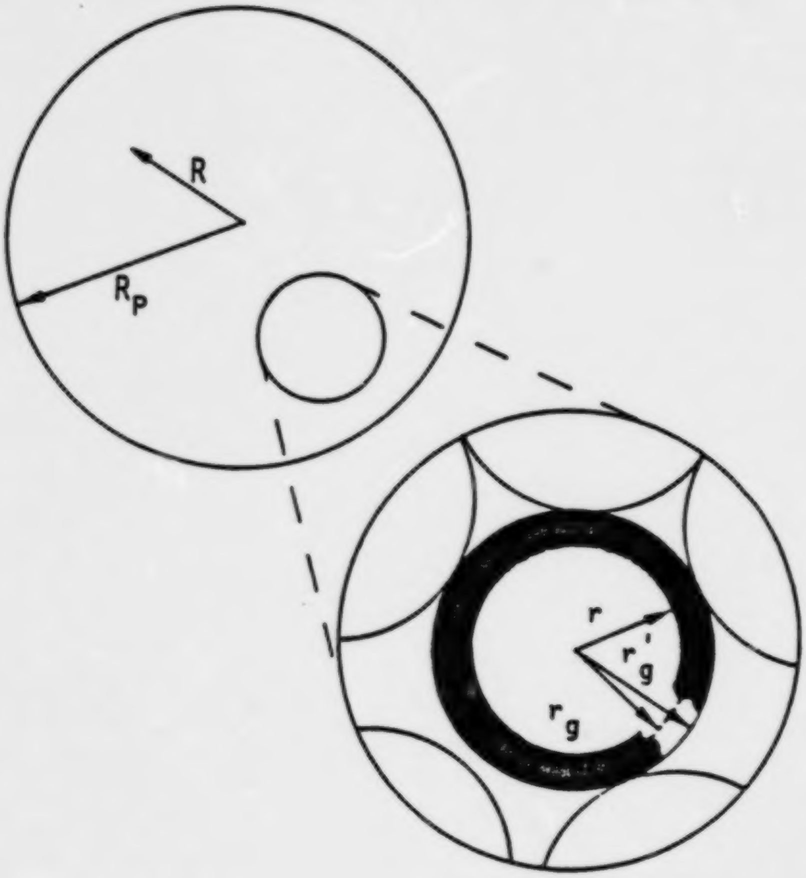

Figure B-1. A schematic of the grain model. The enlarged view of the porous particle shows a drak band of product of radius r_g', the initial grain radius, r_g, and the radius of the unreacted core of reactant, r.

The governing equations are obtained from material balances on the particle and the constituent grains. Starting with the particle, a balance on SO_2 in a spherical shell yields:

$$\frac{d_2C}{DR^2} + \left(\frac{2}{R} + \frac{1}{D_{eff}}\frac{dD_{eff}}{dR}\right)\frac{dC}{dR} - \frac{N}{D_{eff}} = 0 \tag{B.1}$$

where C is the SO_2 concentration, R is the radial coordinate, D_{eff} is the effective diffusivity for porous CaO, and N is the rate at which SO_2 is consumed per unit volume of porous solid. In obtaining equation B.1 a steady state approximation is made as justified by Luss (1968). The boundary conditions are written for the center of the particle (R = 0) and for the outer edge of the particle ($R = R_p$):

- At $R = 0$, $\frac{dC}{DR} = 0$ for all time (B.2)

- At $R = R_p$, $D_{eff}\frac{dC}{dR} = k\,(C_o - C)$ (B.3)

where C_o is the bulk gas concentration of SO_2 and k is a mass transfer coefficient. The latter can be expressed in terms of a Sherwood number,

$$Sh = \frac{kd_p}{D_{AB}}$$

where d_p is the particle diameter and D_{AB} is the ordinary diffusion coefficient for SO_2 in air.

Following the discussion in Section 4.0, the reaction rate term N is given by:

$$N = \frac{C^h}{\frac{1}{K} + \frac{r^2}{D}\ \frac{1}{r} - \frac{1}{r_g}} \cdot A,\ \frac{\text{gmol}}{\text{cm}^3\ \text{sec}} \qquad \text{(B.4)}$$

where h is the reaction order, K is a rate constant, D is the solid product layer diffusion coefficient, r is the radius of the CaO within a grain, r_g' is the radius of a sulfated grain, and A is the interfacial area available for reaction per unit volume of porous solid.

The solution of equations B.1, B.2, and B.3 is obtained by writing them in finite difference form. The resulting simultaneous, non-linear equations are solved by the Newton-Raphson technique. The finite difference equations are set up as follows. Divide the particle radius into N + 1 nodes where node 1 is the particle center. Let $FC^h = -N/D_{eff}$. Then equation B.1 becomes:

$$\frac{d^2C}{dR^2} + \quad \frac{2}{R} + \frac{1}{D_{eff}}\ \frac{dDeff}{dR}\quad \frac{dC}{dR} + FC^h = 0. \qquad \text{(B.5)}$$

Approximate the first and second order derivations as:

$$\left.\frac{dC}{dR}\right|_i \doteq \frac{C_{i+1} - C_{i-1}}{2\Delta R}$$

and

$$\left.\frac{d^2C}{dR^2}\right|_i \doteq \frac{C_{i+1} - 2C_i + C_{i-1}}{(\Delta R)^2}$$

Equation B.6 becomes (for nodes 2, 3, ..., N):

$$\left(\frac{1}{(\Delta R)^2} + \frac{1}{R_i \Delta R} + \frac{DD_i}{D_i}\ \frac{1}{2\Delta R}\right) C_{i+1} - \frac{2}{(\Delta R)^2}\ C_i + F_i\ C_i\ ^h$$

$$+\left(\frac{1}{(\Delta R)^2} - \frac{1}{R_i \Delta R} - \frac{DD_i}{D_i}\ \frac{1}{2\Delta R}\right) C_{i-1} = B_i = 0 \qquad \text{(B.6)}$$

To apply the Newton-Raphson technique it is necessary to calculate the derivatives of equation B.6:

$$P_i = \frac{\partial B_i}{\partial Ci+1} = \left(\frac{1}{(\Delta R)^2} \quad \frac{1}{R_i \Delta R} + \frac{DD_i}{D_i} \quad \frac{1}{2\Delta R} \right) \tag{B.7}$$

$$d_i = \frac{\partial B_i}{\partial C_i} = - \frac{2}{(\Delta R)^2} + F_i \; h \; C_i \; ^{h-1} \tag{B.8}$$

$$q_i = \frac{\partial B_i}{\partial C_{i-1}} = \left(\frac{1}{(\Delta R)^2} - \frac{1}{R_i \Delta R} - \frac{DD_i}{D_i} \quad \frac{1}{2\Delta R} \right) \tag{B.9}$$

At the center of the particle, equation B.2 applies and equation B.5 becomes:

$$\frac{d^2C}{dR^2} + FC^h = 0. \tag{B.10}$$

In finite difference form this becomes:

$$\frac{2}{(\Delta R)^2} \; C_{i+1} - \frac{2}{(\Delta R)^2} \; C_i + F_i \; C_i \; ^h = B_i = 0 \tag{B.11}$$

Equation B.11 is differentiated to give:

$$P_i = \frac{B_1}{C_2} = \frac{2}{(\Delta R)^2} \tag{B.12}$$

$$d_i = \frac{B_i}{C1} = - \frac{2}{(\Delta R)^2} + F_i \; h \; C_i \; ^{h-1} \tag{B.13}$$

For the outer mode equation B.3 becomes:

$$D_{n+1} \left(\frac{C_{n-1} - C_n}{\Delta R} \right) = k \; (C_o - C_{n+1}) \tag{B.14}$$

or $\left(k + \frac{D_{n+1}}{R}\right) C_{n+1} - \frac{D_{n+1}\, C_n}{R} - k\, C_o = B_{n+1} = 0$

Equation (B.14) is differentiated to give:

$$d_{n+1} = \frac{B_{n+1}}{C_{n+1}} = k + \frac{D}{\Delta R} \qquad \text{(B.15)}$$

$$q_{n+1} = \frac{B_{n+1}}{C_n} = - \frac{D}{\Delta R} \qquad \text{(B.16)}$$

The d_1, p_1, and q_1 are arranged in the matrix $\underset{\approx}{Q}$:

$$\underset{\approx}{Q} = \begin{bmatrix} d_i & p_1 & 0 & \cdots & 0 \\ q_2 & d_2 & p_2 & 0 \cdots & 0 \\ 0 & q_3 & d_3 & p_3 \cdots & 0 \\ \cdot\cdot & & & & \\ \cdot\cdot & & & & \\ \cdot\cdot & & & & \\ 0 & \cdot\cdot & & q_{n+1} & d_{n+1} \end{bmatrix}$$

The Newton-Raphson technique is initialized by guessing a SO_2 concentration for each node in the particle. With this initial guess the matrix Q and the vector $\underset{\sim}{B}$ can be evaluated. Corrections to the concentrations can then be calculated by solving the equations:

$$\underset{\approx}{Q}\ \underset{\sim}{\Delta C} = - \underset{\sim}{B}$$

where $\underset{\sim}{\Delta C}$ is the vector of corrections. The revised concentrations are then calculated from the equation:

$$C_1^{NEW} = C_1^{OLD} + \Delta C_1$$

The new concentrations are used to evaluate $\underset{\approx}{Q}$ and $\underset{\sim}{B}$ and the process is repeated until the magnitude of the $\underset{\sim}{B}$ vector is less than some specified epsilon.

B.3 The Distributed Pore Model

The distributed pore model describes mathematically the processes involved in the sulfation of lime.

The differential equations which describe diffusion to the particle surface, sulfation of the external particle surface, pore diffusion, and internal sulfation are discussed below. Overall conversion is the sum of conversions due to reaction on the exterior particle surface and to reaction on the surfaces of the interior pores.

B.3.1 Product Layer Diffusion

A material balance on SO_2 over the annular $CaSO_4$ layer lining the pores yields:

$$\frac{1}{r} \frac{\partial}{\partial r} D_s \, r \frac{d\bar{C}}{d_r} = 0 \qquad (B.17)$$

where the system is assumed to be at steady state. There are two boundary conditions:

$$\bar{C} = C_{r=r_1} \text{ at } r = r_1$$

and (B.18)

$$kC_2 = -D_s \frac{\partial \bar{C}}{\partial r} \text{ at } r = r_2$$

where:

r_1 = pore radius
r_2 = pore radius at reaction interface
C = SO_2 concentration in pores
C_2 = SO_2 concentration at r_2
$\bar{C}$ = SO_2 concentration in the product layer

k = reaction rate constant

D_s = solid product diffusion coefficient

Equations B.17 and B.18 can be solved for C_2:

$$C_2 + C_2 R Bi_s \gamma \ln \gamma - \psi C_o = 0$$

where:

$Bi_s = kr_o/D_s$

$\gamma = r_1/r_2$

$R = r_1/r_0$

$\psi = C/C_o$

C_o = initial bulk SO_2 concentration

α = ratio of the molar volumes of $CaSO_4$ and CaO

r_o = initial pore radius

and where r_1 and r_2 are related by the equation:

$$r_1^2 = \alpha r_o^2 + (1 - \alpha)\, r_2^2$$

B.3.2 Pore Diffusion

A material balance on SO_2 over a section of a pore, assuming steady state conditions, yields:

$$\frac{1}{r_2} \frac{\partial}{\partial y} \left[r_i^2 D \frac{\partial C}{\partial y} \right] = k\, C_2 \qquad (B.19)$$

The associated boundary conditions are:

$$\frac{dC}{dy} = 0 \text{ at } x = 0$$

and (B.20)

$$C = C_s \text{ at } x = \ell$$

The variables are defined as follows:

y = axial distance along pore, measured from the center of the particle
l = pore length
D = diffusivity of SO_2 in pore
C_s = SO_2 concentration at the surface

The rate of change of r_2 with time is given by:

$$\frac{dr_2}{dt} = k\ V_{CaO}\ C_2 \qquad (B.21)$$

where V_{CaO} is the molar volume of CaO.

B.3.2 Numerical Solution

The initial concentration profile for each pore size is found by estimating the concentration at the pore end and then using a fourth order Runge-Kutta method to solve equation B.19 and obtain the pore mouth concentration. If this concentration is not equal to the bulk gas phase concentration, a new pore end concentration is assigned using the secant method and the calculations repeated until the calculated pore mouth concentration equals that in the bulk gas phase of the reactor.

Once the correct initial concentration profile is established for each pore size, the time resolved calculations are begun. The concentration at the reaction interface, C_2, is determined by solving equation B.17. Equation B.21 is then integrated with a fourth order Runge-Kutta procedure to obtain the product-layer radial profile within each pore. The mid-point method is used to integrate this radial profile and obtain percent solid conversion. The interface concentrations are updated and a new concentration profile is determined with the Runge-Kutta and secant schemes. This sequence is repeated at each time step.

If the pore mouth radius becomes zero for a particular pore size, that pore is considered plugged and it is removed from the calculations. The free stream SO_2 concentration is calculated using an overall reactor material balance based on the percent solid conversion and the initial SO_2 concentration.

Appendix C. Tabulation of Experimental Data

C.1 ITR DATA TABLE

Sorbent Type	Injection Temp (°C)	Injection Temp (°F)	Residence Time (sec)	(Ca/S) Molar	% SO_2 Capture	Calcium Utilization
Linwood AH	1150	2100	0.58	1.29	34.8	27.0
Linwood AH	1150	2100	0.37	1.55	36.5	23.6
Linwood AH	1150	2100	0.17	1.30	27.6	21.2
Linwood AH	1200	2190	0.56	1.55	20.5	13.3
Linwood AH	1200	2190	0.36	1.63	22.9	14.1
Linwood AH	1200	2190	0.16	1.63	20.0	12.3
Linwood AH	1250	2280	0.54	1.47	12.4	8.5
Linwood AH	1250	2280	0.16	1.56	11.7	7.5
Linwood AH	1250	2280	0.35	1.82	7.8	4.3
Linwood AH	1300	2370	0.52	1.53	0	0
Linwood AH	1300	2370	0.34	1.33	2.6	2.0

C.2 CTT DATA TABLE

Sorbent Type	Size Range 10-90% by wt. (μm)	Mean Particle Size (μm)	Specific Surface Area (m^2/gm)	Ca (wt %)	Injection Temperature (°F)	Quench Rate (°F/sec)	Residence Time (sec)	Ca/S	SO_2 Capture (%)	SO_2 Capture @ Ca/S = 2 (%)
Linwood $Ca(OH)_2$ (Parent)	0.95 - 16.0	2.2	16.0	51.6	2300	1000	1.54	1.05	25.6	44
Linwood $Ca(OH)_2$	0.95 - 16.0	2.2	16.0	51.6	2300	1000	1.54	1.87	38.1	
Linwood $Ca(OH)_2$	0.95 - 16.0	2.2	16.0	51.6	2300	1000	1.54	2.57	52.0	
Colton $Ca(OH)_2$ (Parent)	0.54 - 24.0	4.0	15.2	51.7	2300	1000	1.54	1.10	19.6	32
Colton $Ca(OH)_2$	0.54 - 24.0	4.0	15.2	51.7	2300	1000	1.54	1.65	27.6	
Colton $Ca(OH)_2$	0.54 - 24.0	4.0	15.2	51.7	2300	1000	1.54	2.39	36.5	
Vicron $CaCO_3$ (Parent)	1.9 - 24.0	9.8	0.72	39.2	2325	1000	1.54	1.70	17.2	21.5
Vicron $CaCO_3$	1.9 - 24.0	9.8	0.72	39.2	2300	1000	1.54	2.16	24.0	
Vicron $CaCO_3$	1.9 - 24.0	9.8	0.72	39.2	2300	400	2.10	2.13	23.3	N/A
Linwood $Ca(OH)_2$	0.95 - 16.0	2.2	16.0	51.6	2300	1000	0.11	2.21	30.0	N/A
Linwood $Ca(OH)_2$	0.95 - 16.0	2.2	16.0	51.6	2300	1000	0.23	2.21	47.5	N/A
Linwood $Ca(OH)_2$	0.95 - 16.0	2.2	16.0	51.6	2300	1000	1.54	2.21	47.0	N/A
Linwood $Ca(OH)_2$	0.95 - 16.0	2.2	16.0	51.6	2300	400	0.20	2.04	34.0	N/A
Linwood $Ca(OH)_2$	0.95 - 16.0	2.2	16.0	51.6	2300	400	0.38	2.04	42.0	N/A
Linwood $Ca(OH)_2$	0.95 - 16.0	2.2	16.0	51.6	2300	400	0.60	2.04	53.0	N/A
Linwood $Ca(OH)_2$	0.95 - 16.0	2.2	16.0	51.6	2300	400	0.91	2.04	62.5	N/A
Linwood $Ca(OH)_2$	0.95 - 16.0	2.2	16.0	51.6	2300	400	2.10	2.04	65.0	N/A
Vicron $CaCO_3$	1.9 - 24.0	9.8	0.72	39.2	2300	1000	0.11	2.16	18.5	N/A
Vicron $CaCO_3$	1.9 - 24.0	9.8	0.72	39.2	2300	1000	0.23	2.16	23.3	N/A
Vicron $CaCO_3$	1.9 - 24.0	9.8	0.72	39.2	2300	1000	1.54	2.16	24.0	N/A
Vicron $CaCO_3$	1.9 - 24.0	9.8	0.72	39.2	2300	400	0.20	1.71	17.4	18.5
Vicron $CaCO_3$	1.9 - 24.0	9.8	0.72	39.2	2300	400	0.20	2.62	20.4	
Vicron $CaCO_3$	1.9 - 24.0	9.8	0.72	39.2	2300	400	0.38	1.74	18.5	20.5
Vicron $CaCO_3$	1.9 - 24.0	9.8	0.72	39.2	2300	400	0.38	2.53	23.3	
Vicron $CaCO_3$	1.9 - 24.0	9.8	0.72	39.2	2300	400	2.10	1.71	22.0	24.0
Vicron $CaCO_3$	1.9 - 24.0	9.8	0.72	39.2	2300	400	2.10	2.53	28.3	

C.2 CTT DATA TABLE (Continued)

Sorbent Type	Size Range 10-90% by wt. (μm)	Mean Particle Size (μm)	Specific Surface Area (m^2/gm)	Ca (wt %)	Injection Temperature (°F)	Quench Rate (°F/sec)	Residence Time (sec)	Ca/S	SO_2 Capture (%)	SO_2 Capture @ Ca/S = 2 (%)
Linwood $Ca(OH)_2$	0.95 - 16.0	2.2	16.0	51.6	2034	1000	1.21	1.78	32.2	34.0
Linwood $Ca(OH)_2$	0.95 - 16.0	2.2	16.0	51.6	2034	1000	1.21	2.47	39.4	
Linwood $Ca(OH)_2$	0.95 - 16.0	2.2	16.0	51.6	2148	1000	1.43	1.88	38.3	41.5
Linwood $Ca(OH)_2$	0.95 - 16.0	2.2	16.0	51.6	2148	1000	1.43	2.45	50.4	
Linwood $Ca(OH)_2$	0.95 - 16.0	2.2	16.0	51.6	2300	1000	1.54	1.66	41.2	47.0
Linwood $Ca(OH)_2$	0.95 - 16.0	2.2	16.0	51.6	2300	1000	1.54	2.31	53.1	
Linwood $Ca(OH)_2$	0.95 - 16.0	2.2	16.0	51.6	2427	1000	1.68	1.55	33.1	40.0
Linwood $Ca(OH)_2$	0.95 - 16.0	2.2	16.0	51.6	2427	1000	1.68	2.58	46.5	
Linwood $Ca(OH)_2$	0.95 - 16.0	2.2	16.0	51.6	2770	1000	1.82	1.71	14.3	25.0
Linwood $Ca(OH)_2$	0.95 - 16.0	2.2	16.0	51.6	2770	1000	1.82	2.48	31.0	
Vicron $CaCO_3$	1.9 - 24.0	9.8	0.72	39.2	2019	1000	1.21	1.75	18.8	21.0
Vicron $CaCO_3$	1.9 - 24.0	9.8	0.72	39.2	2019	1000	1.21	2.49	25.3	
Vicron $CaCO_3$	1.9 - 24.0	9.8	0.72	39.2	2191	1000	1.43	1.50	18.7	23.5
Vicron $CaCO_3$	1.9 - 24.0	9.8	0.72	39.2	2191	1000	1.43	2.44	27.4	
Vicron $CaCO_3$	1.9 - 24.0	9.8	0.72	39.2	2405	1000	1.68	1.73	16.9	20.0
Vicron $CaCO_3$	1.9 - 24.0	9.8	0.72	39.2	2405	1000	1.68	2.38	23.1	
Linwood $Ca(OH)_2$	0.78 - 2.2	1.3	11.51	49.5	2300	400	2.10	1.20	53.6	64.5
Linwood $Ca(OH)_2$	0.78 - 2.2	1.3	11.51	49.5	2300	400	2.10	1.63	58.8	
Linwood $Ca(OH)_2$	0.78 - 2.2	1.3	11.51	49.5	2300	400	2.10	2.06	70.1	
Linwood $Ca(OH)_2$	0.96 - 6.8	2.0	11.33	50.2	2300	400	2.10	1.42	48.6	59.5
Linwood $Ca(OH)_2$	0.96 - 6.8	2.0	11.33	50.2	2300	400	2.10	1.90	55.1	
Linwood $Ca(OH)_2$	0.96 - 6.8	2.0	11.33	50.2	2300	400	2.10	2.15	63.4	
Linwood $Ca(OH)_2$	1.1 - 19.0	9.1	12.79	49.9	2300	400	2.10	1.10	32.4	49.5
Linwood $Ca(OH)_2$	1.1 - 19.0	9.1	12.79	49.9	2300	400	2.10	1.96	48.3	
Linwood $Ca(OH)_2$	1.1 - 19.0	9.1	12.79	49.9	2300	400	2.10	2.58	59.7	
Linwood $Ca(OH)_2$	19.0 - 52.0	30.0	11.87	45.9	2300	400	2.10	1.19	24.1	40.0
Linwood $Ca(OH)_2$	19.0 - 52.0	30.0	11.87	45.9	2300	400	2.10	2.16	43.3	

C.2 CTT DATA TABLE (Continued)

Sorbent Type	Size Range 10-90% by wt. (μm)	Mean Particle Size (μm)	Specific Surface Area (m^2/gm)	Ca (wt %)	Injection Temperature (°F)	Quench Rate (°F/sec)	Residence Time (sec)	Ca/S	SO_2 Capture (%)	SO_2 Capture @ Ca/S = 2 (%)
Colton $Ca(OH)_2$	1.5 - 11.0	5.1	12.71	45.0	2300	400	2.10	1.20	25.5	41.0
Colton $Ca(OH)_2$	1.5 - 11.0	5.1	12.71	45.0	2300	400	2.10	1.54	33.0	
Colton $Ca(OH)_2$	1.5 - 11.0	5.1	12.71	45.0	2300	400	2.10	2.38	47.1	
Colton $Ca(OH)_2$	8.6 - 21.0	14.0	9.80	53.1	2300	400	2.10	1.21	20.8	31.0
Colton $Ca(OH)_2$	8.6 - 21.0	14.0	9.80	53.1	2300	400	2.10	1.80	28.2	
Colton $Ca(OH)_2$	8.6 - 21.0	14.0	9.80	53.1	2300	400	2.10	2.76	39.5	
Colton $Ca(OH)_2$	15.5 - 42.0	26.0	10.87	49.3	2300	400	2.10	1.15	13.4	24.0
Colton $Ca(OH)_2$	15.5 - 42.0	26.0	10.87	49.3	2300	400	2.10	1.69	20.7	
Colton $Ca(OH)_2$	15.5 - 42.0	26.0	10.87	49.3	2300	400	2.10	2.68	32.0	
Linwood $CaCO_3$	1.1 - 4.4	2.2	4.32	41.4	2300	400	2.10	1.19	27.7	50.0
Linwood $CaCO_3$	1.1 - 4.4	2.2	4.32	41.4	2300	400	2.10	1.85	47.9	
Linwood $CaCO_3$	1.1 - 4.4	2.2	4.32	41.4	2300	400	2.10	2.43	61.0	
Linwood $CaCO_3$	1.8 - 7.2	4.4	2.42	43.4	2300	400	2.10	2.54	41.8	38.5
Linwood $CaCO_3$	1.8 - 7.2	4.4	2.42	43.4	2300	400	2.10	1.49	27.4	
Linwood $CaCO_3$	1.8 - 7.2	4.4	2.42	43.4	2300	400	2.10	2.77	46.8	
Linwood $CaCO_3$	1.8 - 7.2	4.4	2.42	43.4	2300	400	2.10	2.16	40.8	
Linwood $CaCO_3$	1.8 - 7.2	4.4	2.42	43.4	2300	400	2.10	1.17	24.2	
Linwood $CaCO_3$	1.8 - 7.2	4.4	2.42	43.4	2300	400	2.10	2.06	40.7	
Linwood $CaCO_3$	1.8 - 7.2	4.4	2.42	43.4	2300	400	2.10	2.81	52.5	
Linwood $CaCO_3$	4.6 - 14.0	8.6	1.28	39.0	2300	400	2.10	2.89	39.0	31.0
Linwood $CaCO_3$	4.6 - 14.0	8.6	1.28	39.0	2300	400	2.10	1.27	21.1	
Linwood $CaCO_3$	4.6 - 14.0	8.6	1.28	39.0	2300	400	2.10	2.02	31.2	
Vicron $CaCO_3$	1.3 - 6.4	3.1	1.67	39.1	2300	400	2.10	1.80	23.2	25.5
Vicron $CaCO_3$	1.3 - 6.4	3.1	1.67	39.1	2300	400	2.10	2.35	30.8	
Vicron $CaCO_3$	1.3 - 6.4	3.1	1.67	39.1	2300	400	2.10	1.32	16.3	
Vicron $CaCO_3$	1.9 - 7.0	4.2	1.36	40.3	2300	400	2.10	2.01	24.3	24.0
Vicron $CaCO_3$	1.9 - 7.0	4.2	1.36	40.3	2300	400	2.10	1.51	18.3	
Vicron $CaCO_3$	4.8 - 14.0	8.8	0.76	39.5	2300	400	2.10	1.31	15.2	24.0
Vicron $CaCO_3$	4.8 - 14.0	8.8	0.76	39.5	2300	400	2.10	2.03	24.1	
Vicron $CaCO_3$	4.8 - 14.0	8.8	0.76	39.5	2300	400	2.10	2.34	29.2	
Vicron $CaCO_3$	11.0 - 29.0	18.0	0.32	40.4	2300	400	2.10	2.44	19.7	18.0
Vicron $CaCO_3$	11.0 - 29.0	18.0	0.32	40.4	2300	400	2.10	1.74	15.6	
Vicron $CaCO_3$	11.0 - 29.0	18.0	0.32	40.4	2300	400	2.10	0.96	9.3	

C.3 BSF DATA TABLES

TABLE C-3. MIXING: SO_2 TRACER DATA

Injector	Injection Temp (°F)	Residence Time (sec)	Radial Distance from ℄ (inches)	SO_2, ppm (dry, 0%O_2)
Radial	2250	0.40	+ 10	2316
Radial	2250	0.40	+ 8	2335
Radial	2250	0.40	+ 6	2296
Radial	2250	0.40	+ 4	2246
Radial	2250	0.40	+ 2	2234
Radial	2250	0.40	0	2239
Radial	2250	0.40	- 2	2290
Radial	2250	0.40	- 4	2242
Radial	2250	0.40	- 6	2241
Radial	2250	0.40	- 8	2238
Radial	2250	0.40	- 10	2179
Radial	2250	0.60	+ 10	1883
Radial	2250	0.60	+ 8	1970
Radial	2250	0.60	+ 6	1980
Radial	2250	0.60	+ 4	2037
Radial	2250	0.60	+ 2	2113
Radial	2250	0.60	0	2197
Radial	2250	0.60	- 2	2285
Radial	2250	0.60	- 4	2306
Radial	2250	0.60	- 6	2366
Radial	2250	0.60	- 8	2367
Radial	2250	0.60	- 10	2419
Radial	2250	0.90	+ 10	2159
Radial	2250	0.90	+ 8	2139
Radial	2250	0.90	+ 6	2122
Radial	2250	0.90	+ 4	2104
Radial	2250	0.90	+ 2	2059

TABLE C-3. MIXING: SO_2 TRACER DATA (Continued)

Injector	Injection Temp (°F)	Residence Time (sec)	Radial Distance from ℄ (inches)	SO_2, ppm (dry, 0% O_2)
Radial	2250	0.90	0	2005
Radial	2250	0.90	- 2	2021
Radial	2250	0.90	- 4	2012
Radial	2250	0.90	- 6	1995
Radial	2250	0.90	- 8	1966
Radial	2250	0.90	- 10	1940
Axial	2250	0.60	+ 8	138
Axial	2250	0.60	+ 6	252
Axial	2250	0.60	+ 4	836
Axial	2250	0.60	+ 2	3143
Axial	2250	0.60	0	5642
Axial	2250	0.60	- 2	6952
Axial	2250	0.60	- 4	2867
Axial	2250	0.60	- 6	601
Axial	2250	0.60	- 8	191

TABLE C-4. SO_2 CAPTURE DATA

Sorbent	Injection Temp (°F)	Quench Rate (°F/sec)	Residence Time (sec)	(Ca/S) Molar	% SO_2 Capture	% SO_2 Capture @Ca/S=2
Linwood AH						
- Axial Injector	2250	200	Exhaust	1.09	18.0	43.5
- Axial Injector	2250	200	Exhaust	2.20	48.7	
- Axial Injector	2250	200	Exhaust	1.44	32.9	
Linwood AH						
- Radial Injector	2260	200	Exhaust	1.36	35.9	53.5
- Radial Injector	2260	200	Exhaust	2.04	53.2	
- Radial Injector	2260	200	Exhaust	1.95	53.6	
- Radial Injector	1870	200	Exhaust	1.22	17.9	30.0
- Radial Injector	1870	200	Exhaust	2.28	33.9	
- Radial Injector	2040	200	Exhaust	1.31	28.9	45.0
- Radial Injector	2040	200	Exhaust	2.07	46.8	
- Radial Injector	2175	200	Exhaust	1.36	34.0	50.0
- Radial Injector	2175	200	Exhaust	2.23	55.7	
- Radial Injector	2345	200	Exhaust	1.41	27.0	40.0
- Radial Injector	2345	200	Exhaust	2.12	42.9	
- Radial Injector	2330	200	Exhaust	0.97	23.0	47.0
- Radial Injector	2330	200	Exhaust	2.00	47.0	
Vicron	2260	200	Exhaust	1.36	13.3	21.0
Vicron	2260	200	Exhaust	2.13	22.5	

C-4. SO_2 CAPTURE DATA (Continued)

Sorbent	Injection Temp (^oF)	Quench Rate (^oF/sec)	Residence Time (sec)	(Ca/S) Molar	% SO_2 Capture	% SO_2 Capture @Ca/S=2
Vicron	2310	200	Exhaust	1.37	13.0	20.0
Vicron	2310	200	Exhaust	2.15	21.9	
Vicron	2170	200	Exhaust	1.34	16.3	25.0
Vicron	2170	200	Exhaust	2.13	27.0	
Vicron	1960	200	Exhaust	1.34	16.2	24.5
Vicron	1960	200	Exhaust	2.13	26.3	
Linwood AH	2260	200	0.40	1.94	22.3	22.5
Linwood AH	2260	200	0.40	2.04	22.5	
Linwood AH	2260	200	1.00	2.04	31.2	30.5
Linwood AH	2260	200	1.65	1.36	25.7	39.0
Linwood AH	2260	200	1.65	2.04	39.9	
Linwood AH	2040	200	0.43	1.31	10.0	16.0
Linwood AH	2040	200	0.43	2.07	16.6	
Linwood AH	2040	200	1.08	1.31	13.0	21.5
Linwood AH	2040	200	1.08	2.07	22.4	
Linwood AH	2040	200	1.75	1.31	18.4	29.0
Linwood AH	2040	200	1.75	2.07	29.9	

Appendix D. Quality Assurance

The collection and anlysis of quality data has been the primary objective of this program. In order to ensure that the reported data is accurate, many quality assurance measures have been taken in all phases of the program. Most of the procedures and measurements used for data acquisition have been standardized by EPA or ASTM and those which have not are described in detail in this appendix.

Three facilities at EER were involved in procuring the data presented in this report; the ITR, CTT, and BSF. All of the quality assurance information presented in this appendix applies to these three facilities.

Appendix D. Quality Assurance

The collection and anlysis of quality data has been the primary objective of this program. In order to ensure that the reported data is accurate, many quality assurance measures have been taken in all phases of the program. Most of the procedures and measurements used for data acquisition have been standardized by EPA or ASTM and those which have not are described in detail in this appendix.

Three facilities at EER were involved in procuring the data presented in this report; the ITR, CTT, and BSF. All of the quality assurance information presented in this appendix applies to these three facilities.

D.1 GAS SPECIES MEASUREMENTS

Exhaust gas-phase species composition was measured using the BSF, ITR and CTT laboratory sampling systems. These systems were constructed in strict conformance with EPA performance specifications and their use helped ensure data quality. The species that were measured included: NO, NO_2, SO_2, CO, O_2, and CO_2, all of which were measured by continuous gas analyzers.

Table D-1 lists the specific instruments and full-scale ranges. The instrument ranges have been selected to exceed the maximum expected concentrations by a small margin.

Figure D-1 shows a schematic diagram of the continuous monitoring system for NO, NO_x, CO, CO_2, and O_2. The system was nearly identical for all three facilities. All components in contact with the sample were stainless steel or Teflon to ensure sample integrity and corrosion resistance. The gas sample was provided to the instruments by a sample conditioning system consisting of a pump, moisture condenser and particulate filters.

Gas phase measurements were made routinely at Port 10B in the BSF and at the exhaust in the CTT and ITR. Phase discrimination probes (see Figure D-2) were used in all cases. The probes supplied two gas streams simultaneously. The main, particle-laden stream, which was used for continuous monitoring of O_2, CO, CO_2, NO_x, and the side, nearly particle-free stream, which was used for SO_2 measurement.

Figure D-3 shows a diagram of the continuous monitoring system for exhaust SO_2 measurements. The SO_2 gas sample in the nearly particulate-free stream was transported in a heated Teflon line maintained above 115°C under vacuum to a heated filter followed by a permeation tube drier. The permeation tube drier selectively removed water vapor from the gas sample. Dry air was used as the dry gas medium in the permeation drier. The sample was then pressurized and delivered to the analyzer. SO_2 concentration was measured using a non-dispersive ultraviolet instrument manufactured by DuPont.

TABLE D-1. BSF AND CTT INSTRUMENTATION

Gas Measured	Type of Instrument	Manufacturer	Model No.	Range	Reference
NO, NO_x	Chemiluminescent	Thermo Electron Corp. (TECO)	10 AR	1000 ppm	Teco Model 10 Operating Manual
CO	Nondispersive Infrared (NDIR)	Anarad, Inc.	(ITR & BSF) AR 500R (CTT) AR600R	500 ppm 10 percent	Anarad AR 500 Operating Manual Anarad AR 600 Operating Manual
CO_2	Nondispersive Infrared (NDIR)	Anarad, Inc. Infrared	(BSF) AR600R (CTT) AR600R (ITR) 703D	20 percent 40 percent 15 percent	Anarad AR 600 Operating Manual Anarad AR 600 Operating Manual Infrared 703D Operating Manual
O_2	Paramagnetic	Beckman Taylor Servomex	(BSF) 755 (CTT) OA250 (ITR) QA137	10 percent 100 percent 100 percent	Beckman 755 Operating Manual Taylor OA250 Operating Manual Taylor QA137 Operating Manual
SO_2	UV Absorption	Dupont	400	5000 ppm	DuPont 400 Operating Manual

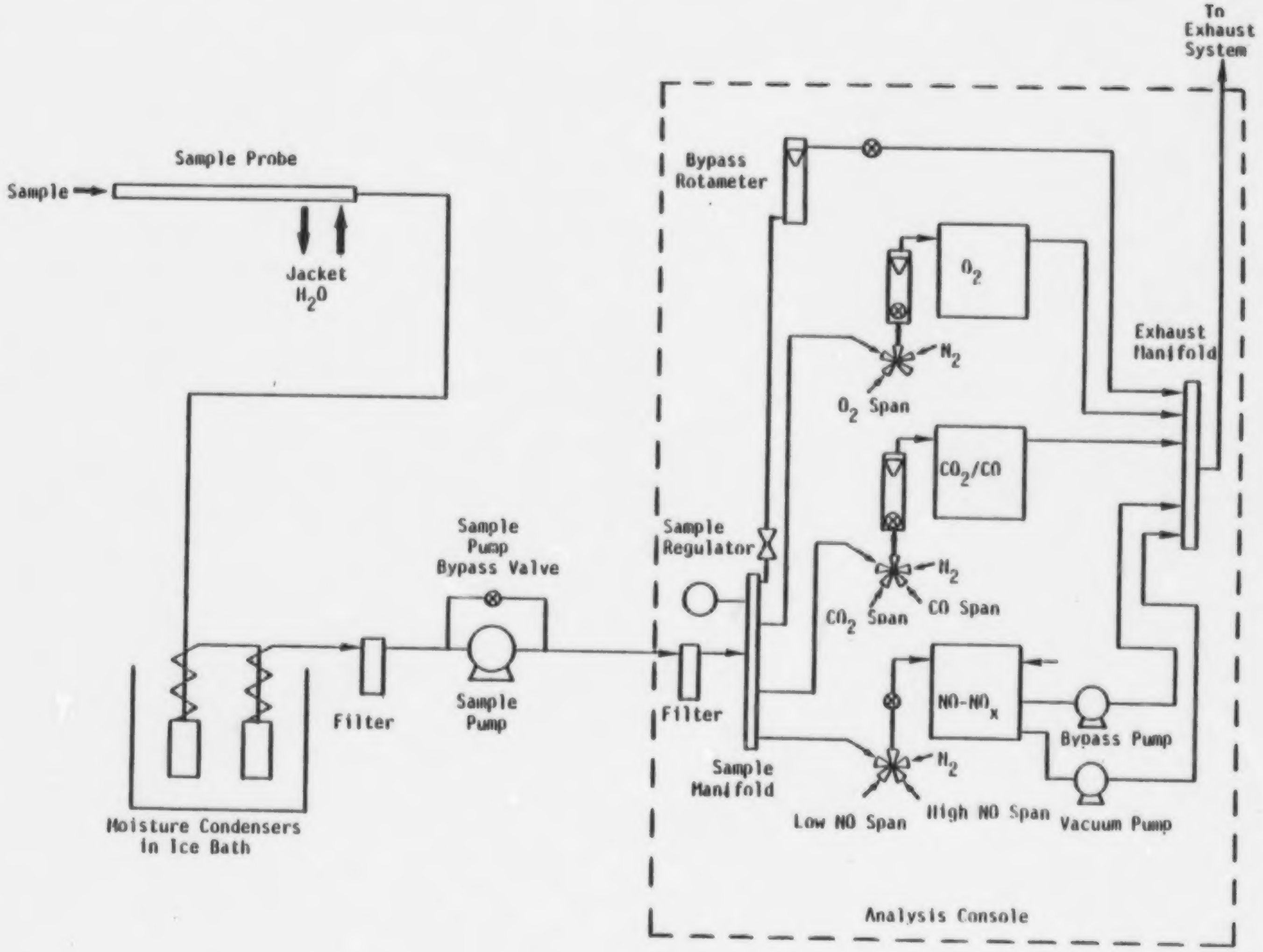
To Exhaust System
Sample
Sample Probe
Jacket H_2O
Bypass Rotameter
O_2
N_2
O_2 Span
Exhaust Manifold
CO_2/CO
Sample Pump Bypass Valve
Sample Regulator
N_2
CO_2 Span
CO Span
$NO-NO_x$
Filter
Sample Pump
Filter
Sample Manifold
N_2
Bypass Pump
Vacuum Pump
Low NO Span
High NO Span
Moisture Condensers in Ice Bath
Analysis Console

Figure D-1. Continuous monitoring sampling system.

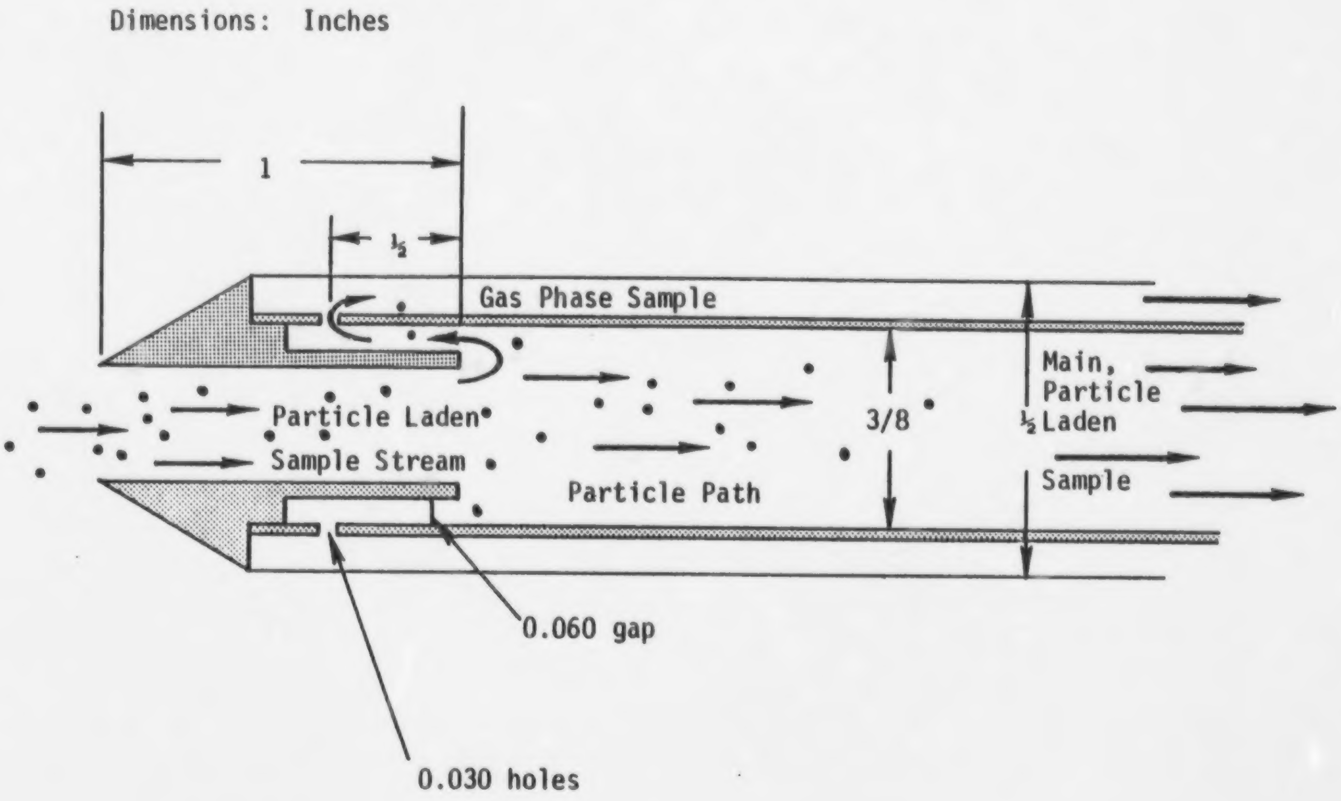
Dimensions: Inches
1
½
Gas Phase Sample
Particle Laden
Sample Stream
Particle Path
3/8
Main,
Particle
Laden
½
Sample
0.060 gap
0.030 holes

Figure D-2. Phase discrimination probe.

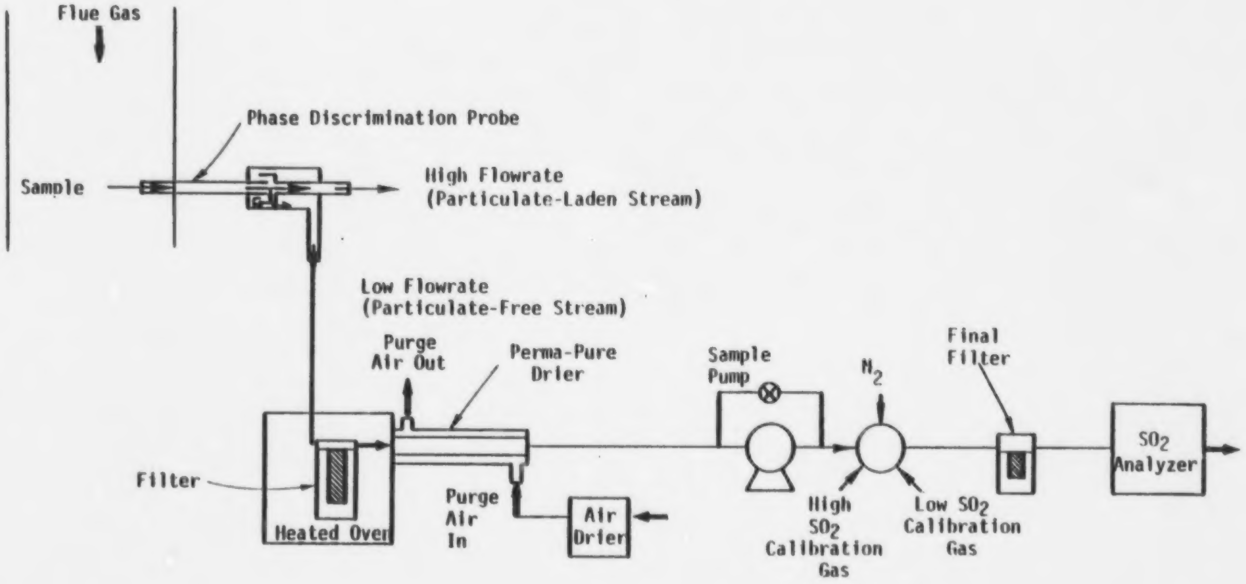
Flue Gas
Phase Discrimination Probe
Sample
High Flowrate
(Particulate-Laden Stream)
Low Flowrate
(Particulate-Free Stream)
Purge
Air Out
Perma-Pure
Drier
Sample
Pump
N_2
Final
Filter
SO_2
Analyzer
Filter
Heated Oven
Purge
Air
In
Air
Drier
High
SO_2
Calibration
Gas
Low SO_2
Calibration
Gas

Figure D-3. SO_2 continuous monitoring system.

Table D-2 gives the precision, accuracy, and completeness data instruments used on the BSF, CTT and ITR. In every case, the program goals for precision and accuracy were met.

TABLE D-2. PRECISION, ACCURACY AND COMPLETENESS DATA FOR GAS SPECIES INSTRUMENTS

Gas Measured	Precision (%)			Accuracy (%)			Completeness (%)		
	Goal	Actual BSF	Actual CTT,ITR	Goal	Actual BSF	Actual CTT,ITR	Goal	Actual BSF	Actual CTT,ITR
NO_x (Chemiluminescent)	2	1.4	0.3	20	14.2	12.3	90	100	100
CO (NDIR)	2	0.4	0.5	20	No Std.	No Std.	90	100	100
CO_2 (NDIR)	2	0.8	0.1	20	6.7	2.5	90	100	100
O_2 (Paramagnetic)	2	0.5	0.2	20	11.2	13.1	90	100	100
SO_2 (UV Absorption)	2	0.2	0.3	20	8.1	10.2	90	100	100

D.2 SOLID SAMPLES

D.2.1 Grab Samples

Grab samples are used to obtain materials for specific surface area and particle size analysis. Suitably sized samples are removed at random from bulk containers of the material to be tested. Since the total quantity of each of the bulk materials involved in this study is quite small (a few kg at most) minimal effort, beyond stirring, needs to be taken in order to ensure the representativeness of the sample.

D.2.2 Solids Analysis

The composition of solid samples was generally determined by EER's Analytical lab though some samples were sent to an independent laboratory. Carbon, Hydrogen and Nitrogen were analyzed on a Perkin-Elmer 240B. Calcium analysis was done with a Chelometric titration method which is covered under ASTM D 2795. Surface area was determined on a Quantachrome Quantasorb unit. The measurements followed the BET model of nitrogen absorption isotherms at 77K. Table D-3 gives the precision and accuracy data for these instruments.

TABLE D-3. SOLID ANALYSES PRECISION AND ACCURACY DATA

MEASUREMENT		PRECISION (%) ACTUAL	PRECISION (%) GOAL	ACCURACY (%) ACTUAL	ACCURACY (%) GOAL
Carbon	Perkin-Elmer 240B	.24	2	0.8	2
Hydrogen		1.38	5	0.6	5
Nitrogen		2.13	10	1.9	10
Ash		0.33	10	1.42	10
Moisture		2.55	10	8.71	10
Calcium - ASTM D2795		1.0	10	0.2	10
BET Surface Area		3.5	10	8.6	20

D.3 TEMPERATURE MEASUREMENTS

High-temperature gas measurements within furnaces are subject to large inaccuracies due to the effects of thermal couple radiation loss. Therefore, in-furnace gas temperatures were measured using a suction pyrometer system as shown in Figure D-4. The suction pyrometer consisted of a high-temperature thermocouple (B type) in a porous ceramic radiation shield. The pyrometer was placed in the gas stream with the opening in the alumina sheath pointing downstream. A high flow rate of furnace gas was withdrawn through the sheath and over the thermocouple to increase convective heat transfer to the thermocouple and reduce radiation loss. As the gas flow rate was increased, the gas temperature increased to a constant value, indicating no additional reduction in radiation loss. Figure D-5 shows the results of the motive side pressure (a measure of suction flow rate) calibration for the CTT. A suction pressure of 40 psig was adopted for all the temperature measurements for the CTT system. The BSF system used a pressure of 30 psig for all temperature measurements (see Figure D-6).

ITR temperature measurements were made using Type-S (Pt/Pt-10% Rh) bare-wire thermocouples. These thermocouples were not calibrated but were manufactured from thermocouple-quality matched wires. Because bare-wire thermocouples can deteriorate rapidly under severe or corrosive conditions, several were kept on hand and were cross-compared regularly. Table D-4 provides data which represent the uniformity and repeatability of the reactor temperature measurements.

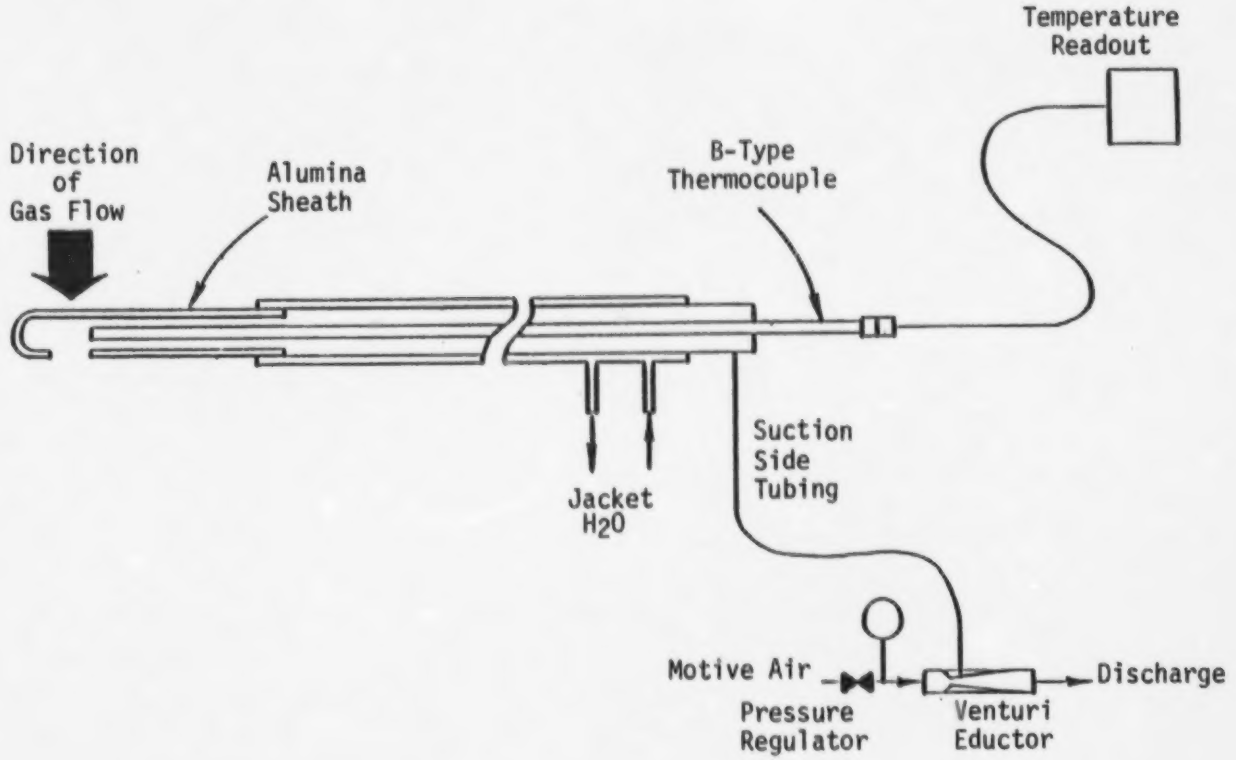
Temperature Readout
Direction of Gas Flow
Alumina Sheath
B-Type Thermocouple
Suction Side Tubing
Jacket H_2O
Motive Air
Pressure Regulator
Venturi Eductor
Discharge

Figure D-4. Gas temperature measurement system.

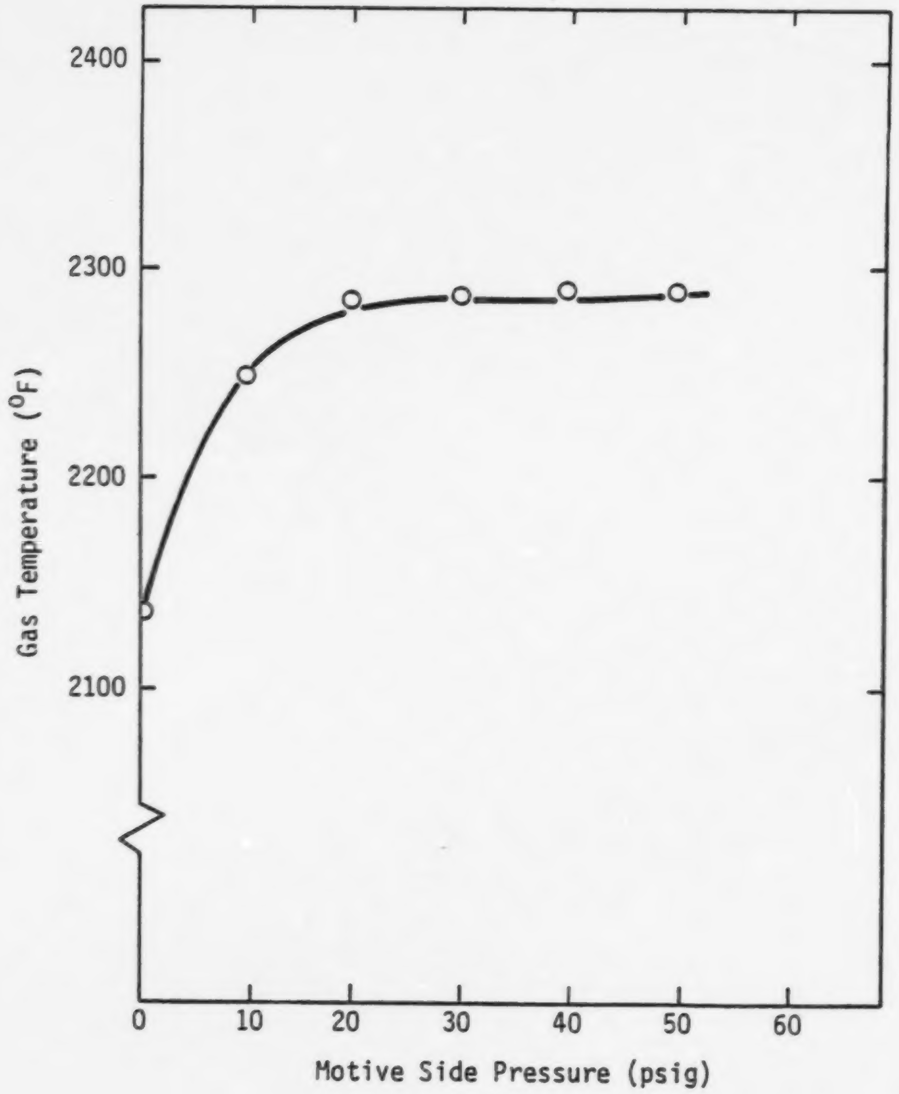

Figure D-5. Suction pyrometer aspirator pressure calibration for CTT.

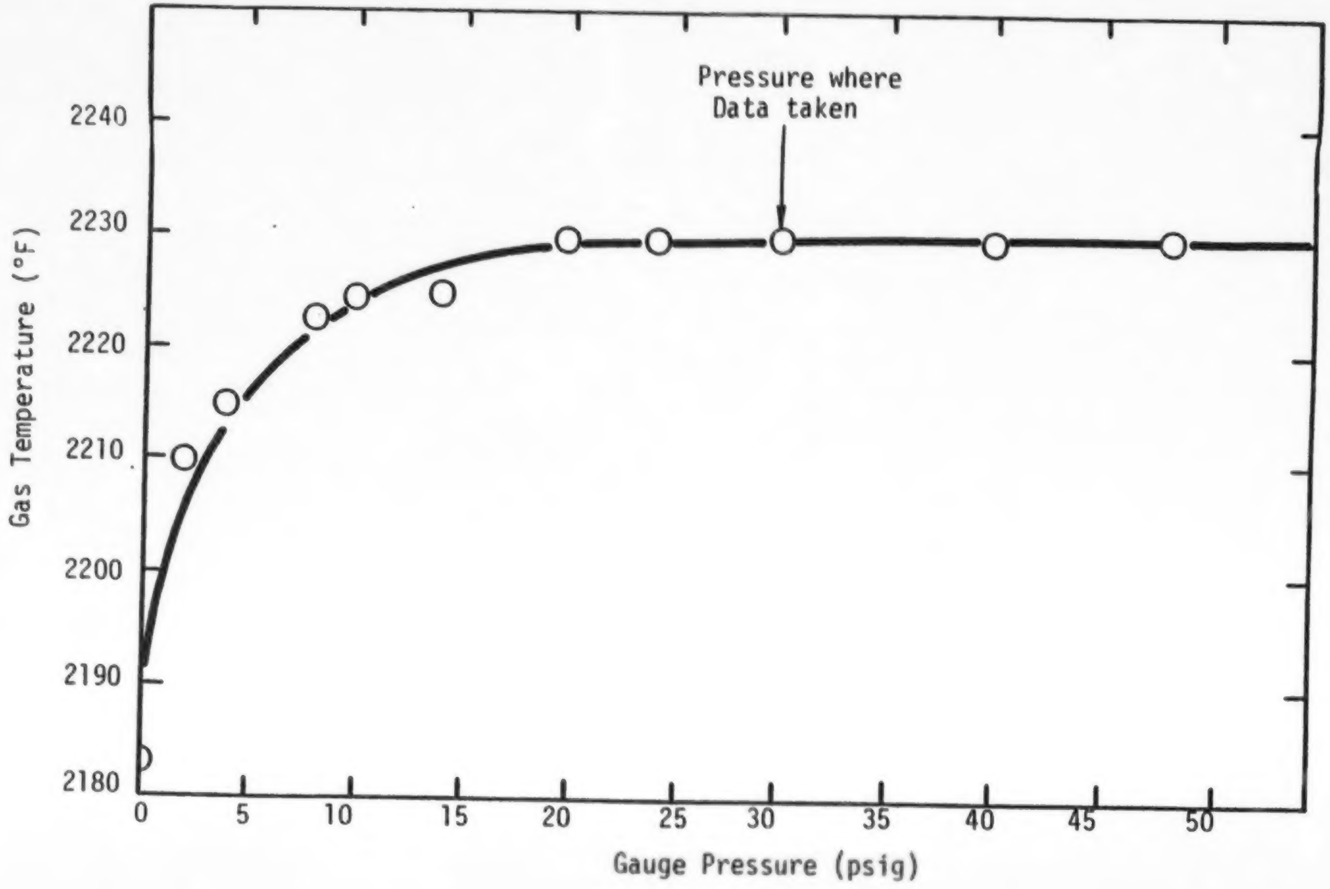

Figure D-6. Suction pyrometer aspirator pressure calibration for BSF.

TABLE D-4. TYPICAL DATA FOR TEMPERATURE VARIATIONS WITHIN THE ISOTHERMAL REACTOR - NOMINAL 1000°C CONDITION

Temperature Measured(°C)	Pct. Dev.
998	- .20
1010	1.00
1014	1.40
1014	1.30
1010	1.00
1008	.800
1006	.600
998	- 200
1010	1.00
1009	.900
1010	1.00
1010	1.00
1009	.90
1005	.50
1000	.00
993	.700
$\bar{X}$=1006	$\bar{X}$= .64
SD=6.03	± .60

D.4 CALIBRATION PROCEDURES

Calibration procedures and frequency for each measurement system are listed in Table D-5. As shown in the table, standard calibration procedures were used for each system. Each system was calibrated at the frequency shown in the table to ensure the accuracy of the measurements were traceable to the calibration standards.

Each of the continuous monitoring instruments was calibrated with three gases: a zero gas and two span gases. Table D-6 lists the span gases used to calibrate instruments for the CTT sample system.

TABLE D-5. CALIBRATION PROCEDURES

MEASUREMENT PARAMETER	CALIBRATION PROCEDURE	CALIBRATION FREQUENCY	CALIBRATION STANDARD	REFERENCE
Fuel Composition:				
Carbon	Standard Samples	Daily	Known quantity of 100% acetanilide	Perkin Elmer 240 B Operating Manual
Hydrogen				
Nitrogen				
Ash				
Moisture				
Sulfur	Standard Sample	Daily	Certified sulfur standards	Leco SC 32 Operating Manual
Exhaust Gas Composition				
NO, NO_2	Compare to standard compressed gas	Daily	EPA Protocol 1 Gases or custom gas blends. See Section 10.0	EPA EMSL Protocol No. 1, June 1, 1978
O_2				
CO				
CO_2				
SO_2				
Hydrocarbons				
Sorbent Surface Area		Daily	Known quantity of N_2	Quantasorb Surface Area Analyzer Operating Manual
Sorbent Flowrate	Weigh feed over measured time with independent balance		Standard weights	

TABLE D-6. CALIBRATION GASES

Gas	Concentration	Percent of Full-Scale	Balance Gas	Grade
NO	836 ppm	84	Nitrogen	Certified Standard
NO	166 ppm	16	Nitrogen	Certified Standard
SO_2	2915 ppm	73	Nitrogen	Certified Standard
SO_2	437 ppm	11	Nitrogen	Certified Standard
CO	1227 ppm	82	Nitrogen	Certified Standard
CO_2	12.3%	31	Nitrogen	Certified Standard
CO_2	5%	13	Nitrogen	Certified Standard
O_2	10%	10	Nitrogen	Certified Standard
O_2	4%	4	Nitrogen	Certified Standard
CO	10%	100	Nitrogen	Certified Standard
CO	2%	20	Nitrogen	Certified Standard

D.5 DATA REDUCTION

Equations used to calculate results for each of the measurements are discussed below. Many of the results are obtained directly from the measurements and thus do not require calculations.

D.5.1 SO_2 Capture

The gas compositions are measured as chart divisions on a strip chart recorder. The measured divisions are converted to concentration (ppm or percent) based on calibrations with certified gases.

SO_2 capture with sorbent injection is defined as:

$$\text{Percent Capture} = \frac{(SO_2)_1 - (SO_2)_2}{(SO_2)_1} \times 100\%$$

where: $(SO_2)_1$ = SO_2 concentration without sorbent, ppm

$(SO_2)_2$ = SO_2 concentration with sorbent injection, ppm

D.5.2 Percent Calcination

Percent calcination is the percentage of the calcium in a sample of initially $CaCO_3$ or $Ca(OH)_2$ which has been converted to CaO due to heating. Percent calcination is calculated directly from results of the 240B (wt% C) and the calcium titration (wt% Ca).

$$\text{Percent Calcination} = 1\left(- \frac{10}{3} \times \frac{\text{wt\% C}}{\text{wt\% Ca}}\right) \times 100\%$$

An alternate check on the percent calcination is obtained by a mass balance involving the results from the 240B (wt% C, wt% H, wt% ash) and the SC32 (wt% S). Tests have shown that during 240B analysis, $CaSO_4$ is retained in the ash, while $Ca(OH)_2$ and $CaCO_3$ are completely devolatilized. Percent calcination is calculated as follows:

$$\text{Percent Calcination} = \left(1 - \frac{14}{3}\left(\frac{\text{wt\% C}}{\text{wt\% Ash} - 2.5 \times \text{wt\% S}}\right)\right) \times 100\%$$

D.5.3 Particle Size Distribution

Particle size distribution, obtained via X-ray sedimentation with a Micromeritics Sedigraph Analyzer, was provided directly as a plot of cumulative mass-percent finer versus equivalent spherical diameter. An example particle size distribution plot is shown in Figure D-7. Scanning electron microscopy was used to provide support to the Sedigraph analysis.

The basis for X-ray sedimentation is a model of each particle as a sphere falling through a fluid at its terminal velocity. The equivalent spherical diameter of a particle is defined as the diameter of a sphere with the same apparent density which would fall at the same rate in the fluid. Numerous tests have been performed by the manufacturer using, e.g., NBS standard glass spheres of various sizes. All of these affirm the accuracy of the technique under near perfect conditions. Real materials such as those studied here provide a challenge to particle size measurement techniques. Interferences such as agglomeration of particles, interpretation of non uniform shapes as spheres, and uncertainties in the apparent porosity must be taken into account. The reader is cautioned to consider these factors when referring to the particle size data shown in this report.

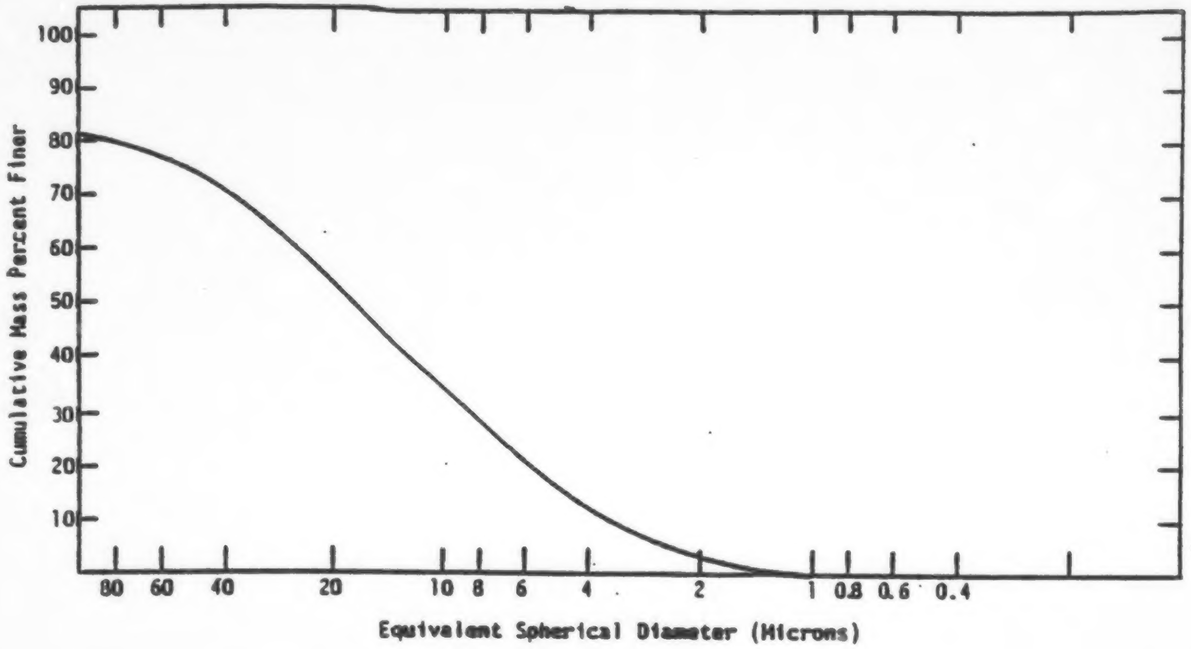

Figure D-7. Example of sorbent particle size distribution.

D.5.4 Specific Surface Area

Specific surface area is measured by a Quantasorb Analyzer by the BET method. This analyzer measures the quantity of nitrogen adsorbed on a sample surface as a function of the relative (to saturation) partial pressure of nitrogen. Two equations are used to determine the specific surface area:

$$\frac{1}{X(Po/P-1)} = \frac{C-1}{X_mC}\,\frac{P}{P_o} + \frac{1}{X_mC}$$

where:

X = weight of N_2 adsorbed at P/Po

P = partial pressure of N_2

P_o = saturation pressure of N_2

X_m = weight of N_2 adsorbed for monolayer coverage

C = a constant which is a function of the heat adsorption and the heat of condensation of N_2

By measuring X for two or more values of P/Po the slope, $(C-1)/x_mc$, and intercept, $1/x_mc$, are obtained. After solving for X_m the specific surface area, S, is obtained from:

$$S = \frac{X_mNA}{M_aM_s}$$

where:

N = Avograro's number

A = cross-sectional area of an adsorbed N_2 molecule

M_a = mass of N_2 molecule

M_s = mass of sample

D.5.5 Combustion Air Flowrate/Distribution

Combustion air flowrate is read directly from rotameters or is calculated from pressure drop measured across laminar flow elements based on the equation:

$$Q = K \left(\frac{\Delta P}{T}\right)^{1/2}$$

D.5.6 Combustion Air, Furnace Gas, and Exhaust Gas Temperatures

Temperatures are measured by thermocouples and provide results in units of degrees centigrade which can then be converted to other temperature scales, as required.

D.5.7 Residence Time

Residence times are calculated by assuming a one-dimensional flow in the furnace. Based on the measured temperatures, the bulk mean residence time (t) was calculated by using the following equation:

$$t = \frac{V}{\dot{V}} \left(\frac{T_o}{T_m}\right)$$

where:

V = volume of furnace zone, ft^3

$\dot{V}$ = volumetric flow rate of gas, SCF S

T_o = 530^oR

T_m = bulk mean gas temperature

= $1/2\ (T_1 + T_2)$

T_1 and T_2 are center line temperatures measured at the entrance and exit of the furnace zone, respectively.

Appendix E. Southern Research Institute Subcontractor Report

MELLON INSTITUTE

MATERIALS CHARACTERIZATION CENTER

Report on

TEM EXAMINATION OF VARIOUS LIME POWDERS

Submitted to

Dr. Robert Dahlin
Southern Research Institute
2000 Ninth Ave. South
Birmingham, AL 35255-5365

SUMMARY

Five samples were embedded and thinned. TEM images of the Longview crush #263-E powders indicated the presence of fine structure that resembled elongated voids.

The two calcined hydrate samples, #113436 and #13298, appeared polycrystalline with grains appoximately 500Å across. The particles had dark center regions (relative to the surrounding surfaces) suggesting probable composition differences. No voids were observed, and no significant differences were noted between the sulfated and the unsulfated specimens. Because of time constraints and instrument malfunctions, the two carbonate specimens could not be examined.

JOB NO 8609002

October 7, 1986

Prepared by: Steven H Axdal
Steven Axdal, Ph.D.

INTRODUCTION

Various powdered samples were submitted to Mellon Institute for examination. These included powders identified as #113436, #113298, #113299, and #113300. It was stated that Samples #113436 and #113298 were calcined and hydrated lime powders; sample #113436 was also sulfated. Samples #113299 and #113300 are carbonates with Sample #113300 also being sulfated.

The samples were examined by SEM up to approximately 100,000X magnification. All micrographs typical of the sample surfaces were submitted to SRI in July of 1986. Briefly, the micrographs indicated porosity on the surfaces of the various powder samples, but no quantitative correlation was established between these results and results from other methods, such as BET measurements.

It has been suggested that examining these powder particles in cross section might reveal more details about the absorption properties of these materials. Specifically, the suspected submicron pores in the particles would be revealed by using transmission electron microscopy (TEM). It was requested that specimens of these four powder samples be cross sectioned and examined using transmission electron microscopy.

An additional sample, Longview raw unsized crush #263-E, was also examined as a practice sample to develop and evaluate the cross sectioning method.

EXPERIMENTAL PROCEDURES AND RESULTS

TEM Foils

For each sample, a few milligrams of powder were mixed with a two part epoxy composition, Araldite GY502 resin and HY502 hardener manufactured by Ciba-Giegy. The powder was added to the epoxy composition in the ratio of approximately one to one by volume. The mixture was cast as a thin sheet on a glass microscope slide coated with Beuhler silicone mold release agent. It was cured overnight at approximately 80°C in a vacuum oven at 20 torr pressure.

Portions of the hardened sample film were ground down to a thickness of approximately five mils using 60 μm abrasive. Then 3 mm diameter TEM disks were punched out. The disks were thinned by bombarding their surfaces with an argon ion beam until the disks perforated in approximately the center.

The specimens were thinned using a Gatan model 600 dual beam argon ion milling instrument operating with an ion beam voltage of 4 KV, and a thinning ion current of approximately 1 milliamperes. During milling, the specimens were tilted 17 degrees, and maintained at approximately -100°C (not measured) by cooling with liquid nitrogen.

TEM

The specimens were examined in a JEOL 100C transmission electron microscope using a 120 kv incident electron beam.

#Longview #263-E

Figure #1 shows the appearance of the edge of the foil in bright field mode. The epoxy matrix material is the uniform grey region observable in the upper right corner of the micrograph. Most of the edge present is a particle. Some fine structure is evident near the middle of the particle edge, and some contour fringes are also evident. Various other areas along the thinned edge of the specimen foil showed regions where particles probably fell out.

The particle stands out more clearly in the dark field imaging mode as shown in Figure #2. The particle appears to be approximately rectangular, with dimensions of about 15 X 35 μm.

Figure #3 shows the diffraction pattern which was observed for the particle. The arrow indicates the diffracted beam used for the dark field image.

A higher magnification micrograph of the particle in Figure #1 is given in Figure #4. The fine structure in the micrograph has a wormlike appearance with apparent dimensions of about 40 X 400Å. The presence of the fine structure seems to depend somewhat on the specific particle. Not all edges seemed to have the same fine structure density. While some changes in the appearance of the sample occurred with the electron beam incident on the specimen, the fine structure did not seem to be related to the beam intensity or the exposure time.

Samples #113436 and #113298

Unlike the previous sample, Longview raw unsized crush #263-E, there was not a noticeable amount of particle dropout during the milling process in these samples. Both powder samples appeared fairly regularly shaped, having a circular or elliptical cross section in the TEM, with the appearance a dark 0.5 μm diameter particle surrounded by a thinner region. This appearance might indicate that the center of the particle is unhydrated and the peripheries are hydrated. Typically, the centers of the particles appeared polycrystalline. However, diffraction patterns were difficult to obtain because of the opacity of the central region. The halo around the center appeared to have nearly the same density as the epoxy matrix. Close examination of the halo material showed a difference in contrast compared to the epoxy. Diffraction patterns from the halo region typically showed diffraction patterns consisting of rings of spots.

Figures #5 and #6 show bright and dark field images of a typical particle in Sample #113436. The dark field images indicate that the individual crystallites in the halo region are on the order of 500Å in diameter. Figures #7 and #8 show the bright and dark field images of another, similar area. (The diffraction pattern for this area is given in Negative #68964 sent to SRI on September 16, 1986.)

Very similar features were observed for Sample #113298 as obtained for Sample #113436; Figures #9 and #10 show typical particle areas. It was observed that after the specimen was exposed to the electron beam for a short period of time, the halo region appeared to become modified, taking on a more pronounced granular appearance. This is noticeable in Figure #10 for sample #113298, but it was also observed when Sample #113436 was examined.

For both samples relatively rapid contrast changes were observed while the specimen was exposed to the beam. Changes to the granular structure were not readily apparent. The granularity simply appeared to sharpen with observation, which was clearly different from the wormlike structures observed in the 263-E powders.

SUMMARY

Five powder samples were embedded and successfully thinned, #113436, #113298, #113299, #113300, and #Longview crushed #263-E. In the TEM, the two calcined and hydrated samples, #113436 and #113298, appeared polycrystalline with very fine grains approximately 500Å in diameter. The center regions of the particles appeared dark surrounded by light thinner region. It is possible that the centers of the particles are unhydrated while the thinner surrounding material is hydrated. Also no voids in the particles and no significant differences between the sulfated and unsulfated particles were observed.

For the Longview crushed #263-E sample, particles contained elongated shaped structures resembling voids. The particle size was larger and less polycrystalline.

The remaining two carbonate samples, #113300 and #113299, have not yet been examined because of time constraints and instrument malfunctions.

TEM of Longview Crush #263-E

Figure #1

20000X

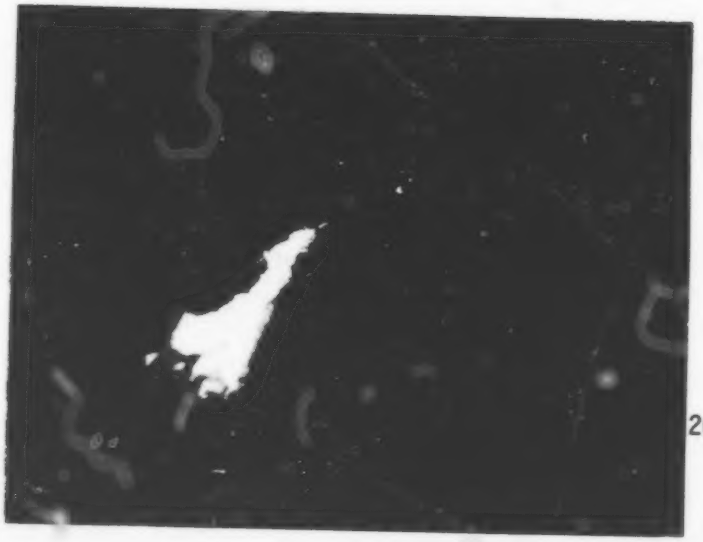

Figure #2

20000X

Reproduced from best available copy.

TEM of Longview Crush #263-E

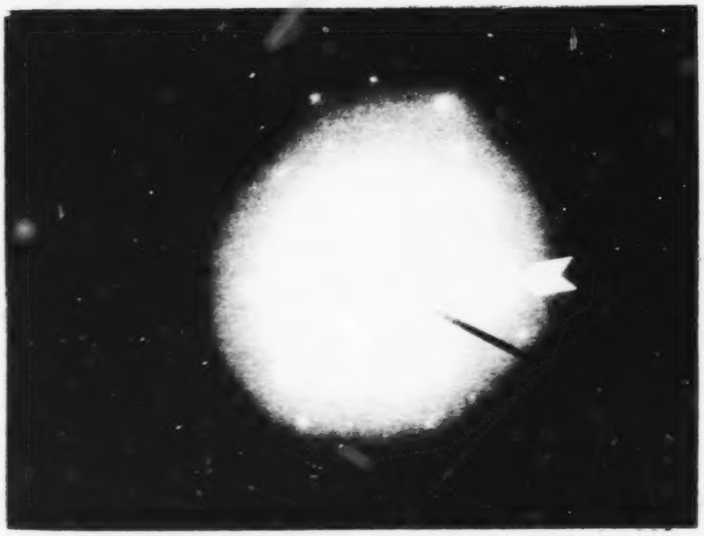

Figure #3

Diffraction Pattern of Particle in Figure #2

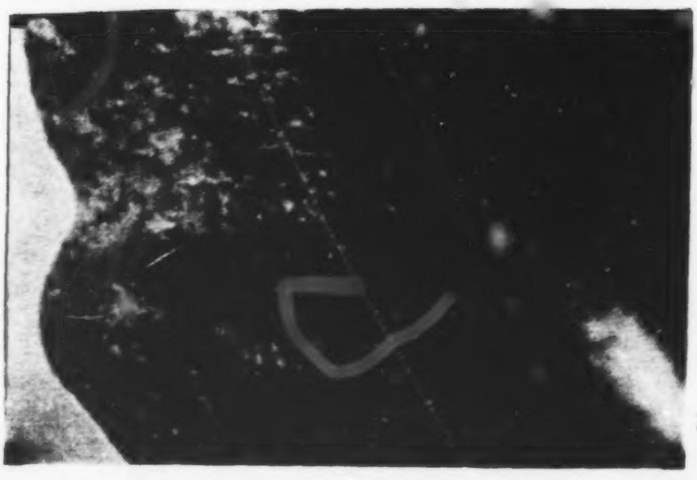

Figure #4

250,000X

TEM of #113436

Figure #5

33000X

Figure #6

33000X

TEM of #113436

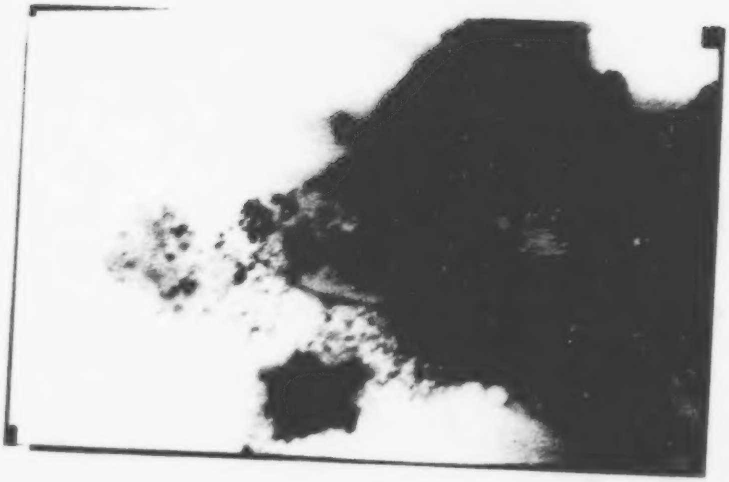

Figure #7

33000X

Figure #8

33000X

TEM of #113298

Figure #9

26000X

Figure #10

26000X